SPECTROSCOPIC AND PHOTOMETRIC MONITORING OF SOUTHERN POST ASYMPTOTIC GIANT BRANCH STARS

A THESIS
SUBMITTED IN PARTIAL FULFILMENT
OF THE REQUIREMENTS FOR THE DEGREE
OF
DOCTOR OF PHILOSOPHY IN ASTRONOMY
IN THE
UNIVERSITY OF CANTERBURY
BY
DANIEL POOLEY

University of Canterbury
2003

Contents

List of Figures

List of Tables

Abstract

A programme of photometric and spectroscopic monitoring has been undertaken in order to investigate the characteristics of suspected post asymptotic giant branch (post-AGB) stars (AI CMi, HD 179821, SAO 209008, HD 70379, HD 95767, HD 172481, HD 168625 and CPD-59 6723).

Long time baseline $BVRI$ photometry was obtained at the Mount John University Observatory (MJUO) over intervals of 1032 and 1463 days. This was complemented with contemporaneous high-resolution spectroscopy also acquired at MJUO.

As a group, post-AGB stars are predicted to have certain broad properties. Analyses of the light curves show that none of the observed stars have stable light and radial velocity curves. Most showed the small amplitude ($\Delta V \sim 0.2$ mag), semi-regular light variations expected for objects with high luminosity to mass ratios. Semi-regular radial velocity variations of between 10-20 km s^{-1} were seen in most of the stars.

Examination of the sodium D lines at high resolution showed many components, between 4 and 7 per star. These are due to a combination of interstellar, circumstellar and photospheric lines. The interstellar lines were used to place lower limits on the distances to the stars. None of the stars showed a clearly identifiable photospheric component. To account for the profiles a range of models were developed, with a combination of photospheric and circumstellar absorptions, in conjunction with chromospheric emission fitting.

Radial velocity measurements revealed generally large mean radial velocities consistent with the stars belonging to the Galactic thick disk population. HD 172481 has a mean radial velocity of ~ -83 km s^{-1}, indicating likely Galactic halo membership.

Hα profiles all showed varying degrees of emission. The hotter stars exhibited P Cygni profiles. For cooler stars the profiles were a combination of large photospheric absorption with a smaller self-absorbed emission superimposed. This emission is caused by mass loss on the order of 10^{-7} $M_{\odot}$ yr^{-1} and arises in a region within a few stellar radii of the star. The profiles are also variable due to relative motion between the three underlying components.

All but one of the stars observed showed signs of cool, 100-400 K, circumstellar material. The amount of extinction provided by this material is expected to be small, on the order of a few tenths of a magnitude. Only

HD 172481 showed clear indications of circumstellar extinction. The masses of these shells were estimated from the 60 μm fluxes acquired by the IRAS satellite.

With the loose classification criteria for post-AGB stars, we have also observed some quite individual behaviour in a number of our objects. AI CMi showed light and spectrum variations similar to the RV Tauri class of variables. HD 70379 showed a variable amplitude due to a combination of two simultaneous radial oscillations. HD 172481 has a cool Mira type companion which causes the I-band light curve to vary with a consistent large amplitude ($\Delta I \sim 0.55$ mag) but with a variable amplitude in the BVR-bands.

HD 95767 proved to be a binary star with a cool companion. During the time of our observations, initial low amplitude variations due to pulsations of the primary, were disrupted by the periastron passage of the companion. This also caused emission lines to be seen in the spectrum.

Chapter 1

Introduction

Post asymptotic giant branch (post-AGB) stars, or pre-planetary nebulae (PPN), are the last stage in the life of low to intermediate mass stars ($0.8 \leq M \leq 7\ M_{\odot}$). They are low-mass supergiants covering a wide range of temperatures, with a strong infrared excess as a result of the gas and dust ejected during earlier eras of the star's life.

The post-AGB phase is a short transitional stage in a star's life lasting anywhere from a few years to a few hundreds of thousands of years. The star has ceased evolving on the asymptotic giant branch (AGB), but hasn't quite reached the temperatures required to ionize a planetary nebula. The remnants of the outer envelope eventually disperse to expose the core and, if this happens quickly enough, to illuminate the gas and dust ejected on the AGB. We then see a planetary nebula (PN).

1.1 The evolution of low and intermediate mass stars

By way of introduction I shall begin with a brief tour of the stellar evolution of a typical post-AGB star. The name of the class is derived from their position on the Hertzsprung-Russell (HR) diagram. In Figure 1.1 we can see the paths taken by various low mass models on this diagram as they age. The key stages are:

1. Main sequence (MS, A-C)
2. Red giant branch (RGB, D-E)
3. Horizontal Branch (HB, F-G)

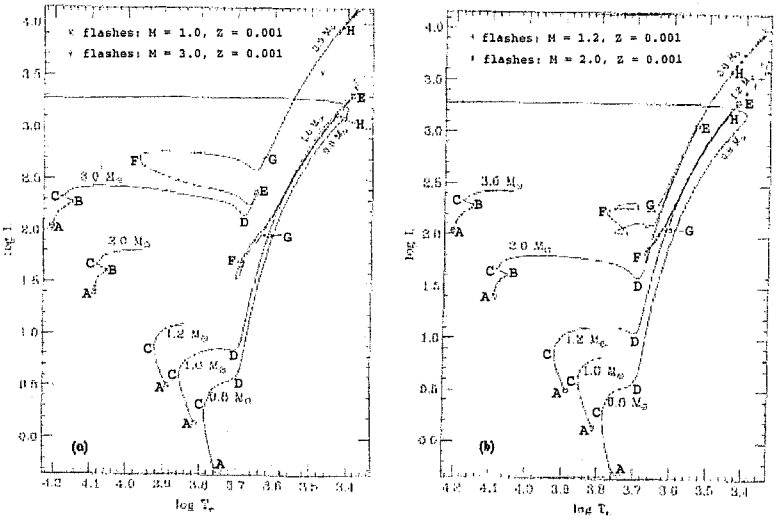

Figure 1.1: The evolution of (a) 0.8, 1.0 and 3.0 and (b) 0.8, 1.2 and 2.0 $M_{\odot}$ stars on the HR diagram (Boothroyd & Sackmann 1988)[22]. The labels on the track correspond to the key points in the evolution identified in the text.

4. Asymptotic branch (AGB, G-H)

5. Planetary nebula (PN) / white dwarf (WD), not shown

The letters A-H identify the key points in stellar evolution marked in Figure 1.1 and in the following text.

1.1.1 ZAMS to AGB

This section covers easily the majority of the star's lifetime. Zero age main sequence (Point A Figure 1.1) marks the point in the star's life when it stops being a condensing ball of gas, and actually becomes a star, defined as the time when hydrogen fusion reactions begin in the stellar core. Typically these stars are still surrounded by large amounts of gas and dust which disperse as the energy released in the core escapes the nascent star. The nuclear reactions slowly accumulate helium as the waste product and this settles in the core. Generally the star will increase in brightness slightly and it will form part of the main sequence which is the locus for about 90% of all stars (Zeilik & Smith 1987)[220].

Solar mass stars will spend several billion years on the main sequence, which falls to tens of millions of years for 7 $M_{\odot}$ stars (Prialnik 2000)[157]. Higher mass stars have a red edge to the MS, marked by point B, when the central stocks of hydrogen are almost exhausted. Point C marks the end of central hydrogen burning and the main site of fusion is now a shell surrounding a helium core. This is the end of the main sequence life of the star. The star expands and cools and moves to the red giant branch (D). As a consequence of the reduced surface gravity there is an increase in the rate of mass loss.

There are some changes in the internal structure at this time with a deep convective envelope reaching down to the central regions of the star. This allows for some of the products of nucleosynthesis to be brought to the surface of the star in what is known as the *first dredge up*. These products are revealed in unusual chemical abundance patterns. Generally this involves a decrease in the amount of ^{12}C and lithium but an increase in ^{14}N (Becker & Iben 1980)[12]. The star will evolve up the RGB to higher luminosities until eventually the helium core becomes hot enough to fuse helium (E) to form carbon and oxygen in the core. For 0.8 $M_{\odot}$ models the central degeneracy is not lifted enough for core He-burning to commence and the star expels its outer envelope in one violent outburst. For heavier stars the degeneracy is lifted allowing He-burning to proceed via the triple α-process. The core expands and the envelope shrinks to preserve the total gravitational energy, and the star moves to hotter temperatures and on to the horizontal branch, where it burns helium in its core. As we can see from Figure 1.1, as the initial mass of the star increases so does the extent of the evolution of the star on the HB to hotter temperatures. Point F marks the hottest point of the star's HB evolution.

If the star is massive enough after the HB phase it will be able to accumulate enough inert carbon and oxygen to displace the site of helium burning (G) from the centre of the star and cause a repeat of the process that caused the star to leave the MS: the star gets larger and cooler; it gets more luminous; and the convective envelope reaches down and mixes more processed material to the surface. This is the *second dredge up* and it occurs only for stars more massive than about 4 $M_{\odot}$ (Blöcker 1999)[20]. This sees a further reduction in the amount of carbon at the surface, and it also reduces the amount of oxygen while increasing the levels of nitrogen (Becker & Iben 1979)[11]. The star is now on the asymptotic giant branch.

1.1.2 AGB

On the early-AGB (E-AGB) most of the energy is provided by the helium burning shell, but this is unstable and in the long term the hydrogen burning shell becomes dominant. So we have a star in which the majority of the mass is tied up in a CO core ($\sim 0.5 - 1\ M_{\odot}$), surrounded by the two shells ($\sim 0.01\ M_{\odot}$), which also serve to increase the mass of the core. Left unchecked the core would eventually reach the carbon burning limit ($\sim 1.4\ M_{\odot}$), but AGB evolution ceases before this stage is reached (Blöcker 1999)[20].

This is not a stable situation, as the He-shell undergoes *thermal pulses* caused by runaway helium burning reactions (Schwarzschild & Härm 1965) [173]. This part of the AGB evolution is also denoted TP-AGB, for thermally pulsing AGB. Thermal pulses disrupt the internal structure of the star: the H-shell is pushed into cooler regions and extinguished, and the He-burning shell providing most of the energy for a short time, until the H-burning shell is re-established. It is possbile for a star to undergo a large number of thermal pulses while on the AGB, with the interpulse period ranging from several thousand down to just tens of years for stars with greater core masses (Paczyński 1975)[146].

In certain cases the convective envelope is able to reach into the depths of the star and retrieve some of the bi-products of the energy generation, causing the star to have unusual photospheric abundances. Although this process is called the *third dredge up*, the name refers to a pattern of behaviour and stellar structure rather than a specific incident. The results of this are visible on the surface of the star as changed chemical abundances, particularly in the appearance of light elements, like lithium and carbon, and heavier, *s*-process elements, such as barium, yttrium and strontium. Non-solar system isotope ratios have been detected in the grains of materials taken from meteorites which are quite consistent with model predictions for AGB abundances (Lewis et al. 1990[117], Zinner & Amari 1999[221]).

Mass-loss rates for AGB stars range from $10^{-7}\ M_{\odot}\ \mathrm{yr}^{-1}$ for young AGB stars which can increase to $10^{-4}\ M_{\odot}\ \mathrm{yr}^{-1}$ for the more massive stars which are capable of evolving further along the AGB (Habing 1996)[74]. This is provided by the action of radiation pressure on dust grains which form in the cool stellar atmospheres. In general these dusty winds are spherically symmetric as can be seen in Hubble Space Telescope images of some PN and PPN (Kwok et al. 2001)[109]. Thermal pulses can also provide temporary rises in the mass loss rate, the size of which varies depending on the model adopted (Steffen & Schönberner 2001)[177].

Despite the great detail of the preceeding evolutionary scenarios it should

be noted that they are quite sensitive to the various parameters adopted. For example, Blöcker (1993)[17] showed that the post-AGB evolution of a 0.84 $M_{\odot}$ object depends on the initial ZAMS mass, which generate different internal structures within the star causing it to fade differently. The third dredge up is also subject to a great deal of model specific variation, depending on the choice of the evolutionary model adopted, treatment of convection, and what numerical averaging methods are employed (see Lugaro et al. 2003[124] and references therein). Additionally different authors adopt different regimes for the critically important mass loss. Generally they start with the Reimers' rate (Reimers 1975)[160] which relates mass, luminosity and radius to the mass loss rate of red giant stars. From there various modifications are adopted based upon the observed mass-loss rates of AGB stars, e.g., Volk & Kwok (1989)[207], Vassiliadis & Wood (1993)[202], and Blöcker (1995)[19]. As yet there is no mass-loss regime derived from first principles. The aforementioned papers use observations to decide how the mass loss behaves, rather than using the stellar model parameters to determine how the star loses matter. Also none of these papers investigate fully the role of pulsations in post-AGB mass loss.

1.1.3 Post-AGB evolution

Once the envelope mass reaches a certain value, generally believed to be about 10^{-2} $M_{\odot}$ (Blöcker 1995)[19], then it is unable to sustain high mass-loss rates and the star moves off the AGB and becomes a post-AGB star. These stars are still shedding their outer envelopes but not as rapidly. The gas and dust ejected during the superwind phase (Renzini 1981)[161] becomes detached and the central star is slowly revealed. As the envelope disperses mass-loss rates are now of the order of 10^{-7} $M_{\odot}$ yr^{-1} (Schönberner & Steffen 2001)[171] and progressively hotter layers of the star are seen. On the HR diagram the star evolves at constant luminosity to hotter temperatures, before the whole envelope is either dispersed or consumed by the hydrogen burning shell, and the stellar remnant is exposed. If this warming of the central star occurs fast enough ($t \leq 1000$ yr) then the UV radiation will be able to illuminate the expanding shell and cause it to fluoresce. A planetary nebula is seen. This is the distinguishing feature between the larger class of post-AGB stars and PPN. The latter are massive enough for their post-AGB evolution to be completed before the dispersal of the stellar envelope. However, the terms are often used interchangeably.

From Figure 1.2 it can be seen that the models predict that the more massive the stellar remnant is then the shorter the post-AGB phase. This

is due to higher mass loss rates for the more massive stars (Schönberner 1979)[169]. The effective temperature of the star is a function of the mass of the envelope. This depends on the mass loss and upon the rate at which nuclear reactions are proceeding. The models of Schönberner (1983)[170] predict that the former will dominate in the case of higher luminosity stars.

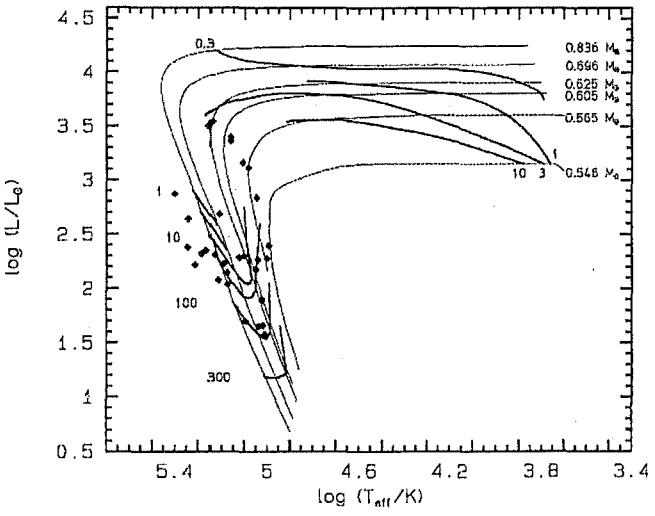

Figure 1.2: Figure 6 from Blöcker (1993)[18] showing evolutionary tracks for six models with observational data for optically thick planetary nebulae. The time marks are in thousands of years.

However this is not the only evolutionary track through this region. Much theoretical interest has been generated in so-called "born again" post-AGB stars like FG Sge and Sakurai's Object (see Figure 1.3). The current theoretical interpretation of these peculiar objects is that they have already evolved from the AGB and have experienced a final thermal pulse at some stage in their evolution (Asplund 1999)[6].

If the star is still obtaining energy from a helium burning shell then the star can undergo a thermal pulse. If this pulse occurs just before the star turns off the AGB, then it can cause the stellar envelope to be enriched with carbon and by mixing hydrogen down into the shell burning regions can cause hydrogen to be depleted. Late, and very late, thermal pulses have also been considered and these produce even greater levels of hydrogen deficiency than the final thermal pulse. These occur on the post-AGB track and cooling branch respectively. The latter is especially successful in providing models

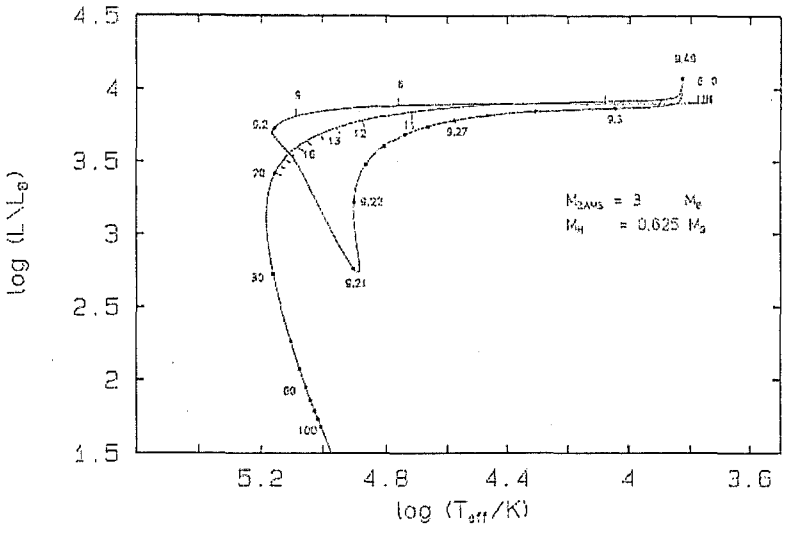

Figure 1.3: An example of a late thermal pulse taken from Blöcker (1995)[19]. The ticks on the track are in thousands of years.

with abundances similar to the H-deficient central stars of planetary nebulae.

1.2 Observational aspects of post-AGB stars

Identifying post-AGB stars is not an easy task as they do not have any single key traits. As well as being supergiant stars, the assignation of the label "post-AGB" involves all of the following characteristics.

1.2.1 Radial velocities

Most post-AGB stars have evolved from low-mass stars and will therefore be relatively old objects. In different epochs star formation occurred in different parts of the Galaxy and these regions have different kinematics (Harpaz 1994)[76]. Currently the main site of star formation is the thin disk. When the current post-AGB stars were forming this was the thick disk. The velocities of the two groups are different with the thick disk stars having greater vertical and slower rotational velocities than the younger stars in the thin disk. Other ancient sites of star formation are the halo and bulge, each with its own velocity law. In all three cases for old stars

the average space motions will combine to provide them with higher radial velocities overall than those observed for younger stars in the thin disk.

1.2.2 Infrared signature

The advent of the InfraRed Astronomical Satellite, IRAS, greatly enhanced the search for post-AGB stars. Indeed the key selection criteria for post-AGB star candidacy have been supergiant luminosity class combined with an infrared excess, e.g., Volk & Kwok (1989)[207], Oudmaijer et al. (1992)[145], Trams et al. (1991)[186] and van der Veen et al. (1989)[191]. However it could be that such samples are incomplete and closer attention is needed to the evolution of the star and its environment during the early post-AGB stages (van Hoof et al. 1997)[196].

The chemistry of the circumstellar environment is also a function of the evolution of the star on the AGB. Lower-mass stars will leave the AGB after only a few thermal pulses. Consequently the surface C/O ratio will be quite low and this is reflected in the composition of the gas and dust around the star, which will consist of CO and silicate material respectively. For higher mass stars the nucleosynthesis is able to produce enhanced amounts of C-rich material which ends up as graphite and other carbon compounds in the circumstellar environment. Intriguingly some stars show both silicate and carbon signatures in their infrared and microwave emission indicating a rapid transition between the two states. O-rich material is characterized by an emission peak at 9.7 μm due to SiO, while the 21 μm signature of C-rich objects has recently been attributed to titanium carbide (Von Helden et al. 2000)[208].

1.2.3 Photospheric abundances

Lithium has been much discussed in the literature. As the lightest metal it is easily destroyed in stellar interiors due to the PP II reaction chain (Cowley 1995)[37]. ^{7}Li is produced by the Cameron-Fowler mechanism (Cameron & Fowler 1971)[30] which requires α-capture by ^{3}He, to form ^{7}Be, which subsequently decays to ^{7}Li. Boothroyd & Sackmann (1992)[23] showed that under hot bottom burning (HBB), i.e., when the temperature at the bottom of the convective envelope exceeded 5×10^{7} K, stars with $M > 4M_{\odot}$ were able to reach lithium abundances as high as [Li/H]= +3.4.

One of the key changes that stars undergo when they reach the TP-AGB is that the C/O ratio increases. This is due to convection established during the pulse reaching far enough into the star to mix the products of shell He-

burning to the surface. As the stars spend more time on the AGB and have more thermal pulses, then more carbon is mixed into the envelope and the C/O ratio is increased further. HBB also produces a change in the carbon isotope ratio, cycling ^{12}C to ^{14}N via ^{13}C. Thus it is possible for HBB to destroy ^{12}C and prevent (or delay) the formation of a C-star (Boothroyd et al. 1993)[25]. However, this is not effective in low mass ($M < 4\ M_{\odot}$) models since the temperatures at the base of the envelope are not hot enough (Sackmann & Boothroyd 1992)[165]. Wasserburg, Boothroyd & Sackmann (1995)[210] proposed that in some RGB stars meridional currents induce an additional mixing which can account for the ^{12}C/^{13}C ratios, low ^{18}O abundances and high Li-abundances in these stars. This is cool bottom processing (CBP) and it may operate in AGB stars during the thermal pulse phases (Boothroyd & Sackmann 1999)[24]. Both CBP and HBB cause lithium to be produced and then transport enough of it away to cooler layers before it is destroyed.

The *s*-process, or "slow" neutron enrichment process, is a nucleosynthesis reaction scheme which allows a heavy nucleon to be built up from a lighter seed nucleus via the capture of neutrons on timescales much longer than those of the resulting β-decay schemes (Burbidge et al. 1957)[27]. In this way it is possible to build up nucleons heavier than iron, like strontium, yttrium and barium. The source of these neutrons in the interiors of AGB stars has two main candidate reactions: ^{22}Ne(α,n)^{25}Mg (Cameron 1960)[29] and ^{13}C(α,n)^{16}O (Cameron 1955)[28]. During a thermal pulse the former is not active as the ambient temperatures are considerably less than the 3×10^{8} K required for ^{22}Ne to burn (Lattanzio 1993)[111]. The latter requires additional protons to be mixed into ^{12}C rich layers so that enough ^{13}C can be produced via ^{12}C(p,γ)^{13}N(β^{+}, ν)^{13}C (Iben & Renzini 1982)[92]. The intershell region is the site of *s*-process nucleosynthesis.

1.2.4 Pulsation

Interestingly only a few radial velocity studies have been done of post-AGB stars (e.g., Hrivnak et al. 2001)[88]. But due to the extremely high $L : M$ ratio these stars present a challenge to theoreticians.

Some F- and G-type supergiant stars have effective temperatures which are too hot for them to lie in the classical instability strip (Gautschy & Saio 1996)[65]. However, theoretical studies have shown that pulsations can be excited across the HR diagram provided that the $L : M$ ratio is large enough. Aikawa (1991)[1] examined non-linear pulsations in post-AGB stars and found that his models produced irregular low amplitude radial pulsa-

tions. Zalewski (1993)[217] showed that with the OPAL opacities (Rogers & Iglesias 1994)[164] for these stars, the pulsational instability strip extended to higher temperatures. His nonlinear models predicted low amplitude semi-regular photometric variations, on the order of 0.04 mag between 8000 and 16000 K, with radial velocity variations of about 30 km s^{-1}. More generally he also found that the fundamental, first and second overtones are stable in the regions of the HR diagram where post-AGB stars lie. Gautschy (1993)[64] confirmed this result and showed that the iron bump in the OPAL opacities, as well as He II, He I and H ionisation, can also generate instabilities in these high luminosity low mass scenarios.

Hrivnak et al. (2001)[88] monitored about 40 northern PPN candidates photometrically, and nine of these spectroscopically. The results broadly confirm the models, in that all of the stars, which span spectral type K to O, showed photometric variability, with a range of 0.15 to 0.40 mag. Seven stars of spectral types F and G, exhibited periodic variations from 45 to 150 d but with variable amplitudes. And the early type stars exhibited variations with periods of less than 10 d. The radial velocity monitoring found peak-to-peak variations of around 10 km s^{-1} in all nine stars.

More recent dynamical studies have focused on the behaviour of HD 56126 (SAO 96709). Fokin et al. (2001)[60] built on earlier work by Jeannin et al. (1996)[94] and Barthès et al. (2000)[10], producing a series of models in the range: $M = 0.6\text{-}0.8\ M_{\odot}$, $L = 4500\text{-}8000\ L_{\odot}$ and $T_{\rm eff} = 5600\text{-}6300$ K. Metal line velocities change by 10-15 km s^{-1}, and the shape of Hα and Hβ profiles were reported to be variable on timescales of a week (Barthès et al. 2000[10]; Lèbre et al. 1996)[115]. This suggests large amplitude ($\sim 40 - 47$ km s^{-1}) shock waves propagating in the atmosphere. However, the photometric variation is quite small $\Delta V = 0.06\text{-}0.15$ mag (Bogaert 1994)[21]. Barthès et al. (2000)[10] found that the radial velocities and the photometry had a main period of 36.8 ± 0.2 d, with no period near 70 d, which would indicate that the star is an RV Tauri variable. Linear non-adiabatic analysis indicated that the star was oscillating in the first overtone mode.

Pulsational models have indicated that post-AGB stars should pulsate. The exact details of the pulsations depend on the details of the models and so it is important for modellers to get observations with which to constrain their models. This will have effects further down the evolutionary chain by limiting the choices of parameters that influence the models of AGB stars.

1.3 Circumstellar environment

One of the selection criteria for a post-AGB candidate is the presence of an infrared excess. This is generated by gas and dust ejected by the star on the AGB absorbing the star's radiation and re-emitting it in the infrared. Post-AGB stars can be separated into two groups on the basis of their spectral energy distributions (SED, see Van Winckel 1999)[199].

The first group has a double peaked SED consisting of a stellar and cool dust ($T_{\rm d} \sim 100 - 200$ K) component. Examples of these can be found in Hrivnak et al. (1989)[87]. This is due to an old expanding shell of material ejected from the star on the AGB, which has become detached from the star.

The other group of stars shows a hot dust signature ($\sim$ 500 to 1500 K), in addition to the stellar feature (Trams et al. 1991)[186]. Closer investigation, including radial velocity studies, have found that there is a correlation between hot dust and binarity. This is a significant result, as the presence of a companion star will effect the evolution of both stars.

1.4 Role of binarity

One key area in which binarity manifests itself is that all of the stars with extremely low iron abundances, [Fe/H]≤ -3 in the case of HR 4049 (Lambert et al. 1988)[110], are binaries (Van Winckel et al. 1995)[200]. The depletion causes unusual surface abundances which resemble those expected from the third dredge up. In particular the ratios of C:O and CNO:Fe will all be increased. Venn & Lambert (1990)[204] explained these ratios in the context of the λ Boötis stars, proposing a mechanism which locks away refractory elements like iron in dust grains which are then separated from the gas by radiation pressure. The metal depleted gas then settles back on the photosphere. In such stars [Zn/Fe] will be higher than for other iron peak elements, as zinc has a lower boiling point and does not condense onto dust grains so readily.

There are problems with the binary orbits, in particular with non-circular and short period orbits, problems that are shared with barium stars (Jorissen 1999)[98]. Both these problems arise when one considers the AGB evolution of either or both members. There should be a lack of short period orbits as the stars in such systems will merge on the AGB. For wider binaries the filling of the stellar Roche lobe will cause a mass and momentum transfer which will circularize the orbits. This could be resolved by the system

interacting with a circumbinary disk in a way that increases the eccentricity (Lublow & Artymowicz 1992)[122].

Livio & Soker (1988)[120] have shown that binary systems are an effective way to generate the bi-polar nebulae seen around many PPN.

1.5 UU Herculis stars

The post-AGB stage incorporates many different types of unusual star, including RV Tauri stars, W Virginis and R CrB variables. The UU Herculis stars are also possible members of this class. Their main characteristics are (Fernie 1981[56]; 1993[57]):

1. a variable pulsation amplitude;
2. sudden halt in the middle of a cycle;
3. periods from 40 to 70 days, but mostly about 45 d;
4. radial velocity not variable over a pulsation cycle;
5. saw-tooth rather than sinusoidal light curve, potentially with different rates of rise and fall;

Based upon an abundance analysis of the prototype star, Klochkova et al. (1997)[107] concluded that the underabundance of iron along with depleted *s*-process elements indicates that only the first dredge up has occurred and therefore the star is a low-mass halo object but not a post-AGB star. Another indication of their evolutionary status comes from the lack of change in the period of oscillation (Fernie 1989)[58]. Even though they have high Galactic latitude, high velocity and unusual abundances the lack of a change in period implies halo objects rather than post-AGB, as the latter would be expected to change as they rapidly evolve to higher temperatures.

1.6 Introduction to the thesis

In this thesis photometric and spectroscopic observations of post-AGB stars and some related objects are presented with a view to understanding both the dynamical aspects of post-AGB stars and also how they relate to other supergiant stars.

In Chapter 2 the photometric programme is discussed, including the instrumentation, acquisition of data and their preliminary reduction. This

part of the project has been carried out at the Mount John University Observatory (MJUO) where approximately four years of multicolour *BVRI* photometry has been obtained for the stars. These data are presented in Appendix A.

The techniques used to analyse the data are also presented in this chapter. The emphasis of these is to identify particular periodicities within the photometry and to explore some of the interstellar and circumstellar features exhibited by the stars.

Chapter 3 summarizes the spectroscopic component of the programme, including the acquisition, reduction and analysis of the spectra. Again the emphasis is on period searching, but we also examine techniques relating to multiple component fitting to line profiles and some unusual spectral features. Appendix B is the observational log for the project and Appendix C contains the radial velocity data presented in the programme.

The main body of the thesis, Chapters 4 to 11, deals with the results of individual stars starting with the coolest and finishing with the hottest. This provides a sequence to investigate the properties of post-AGB stars as they age.

Finally in Chapter 12 the main findings of the thesis are presented along with suggestions for future work.

Preliminary results for HD 70379, HD 172481 and HD 168625 were presented as a poster paper at IAU Symposium 191 *Asymptotic giant branch stars* and subsequently appeared in the conference proceedings (abstract only) and in Southern Stars (Pooley et al. 1999)[153].

Chapter 4 on AI CMi was presented in part as part of a poster paper at the Astronomical Society of Australia meeting in Hobart in 2000 (Pooley et al. 2000)[154].

Chapter 2

Photometry

As a useful tool in determining the nature of these stars $BVRI$ photometry has been acquired from the Mt John University Observatory (MJUO) in the South Island of New Zealand: latitude 43° 59.2″ S; longitude 170° 27.9″ E; and an altitude of 1029 metres above sea level.

2.1 Photometric acquisition

2.1.1 Photometric instrumentation at MJUO

The data used in this part of the project were collected as part of the service observing programme undertaken by Alan Gilmore and Pam Kilmartin. The primary telescope used was the 0.61-metre Optical Craftsmen (OC) telescope. This is a fork mounted telescope and is used at a focal ratio of f/13.5 with the instruments at the Cassegrain focus.

The detector was one of the two thermoelectrically cooled single channel photometers: the EMI 9558 B or the EMI 6094 B. For this programme Johnson BV and the Cousins RI filters were used. For some stars the occasional measurement was obtained with the Johnson U filter.

2.1.2 The post-AGB star monitoring programme

The photometric monitoring programme covering 28 stars was initiated in 1997 October and continued until mid-2001 providing a baseline of 1613 days (4.4 years). Prior to this programme some of these stars had no significant $BVRI$ photometric coverage at all, while others had already been found to be variable and were included to provide a point of reference or to check for possible evolutionary effects depending on when the star was last monitored.

For each star the comparison and check stars were selected on the basis of being near the object star, as well as matching its brightness and colour indices as closely as possible. Consequently the initial scheme of selecting calibration stars based upon their spectral type proved unsatisfactory as the target stars are noticeably reddened and the spectral type is not a particularly accurate indicator of colour. So in general, stars about one spectral type later than the target star were selected as comparison and check stars.

2.1.3 Acquisition of data

There are four *photometric coefficients* used to reduce the raw data collected each night:

i **Scale constant.** This should be close to 0 for V and 1 for the colour indices. It relates the raw colour index to the standard.

ii **Zero point.** A correction to compensate mainly for temperature variations in the detector. Normally it will affect only the comparison's V magnitude.

iii **Primary extinction.** Compensates for atmospheric absorption in each band. It is the most variable of these coefficients. A mean extinction is determined at varying intervals throughout the night. Note that the difference in air mass between the variable and its calibration stars will be very small, and consequently so will the *extinction error.*

iv **Secondary extinction.** Corrects for the differences within a band due to colour differences between stars.

The comparison is reduced directly using the photometric coefficients adopted for that night. Its values will therefore be a measure of how well these coefficients relate to the actual observing conditions on that night, since not all of these coefficients are calculated every night. For example, the zero point may be affected by anomalous detector temperatures. Cloud can introduce large night-to-night variations, and if the brightness varies with air mass then the adopted extinction would be incorrect.

However, these errors may not necessarily propagate to the other stars' results. All the other data are obtained differentially from the comparison. Thus slow variations in transparency can be removed. In practice, where the comparison measures bracket those of the other stars, these are interpolated. This can be seen in Figure 2.1. The comparison (top) shows an apparent

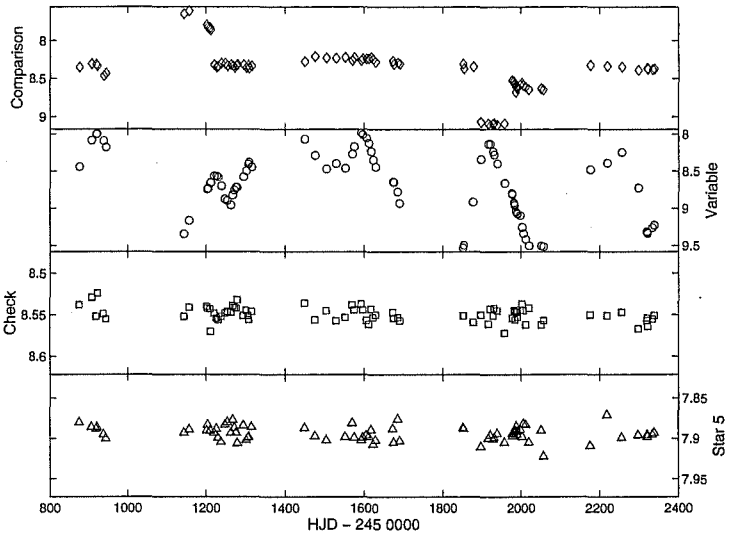

Figure 2.1: V-band magnitudes for AI CMi and its comparison and check stars.

peak-to-peak variation in the V-band of about 1.3 magnitudes, but the two check stars remain constant to within ± 0.05 magnitudes. The variation in the comparison is due to the variation in the photometric coefficients not due to actual stellar brightness changes.

The best way to check for night-to-night consistency is to see how the check stars behave. Variations mean either the comparison or the check is variable. This is why it is a good idea to include two check stars for each variable. The primary is referred to as **Check** and the secondary as **Star 5**.

Initiating an observing programme means arbitrary values will be assigned to the comparison and check stars on the basis of a couple of observations to test their constancy. These may later be recalibrated.

Normally the observing sequence is sky, comparison, variable, check, variable, star 5, comparison, sky. However only one sky value may be acquired if the sky contribution is small. The filter sequence is always $BRVI$. At the start of a night the observer specifies the ratio of exposure times in each filter to get enough counts in each. Typically for $BVRI$ the ratios are $1:1:1:5$. Thus a base observation time of 5 seconds leads to integrations of 5, 5, 5, and 25 seconds in the respective filters. The actual observing time for each star within a field may be varied to get statistically significant

counts.

Some simple filtering is employed based upon the V-band photometry of the check stars, to determine whether or not the photometry for a given night is to be included for analysis. The two lowest and highest values are removed and the mean and standard deviation are determined from this subset. Points from the full sample which are found to lie within three standard deviations of the subsample mean are retained. Nights for which the check star brightnesses lie outside this range are rejected and do not appear in the analysed data set.

2.1.4 $JHKL$ photometry from SAAO

For a number of the stars in this programme, $JHKL$ photometry was acquired from the South African Astronomical Observatory (SAAO) by Dr Karen Pollard using the mark 3 infrared photometer with an InSb detector on the 1.9m Radcliffe telescope. This system has been calibrated by Carter (1990)[32] and is accurate to better than ± 0.04 magnitudes at JHK and ± 0.06 mag at L (Evans et al. 1988)[54].

2.2 Analysing the photometry

2.2.1 Dereddening

Most of the stars in this programme show significant reddening. For these supergiant stars the lines of sight in the Galaxy will encounter one or more of dust clouds and thus be affected by reddening. Additionally these stars show considerable infrared excess, indicating a large amount of circumstellar (CS) gas and dust which may also generate extinction in its local environment.

2.2.2 General properties of dust

For stars at large distances one would expect the light to encounter some dust at some stage. This has two major effects on the light:

1. it diminishes the light (*extinction*), and
2. it produces a change in the observed distribution of the light (*reddening*).

The former is fairly obvious, but the latter is a more subtle effect due to the preferential extinction of shorter wavelengths over longer ones.

For a given photometric band at a wavelength of λ, the extinction in that band, A_λ, is defined as the difference between the observed (m_λ) and intrinsic ($m_{\lambda o}$) magnitudes,

$$A_\lambda = m_\lambda - m_{\lambda o}. \tag{2.1}$$

The size of A_λ depends not just on the wavelength, but is also a function of the position in the Galaxy. Extinction is larger where there is more dust, and this is generally highest in the Galactic plane where most of the dust and gas is.

Extinction also distorts the expected colours. A colour index is defined as the difference between the magnitudes in two bands, eg:

$$CI = m_{\lambda_1} - m_{\lambda_2}, \tag{2.2}$$

where in general $\lambda_1 < \lambda_2$. CI is a measure of the ratio between the fluxes in two bands expressed in the magnitude scale. The amount of extinction depends upon wavelength and is generally higher at shorter wavelengths. This *reddens* starlight. So stars show higher temperatures from spectral typing than one would expect from their photometric colours. The *colour excess* is the difference between the observed and the intrinsic colours:

$$\begin{aligned} E_{\lambda_1-\lambda_2} &= CI - CI_o \\ &= (m_{\lambda_1} - m_{\lambda_2}) - (m_{\lambda_{1o}} - m_{\lambda_{2o}}) \\ &= (m_{\lambda_1} - m_{\lambda_{1o}}) - (m_{\lambda_2} - m_{\lambda_{2o}}) \\ \Rightarrow &= (A_{\lambda_1} - A_{\lambda_2}). \end{aligned} \tag{2.3}$$

Thus the colour excess can tell us about the extinction in the two bands.

For the Johnson system it is common to use the B and V-bands. A particularly nice feature is that for interstellar (IS) dust the ratio of total to selective absorption, R_V, is a constant and is given by:

$$\begin{aligned} R_V &= \frac{A_V}{E_{B-V}}, \\ R_V &\simeq 3.05 \pm 0.15. \end{aligned} \tag{2.4}$$

This is a consequence of the mean size of the dust particles, which are on the order of 0.05 μm for IS dust (Scheffler & Elsässer 1988)[167]. Larger values of R_V correspond to more neutral extinction from larger particles

which don't have such a strong preference for scattering shorter wavelengths. Cardelli et al. (1989)[31] devised a parametrization of the way that the extinction behaves as a function of R_V. In this scheme the extinction is normalized in the V-band and the extinction in one of the $UBVRIJHKL$-bands, A_λ, is given by:

$$A_\lambda = a_\lambda + \frac{b_\lambda}{R_V}, \tag{2.5}$$

where a_λ and b_λ are the band specific coefficients listed in Table 2.1. So once the visual extinction is obtained the other extinctions, and therefore the colour excesses, will follow. One thing to bear in mind is that the specified system is Johnson and MJUO uses the Cousins R and I-bands. The mean bandpasses of the systems are different and produce a noticeable shortfall in the dereddened magnitudes which causes the blackbody fits to predict higher temperatures for the stellar component. So to obtain the appropriate reddening the values for the Johnson system are calculated and then a cubic spline is fit to these data to interpolate the values at the Cousins wavelengths.

Band	a_λ	b_λ
U	0.9530	1.9090
B	0.9982	1.0495
V	1.0000	0.0000
R	0.8686	-0.3660
I	0.6800	-0.6239
J	0.4008	-0.3679
H	0.2693	-0.2693
K	0.1615	-0.1485
L	0.0800	-0.0734

Table 2.1: Coefficients for the extinction parametrization of Cardelli et al. (1989)[31].

The paper of Hakkila et al. (1997)[75] provides an overview of some key papers concerning the Galactic extinction law. These include the studies of Fitzgerald (1968)[59], Neckel & Klare (1980)[137] and Arenou et al. (1992)[4]. They also provide a computer code (EXTINCT.FOR) which can

compute the extinctions for the various regimes covered and combine them to obtain an average value.

So to deredden the observed colours of a star the first step is estimating the nett colour excess using the spectral type. The intrinsic colours are taken from Cox (2000)[38]. Equation 2.4 is then used to get the total visual extinction along the line of sight. Although the extinction laws for IS and circumstellar dust may be different due to a different mix of grain sizes and compositions, there is not enough information available at present to justify using a different one for the circumstellar material. This is then used to correct the apparent visual magnitude, and using the absolute visual magnitude, a distance modulus and a distance are also calculated. This distance will provide an upper estimate as there will probably be some contribution from the CS matter.

$$\begin{aligned} m_V - M_V &= 5\log d - 5 + A_V \\ \Rightarrow d &= 10^{\frac{m_V - M_V + 5 - A_V}{5}}. \end{aligned} \tag{2.6}$$

Most of the error in the derived distance is going to come in through the estimated absolute visual magnitude. The error in m_V is of the order of several thousandths of a magnitude. A_V is derived through a combination of $B-V$ colour measurements and an estimate of spectral type. Its errors will be dominated by uncertainties in the latter, which are on the order of tenths of a magnitude. Assuming the colour-type calibration to have negligible errors, errors in the assigned spectral type will peak where $B-V$ changes most rapidly across a spectral class. This is most apparent in late F- and early G-type supergiants and amounts to at most 0.2 magnitudes for a two sub-type error (On average it is 0.07). Compared with these, a ± 2 magnitude uncertainty in M_V due to luminosity variations within a luminosity class, is very much larger and leads to distance estimates which vary by a factor of 2.5. Unfortunately this means that virtually any reasonable distance is possible, and the values derived should be treated with some skepticism. This also applies to the values obtained for the IS contribution to the total extinction, which will also be uncertain by about the size of the error in the absolute magnitude.

For most of the stars dereddened in this way the results are sensible in that the total extinction is more than that estimated from IS dust along the line of sight. For a few stars this is not the case, with the total extinction being less than that from the ISM. This is due to an incorrectly determined spectral type, distance or from an anomalous Galactic extinction law along

the line of sight to the star.

2.2.3 Circumstellar dust mass

To estimate the mass of circumstellar dust we have used the prescription of Soifer et al. (1986)[176], which is based upon earlier work by Hildebrand (1983)[81]. This work derives a relationship between the observed infrared flux and the emitting mass, assuming an idealized isothermal dust cloud composed of identical spherical dust grains of radius a. The flux density, $F(\nu)$, from a cloud at a distance D, comprising N dust grains each of cross section σ and emissivity $Q(\nu)$ at a temperature of T, is given by

$$F(\nu) = N[\sigma/D^2]Q(\nu)B(\nu,T), \tag{2.7}$$

where $B(\nu,T)$ is the blackbody flux at the frequency ν of a body at temperature T. The volume of dust will be

$$V = Nv, \tag{2.8}$$

where v is the volume of a single grain. Assuming a grain density, ρ, and after eliminating N from equations 2.7 and 2.8 the dust mass is

$$\begin{aligned} M_{\rm d} &= V\rho \\ &= [F(\nu)D^2/B(\nu,T)][(4/3)a/Q(\nu)]\rho \\ &= \frac{F(\nu)D^2}{B(\nu,T)K(\nu)}, \end{aligned} \tag{2.9}$$

where $K(\nu)$ is the mass absorption coefficient for the dust. Taking the values for grain size ($a = 0.1$ μm) and a grain density ($\rho = 3$ g cm^{-3}) from Hildebrand (1983)[81], the only remaining dust parameter to be determined is the emissivity. In this case a power law dependence on frequency is assumed, $K(\nu) \propto \nu^{\beta}$, where $\beta = 1.5$ (Soifer et al. 1986)[176]. This is the mean of the values specified in Hildebrand (1983)[81]. Starting with the silicate absorption coefficient at 20 μm from Draine & Lee (1984)[44] and extrapolating to 60 μm, we obtain $K(60\ \mu\text{m}) = 230$ cm^2 g^{-1}. So we now have a relationship which contains only one unmeasured quantity, the distance to the star.

As a simple estimate of the radius of the shell, $R_{\rm d}$, we have considered that the star, at temperature $T_\star$, and dust, at $T_{\rm d}$, are in thermal equilibrium, so that the luminosities are the same.

$$R_{\rm d} = \frac{1}{2}\left(\frac{T_\star}{T_{\rm d}}\right)^2 R_\star \tag{2.10}$$

Thus we have a relationship between the size of the star and the size of the dust shell.

2.2.4 Period analysis

The main tool for investigating periodicities in the photometry is the Lomb-Scargle Fourier method (Lomb 1976[121], Scargle 1982[166], Horne and Baliunas 1986[85]). This method has been designed with unevenly sampled data in mind by assessing the data on a per point basis not per time interval as is most usually done in periodogram analyses. This is because it evaluates the data, sines and cosines only at the times of observations, and thus the intervals between the points are less important.

For a set of N observations, y_i, taken at times $t_i, i = 1, ..., N$ the Lomb-Scargle algorithm fits the model:

$$y_i = a_1 \cos\omega(t_i - \tau) + a_2 \sin\omega(t_i - \tau), \tag{2.11}$$

where a_1 and a_2 are the unknowns for a pre-selected frequency ω and τ, the time-offset, is defined by:

$$\tan(2\omega\tau) = \frac{\Sigma_i \sin 2\omega t_i}{\Sigma_i \cos 2\omega t_i}. \tag{2.12}$$

This constant has the effect of leaving the resulting periodogram impervious to shifting the time data by a constant.

The normalized periodogram P_N is given by:

$$P_N(\omega) = \frac{1}{2\sigma^2}\left\{\frac{[\Sigma_i(y_i - \bar{y})\cos\omega(t_i - \tau)]^2}{\Sigma_i \cos^2\omega(t_i - \tau)} + \frac{[\Sigma_i(y_i - \bar{y})\sin\omega(t_i - \tau)]^2}{\Sigma_i \sin^2\omega(t_i - \tau)},\right\} \tag{2.13}$$

and it has the nice property of providing a false alarm probability for each period. What this means is that the probability of finding a peak of height z or more in a periodogram of a spectrum of white noise is:

$$P(>z) = 1 - (1 - e^{-z})^M P(>z) \approx Me^{-z},$$

where M is the number of independent frequencies. In practice, since $P(>z)$ is usually quite small, it is possible to expand the exponential and ignore

the higher order terms. As the various significance levels used are generally an order of magnitude apart, $P(> z)$ is more sensitive to the height of z than on M. z is the peak signal-to-noise ratio. Sampling up to the Nyquist frequency of the data set implies $M \sim N$. The best estimates of M can be obtained through a Monte Carlo analysis.

The Lomb-Scargle program used was provided as part of the Starlink PERIOD suite, which also included Fourier Transform, CLEAN, PDM and least squares period finding programs.

2.2.5 Blackbody fits to the spectral energy distribution

For a number of stars $JHKL$ photometry was acquired and analysed as part of the spectral energy distribution (SED) of the star in order to investigate its local environment. Each SED consists of $UBVRIJHKL$ plus IRAS 12, 25, 60 and 100 μm photometry. The magnitudes are converted into fluxes via the calibrations of Bessell (1979, for $UBVRI$)[16] and Wilson (1972, for $JHKL$)[215]. Up to three blackbody curves are fitted by the function minimization routine FMINSEARCH in Matlab. FMINSEARCH uses the multi-dimensional unconstrained nonlinear Nelder-Mead algorithm, which seeks a local minimum to a specified function.

The main parameter in these fits is the temperature. As real stars are subject to line blanketing, which will depress the level of the continuum compared to a blackbody, it was necessary to do some calibration. $UBVRI$ photometry and effective temperature data for supergiant stars were taken from Cox (2000)[38] and $JHKL$ was taken from Ducati et al. (2001)[45]. These were used to generate synthetic stellar SEDs over the range of spectral types encountered in this programme. The results, presented in Table 2.2 and Figure 2.2, show that for most of the stars in the project a correction is necessary to establish the appropriate stellar temperature from the blackbody fits. The minimum in the correction applied to the fits, at about spectral type G2, also coincides with the minimum in the RMS of the fit. At these temperatures the photometry has a roughly equal distribution about the Wien maximum and is thus able to provide a better fit to the data. The reason for doing the fit for both $UBV...KL$ and $BV...KL$ is that some of our stars do not have U-band photometry and the calibration must also be done for these cases.

Sp T	$T_\star$ (K)	T_{bb} (K)	Corr. (K)	T_{bb} (K)	Corr. (K)
		U		No U	
B2	17600	18166.60	-566.60	24496.78	-6896.78
B5	13600	14363.48	-763.48	17269.38	-3669.38
B8	11100	11567.97	-467.96	14326.88	-3226.88
A0	9980	10457.11	-477.11	12857.55	-2877.55
A2	9380	9661.11	-281.11	11610.58	-2230.58
A5	8610	8827.20	-217.20	10301.18	-1691.18
F0	7460	7905.45	-445.45	8854.60	-1394.60
F2	7030	7558.25	-528.25	8266.77	-1236.77
F5	6370	7054.75	-684.75	7522.80	-1152.80
F8	5750	6191.83	-441.83	6383.83	-633.83
G0	5370	5651.04	-281.04	5629.58	-259.58
G2	5190	5148.69	41.31	5187.47	2.53
G5	4930	4716.10	213.90	4731.95	198.05
G8	4700	4356.04	343.96	4361.47	338.53
K0	4500	4115.15	384.85	4116.54	383.46
M3	3222	3133.57	88.43	3131.50	90.50

Table 2.2: Calibration of the blackbody fits to stellar photometry and effective temperatures.

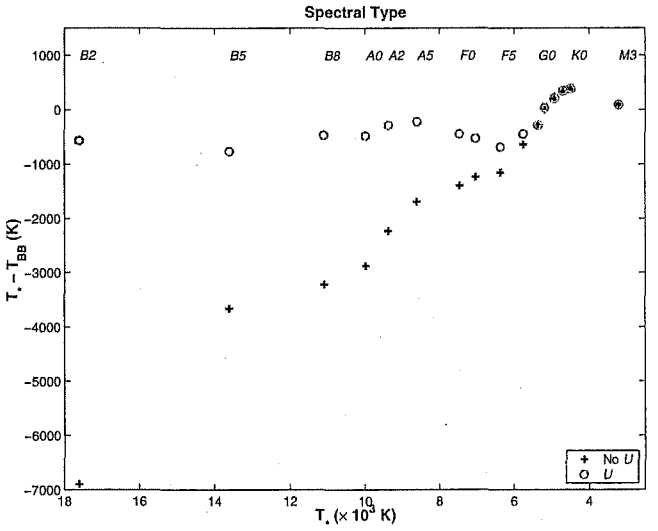

Figure 2.2: Calibration of the blackbody fits to stellar photometry and effective temperatures. The circles represent the values derived by including U-band photometry, and the pluses are those derived without. The data are given in Table 2.2.

Chapter 3

Spectroscopy of post-AGB stars

In this chapter we describe the details of the spectroscopic part of our monitoring programme.

3.1 Acquiring the spectra

To acquire the spectra for this programme the 1-metre McLellan Telescope at MJUO was usesd in conjunction with either the échelle or HERCULES spectrographs. For all of the instruments the telescope was used at f/13.5.

3.1.1 Échelle spectroscopy

The échelle spectrograph (Hearnshaw 1977)[77] was mounted at the Cassegrain focus of the McLellan and was used with the Photometrics series 200 CCD (Barnes et al. 2000)[9] and a focal reducer (Tobin et al. 1998)[184] to give dispersions of ~ 2.6 Å/mm.

Three main regions of the échelleogram were observed during the course of this programme. They are designated *red*, *red minus* and *blue*. The first two used the "red" cross dispersion grating which is blazed at 7000 Å. They differ mainly in the tilt of the échelle grating, so that the red region samples the centre of the échelleogram but the red minus region covers the same orders but lower wavelengths (see Table 3.1). Red minus spectra also suffer from significant gradients as they are closer to one side of the échelleogram, and the signal-to-noise changes perceptibly along each order. The red spectra provide coverage from about 5430 to 8550 Å in sections

about 100 Å wide. This region includes Hα, Na D lines, and 2 members of the Ca II infrared triplet. Order 34 also includes the interesting λ6708 Li I line which is an indicator of recent mixing activity (see §1.2.3). The red minus spectra include a wider selection of singly ionized metal lines as well as the strong diffuse interstellar bands at 5780, 5790 and 6280 Å.

The blue region used the "blue" cross grating. This has a blaze of 4000 Å and covers the wavelength sections given in Table 3.2. The main lines of interest are the Balmer lines Hγ to H 12 plus the Ca II H and K lines and the diffuse interstellar band at 4430 Å.

Order #		Red Minus		Red	
Abs	Rel	λ_{low}(Å)	λ_{high}(Å)	λ_{low}(Å)	λ_{high}(Å)
42	1	5365	5440	5427	5498
41	2	5495	5572	5559	5632
40	3	5632	5711	5698	5773
39	4	5776	5856	5844	5921
38	5	5928	6011	5998	6077
37	6	6089	6173	6160	6240
36	7	6257	6344	6330	6414
35	8	6436	6525	6510	6597
34	9	6625	6717	6702	6790
33	10	6826	6920	6905	6996
32	11	7038	7135	7120	7214
31	12	7266	7365	7350	7450
30	13	7507	7611	7595	7694
29	14	7767	7872	7857	7960
28	15	8045	8153	8137	8242
27	16	8339	8454	8437	8548

Table 3.1: Approximate coverage and order numbers for the red and red minus regions. The 2 order numbers given denote absolute (Abs) and relative (Rel). λ_{low} and λ_{high} are the lower and upper wavelength limits for each order.

3.1.2 HERCULES

HERCULES, the **H**igh **E**fficiency and **R**esolution **C**anterbury **U**niversity **L**arge **É**chelle **S**pectrograph (Hearnshaw et al. 2002)[78], came on-line in April 2001. It is a fibre-fed device, with the spectrograph contained in

Order #		Blue	
Abs	Rel	λ_{low}(Å)	λ_{high}(Å)
23	1	3764	3812
22	2	3827	3875
21	3	3891	3941
19	4	3958	4009
18	5	4027	4079
17	6	4099	4151
16	7	4173	4226
15	8	4250	4304
14	9	4330	4385
13	10	4413	4469
12	11	4499	4556
11	12	4588	4649
10	13	4682	4742

Table 3.2: Approximate wavelength coverage of the blue échelle region. The same table headings apply as in Table 3.1.

a temperature controlled vacuum tank and provided 46 orders in all with wavelength ranges and order numbers listed in Table 3.3.

As can be seen from Tables 3.1 and 3.3, HERCULES has a significant overlap with the red and red minus échelle spectra, and so provides coverage of some of the features in both, including Hα, Na D lines and λ6280 DIB. It also covers a range of slightly shorter wavelengths and additionally observes Hβ and some strong Fe II multiplets.

There are three modes in which HERCULES may be used. The first is with a 100 μm diameter fibre, providing a resolving power of $R \equiv \lambda/\Delta\lambda = 35000$. A resolving power of 70000 is possible in the other two settings: either a 50 μm fibre; or a combination of a 50 μm slit plus a 100 μm fibre. The main discriminating factor to determine the fibre setting is the seeing, with the larger fibre is generally preferred when the seeing exceeds about $2''$.

3.1.3 Detector

The primary detector used for this project was the Photometrics Series 200 CCD system. This is a cryogenic detector system consisting of a SITe SI 003 1024 $\times$ 1024 thinned CCD with 24 μm square pixels and overcoated with

Order #		HERCULES		Order #		HERCULES	
Abs	Rel	λ_{low}(Å)	λ_{high}(Å)	Abs	Rel	λ_{low}(Å)	λ_{high}(Å)
125	1	4546	4578	102	24	5570	5609
124	2	4583	4615	101	25	5625	5665
123	3	4620	4653	100	26	5681	5721
122	4	4656	4692	99	27	5739	5779
121	5	4696	4729	98	28	5797	5838
120	6	4735	4769	97	29	5857	5898
119	7	4775	4809	96	30	5918	5960
118	8	4815	4850	95	31	5980	6022
117	9	4856	4891	94	32	6044	6086
116	10	4899	4933	93	33	6109	6151
115	11	4941	4976	92	34	6175	6219
114	12	4984	5019	91	35	6243	6287
113	13	5029	5064	90	36	6312	6356
112	14	5074	5109	89	37	6383	6428
111	15	5119	5155	88	38	6455	6501
110	16	5165	5201	87	39	6529	6575
109	17	5213	5250	86	40	6605	6652
108	18	5261	5298	85	41	6683	6730
107	19	5310	5347	84	42	6762	6810
106	20	5360	5398	83	43	6844	6892
105	21	5410	5449	82	44	6927	6976
104	22	5463	5501	81	45	7012	7062
103	23	5516	5555	80	46	7100	7150

Table 3.3: Approximate wavelength coverage of the HERCULES spectra. Table headings are the same as in Table 3.1.

Metachrome II. It has a quantum efficiency of about 70% between 6000 and 7000 Å (Barnes et al. 2000)[9].

3.1.4 Reduction Procedure

The same reduction procedure has been used for all of the high resolution spectra obtained for this thesis regardless of the instrument of origin. To do this extensive use was made of the Starlink FIGARO and ECHOMOP packages.

This requires conversion of the image files from FITS (Flexible Image Transport System) format to Starlink NDF (N-dimensional Data Format) files. All the images are subject to a bias subtraction and removal of the bias strip. A quarter turn clockwise and a vertical flip are also performed on HERCULES images to have the wavelengths increase from left to right and bottom to top, which is expected by the software. The object image then has cosmic rays removed by the FIGARO command BCLEAN. This looks for sudden jumps in pixel-to-pixel variations which are then smoothed out using the values of nearby pixels. The individual flat fields are added to produce a single high signal-to-noise image.

MAKETRACE is a collection of ECHOMOP commands and parameters which takes a cleaned object spectrum and the flat field to assess where on the chip the imaged stellar spectra are to be found. It also models the response of the CCD and locates the dekker.

MAKEWAVE is normally used only once to provide the necessary data and NDF structures required for ECHOMOP to do a first approximation to the wavelength solution. Often the accuracy of some of the fits in the orders is quite poor and it is necessary to correct these by hand.

One of the peculiarities of the ECHOMOP package is that when performing the optimal spectrum extraction described by Horne (1986)[85], about 40% of the arc lines are given integer values for their pixel position. For arc lines which are saturated this is expected, however there are only 20 out of several hundred such lines. No explanation was forthcoming from the ECHOMOP helpdesk. So we used profile weighted extraction to obtain the arc line centres for wavelength calibration and then performed the optimal extraction to boost the signal in the spectra. Doing this produced a reduction in the RMS radial velocity of radial velocity standard star spectra from 1.2 km s^{-1} to 0.7 km s^{-1}. It does seem to introduce a slight shift in radial velocity of +0.016 km s^{-1} as measured in the position of arc lines. However, this is not detectable in the stellar radial velocity curves.

REDUCE is the automated procedure for compiling a series of extracted

one dimensional spectra. A quick examination of the extracted spectra at this stage is required to espy any remaining cosmic rays which are removed with interactive graphical interface CLEAN.

Because ECHOMOP only provides one dimensional fitting for its wavelength solution, and it was deemed necessary for a two dimensional fitting procedure to be used. The ECHOMOP wavelength solutions relate the pixel number, x, to a wavelength, λ, along each order separately, i.e., $\lambda = P_i(x)$, where P_i is a polynomial of degree i. In our first approximations we used $i = 3$ (4 coefficients) which provides a good fit along each order without the scatter introduced with higher order polynomials. The two dimensional fit recognizes that the orders are not separate entities and that they are related by the so-called échelle equation: $m\lambda = d \sin\theta$, where m is the order number, d is the spacing between the rules on the grating, and θ is the angle at which the incident light is diffracted. This fit uses $\lambda = P_{i,j}(x, m)$, and introduces a greater degree of robustness in the solution.

From here the spectra are heliocentrically corrected, linearized and rebinned to 20 points per angstrom (40 for HERCULES spectra), starting and ending at a whole number. This allows subsequent manipulation of the data involving spectrum addition, subtraction or cross correlation to be performed easily without having to readjust the values of the pixel centres.

Normalization of spectra was performed with the FITCONT program, which divides each spectrum into six sections, and an average value for each is used to produce a normalizing spline curve. Some spectra required additional normalization which is done interactively with the FIGARO CFIT routine. For HERCULES spectra it was possible to extract a flat field spectrum which was then heavily smoothed and used to remove the spectral response across each order.

A final smoothing is performed with a Gaussian of a size less than the size of the slit over the data. This removes the high frequency noise and is just as effective, and faster than, using a Fourier transform in conjunction with a filter.

3.2 Analysis of the spectra

3.2.1 Spectral Line Parameters

Here we look at how the various line parameters are determined from our normalized one dimensional spectra.

Feature identification and atomic data

For our rest wavelength information we used the solar spectrum atlas of Pierce & Breckenridge (1974)[151]. This provides a consistent sample of wavelengths to eight significant figures. The few remaining lines which required wavelengths were covered by Nave et al. (1996)[136] for Fe I lines, Moore (1972)[134] and the online database available at the National Institute of Standards and Technology (NIST).

For the most part the Vienna Atomic Line Database (VALD) provided the atomic parameters used in our synthetic spectra (Piskunov et al. 1995) [152].

Molecular bands featured in a few of the stars and it was necessary to utilize spectra of the bright red star Mira as templates. Most of the original identifications were drawn from Pearse & Gaydon (1976)[149] updated with references to the TiO ϵ system found in Valenti et al. (1998)[188].

Diffuse interstellar bands (DIBs)

Diffuse interstellar bands (DIBs) are a feature in some of the stars in our programme and provide a useful check on the radial velocities and on the equivalent widths as well as providing some information about the extinction along the line of sight. The materials responsible for DIBs remain unknown although the bands have been known of for many years (Herbig 1975)[79]. The main reference for the "rest" wavelengths and ratio of equivalent width to selective extinction is Jenniskens & Désert (1994)[95]. In Table 3.4 we present the subset of properties in this paper for the lines we have identified in our spectra. The properties in this paper are averages based upon observations of six stars, and it should be noted that for different lines of sight the ratios of different bands is not a constant (e.g., Ehrenfreund et al. 1997)[51] and so the derived reddenings should be treated cautiously. For a more thorough review of DIBs see Herbig (1995)[80].

Radial Velocity

Two methods were used to obtain radial velocities of lines in this programme. Mostly the line bisector method (Wallerstein et al. 1992)[209] was employed. This takes the average velocity of points at 10, 20 and 30% from the bottom of the bisector. These points are chosen to limit the influence of nearby lines and to avoid the limits imposed by pixel size in obtaining the minimum point.

λ (Å)	W/$E(B-V)$	Err W/$E(B-V)$
4428.88	2.231	0.595
5779.48	0.647	0.053
5780.59	0.579	-
5797.11	0.132	0.019
5849.78	0.048	0.008
6194.87	0.006	0.003
6196.19	0.061	0.005
6199.21	0.008	0.003
6203.19	0.107	0.016
6270.06	0.076	0.019
6284.31	0.618	0.049
6287.12	0.014	0.010
6367.22	0.017	0.004
6376.07	0.026	0.005
6379.27	0.078	0.024
6993.18	0.116	0.020

Table 3.4: Properties of DIBs observed in this programme from Jenniskens & Désert (1994)[95].

But for some of our stars the line profiles contained more than one component and it was necessary to fit two or more Gaussians to these profiles. This was done interactively using the Starlink package GAUSS. In Figure 3.1 the results of measuring equivalent widths and radial velocities from a synthetic combined emission plus absorption profile are presented. The difference between the observed and expected values are presented as a function of the wavelength separation. The divergence of the measured values from the expected ones becomes most acute when the two lines are less than 0.5 Å apart. For the equivalent width the errors peak at 0.033 Å and the radial velocity discrepancy reaches 1.4 km s^{-1}.

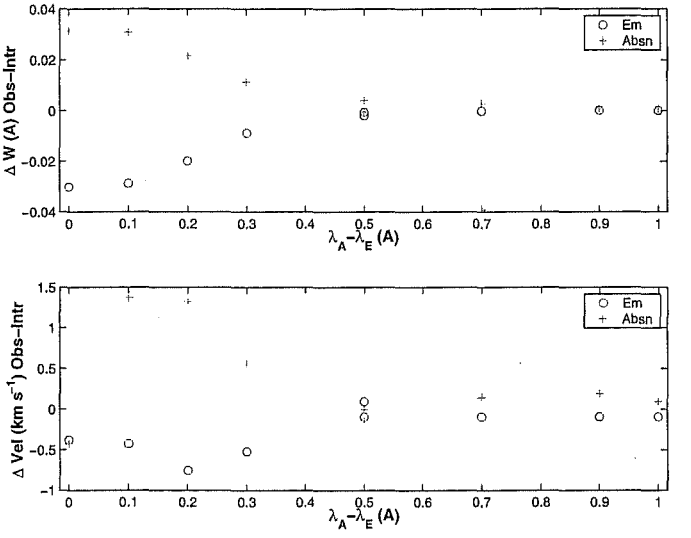

Figure 3.1: Differences between observed and intrinsic equivalent width (ΔW, a) and radial velocity (ΔVel, b) for the components of a line profile containing an emission and an absorption profile. λ_A is the wavelength of the absorption and λ_E that of the emission.

Equivalent Widths

Here we employ the automatic Gaussian fitting procedure outlined in Cottrell & Lambert (1982)[36]. Once the spectrum is subset to isolate the line of interest we then find the line depth (d) and the half width at half height ($hwhh$). The area of the corresponding Gaussian is then:

$$W = \sqrt{(\pi/\ln 2)}(1-d)(hwhh). \tag{3.1}$$

Asymmetry Parameter

As the shape of the lines were also of interest, we created an asymmetry parameter to provide some measure of their symmetry. So we decided to look at the position of the bisector at 10 and 90% of the line depth. Initially the difference between the two values was employed. However, this did not allow for direct comparison between lines of different intensities, as two lines which have identical shapes but a different scale, will have bisectors which cover a different range of abscissa values.

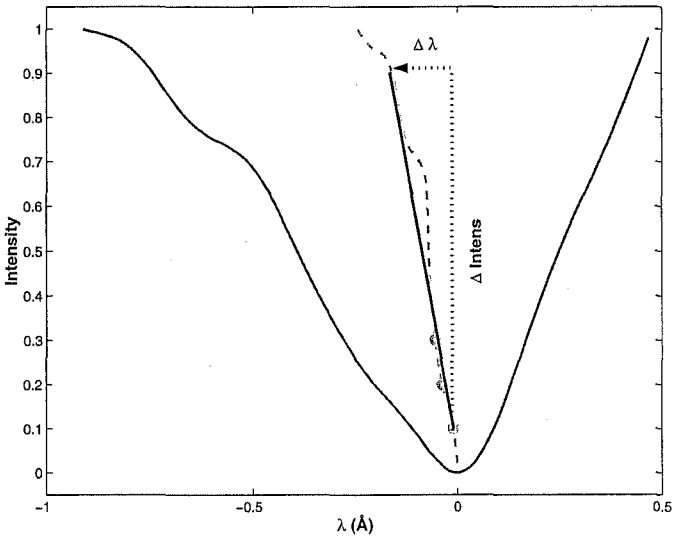

Figure 3.2: Defining the asymmetry parameter, A. $\Delta\lambda$ and ΔIntens as defined in the text. The solid curve is the line profile, the dashed line is the bisector and the circles mark the points from which the radial velocity is taken.

So this simple scheme was abandoned in favour of that outlined in Figure 3.2. The height of the line is normalized and the slope of the line directly connecting the 10 and 90% depth points is calculated. It is the slope of this line that ultimately determines the degree of asymmetry (see Figure 3.2) and we define the asymmetry parameter as:

$$A = \text{atan}(\Delta\lambda/\Delta\text{Intens}), \tag{3.2}$$

where $\Delta\lambda$ is the wavelength shift in angstroms and ΔIntens is difference between the points in the normalized intensity scale, 0.8. $\Delta\lambda$ is measured from the lower point so that it, and therefore A, is positive if the line asymmetry favours the blue. The wavelength shift between the two points, rather than the velocity difference, is used as the change in wavelength is of the same order as the vertical change in normalized intensity, but the corresponding velocity shifts are at *least* an order of magnitude higher. When velocity is used the resulting slope angles are clustered close to 90° due to the arctan function.

3.2.2 λ7774 O I triplet

The O I triplet at 7774 Å, shown in Figure 3.3, is a well known luminosity indicator for F-G stars (Keenan & Hynek, 1950)[102]. It consists of three lines at $\lambda\lambda$7771.9615, 7774.1790 and 7775.3998, produced by the transition from the low energy metastable $3s^5S^0_2$ level to the $3p^5P_{3,2,1}$ levels. Its sensitivity to stellar luminosity stems from the extended lifetime of the lower level in low gravity stars due to reduced collisional de-excitation. In such atmospheres there is a much larger population of oxygen atoms in this level and so the lines are stronger (Faraggiana et al. 1988)[55].

Subsequent investigations have produced calibrations linking the total equivalent width of the triplet to the luminosity of the star, eg Baker (1974)[7] and Osmer (1972)[142]. Using the $M_V - W(\text{O I } \lambda7774)$ relationship provided in Arellano Ferro et al. (1991)[3]:

$$M_V = 1.52 - 6.33W(\text{O I}) + 0.85W(\text{O I})^2 - 3.74(b-y)_\text{o}, \tag{3.3}$$

coupled with Gray's (1992)[72] relationship between temperature and $(b-y)_\text{o}$:

$$\theta_\text{e} = 5040/T_\text{eff} = \begin{cases} 0.636 + 0.510(b-y)_\text{o}, & 0 < (b-y)_\text{o} < 0.11 \\ 0.513 + 1.603(b-y)_\text{o}, & 0.11 < (b-y)_\text{o} < 0.450. \end{cases} \tag{3.4}$$

We can thus use the effective temperature of a star in conjunction with the equivalent width of the λ7774 O I feature to predict the luminosity of the star. Admittedly these empirical calibrations are for normal supergiant stars but it its worth using them to take advantage of overall similarities.

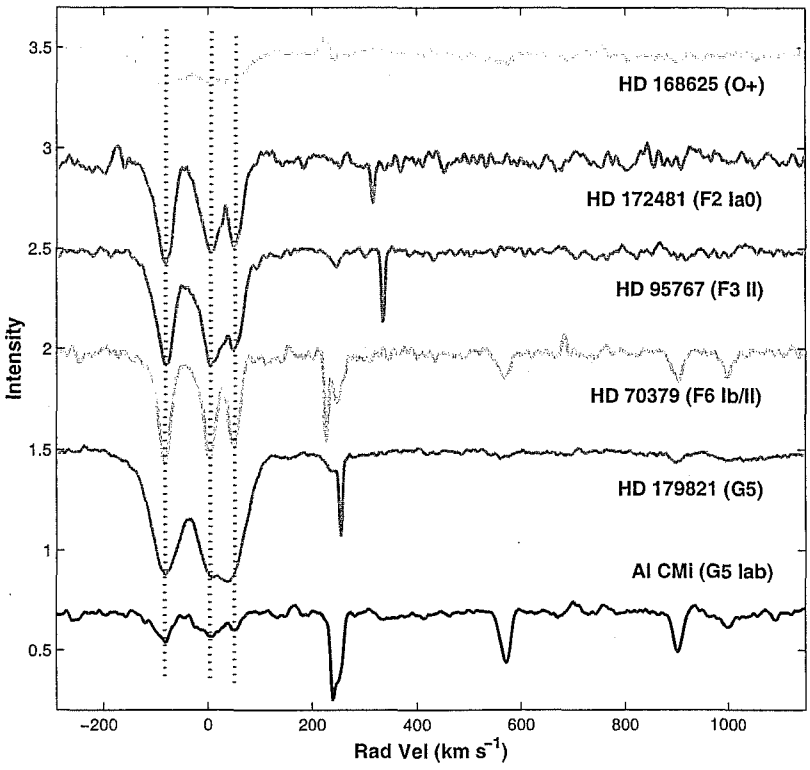

Figure 3.3: λ7774 O I multiplet (dotted lines) for some of the stars in this programme. The spectral types listed are from SIMBAD. Note that the sharp feature at $\sim$ 200-300 km s^{-1} is due to the bad column in the PM 200 chip.

Although not part of the red region we monitored, we have observed the feature for six of our stars using the red minus setting and these are displayed in Figure 3.3. Note that HD 168625 is too hot for the calibration to be applied.

3.2.3 Galactic rotation curve

In general the stars observed as part of this project display multiple component Na D line profiles, and part of the work done has been to determine whether the various components are stellar, circumstellar or interstellar. The latter should be distinguishable by their narrow width, lack of variability and radial velocity. Since Galactic dust clouds are concentrated in the spiral arms we have used combined models to differentiate between the arms.

Taylor & Cordes (1993)[181] provide a model of the Galactic arm structure based upon the distribution of free electrons specifically from pulsar dispersion distance estimates. They provide a cubic spline interpolation for the four main arms which is shown in Figure 3.4. To obtain the radial velocities we first calculate the Galactocentric distance for the points along the line of sight and these distances are used in conjunction with the rotation curve of Einasto (1979)[52] to get the corresponding Galactic rotation velocities. It is then a simple matter to convert these to radial velocities. The expected radial velocities for components moving with each spiral arm can be obtained from the distance estimate from the Taylor & Cordes model.

An important modification to this is the solar motion with respect to the local standard of rest. Dehnen & Binney (1998)[43] analysed proper motions provided by Hipparcos and derived the three components of the solar motion with respect to the local standard of rest to be $(U_o,\ V_o,\ W_o) = (+10.0 \pm 0.4,\ +5.3 \pm 0.6,\ +7.2 \pm 0.4)$ km s^{-1}. This is towards the centre, up from the Galactic plane and along the general direction of Galactic rotation. In other words a total space velocity of 13.37 km s^{-1} at $+32.57°$ to the Galactic plane, in the direction of Galactic longitude of 27.47°.

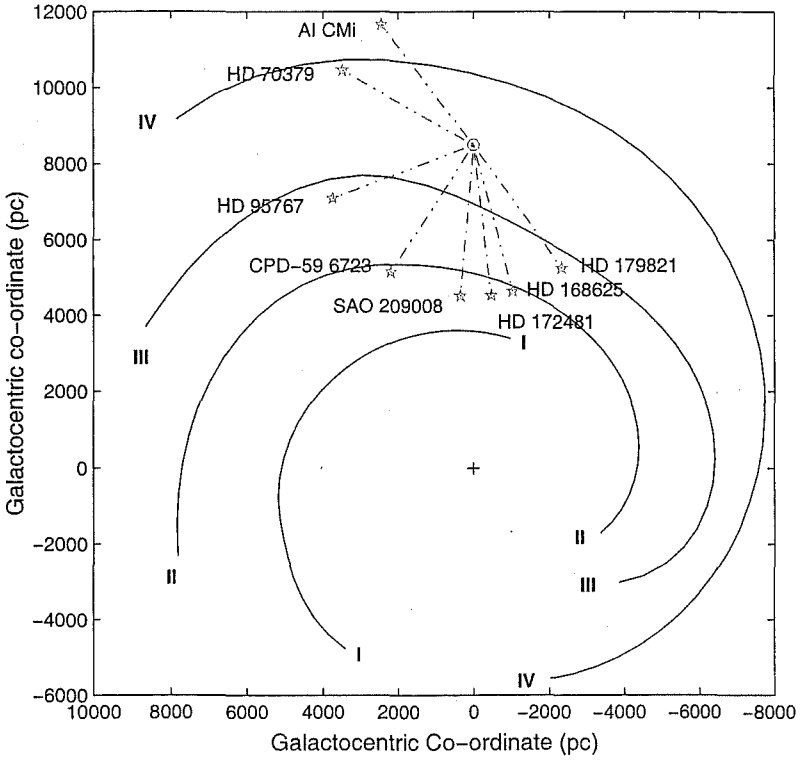

Figure 3.4: Taylor & Cordes (1993)[181] model of the spiral arms of the Galaxy. The arms labelled (I-IV) are Norma, Scutum-Crux, Sagittarius and Perseus. Also shown are the lines of sight to the stars in this thesis out to 4 kpc.

Chapter 4

AI CMi

4.1 Introduction & historical background

In the GCVS (Kholopov 1985)[103], AI CMi (= IRAS 07331+0021, see Table 4.1), was designated as an L-type (slow irregular) variable with a photographic amplitude of 0.8 magnitudes. On the basis of objective prism spectra it has been classified as a supergiant star (G5 Iab) by MacConnell & Bidelmann (1976)[125]. Eggen (1983)[48] used intermediate-band filters similar to the Strömgren system and considered it to be a massive supergiant in the Hertzsprung gap which lacked the repeatable light curves of Cepheids. Photometrically he found non-periodic variations of a cycle lasting less than 100 days and v magnitude varying from 7.91 to 9.30.

Coordinates	α	$07^{\mathrm{h}}\ 35^{\mathrm{m}}\ 41.06^{\mathrm{s}}$
(Epoch 2000.0)	δ	$+00°\ 14'\ 58.5''$
Galactic	l	217.80
coordinates	b	+9.95
Mean Brightness	V	8.80
Spectral Type		G5 Iab

Table 4.1: Basic parameters of AI CMi.

On the basis of a single spectrum, Luck & Bond (1989)[123] considered it to be a low-mass supergiant, possibly an RV Tauri (RVT) star. They found moderate s-process underabundances ($[s/\mathrm{H}] = -0.5$) and significant metal deficiencies ($[\mathrm{Fe/H}] = -1.0$). Model parameters derived were $T = 4250$ K, $\log g = -0.8$ and $\xi_t = 4$ km s^{-1}. By the mid-90's Klochkova & Panuchuk

(1996, KP96 hereafter, see Table 4.2)[106] had detected the presence of TiO bands in the spectrum but only at "cool" phases. Overall they found slight α-element enhancement ($[\alpha/\mathrm{H}] = +0.33$) and s-process underabundances ($[s/\mathrm{H}] = -0.35$). In combination with the average radial velocity ($V_r = +48.2$ km s^{-1}) they concluded the star was either a halo object or a member of the old thick disk.

Date	T (K)	$\log g$	ξ_t	[Fe/H]	Notes
24-02-81	4250	-0.8	4.0	-1.03	Luck & Bond (1989)[123]
11-01-93	4500	0.0	3.0	-1.19	"Hot"
12-03-93	4500	1.0	3.5	-1.19	"Hot"
11-12-95	4100	-0.75	4.0	-1.03	"Cool"

Table 4.2: Model parameters adopted for AI CMi by Klochkova & Panuchuk (1996)[106].

Garcia-Larío et al. (1990)[62] examined the infrared characteristics of the star and found that the observed JHK colours were consistent with the classification as a G5 Iab, but the IRAS photometry indicated the presence of circumstellar dust. Their JKL measures were 0.16 dimmer than earlier measurements presented in Eggen (1983)[48]. They concluded the star was probably a pre-planetary nebula.

AI CMi has also been observed at radio wavelengths. te Lintel Hekkert et al. (1991)[182], David et al. (1993)[39] and Chengalur et al. (1993)[33] all detected the star in the 1612 MHz OH maser, while Engels & Lewis (1996)[53] found 22 GHz H_2O emission. The OH maser line profiles show two peaks separated by 9 km s^{-1}, implying a low ejection velocity on the order of 5 km s^{-1}. However emission from carbon-containing molecules has not been found. Neither Nyman et al. (1992)[139], looking for CO(1-0), nor Omont et al. (1993)[141], looking for CO(2-1) 230 GHz or HCN(1-0) 89 GHz, detected the star. The main conclusion of these papers is that the circumstellar environment is a slowly expanding oxygen-rich region and that the star is post-AGB (PPN).

The IRAS colour-colour diagram of van der Veen (1988)[190] puts AI CMi in the "PN or non-variable with very cool shells" group.

4.2 Photometry

The data for AI CMi comprise 82 points spanning 1463 days. Three stars have been used to calibrate the photometry: HD 60137 was used as the comparison star; HD 60359 and HD 60580 were the primary and secondary check stars respectively. Their basic properties are listed in Table 4.3. Neither of the check stars showed any significant variability over the course of the programme with V-band photometry RMS for both stars of 0.009 magnitudes.

Identifier	$\alpha(2000.0)$	$\delta(2000.0)$	B	V	SpT
HD 60137	$07^{h}\ 33^{m}\ 11.7^{s}$	$+00°51'17.9''$	9.54	8.30	G5
HD 60359	$07^{h}\ 34^{m}\ 10.9^{s}$	$+00°51'25.1''$	9.65	8.51	G5
HD 60580	$07^{h}\ 35^{m}\ 17.2^{s}$	$+00°32'44.8''$	8.75	7.83	G5

Table 4.3: SIMBAD data for the photometry calibration stars of AI CMi.

Table A.1 contains the V-band and colour data which are summarized in Table 4.4 and plotted in Figures 4.1 and 4.2. It has the largest amplitude of any of the stars in this programme, reaching a maximum peak-to-peak amplitude of 1.67 magnitudes in R (see Figure 4.2). Also, unusually for this sample of stars, $(B-V)$ and $(V-R)$ get bluer as it dims in V, but $(V-I)$ gets redder (see Figure 4.3). There may also be a slight phase differential between the passbands.

	B	V	R	I
Mean	10.210	8.679	7.903	6.899
Range	1.338	1.546	1.679	1.241
Error	0.002	0.001	0.002	0.003

Table 4.4: General properties of the $BVRI$ photometry for AI CMi. The mean magnitude for each band is given along with the range of the change and the mean error.

4.2.1 Analysis of the photometry

AI CMi presents colour variations which are quite different to those of the RV Tauri (RVT) variables. Changes in $(V-I)$ are in the opposite direction

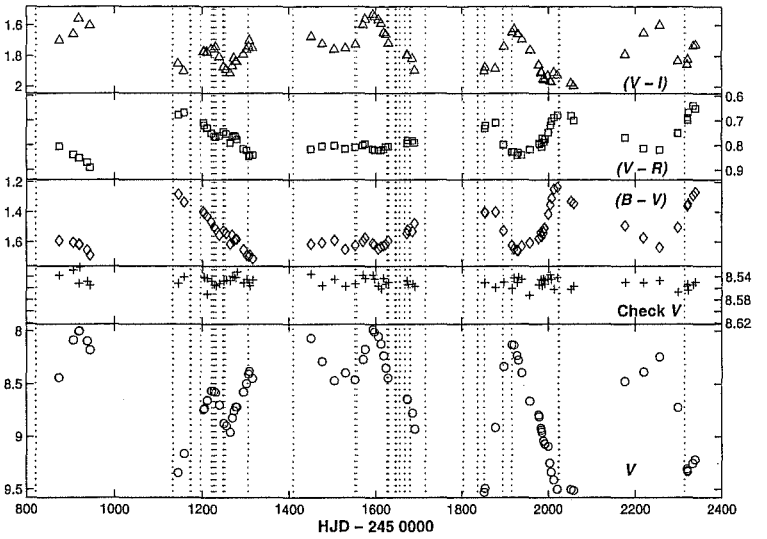

Figure 4.1: MJUO V-band and colour photometry of AI CMi. The vertical dotted lines indicate when high resolution spectra were acquired.

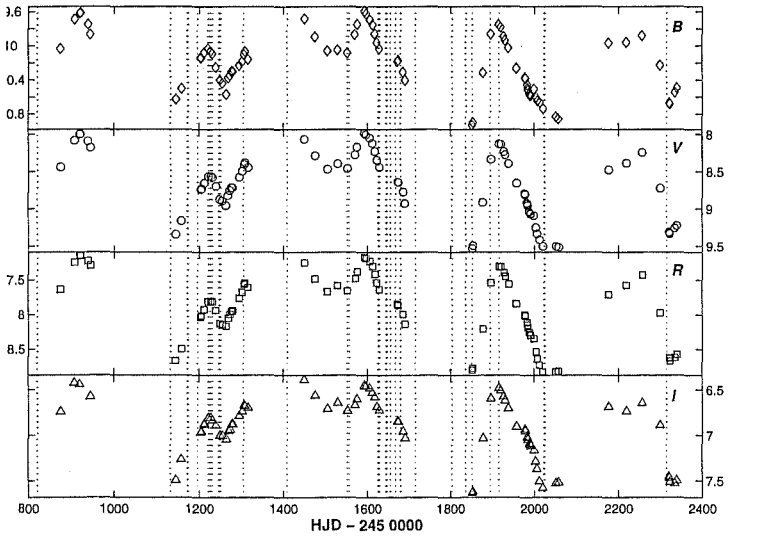

Figure 4.2: MJUO $BVRI$ photometry for AI CMi.

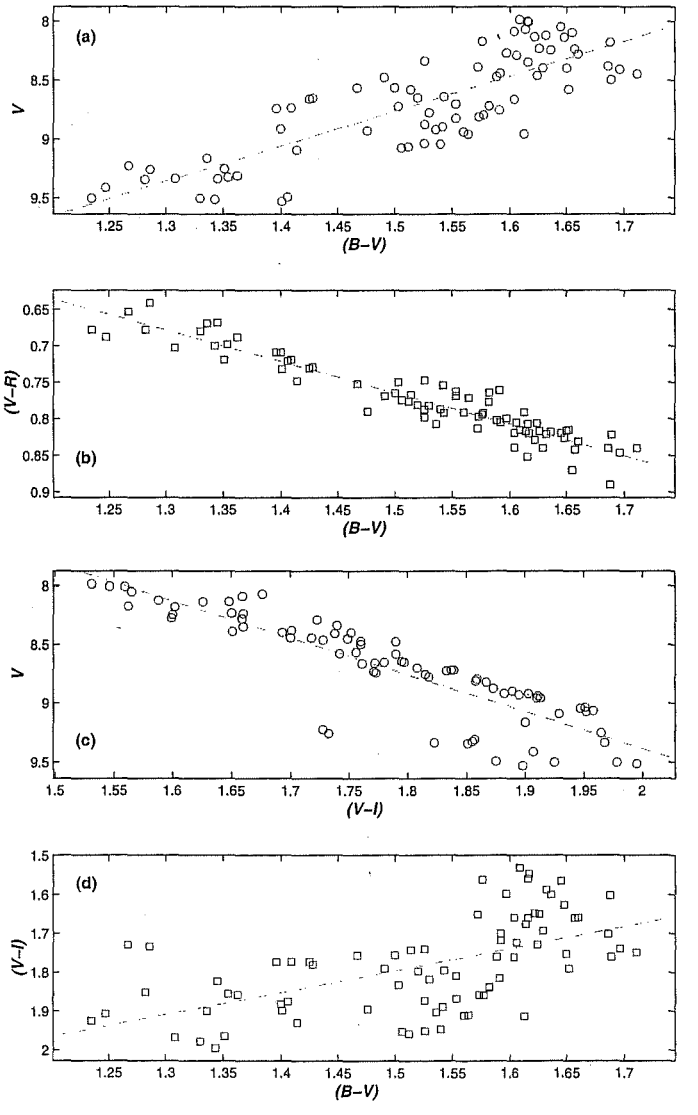

Figure 4.3: Two colour-magnitude (a, c) and colour-colour (b, d) diagrams for AI CMi. The lines of best fit are included and have the values $V = 13.22 - 2.97(B-V)$, $(V-R) = 0.12 + 0.43(B-V)$, $V = 3.09 + 3.15(V-I)$ and $(V-I) = 2.64 - 0.57(B-V)$, respectively.

to those in $(B-V)$ or $(V-R)$. Indeed $(V-I)$ closely follows the V-band, becoming redder as the star gets dimmer. $(B-V)$ and $(V-R)$ on the other hand, are reddest when the star is bright. The lack of a sizeable phase shift between the various bands means that the colour changes are driven primarily by the size of the changes in each individual band (see Table 4.4). From mean light to maximum the V flux has increased proportionately more than the I flux, implying a bluer colour in $(V-I)$. The B flux will also have increased less than the V, and so $(B-V)$ becomes redder.

An additional feature of RV Tauri photometry is that the colours are bluest on the ascending branches from minima. AI CMi is bluest in $(B-V)$ and $(V-R)$ when the star is at minimum brightness. This suggests that the shock mechanism which drives the variations in RV Tauri stars, is not responsible for the changes in AI CMi. So there is a need to consider other options for a mechanism to change the colours.

One possibility is line blanketing due to increased levels of TiO in the atmosphere. These have a greater concentration in the V and R-bands than in either B or I. They would also effect each band simultaneously, meaning no phase shift between them. So as the star cools and TiO forms in the atmosphere it removes proportionately more light from V and R and thus causes the colour indices to change as they do. An additional contribution to the B-band flux are the neutral metal emission lines which will have a small positive effect, reducing the size of the flux reduction by the oxide bands.

Lomb-Scargle analysis of the V photometry from MJUO (Figure 4.4, panel b) shows up two main peaks: one at 0.0060 d^{-1} and the other at 0.0032 d^{-1} corresponding to periods of 167 ± 5 and 310 ± 30 days respectively. Interestingly these appear to be composite peaks with smaller peaks about 0.0007 d^{-1} higher than the main peaks. This shift is roughly equivalent to the period of the whole photometry. The uncertainty in the frequencies is ±0.00017 d^{-1}. The periodogram also provides another point of difference from the class of RV Tauri stars, in that there is no peak at half of the main period, i.e., at 80-85 d.

The *uvby* and *RI* photometry provided by Eggen (1983)[48] were also analysed to see whether any distinctive shift had occurred in the pattern of oscillation over the intervening twenty or so years. Eggen's y data is made up of 90 points covering 843 days, while the *RI* photometry consists of 25 points spanning 811 days. A comparison of the y light curve with the MJUO V light curve (Figure 4.5) shows superficially similar behaviour: there appears to be a large oscillation of a few hundred days which has a smaller one superimposed on top of it. The periodogram (Fig 4.4, panel

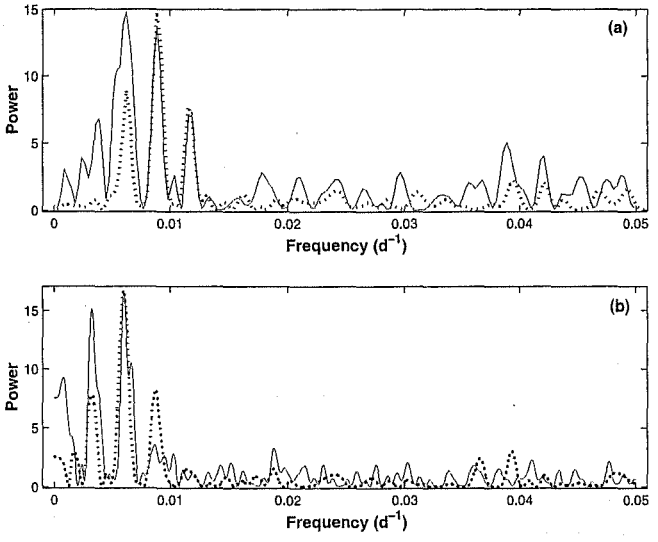

Figure 4.4: Lomb-Scargle periodograms for (a) Eggen's y and (b) MJUO V photometry of AI CMi. The solid lines are the power spectra and the dotted ones are the window functions for 167 (0.0060 d^{-1}) and 112 d (0.0089 d^{-1}) respectively.

b) confirms this, with the same principal peak at 161 ± 7 d (0.0063 d^{-1}). However the secondary peak at 310 d is no longer present but rather there is a peak at 0.0089 d^{-1} (112±4 d). In addition, there are two smaller peaks at 0.0039 and 0.0119 d^{-1} (260 and 85 days respectively).

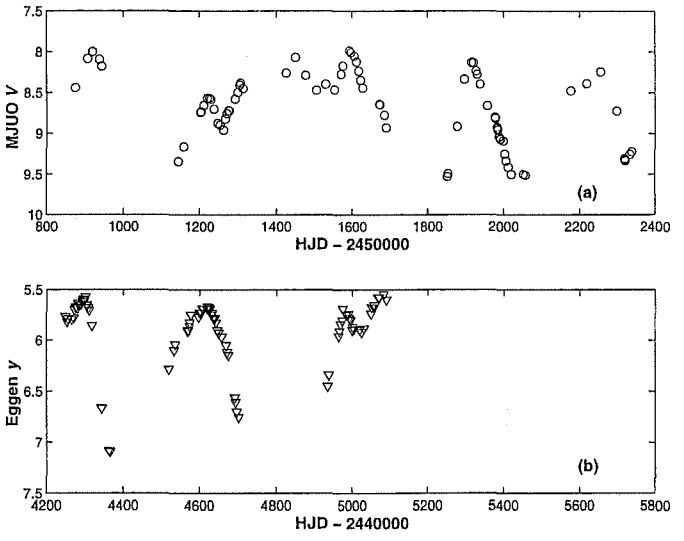

Figure 4.5: (a) MJUO V and (b) Eggen y-band photometry of AI CMi.

Tuchmann et al. (1993)[187] predicted that the rate of period change due to ongoing post-AGB evolution is between -0.001 to -0.3 d yr^{-1}. So if AI CMi has been undergoing post-AGB evolution there will be a shift in the main period of about -0.02 to -6 d between the MJUO and Eggen photometry. Unfortunately the margin of error on the main peak at 167 d is about 12 d, too large to detect such changes. So one must look to spectroscopic changes, due to the corresponding increase in effective temperature, to see if there has been any evolutionary effects in AI CMi.

An interesting feature is the disappearance of the prominent 112 d peak detected in the y-band periodograms. This is reminiscent of the mode switching behaviour of various semi-regular variables, such as R Doradus (Bedding et al. 1998)[13], perhaps due to a weakly chaotic oscillation.

The ratio of the main periods in the y periodogram, 0.7 (= 112 : 160), is the ratio one would expect from the fundamental and first overtone. So in the 1980's the star was probably oscillating in a combination of the first overtone and fundamental, but by the late 1990's the first overtone mode has faded and the star now oscillates almost exclusively in the fundamental.

To see how the periodograms would look for a star with multiple modes which change in amplitude over time, some synthetic light curves were generated based upon two equal amplitude sinusoidal variations with periods of 112 and 130 days. The reason for choosing 130 over 160 days is that the window functions for 112 and 160 days have significant overlapping sidelobes (see Figure 4.4), whereas 130 days produces no significant contribution at the frequencies present in the 112 day frequency spectrum. These are due to the presence of an annual variation in the photometry due to observing seasons, which produces lobes at frequencies of $f \pm 0.0027$ d^{-1}. Figure 4.6 shows the results for three curves: dotted is the power spectrum when both variations are present with constant amplitude; solid shows what happens when the 112 day cycle linearly diminishes to 0 over the course of the sequence; and the dashed lines is for a light curve with just a 130 d period. The key point of this is that the power detected in each frequency is a measure of its *significance* rather than the actual power present. The power in the peak at 0.0077 d^{-1} ranges from 39.6, through 31.9 to 10.6, even though the amplitude of the 130 d oscillation is the same for all of the light curves.

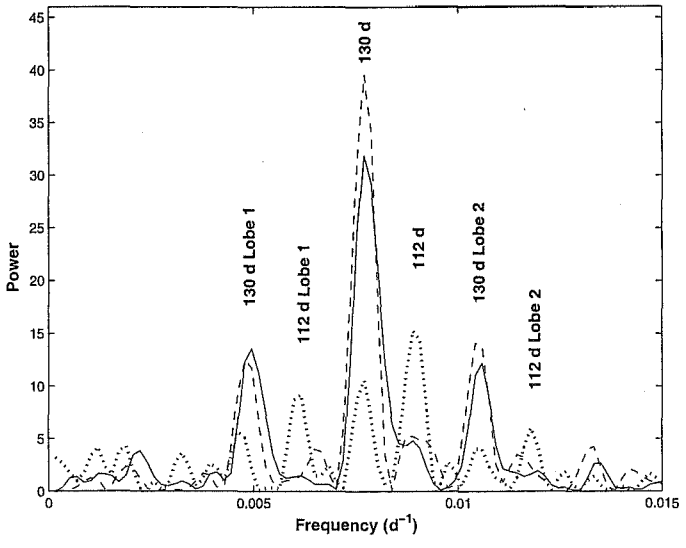

Figure 4.6: Lomb-Scargle periodograms of three synthetic light curves.

What this tells us is that the power statistic produced by the Lomb-Scargle algorithm is ultimately a relative measure of the significance within a data set that a particular frequency has, rather than some absolute measure of the power. So for AI CMi, the significance of the 112 d signal is very much

reduced when the y-band photometry is compared to the MJUO V-band.

4.3 Spectral energy distribution and reddening

AI CMi is another star for which a few measures of $JHKL$ photometry were obtained from the SAAO. These are summarized in Table 4.5 along with the IRAS photometry.

	J	H	K	L	12	25	60	100
Band	5.825	5.265	4.893	4.194	15.32	68.11	18.51	3.68
Error	0.010	0.008	0.008	0.011	0.77	3.41	1.85	0.33

Table 4.5: Summary of the infrared photometry compiled for AI CMi. $JHKL$ is from SAAO on the night of 1996 December 20. The IRAS photometry is in janskys.

Combined with the mean data for the MJUO $BVRI$ photometry (Table 4.4) this presents the overall picture of a star with significant infrared excess due to cooler matter, but little indication of a contribution from warmer dust or a cool stellar companion at a few thousand kelvins.

The $JHKL$ photometry collected at SAAO is between 0.15 and 0.24 magnitudes brighter than those of Garcia-Larío et al. (1990)[62] and, within the quoted uncertainties, are the same as the JKL photometry of Elias (Eggen 1983)[48]. In spite of this variability, the L-band photometry lies above the blackbody fit regardless of which value is chosen. The same is true of the M-band datum provided by Garcia-Larío et al.. This strongly indicates the presence of extra flux at these wavelengths over and above the stellar flux, probably from the inner edge of the dust shell. Because it involves both stellar and circumstellar contributions it has been not been used to fit the stellar energy distribution.

Adopting the spectral classification of Bidelmann & MacConnell (1976) [125], G5Iab, to deredden the photometry, produces a colour excess of $E(B-V) = 0.51$. This implies a total visual extinction, due to both Galactic and circumstellar dust, of 1.56 magnitudes assuming the standard interstellar reddening law. However, the presence of TiO bands in the majority of the MJUO spectra for AI CMi (see §4.4.4) implies a later spectral type. According to Jaschek & Jaschek (1995)[93] TiO bands are not seen in normal stellar spectra until K5. Indeed, K4 is the spectral type one would obtain from the observed $(B-V)$ colour index. Assuming that the total visual

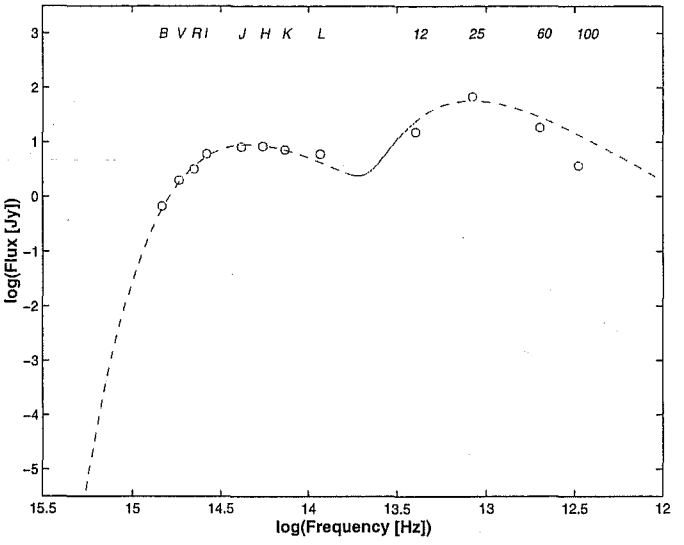

Figure 4.7: Blackbody fits for the dereddened SED of AI CMi. The mean MJUO $BVRI$ magnitudes have been used along with SAAO $JHKL$ and IRAS fluxes. The two curves have temperatures of 3800 and 206 K.

extinction is entirely due to interstellar material requires a spectral type of K3 from $A_V = 0.26 \pm 0.15$ (Hakkila et al. 1997)[75] at a distance of 2.9 kpc. This implies an absolute magnitude of $M_V = -3.86$.

Extending this over all of the bands using the general extinction relationships of Cardelli et al. (1989)[31], produces the dereddened spectral energy distribution displayed in Figure 4.7. This is fitted by a combination of two blackbodies with temperatures of 3800 and 206 K. The RMS error on the fit is 0.18 and the corrected stellar temperature is 4200 K. Which is quite compatible with the "cool" model atmosphere temperatures listed in Table 4.2.

The IRAS fluxes are not especially well fit by a blackbody. This may be due to the dust having a different distribution that the simple model assumes. The L data shows hints of variable amounts of matter closer to the star and it is possible that IRAS observed the star during an unusual outburst.

From the 60 μm flux and the derived stellar and dust temperatures, there is 3.9×10^{-3} $M_\odot$ of circumstellar material at a distance of 2.1×10^2 $R_\star$ from the central star.

4.4 Spectroscopy

There are a total of 51 high-resolution MJUO spectra of AI CMi covering 1494 days. There are three distinct types of spectra exhibited by AI CMi. Borrowing the notation of KP96 we shall denote them, "hot", "cool" and a new "cold" category. The signatures of each are different:

- **Hot** This is the star at its most normal. There is no overt emission anywhere in the spectrum, including Hα, and the few remaining molecular bands are only faintly visible. There is just one sample "hot" spectrum taken on HJD 2451409. The star is close to maximum brightness ($V \sim 8.4$) and is also quite red, $(B-V) \sim 1.6$.
- **Cool** The star now displays the TiO molecular profiles seen by KP96 and Hα shows a strong emission peak on the blue wing of the absorption core. This is the type of spectrum observed most often.
- **Cold** In this newly observed stage the spectrum still shows the molecular features and Hα emission, but it now exhibits numerous narrow emission lines associated with low excitation levels of neutral metals, particularly Ti I, Fe I and Ni I. The molecular bands seen during the "cool" phase are visible but are weaker. Photometrically the star is at its dimmest in V (> 9.1) and bluest, $(B-V) < 1.2$. These emission lines are seen in spectra from HJD 2451132 to 1175, HJD 2451716 to 1837 and also HJD 2452026 and 2452314.

Sample spectra are presented in Figure 4.8 which shows the region around Hα. In subsequent sections molecular and emission line features are listed and identified.

The behaviour of the star near maximum light is a little inconsistent. The hot spectrum discussed above is rather different to the only other spectrum near maximum light (HJD 2451916). This spectrum has deeper absorption lines than the hot spectrum, as well as significant molecular bands and the strongest Hα emission seen in any spectrum.

Although the spectra are subject to strong interference from molecular bands, there is no evidence of any diffuse interstellar bands in the spectra of AI CMi. This includes $\lambda\lambda$4430, 5870, 6196 and 6379.

4.4.1 Radial Velocities

Looking for photospheric velocities in AI CMi is a significant challenge. This stems from the fact that the photospheric brightness and temperature

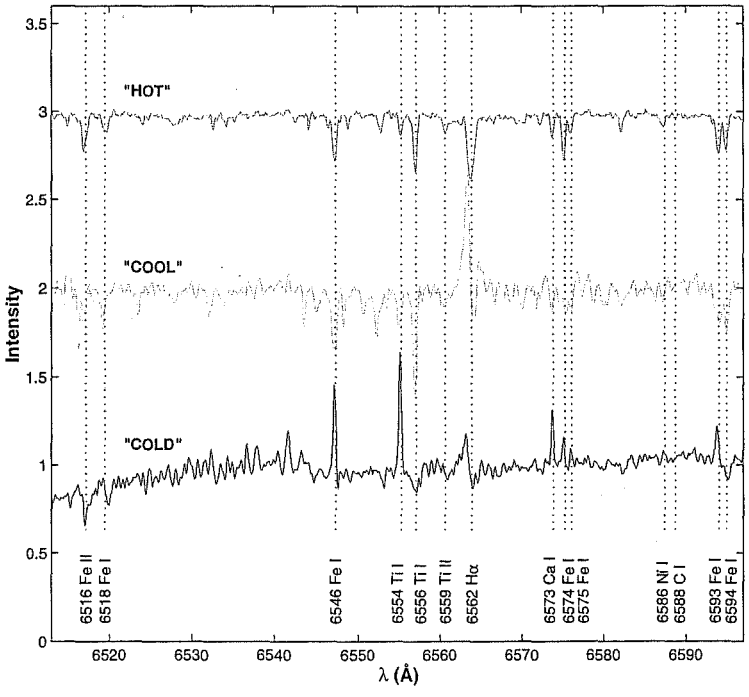

Figure 4.8: Examples of the three types of spectra seen in AI CMi. They were normalized at the base of any Hα emission and then offset.

changes so much that the line profiles in the spectrum are subject to a great deal of interference. At minimum light there are many narrow emission lines visible due to the same species responsible for the photospheric absorption lines (see §4.4.5). The most prominent lines in the spectrum of AI CMi have quite low excitation potentials and are the most effected by the emission. Even if this does not exceed the continuum level it will still produce an asymmetry in the absorption profile and therefore the bisector method used with other stars is not applicable here. A naïve use of this procedure, illustrated in Figure 4.9 with the circles, finds radial velocity amplitudes of between 10 and 20 km s^{-1}. This includes lines which do not show overt emission. The largest amplitudes are found in lines with more prominent emission, and the highest radial velocities occur when the emission lines are at their strongest. There is also the issue of interference from molecular bands, which produce many fine lines that can change the line shape and also obscure the position of the local continuum (§4.4.4). The other radial velocities presented in Figure 4.9 have been obtained with the GAUSS interactive component fitting package, and assume that the lines consist of one absorption and one emission component.

The velocities observed for the emission components in Figure 4.9 are quite stable, showing a variation of only a couple of km s^{-1}. The absorption components show a greater degree of scatter with an RMS of 2 km s^{-1}. Although a binary companion cannot be completely ruled out, there are no long term trends in the radial velocity data indicative of a binary companion with a period on the order of a few years. The shape of the line and how it changes as the star changes brightness is illustrated in Figure 4.10. This sequence shows how the part of the composite profile in absorption will give a red-shift at minimum and appear to accelerate as the rising continuum causes the relative contribution of the absorption to decrease.

Following the suggestion by Luck & Bond (1989)[123] that the star may be an RV Tauri variable, evidence of line doubling was also looked for. This splitting of absorption lines in RV Tauri stars is seen in these stars at phases 0.25 and 0.75, when the star is brightening from deep and shallow minima respectively. This is due to the presence of two shock waves in the atmosphere. These cause different layers within the star to move at different velocities and thus change the line profile. No such changes were observed.

4.4.2 Hα Profile

As shown in Figure 4.11a, the Hα profile is variable. It most often appears as a wide emission peak interrupted by a narrow absorption spike, which

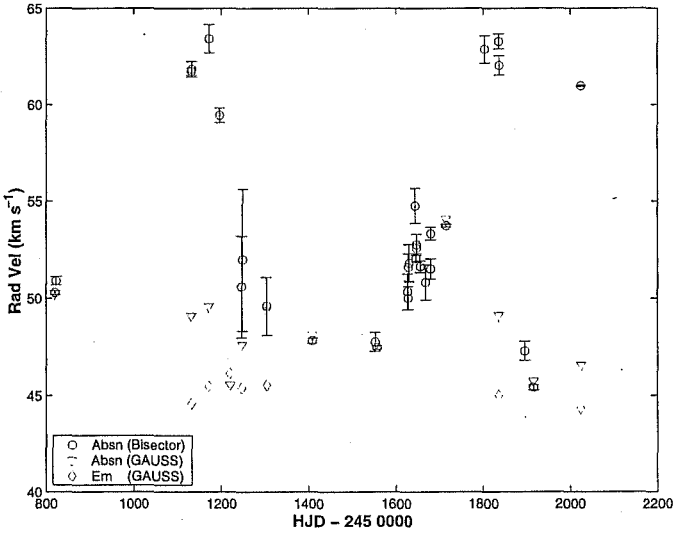

Figure 4.9: Radial velocity of λ5866 Ti I for AI CMi. The circles and error bars are from the bisector method on the absorption component only, inverted triangles are the velocity of the absorption and diamonds are the emission component determined from fitting separate components to the line profile.

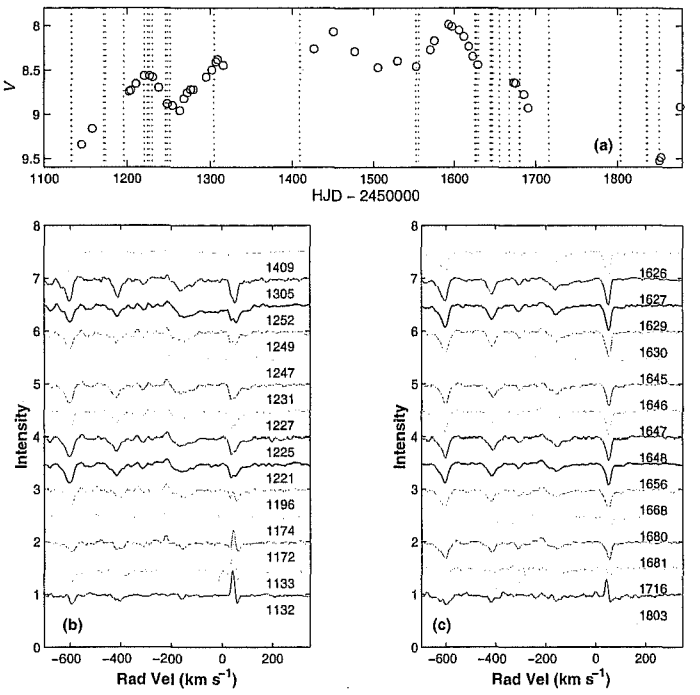

Figure 4.10: The behaviour of λ5866 Ti I line profile as AI CMi brightens. (a) V-band photometry is plotted along with spectrum segments of the rise from minimum (b, bottom to top) and the fall back to minimum (c, top to bottom). The emission is clearly dependent upon the photometric brightness, see how it strengthens during the small dip from HJD 2451250 to 2451350.

is offset slightly to the red. However, the spectrum of HJD 2451409 (near maximum light) has a total absence of emission, reproducing the line profile reported by KP96, but this is not repeated in the next spectrum taken at maximum light (HJD 2451916). Indeed the emission reaches its highest level for any of the MJUO spectra.

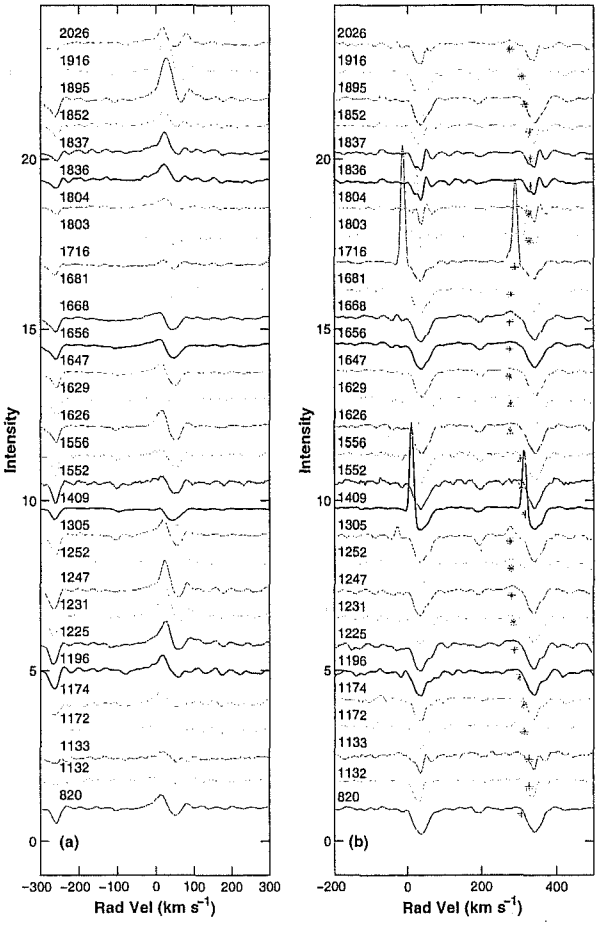

Figure 4.11: (a) Hα and (b) Na D line profile variation in the spectrum of AI CMi. The asterisks in (b) denote the position of night sky emission components in the Na D_1 line.

The emission from Hα does seem to show a periodic aspect in its intensity. The other time when it is also quite strong is around HJD 2451247. On both occasions the star has recovered from a deep minimum, with the larger

emission occurring when the star has brightened by the most. Perhaps this due to recombination of hydrogen in the wake of a shock front.

4.4.3 Sodium D lines

Only one high resolution HERCULES spectrum was acquired of AI CMi and the region around the D lines is presented in Figure 4.12 and the components listed in Table 4.6. For this night a heliocentric correction of +11.4 km s^{-1} has been applied. The star is also in a deep minimum and presents a significant emission profile plus numerous features due to molecular bands.

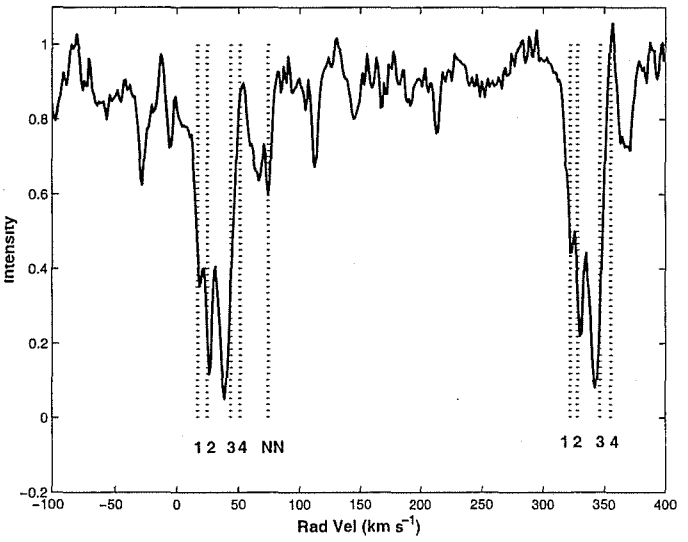

Figure 4.12: HERCULES spectrum of AI CMi Na D lines. The vertical lines indicate the positions of the components listed in Table 4.6.

From the Na D line sequence displayed in Figure 4.11 (b), spectra acquired between HJD 2451132 and 2451196 and also between 2451800 and 2451900 appear to show the Na D lines doubling. However, the star is also at its dimmest during these times and has more to do with the behaviour of other neutral metal lines discussed further in §4.4.5.

Like the other stars in the sample AI CMi lacks an absorption feature at the stellar velocity. Component 4 provides a match but it is an emission line. Given the behaviour of this line in relation to other narrow emission lines, it is most likely to be blue-shifted with respect to the star, just like the other neutral metal lines.

#	λ (Å)	W (Å)	Rad Vel (km s^{-1})	Notes
1	5890.300	0.047	17.0	IS?
2	5890.450	0.075	24.6	IS?
3	5890.822	0.477	43.6	CS + PS
4	5890.975	−0.146	51.3	CS EM
NN	5891.425	0.035	74.3	
1	5896.300	0.054	18.7	As above
2	5896.419	0.004	24.8	
3	5896.775	0.700	42.9	
4	5896.950	−0.223	51.8	

Table 4.6: The components of the Na D lines of the mean échelle spectrum of AI CMi. The RMS error on the fits is 0.056 Å. A negative equivalent width (W) means that the feature is in emission. NN denotes a non-sodium line, CS a circumstellar feature, IS interstellar, PS photospheric and EM emission. ? indicates tentative identification. Only the heliocentric ($\odot$ frame) radial velocities are given.

A second variable feature lies at the velocity one would expect from the heliocentric correction, indicated by the asterisks on the Na D_1 lines in Figure 4.11b. Inspection of the image spectra confirms that these are night sky emission lines.

The line of sight to AI CMi will intercept the Perseus spiral arm at 2090 pc ($z = 360$ pc) with a kinematic radial velocity of +34 km s^{-1}. Although component 1 is not a good match to this velocity it is less likely to be due to circumstellar matter ejected by the star. The stellar frame velocity is +40 km s^{-1} which is considerably higher than the 5 km s^{-1} expansion velocity seen in the OH maser profiles, e.g., David et al. (1993)[39]. The observed heliocentric radial velocity, $\sim$ +50 km s^{-1}, is produced by Galactic rotation at approximately 4 kpc ($z = 690$ pc).

4.4.4 Molecular features

In Table 4.7 is a list of the identified band heads found in the spectra of AI CMi. This has been achieved by using a spectrum of Mira as a template with the actual identifications taken from references found in Pearse & Gaydon (1976)[149] and also Valenti et al. (1998)[188] for the TiO ϵ system. Mostly the bands are from titanium oxide but there is also vanadium and zirconium oxides. Interestingly some of the bands reach their strongest not at minimum light but during the "cool" phase observed at mean brightness.

Molecule	System	λ (Å)	Occurrence Max	Mean	Min
TiO	Blue-Green(1,0)	5448.3	Wk	Pk	Y
TiO	Orange(0,0)	5597.6	Wk	Y	
TiO	Orange(0,0)	5603.6		Y?	
TiO	Orange(1,1)	5629.3		Y?	Y?
ZrO	Yellow(0,0)	5718.1		Wk	?
TiO	Orange(4,4)	5727.4		Y	Wk
VO	Red(0,0)	5736.7		Y	
TiO	Blue-Green(0,2)	5758.5	Y	Y	Y?
TiO	Blue-Green(2,4)	5761.7		Wk?	Y?
TiO	Orange-Red(1,0)	5847		Y	Y
TiO	Red (1,0)	5852			
TiO	Blue-Green(2,4)	5861.7		Wk?	
TiO	Orange-Red(1,0)	5872	Y	Wk?	
TiO	Orange-Red(1,0)	5875		Wk	Wk?
		6000	Y	Y	Y?
TiO	Orange-Red(3,2)	6003		Y?	Y?
	Orange-Red(4,3)	6003		Y?	Y?
		6035		Wk	
		6051		Wk	Wk
		6058		Wk	
		6173		Y	Y
TiO	Orange-Red(0,0)	6183.5	Y	Y	
TiO	Orange-Red(0,0)	6186	Y	V Wk	
TiO	Orange-Red(0,0)	6186.90	Y	V Wk	
		6211		Y?	
	Orange-Red(0,0)?	6213	Y	Wk?	Y?
		6220		Wk?	
		6224			

Molecule	System	λ (Å)	Occurrence Max	Mean	Min
ZrO	Red (0,0)	6344.9		Wk	
		6351		Y	Y
	Red (0,0)?	6358	Y?	Y	?
		6359	Y?	Y	?
TiO	Blue-Green(8,5)	6385		Y	Y
		6394		Y?	?
		6400		Y	?
		6513		Y	Y?
VO	Red (1,3)	6532.8		Wk	Y?
ZrO	Red (2,2)	6543.0		Y	Y
		6574		Y	
TiO	Red(1,0)	6714.4	Y	Y	
	Red(2,1)?	6717		Y	
TiO	Red(2,1),(1,0)	6719.3		Y	
	Red(2,1)?	6750 B	Y?	Y	
		6781		Y	Y
VO	Red(0,3)	6919		Y	Y
		6952		Y	Y
ZrO	Red(3,4)	6993		Y?	Y
TiO	Red (0,0)	7125.6	Y	Y	?
TiO	Red (1,1)	7159.0	Y	Y	?
TiO	Red (1,1)R_c	7197.7		Y	
	Red (2,2)R_a			Y	
TiO	Red (1,2)	7666.4		Y	Y
TiO	Red (0,1)R_c	7672.1		Y	
	Red (1,2)Q_a	7672.1		Y	
TiO	Red (3,4)	7861.0		Y	Y
		7868		Y	
TiO	Orange-Red(2,1)	7907		Y	Y
TiO	Red (4,5)Q_a	7907.3		Y?	Y?
TiO	Red (3,4)R_c	7907.3		Y?	Y?
		7915		Y	Y
VO	Extr Red (0,0)	7938.9		Wk	Y
		8207		Y	Y
		8227		Y	

Molecule	System	λ (Å)	Occurrence Max	Mean	Min
TiO	Orange-Red(0,0)	8442	Wk?	Y	Y
TiO	Orange-Red(0,0)	8452		Y	Y
TiO	Orange-Red(1,1)	8495		Y?	
TiO	Orange-Red(1,1)	8506	?	Y	?
TiO	Orange-Red(1,1)	8516		Y?	Y

Table 4.7: Molecular band heads visible in the échelle spectrum of AI CMi. Y denotes a positive identification, with Wk and V Wk for bands which are present but weak or very weak. ? marks dubious identifications.

4.4.5 Narrow emission features

These are the distinctive features of "cold" spectra. Unlike the molecular lines these are a less common phenomenon, but their occurrence is frequent enough for it to be surprising that they have not been observed before. The most prominent emission lines belong to Ti I. Other species to contribute are Ni I, Fe I, Na I, Ca I, Ca II, Co I, Sc I, K I and V I. The details are listed in Table 4.4.5.

They are most strikingly observed in spectra taken when the photometric magnitude is fainter than about $V = 9.1$, but it is possible to detect them in the cores of absorption lines in brighter spectra. This is shown in Figure 4.13.

There are however a number of absorption lines visible in the spectrum at minimum which seem to congregate near the blue end of the spectra. This is true for HERCULES spectra as well. In the HERCULES spectra it may also be that the emission lines show some sort of structure.

Identification			Type	Notes
λ (Å)	Species	RMT		
5429.1442	Ti I	259	IPC	E 43.9
5429.7055	Fe I	15	+CE	EA 39.7+56.6
5445.0502	Fe I	1163	CE	EA 38.7+56.7
5446.9238	Fe I	13	CE	EA 40.1+55.7
5455.6178	Fe I	15	CE	EA 36.4+54.6
5460.5021	Ti I	3	CE	EA 39.4+56.4
5471.1983	Ti I	106	E	42.1
5472.7095	Ti I	107	E	40.1
5476.9125	Ni I	59	CE	40.8
5476.2930	Fe I	1029		A
5476.5718	Fe I	1062		A
5481.8681	Ti I	39	E	E 41.1
5483.1017	Fe I	1061	E	E 52.4
5483.3577	Co I	39	E	E 38.6
5490.1520	Ti I	107	IPC	E 41.0
5565.4801	Ti I	229	IPC	EA 42.3+58.8
5577.350	[O I]	3F	IPC	E 21.7
	Atf			A
5592.2637	Ni I	69	IPC	EA 40.7+57.2
5700.1629	Sc I	12	E	E 43.9
5701.5527	Fe I	209	CE	EA 41.4+59.0
5711.8846	Fe I	1087	CE	E 36.4
5712.1361	Fe I	686		A 50.0
5715.0882	Ni I	231	E	E 44.2
5727.0529	V I	35	IPC	EA 41.3+59.5
5739.4752	Ti I	228	E	E 43.0
5739.9840	Ti I	228	E	E 43.4
5739.9896	Ti I	228		E 43.1
5866.4558	Ti I	72	IPC	EA 43.0+60.7
5880.2726	Ti I	70	IPC	EA 41.5+57.4
5889.9661	Na I	1	CE	E 50.4
5895.9321	Na I	1	CE	E 50.5
5899.2972	Ti I	72	IPC	EA 41.2+60.3
5903.3170	Ti I	71	E	E 40.3
5918.5394	Ti I	71	E	E 43.3

Identification			Type	Notes
λ (Å)	Species	RMT		
5999.04	Ti I		E	E 40.6?
5999.68	Ti I		E	E 40.7?
6018.2977	Fe I	1176	E	E 49.3
6064.6318	Ti I	69	IPC	E 42.5
6065.4921	Fe I	207		A 58.0
6210.6589	Sc I	2	IPC	E 43.0
6239.9431	Fe II	74	E	E 34.8
6336.1082	Ti I	103	PC	E 42.3
6336.8328	Fe I	186		A
6366.4867	Ni I	230	E	MB
6378.2568	Ni I	247	E	
6400.0101	Fe I	816	IPC	?
6400.3240	Fe I	13		?
6546.2790	Ti I	102	IPC	E 43.0
6546.2479	Fe I	268		A?
6554.2315	Ti I	102	E	E 43.0
6556.0707	Ti I	102	CE	
6562.8163	H I	1	IPC	
6562.8163	H I	1	CE?	
6572.7842	Ca I	1	E	E 43.3
6574.2325	Fe I	13	E	E 41.2
6575.1800	Ti I		E	E 39.9?
6575.0229	Fe I	206		?
6592.5153	Ni I	248	PC	?
6593.9221	Fe I	268		?
6743.1289	Ti I	48	E	E 42.6
6745.5200	Ti I		E	E 44.6
6767.7817	Ni I	57	IPC	EA 42.2 + 57.1
7130.2370	Ni I		E	E 41.8
7138.9117	Ti I	99	E	E 42.4
7188.6205	Ti I	99	E	E 42.0
7189.8738	Ti I	285	E	E 44.3
7209.5166	Ti I	99	PC	A? E 39.4
7357.7364	Ti I	97	E	MB E 43.8
7364.1077	Ti I	97	E	E 46.9

Identification			Type	Notes
λ (Å)	Species	RMT		
	Band		E	
7440.5822	Ti I	225	E	E 46.2
7664.9110	K I	1	E	
	Band		E	MB
7949.1586	Ti I	125	E	E 45.0
8434.9718	Ti I	33	CE	
8435.6633	Ti I	33	CE	
8436.9279	Ti I	224	PC	E
8439.5798	Fe I	1172		A
8450.8979	Ti I	224	E	MB E 44.2
8457.1	Ti I		E	MB E 44.3
8468.4174	Fe I	60	PC	? E 49.3
8467.1551	Ti I	182	??	?
	Band			MB
8498.0524	Ca II	2	E	MB
8498.0524	Ca II	2	CE	MB
8514.0826	Fe I	60	E	
8518.3942	Ti I	150	E	
8518.0221	Ti I	182		?
8539.3760	Ti I		E	E 42.4
8542.1261	Ca II	2	CE	EA 43.2 + 57.6
8546.0926	Ti I	150	E	E

Table 4.8: Observed emission lines in the spectrum of AI CMi (HJD 2451132). The type designation is PC for P Cygni-like, IPC for inverse P Cygni-like, E for a single emission peak and CE for emission surrounded by absorption. MB means that the spectrum is quite jagged due to a nearby molecular band. There is also one artefact of the reduction labelled Atf. The numbers in the notes column are radial velocities.

The velocities of the emission components have been obtained by fitting Gaussian components to the lines. What they reveal is that from 30 absorption lines the mean velocity is $+54 \pm 4$ km s^{-1} compared to $+43 \pm 3$ km s^{-1} for 57 emission features. The emission features are always blue-shifted with respect to the absorption. Recall the narrow self-absorption feature in the Hα profile, which is at longer wavelengths than the emission. Comparing the velocities of the emission components over the course of this programme indicates that they are quite stable within the uncertainties. Coupled with

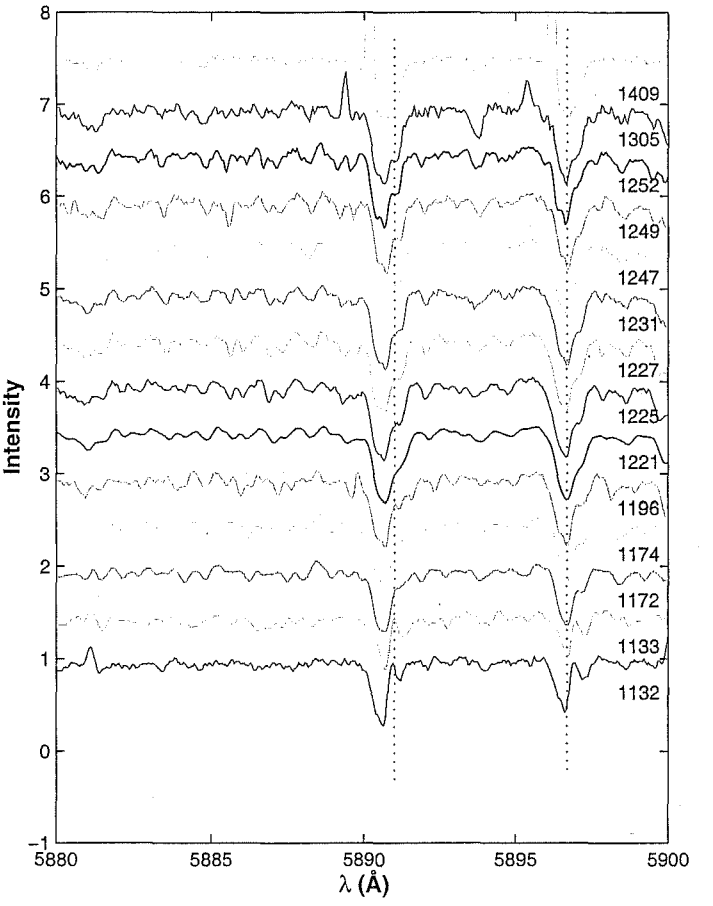

Figure 4.13: The fading of the narrow emission lines in the spectrum of AI CMi. The star has brightened from $V = 10.99$ to $V = 6.22$ and the spectra are labelled with HJD−2450000. The vertical dotted lines indicate the position of the emission (D_2 line) and central absorption (D_1).

their small width, this seems to point to a chromospheric origin. Or it could indicate the interface between the on going mass loss from AI CMi and the ISM or perhaps slower moving material ejected earlier on the AGB.

4.5 Discussion

The types of spectra, linked as they are with photometric brightness, are the kind that is observed in many RV Tauri stars. For example Howell et al. (1983)[86] observed R Scuti close to a deep minimum and found numerous fine emission lines from neutral metal lines as well as strong TiO bands. A later spectrum during a shallow minimum recovers the bands but does not reveal the sharp emission lines.

There are no signs of doubling of absorption lines due to the propagation of shocks as is seen in RV Tauri stars. However, the behaviour and general appearance of the Hα profile is very similar to that described by Gillet et al. (1989)[66] for R Scuti. This is attributed to shocks propagating in the atmosphere. Perhaps AI CMi is unable to generate the regular pattern observed in normal RV Tauri stars, but large scale shocks appear at deep minima which are able to travel out through the atmosphere and heat it, destroying TiO, increasing the optical depth and allowing the star to brighten.

From the combination of spectroscopic and photometric behaviour it would seem likely that AI CMi is more closely related to the class of RV Tauri stars rather than the pseudocepheid class mooted by Eggen (1983)[48]. However it isn't in the classic RVT mould, since its light curve does not exhibit the nice alternating maxima and minima associated with classical RVTs. But the correlation of spectral features to photometric brightness coupled with the pattern of abundances and the systemic radial velocity all indicate that it is very closely related. Comparisons with Eggen's photometric data suggest a hint of mode switching possibly due to a weakly chaotic oscillation but longer base-line photometry needs to be done to confirm this.

That the blue peak of the Hα emission is consistently stronger than the red, is perhaps indicative of emission being due to the same processes which cause the narrow emission lines. These are generally offset to the blue with respect to their absorption components.

4.6 Conclusion

AI CMi was revisited in order to check the star for binary companions and to re-evaluate the photometric variability after 20 years. No evidence for a

companion object was found. MJUO $BVRI$ data showed that the colour changes were not directly driven by temperature changes within the star as the star was redder at maximum in $(B-V)$ and $(V-R)$, but bluer in $(V-I)$. The reverse is true at minimum light. Most likely this is due to the presence of TiObands in the spectrum. This would rule out Eggen's pseudocepheid model of the star. These changes are also incompatible with those of RV Tauri stars which are bluest in $(B-V)$ when the star is brightening from a minimum.

Periodogram analysis of both MJUO V-band and Eggen's y-band showed some interesting features. In both data sets there is a prominent 165 day period. However, for Eggen's data this is accompanied by a peak at 112 d which is absent from the MJUO data. This is reminiscent of the mode switching behaviour seen in long period variables rather than some evolutionary effect.

The $JHKL$ data collected at SAAO shows that AI CMi is also variable at these wavelengths too, although we have not explored the exact extent of this. A total visual extinction of 0.26 magnitudes was found considering the star to be K3, with no contribution from circumstellar material. This indicates a distance to the star of 2.9 kpc. From the analysis of the sodium D line components we have identified one with a velocity compatible with being in the Sagittarius arm, which implies a minimum distance of 2.1 kpc. The SED is well fit with two blackbodies at 3800 and 206 K. The stellar temperature is 4200 K and there was 0.4 $M_{\odot}$ of circumstellar material at 210 $R_{\star}$.

The brightness variation ($\Delta V = 1.5$ magnitudes) is large enough for the star to display considerable changes in its spectrum. Three types of spectra are observed. The cold phase, containing numerous narrow emission lines from neutral metal species, are seen only when the star is dim. As the star recovers from its minima these lines are absorbed back into the continuum. They are also blue-shifted with respect to corresponding absorption features by 9 ± 7 km s^{-1}. This strongly points to an outward flowing chromospheric origin of the lines.

Molecular features are also seen in the spectrum and are at their strongest during the cool phase, seen in the middle range of AI CMi brightness. The behaviour at maximum light is inconsistent. Two spectra were collected at around this phase. One resembles the normal cool spectra with TiO bands and enhanced Hα emission, and the other, the so-called hot spectrum has no emission and only a few band heads are weakly visible. Hα emission is at its most intense when the star has brightened from a deep minimum.

Chapter 5

HD 179821

5.1 Introduction & historical background

HD 179821 (= IRAS 19114+0002, and see Table 5.1) has generated a great deal of interest as it presents aspects which are compatible with it being a massive ($M > 30M_{\odot}$) supergiant star and at other times a lower mass ($M \sim 1M_{\odot}$) post-AGB star.

Coordinates	α	$19^{h}\ 13^{m}\ 58.51^{s}$
(Epoch 2000.0)	δ	$+00°\ 07'\ 31.9''$
Galactic	l	35.62
coordinates	b	-4.96
Mean Brightness	B	9.7
	V	8.3
Spectral Type		G5

Table 5.1: Basic parameters of HD 179821.

Zuckerman & Dyck (1986)[222] examined the CO (1-0) emission from the star and found an outflow velocity of 33.9 km s^{-1}. This is very high compared to he typical post-AGB star value of 15 km s^{-1} (van der Veen et al. 1993)[192] and is indicative of a more massive object. They also noted that the high stellar radial velocity of +105.0 km s^{-1} could be indicating that this object is following the Galactic rotation curve at a distance of 6 kpc. However this would place the star 500 pc below the Galactic plane and the scale height for massive stars is only 60 pc (Mihalas & Binney 1981)[130]. To account for this they suggested that the star was an evolved O-type

runaway, but this would also mean that the star's kinematics would not be due to Galactic rotation and so their distance estimate would be redundant.

Other microwave observations have confirmed that the circumstellar environment of HD 179821 is oxygen rich. Maser and molecular emission has been detected by Likkel (1989, OH)[118], van der Veen, Trams & Waters (1993, CO)[192], Bujarrabal et al. (1992, CO, SiO) [26] and Josselin & Lèbre (2001, CO, HCO^+)[99]. The last two papers also measured the $^{12}C/^{13}C$ ratio with Josselin & Lèbre concluding that the ratio is under 5 for HD 179821, which is typical for evolved stars. Non-detected masers include water (Likkel 1989 [118] and Zuckerman & Lo 1987)[223], CS and HCN (Bujarrabal et al. 1992)[26]. Waters et al. (1996)[211] used ISO spectra to show that the dust is a mix of amorphous and crystalline silicates.

Jura & Werner (1999)[101] studied mid-infrared images of the star and surrounding nebula and interpreted their findings on the basis of a $30M_{\odot}$ supergiant. They claimed that the high outflow velocity (35 km s^{-1}) and radial velocity (+99 km s^{-1}) are best supported by the high mass model. Jura et al. (2001)[100] followed this with a map of ^{12}CO $(1-0)$ around the star which showed a slightly asymmetric emission shell extending from $4''$ to $12''$ from the star. To account for this they required that until 1600 years ago the star was a red hypergiant losing 3×10^{-4} $M_{\odot}$ yr^{-1}.

Three abundance analyses have also failed to decisively answer the question of the star's nature. Začs et al. (1996)[218] used a $T = 6800$ K and $\log g = 1.3$ model atmosphere and found a star with solar metallicity, α-process element deficiencies, with s-process element enhancement ($[s/H] = +0.70$). Reddy & Hrivnak (1999)[158] used a similar model atmosphere ($T = 6750$ K, $\log g = 0.5$ and $\xi_t = 5.25$ km s^{-1}) to determine the abundances of carbon ([C/Fe]= +0.2), nitrogen ([N/Fe]= +1.3) and oxygen ([O/Fe]= +0.2). These abundances implied that the star has been through the AGB phase and is therefore a low mass star. However the luminosity derived from the λ7774 O I triplet and the distance from sodium D lines point to a much more luminous, and therefore massive, object. The most recent abundance analysis (Thévenin et al. 2000)[183] derived somewhat different atmospheric parameters of $T = 5660$ K, $\log g = -1.0$, $\xi_t = 11.0$ km s^{-1} and [Fe/H]= −0.5. Consequently their adopted s-process abundances are lower than those in either Začs et al. or Reddy & Hrivnak. They claim that the parameters derived in those papers are erroneous because non-LTE effects may be masking the real ionisation balance and therefore causing them to overestimate the abundance of metals in the stellar atmosphere. They conclude that the star is not likely to have undergone the third dredge-up.

Arkhipova et al. (2001)[5] published nearly ten years of UBV photometry

on HD 179821. What they found were semi-regular light variations in all bands with the largest amplitude in U, and an increase in the levels of the U and B fluxes over time. They derived a colour excess of $E(B-V) = 1.0$ assuming the star to be F3I, and they claimed the star was a low to intermediate mass post-AGB star.

More recent papers have concentrated on the circumstellar environment. Gledhill et al. (2001)[70] and Gledhill & Takami (2001)[71] imaged a dust shell around the star in J and K-bands. The former paper finds a resolved ring of scattered light surrounding the star at a radius of 1.1 to 1.6″. They assume a distance of 6 kpc and derive a inner radius of 1.44×10^{15} m and a dust mass of 0.08 $M_{\odot}$. The dust is also distributed in a detached shell with a high degree of spherical symmetry implying a constant mass loss rate sometime in the recent past. They also note that their models do not constrain the distance to the star as the dust density could be increased to have the same shell brightness at closer distances.

In this chapter we present the results of our spectroscopic and photometric monitoring of HD 179821.

5.2 Photometry

The photometry of this star was carried out using the three calibration stars listed in Table 5.2 and comprises 38 points covering 1400 days. V-band and colour data are presented in Table A.2. HD 179769 was the comparison while HD 179894 and HD 179378 served as the primary and secondary check stars. Neither of the check stars have shown any significant variation over the course of our programme, with V-band RMS errors of 0.010 and 0.007 magnitudes respectively.

Identifier	α(2000.0)	δ(2000.0)	B	V	SpT
HD 179769	$19^{\rm h}\ 13^{\rm m}\ 55.8^{\rm s}$	+00° 06′ 12.7″	9.75	8.75	G0
HD 179894	$19^{\rm h}\ 14^{\rm m}\ 20.0^{\rm s}$	+00° 18′ 02.7″	10.11	9.45	G0
HD 179378	$19^{\rm h}\ 12^{\rm m}\ 18.5^{\rm s}$	+00° 06′ 36.7″	9.35	8.75	G5

Table 5.2: Basic data for the photometry calibration stars of HD 179821.

The resulting photometry is displayed in Figures 5.1 and 5.2 and summarized in Table 5.3. From these we can see that the star is a variable with a variation which has a peak-to-peak amplitude of ~ 0.3 magnitudes in B. The colours change roughly in step with the star generally being bluer in

all colour indices when it is brighter although the colour changes are not as closely linked as they are for other stars in our programme.

	B	V	R	I
Mean	9.503	7.980	7.177	6.363
Range	0.322	0.176	0.184	0.174
Error	0.002	0.001	0.002	0.002

Table 5.3: Some general properties of the $BVRI$ photometry for HD 179821. The mean magnitude for each colour is given along with the range of the change and the mean error in photometry.

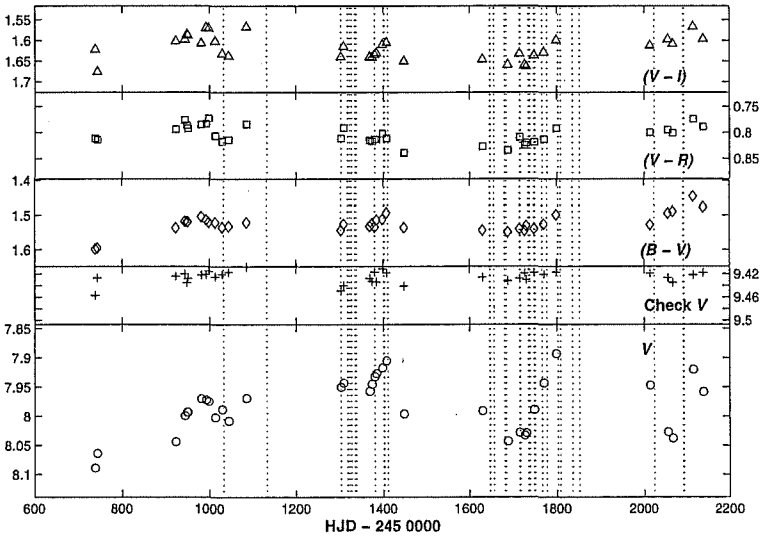

Figure 5.1: V and colour photometry of HD 179821 and the primary check star HD 179894 taken from MJUO. The dotted lines indicate when échelle spectra were taken.

5.2.1 Analysis of the photometry

HD 179821 does not present light curves which show a high degree of repeatability indicative of a consistent variation. The periodograms for the photometry are displayed in Figure 5.3 along with a window function with a period of 193 d (0.0052 d^{-1}), the highest peak in the power spectrum.

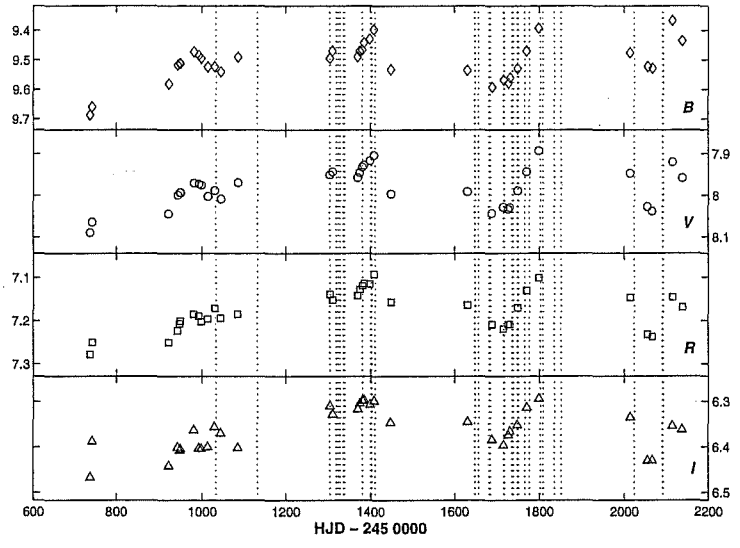

Figure 5.2: $BVRI$ photometry of HD 179821 from MJUO.

The main peaks found are listed in Table 5.4, along with the corresponding periods and uncertainties.

The main peak in the periodograms has a period of 193 d which is close to half a year, or the length of the observing season for a star on the celestial equator. The average length of the four main observing seasons is 150 days, and the average separation between them is 198 days. To test the veracity of the period the photometry was phased to about 199 d as shown in Figure 5.4. This period was selected on the basis of a local minimum in the RMS about the mean sine curve, and although the amplitude of the variation changes, the positions of the main peaks are reproduced. The periods for the B, R, and I-bands were 198, 193 and 199 d respectively. This means that the peak is due to a genuine variation in the photometry, not a period introduced due to the sampling frequency.

We also examined the UBV data of Table 1 in Arkhipova et al. (2001)[5] for periodicities. The results are presented in Figure 5.5 and summarized in Table 5.5. Their photometry extends from HJD 2448027 (1990 May 15) to 2451470 (1999 October 18) comprising 169 points. There is an overlap of approximately two years between their programme and ours, and a small correction of -0.06 magnitudes was made to their V-band measures to bring them into line with the MJUO V.

We decided against examining a periodogram from the combined data

Frequency ($\times 10^{-3}$ d^{-1})	Power	Period (d)	ΔP (d)
0.89	5.8	1120	190
2.32	3.8	430	30
3.93	4.0	255	10
5.18	7.4	193	6
6.97	4.6	144	4
8.21	4.8	122	3
9.82	7.1	102	2

Table 5.4: Main peaks in the Lomb-Scargle power spectra of HD 179821 from MJUO V-photometry. The uncertainties in the frequencies are 0.18×10^{-3} d^{-1}.

Frequency ($\times 10^{-3}$ d^{-1})	Power	Period (d)	ΔP (d)
0.87	20.1	1150	90
1.74	15.5	570	20
2.47	13.7	405	10
4.14	11.4	221	4
6.90	12.0	145	2
9.80	10.6	102	1

Table 5.5: Main peaks in the Lomb-Scargle power spectra of HD 179821 from Arkhipova et al. (2001)[5] V-photometry. The uncertainties in the frequencies are 0.07×10^{-3} d^{-1}.

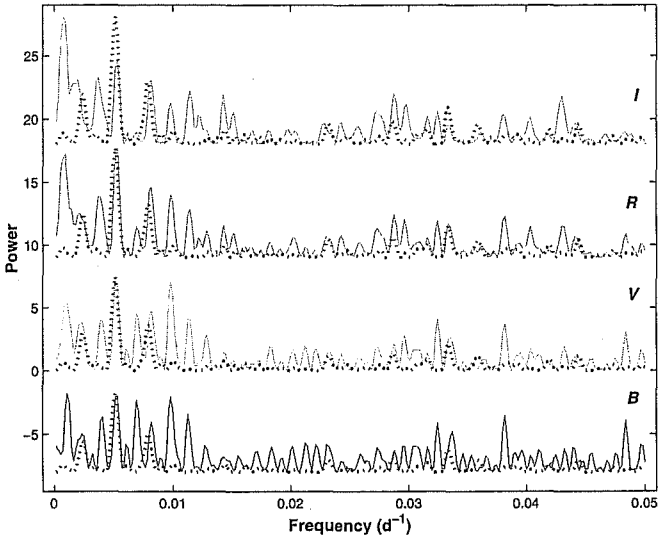

Figure 5.3: Lomb-Scargle periodograms for MJUO $BVRI$ photometry of HD 179821. The window function for a 193 d (0.0052 d^{-1}) period is shown as a dotted line.

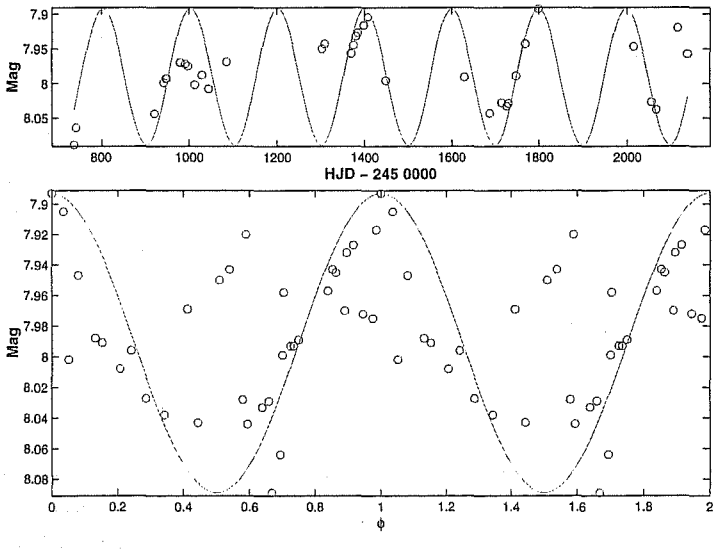

Figure 5.4: V-band MJUO photometry of HD 179821 phased to 199 d.

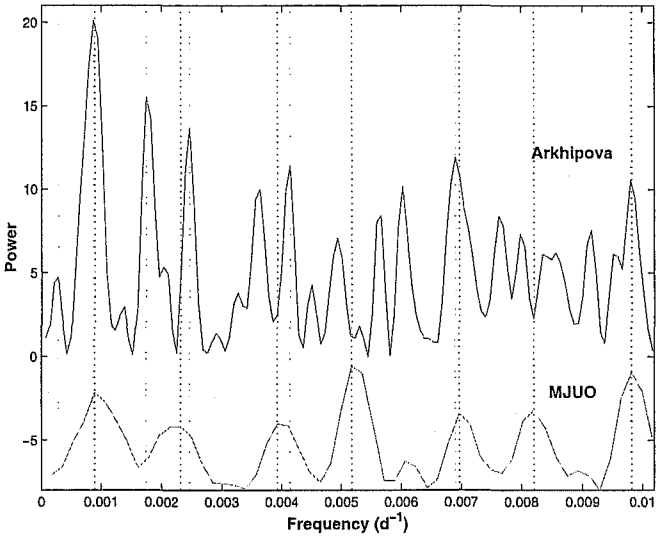

Figure 5.5: Lomb-Scargle periodograms for V-band photometry from MJUO and Arkhipova et al. (2001)[5]. The vertical lines are at the frequencies of the peaks listed in Tables 5.4 and 5.5.

sets as this is completely dominated by the photometry of Arkhipova et al. and it was considered more instructive to examine the periodograms separately. The first thing to notice from Figure 5.5 is that the most significant peak in the MJUO photometry (0.0052 d^{-1}) is missing from the Arkhipova periodogram. This might hint that this period is a recent development in the star's variability. However it is possible to phase the photometry of Arkhipova et al. to 205 d although the sampling rate during the first part of the programme is not particularly high. The first two periods listed in Table 5.5 have a ratio of almost 2:1 and we are probably seeing an alias at 570 d. The 1120, 144 and 102 d peaks in the MJUO are represented in the Russians' data. In the MJUO periodogram the 1120 day peak may possibly be due to the length of the programme but its appearance in the long-term photometry suggests a genuine physical cause.

It is possible to find a significant peak at 190 d in the V-band photometry of Arkhipova et al. This requires that the 1150 and 3443 d peaks be removed by prewhitening the data. A recent paper by Le Coroller et al. (2003)[114] does this to concentrate on periods in the range of 50 to a few hundred days. Their periodograms show two main peaks at 200 and 140 days, which are also present in our power spectra. It is not exactly clear why the 1150 d

peak should be removed other than to highlight the 190 d peak.

5.3 Spectral energy distribution and reddening

In Figure 5.6 we present the results of fitting two blackbody curves to the visual and infrared photometry of this star. No $JHKL$ of this star was acquired at SAAO and to complete the SED we have used the photometry of van der Veen et al. (1989)[191]. The U-band point was the average of the photometry of Arkhipova et al. during the overlap with our photometric programme. The infrared data are listed in Table 5.6 along with their uncertainties.

	J	H	K	L	12	25	60	100
Band	5.20	4.70	4.60	4.10	31.33	648.30	515.90	168.10
Error	0.05	0.05	0.05	0.08	1.88	32.42	30.95	20.17

Table 5.6: Summary of the infrared photometry compiled for HD 179821. $JHKL$ is taken from van der Veen et al. (1989)[191].

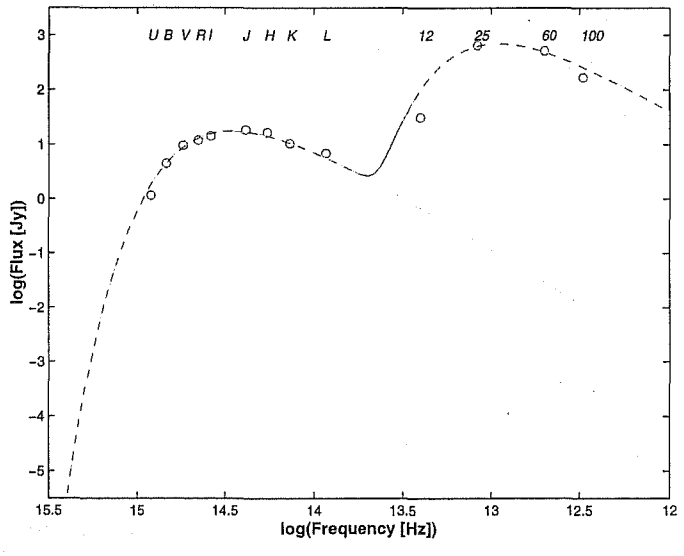

Figure 5.6: The blackbody fits for HD 179821 using the mean data for $BVRI$. The curves have temperatures of 6300 and 155 K.

The SED of HD 179821 shows no indication of either warm dust or a cool stellar component, and as such has been fit by two blackbody curves. The only issue is how much light is removed by dust in the line of sight.

Arkhipova et al. considered the spectral type of HD 179821 to be F3, which is quite compatible with the model atmosphere parameters of Začs et al. (1996)[218] and Reddy & Hrivnak (1999)[158]. These imply a colour excess of 1.3 magnitudes and a total visual extinction of 3.9 magnitudes. The alternative model of Thévenin et al. (2000) is more compatible with a spectral type of F8. This produces a total extinction of 2.9 magnitudes. A third dereddening involves the quoted spectral type in the SAO catalogue of G5 and requires $A_V = 1.53$.

Calculations of the visual extinction as a function of distance for this line of sight (Hakkila et al. 1997)[75] show that the interstellar visual extinction rises rapidly to 2.4 ± 0.7 magnitudes at 1.5 kpc, and slowly from there to reach 2.8 ± 0.7 mag at 7.5 kpc so this does not constrain the high extinction models.

Gledhill & Takami (2001)[71] calculated that their scattered light model would produce a V-band extinction of between 1 and 2 magnitudes at a distance of 6 kpc. They noted that this does not constrain the distance to the star, as it is possible for the dust density to increase to maintain the optical depth. In this case then it may well be feasible to use a 5660 K star to generate the SED.

One thing to notice is that the Hα line profile is best fit with a cooler stellar model that a hot one. In Figure 5.11 the absorption wings more closely resemble G-type than F-type supergiants.

The frequencies present in the photometry also favour the cooler star model. By considering it to have a similar pulsation constant to the F-type programme stars HD 70379 and HD 95767, the longer periods in the periodograms of HD 179821 point to a less dense, and therefore a cooler, star.

For this reason the adopted reddening was that associated with the model of Thévenin et al., $A_V = 2.9$ mag. Within uncertainties the total extinction is compatible with the maximum IS extinction predicted for this line of sight and thus the upper limit to the distance to HD 179821 is 4 kpc. This implies a very luminous star, $M_V = -7.7$. The blackbody fits require two curves at 6300 and 155 K, which implies a stellar temperature of 5800 K. The amount of circumstellar dust around this star is quite large compared with the other stars in this programme. $M/D^2 = 2.2 \times 10^{-4}\ M_\odot$ kpc^{-2} derived from the 60 μm flux predicts 0.4 $M_\odot$ of dust and gas at a radius of 700 $R_\star$ from the central star.

5.4 Spectroscopy

HD 179821 displays an absorption spectrum with emission observed in Hα and the Ca II triplet. The spectrum is somewhat unusual for our programme in that the absorption lines are quite broad. The typical FWHM are about 0.4 Å larger than for most of the other stars in our sample. It also has some quite complex structure in the Na D lines and also displays a number of diffuse interstellar bands. There is no trace of the 6708 Å Li I line, which would indicate a that the star had recently experienced the third dredge up.

5.4.1 Radial Velocities

The radial velocities obtained for a number of lines are displayed in Figure 5.7 and summarized in Table 5.7. The data are available in Tables C.1 and C.2 of Appendix C. The scatter is quite large, which means that long term trends are not obvious from the curves. The lines with lower amplitudes are Hα and λ8498 Ca II lines, and they also have the highest mean values, which perhaps indicates outflowing material higher in the atmosphere.

λ_o (Å)	6347	6371	6562	8446	8498
Species	Si II	Si II	Hα	O I	Ca II
χ (eV)	8.12	8.12	10.19	9.52	1.69
n	29	17	29	27	29
μ_{rv} (km s^{-1})	86.07	84.22	94.64	90.86	93.64
σ_{rv} (km s^{-1})	3.45	3.81	2.08	3.33	1.21
Δ_{rv} (km s^{-1})	0.39	0.43	0.39	0.36	0.66

λ_o (Å)	5432	5615	5853	6757	7896
Species	Fe I	Fe I	Ba II	S I	Mg II
χ (eV)	1.01	3.32	0.60	7.87	10.00
n	27	28	23	21	28
μ_{rv} (km s^{-1})	90.14	83.79	88.66	82.50	93.67
σ_{rv} (km s^{-1})	4.05	3.83	5.08	3.88	3.46
Δ_{rv} (km s^{-1})	0.67	0.68	0.52	0.50	0.35

Table 5.7: Summary of the radial velocity for 10 lines in HD 179821. μ_{rv} is the mean velocity, σ_{rv} is the standard deviation, and Δ_{rv} is the mean error, all in km s^{-1}. n is the number of measures.

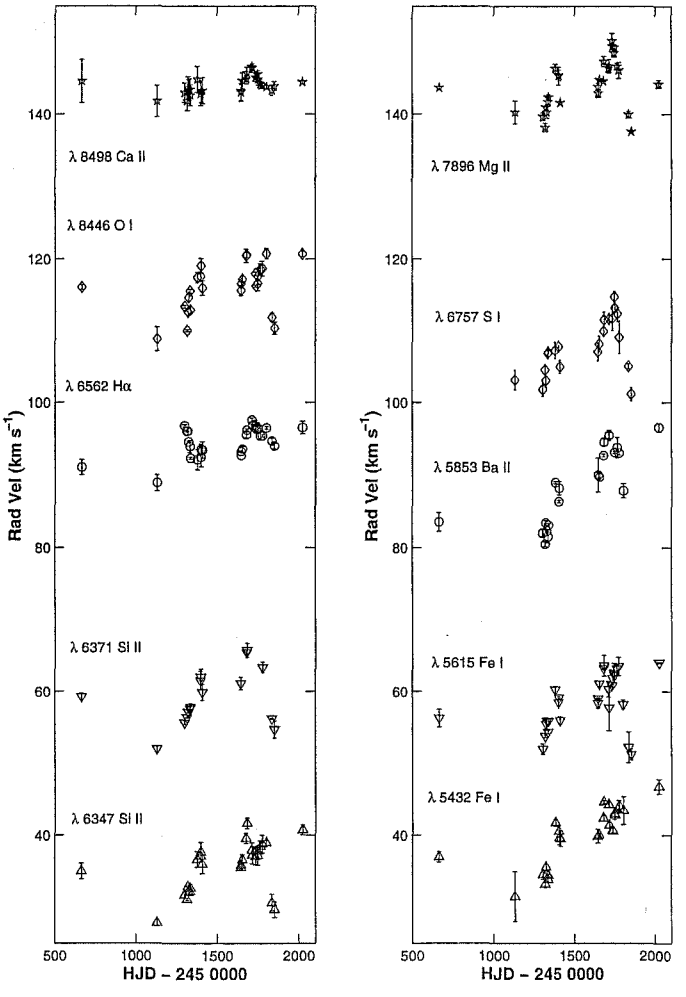

Figure 5.7: Radial velocity variations for HD 179821. λ6562 Hα and λ5853 Ba II are shown at their observed velocities. The other lines are displaced from these by $\pm$25 or $\pm$50 km s^{-1}.

The radial velocities for a number of lines were analysed for periodicities using the Lomb-Scargle technique (Figure 5.8). Although the variations are less well sampled and subject to a greater uncertainty than the photometry, the pure absorption lines show evidence of a main oscillation with a period at 272 ± 14 d (0.0037 ± 0.0002 d^{-1}). An example of the phasing of the radial velocities is presented in Figure 5.9, where we apply a 275 d period to the λ5853 Ba II radial velocities. This compares well with the 255 ± 11 d cycle detected in the photometry.

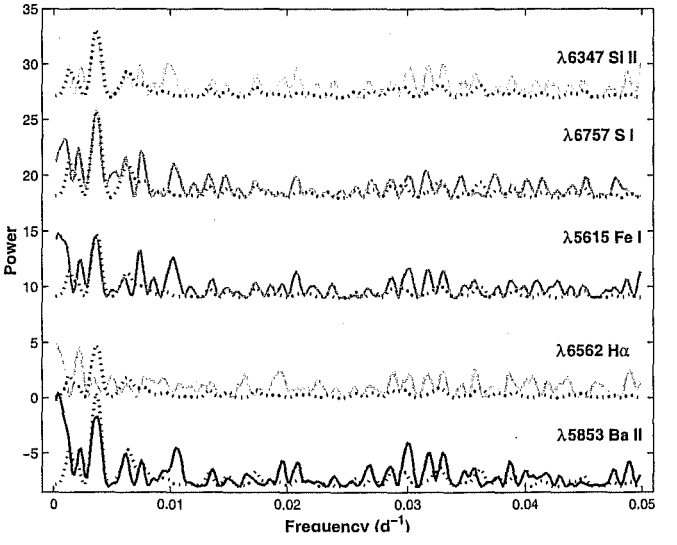

Figure 5.8: Lomb-Scargle periodograms for radial velocities in the spectrum of HD 179821. The dotted line is the window function for 271 days.

5.4.2 Hα Profile

The Hα profile of HD 179821, presented in Figures 5.10a and 5.11, very much resembles that of other post-AGB stars. There are broad absorption wings with a sharp, deep absorption core flanked by smaller variable emission peaks. The absorption at about -50 km s^{-1} is due to Ti II. It should be noted that the wings are not as pronounced as for the F-type post-AGB stars. This is a feature which strongly reminsicent of that of SAO 209008 (see §6.3.2).

Comparing the Hα profile of HD 179821 with other spectral standards, as in Figure 5.11a, emphasizes this point. As the temperature of the stan-

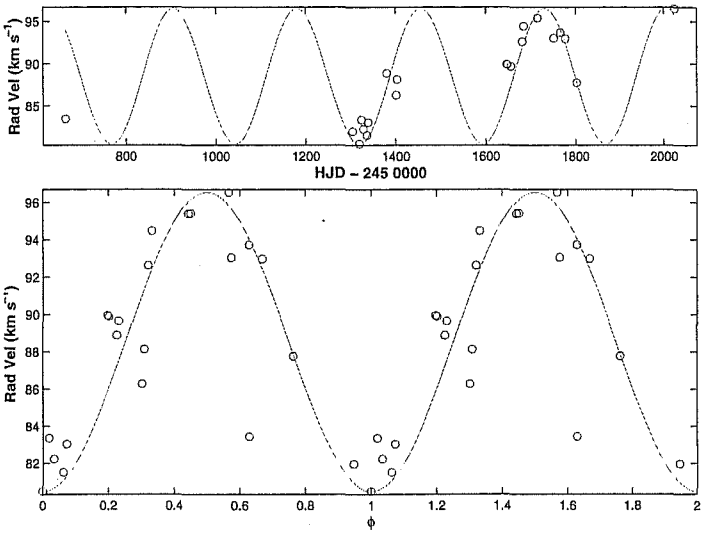

Figure 5.9: Radial velocity of the λ5853 Ba II line of HD 179821 phased to 275 d.

dard increases, the wide absorption wings become more pronounced. So to reproduce the observed Hα profile there has to be an additional wider emission as well as a narrower self-absorbed profile. Such profiles can be generated by a number of processes including light scattering from a large emission peak off the thermalized electrons, as in the case of P Cygni (Bernat & Lambert 1978)[14], Raman scattering of Lyβ photons (Lee 2000)[116] or from fast stellar winds. Raman scattering can be discounted due to the lack of evidence for a strong local source of Lyβ. Specifically there is a lack of extra short wavelength flux in the SED. Generating a single large emission feature at Hα would also produce a smaller feature at Hβ which is also not observed, ruling out scattering from electrons. The radial velocities show no significant gradient indicative of an expanding atmosphere required for a fast wind. So most likely there is just a small amount of emission added to a late F or early G-type Hα profile.

5.4.3 Sodium D Lines

As can be seen from Figure 5.12, HD 179821 is another star with a very complicated set of Na D lines, although in contrast to HD 172481 (see §9.4.3), the lines are not separated into two distinct groups. We fit 6 components

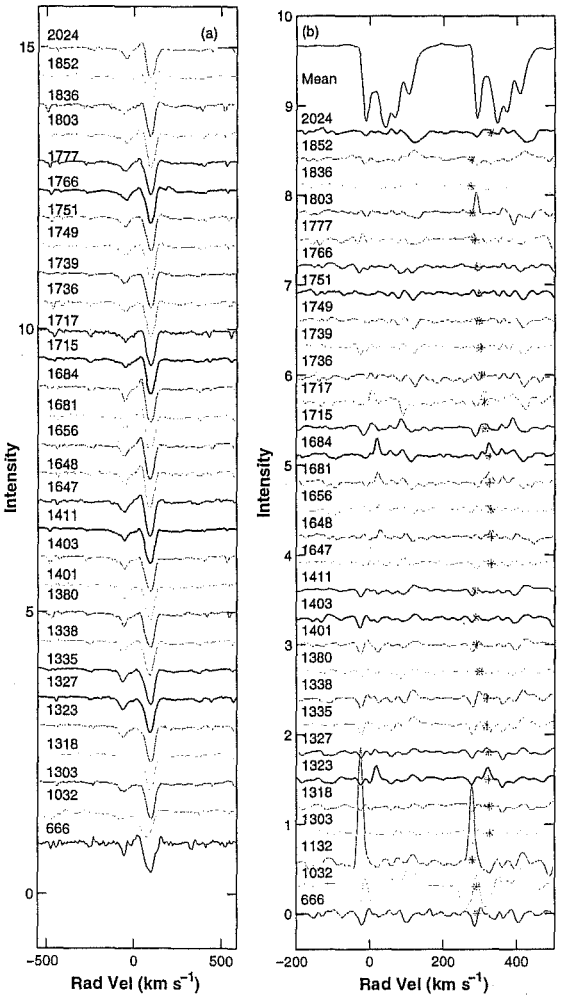

Figure 5.10: Time sequence of (a) Hα profiles and (b) Na D residual profiles for HD 179821. The asterisk indicates the position of any night sky lines in the D_1 residual.

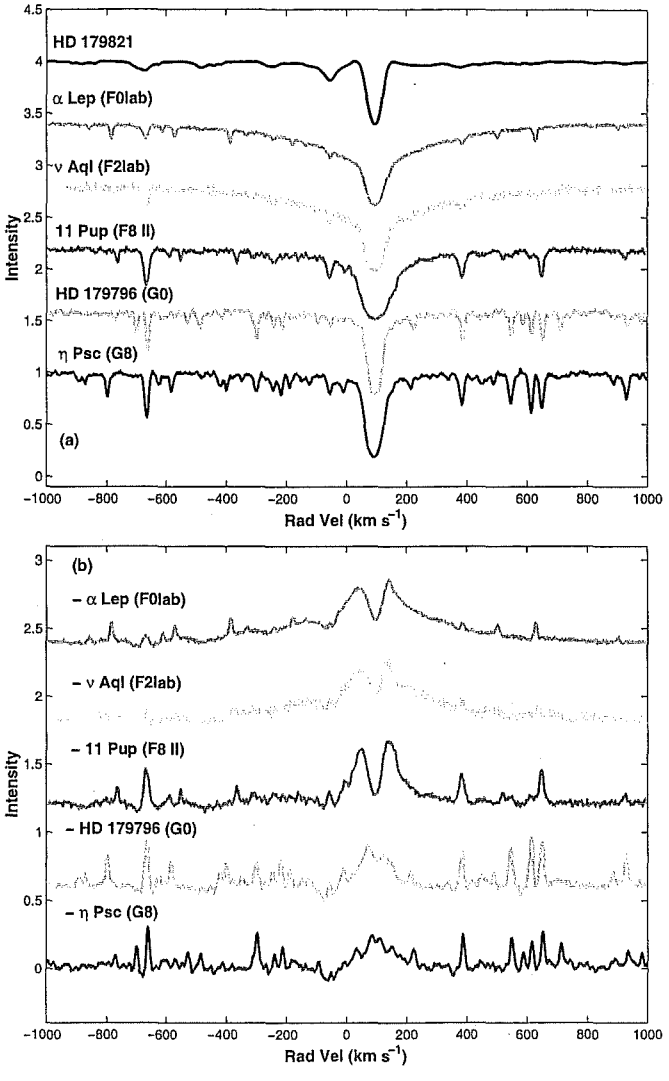

Figure 5.11: Hα profile of HD 179821 compared with some F and G-type stars. (a) The profiles in the frame of HD 179821 and (b) the residuals.

to the HERCULES spectrum.

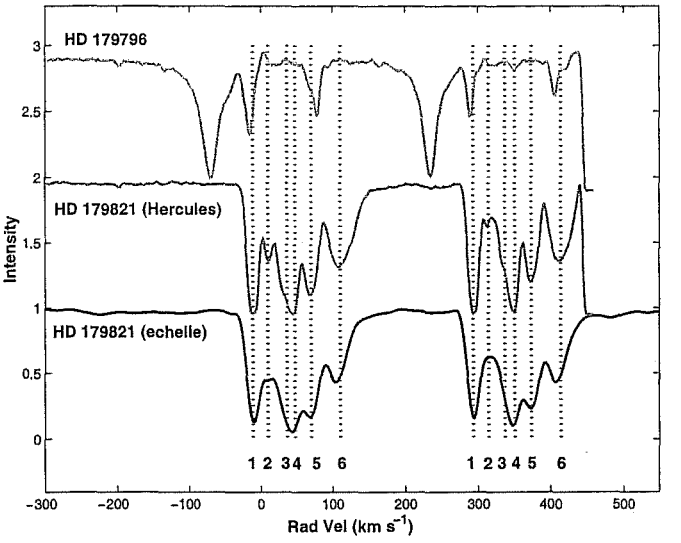

Figure 5.12: The mean Na D line échelle profile for HD 179821 compared with HERCULES spectra of the star and nearby HD 179796. The components are labelled according to Table 5.8.

Comparing the mean Na D line profiles with those of Začs et al. (1996) [218] and Reddy & Hrivnak (1999)[158] do not indicate any significant differences. The five components identified by Začs et al. are still present. This would suggest that the D lines have been stable over the last decade. Our analysis recovers two of their absorption features, at -11.1 and 41.9 km s^{-1}, corresponding to components 1 and 4 in Table 5.8. The gap between these components is best fit with another absorption at about $+8.5$ km s^{-1} (Reddy & Hrivnak component 4). This feature may well be variable, although this may be due to contamination from night sky emission. Components 3-5 are quite difficult to quantify as it is not clear whether or not there is an emission at a velocity of $+57.5$ km s^{-1}. There is also an additional weak absorption feature at $+28.9$ km s^{-1} which is present in the Na D lines observed by Reddy & Hrivnak, but not included in their analysis.

Začs et al. debated whether the most red-shifted absorption was a single high velocity feature ($\sim +106.8$ km s^{-1}) or whether it was due to a lower velocity line bisected by an emission at $\sim +87.2$ km s^{-1}. Reddy & Hrivnak also mention this and point out that this feature is also seen in other post-AGB stars. They offer no speculation. Given the model atmo-

#	λ (Å)	W (Å)	Rad Vel (km s^{-1})		Notes
			$\odot$ frame	$\star$ frame	
1	5889.750	0.400	−11.0	110.2	IS, LSR
2	5890.157	0.084	9.7	89.5	IS $d = 1.2$ kpc
3	5890.677	0.654	36.2	63.1	IS $d = 2.3$ kpc
4	5890.906	0.652	47.8	51.4	IS $d = 3.0$ kpc
5	5891.344	0.323	70.1	29.1	CS?
6	5892.147	0.548	111.0	−11.7	PS + EM?
1	5895.725	0.376	−10.5	109.8	IS, LSR
2	5896.144	0.075	10.8	88.5	IS $d = 1.2$ kpc
3	5896.583	0.303	33.1	66.1	IS $d = 2.3$ kpc
4	5896.861	0.231	47.2	52.0	IS $d = 3.0$ kpc
5	5897.300	0.301	69.6	29.7	CS?
6	5898.107	0.493	110.6	−11.3	PS + EM?

Table 5.8: The components of the Na D lines of HD 179821 determined from the HERCULES spectra assuming that all the components are in absorption. See Figure 5.12 for identifications. CS in the notes means a circumstellar feature, IS interstellar, PS photospheric and EM emission. ? indicates tentative identification. Both the heliocentric ($\odot$ frame) and stellar rest frame ($\star$ frame) radial velocities are given.

spheres used and the sodium abundances derived, synthetic spectra produce very detectable photospheric D lines, with equivalent widths of at least 0.5 Å. The mean photospheric velocity from 64 symmetric absorption lines is $+99.6\pm0.1$ km s^{-1} and one would expect to observe an absorption feature at this radial velocity. This favours the latter scenario and we require an emission feature at $+88.1$ km s^{-1}. Additionally Začs et al. used the equivalent width of this feature, and that at -11 km s^{-1}, to estimate the abundance of sodium. Both components gave a deficiency compared to other sodium lines. This lends support to the claim for a photospheric absorption plus an emission line as a larger equivalent width for the absorption would mean an increase in the derived abundance.

Component 1 is an interstellar feature. Not only is it quite narrow compared to the other lines in the spectrum of HD 179821, but there is a shallower but similar feature in the spectrum of the nearby star HD 179796 ($V = 9.9$, separation 6′). Given that the radial velocity of this star is about -69 km s^{-1}, it is unlikely to be in-falling circumstellar material.

Although the Na D lines have a consistent profile during the course of the programme, there is one outstanding spectrum (HJD 2451032) which has a very much diminished component 4 but more intriguingly it has also developed a new component at about -45.0 km s^{-1} in the heliocentric frame. This is not material which has migrated from the photospheric line (component 4). The fact that this has not been observed again may indicate that this is a dubious feature perhaps introduced by some undetermined effect pertaining to the observing conditions on that particular night.

Component 5 has a stellar frame radial velocity of $+29.4$ km s^{-1} which is close to the 33.9 km s^{-1} Zuckerman & Dyck (1986)[222] found from CO (1-0) maser emission. It is possible that these could be due to the material from the same ejected shell of material.

At a distance of 6 kpc, HD 179821 would lie 520 pc below the Galactic plane and would have a nett radial velocity of $+83$ km s^{-1}. The line of sight intercepts the Sagittarius spiral arm at a distance of 3 kpc ($z = -260$ pc) and the mean rotational radial velocity is $+41$ km s^{-1}. This is a good match to component 4. From the radial velocities of components 2 and 3 the rotation curve predicts that these features should be due to clouds lying at 1200 and 2300 pc. The motion of the Sun with respect to the LSR produces a radial velocity of -11.2 km s^{-1}, i.e., towards HD 179821, and a good match to the velocity of component 1.

λ (Å)	W (Å)	$E(B-V)$	$\Delta E(B-V)$	Rad Vel (km s^{-1})
5780.59	0.24	0.42	–	−15.1
5797.11	0.15	1.11	0.16	−13.3
5849.78	0.07	1.35	0.23	−9.2
6196.19	0.05	0.74	0.06	−20.3
6199.21	0.01	0.63	0.23	−23.0
6203.19	0.12	1.15	0.17	−25.1
6270.06	0.06	0.82	0.20	−33.7
6367.22	0.01	0.53	0.12	−6.6
6376.07	0.02	0.58	0.11	−13.8
6379.27	0.10	1.24	0.38	−9.1
Mean		0.89	0.17	−16.9
σ		0.33	0.10	8.5

Table 5.9: Colour excess and radial velocity of some DIBs observed in the spectrum of HD 179821. λ is the rest wavelength, W the equivalent width, $E(B-V)$ and $\Delta E(B-V)$ are the derived colour excess and uncertainty.

5.4.4 Diffuse interstellar bands

There are a number of diffuse interstellar bands (DIBs) visible in the spectrum of HD 179821. These are listed in Table 5.9 along with some other estimated parameters.

Začs et al. (1999)[219] measured 8 diffuse interstellar bands in the spectrum of HD 179821. They derived a line of sight colour excess of $E(B-V) \simeq 0.9 \pm 0.2$ and six of lines had radial velocities between −13 and −10 km s^{-1}. Interestingly although the HD 179796 spectrum clearly shows the −11 km s^{-1} Na D lines, there is no clear indication of any of the DIBs listed above. This line is much stronger in HD 179821 and we so there could be a variation in the density or composition of this cloud between the two lines of sight.

We find a nett colour excess of 0.9 ± 0.2 from 10 interstellar bands, translating to $A_V = 2.7 \pm 0.5$ mag. This is compatible with the extinction required for an F8 star and with the estimate of Začs et al. However some of the radial velocities are inconsistent and will require further study.

5.4.5 λ7774 O I triplet

From the red minus spectrum taken on HJD 2451306 we obtained an equivalent width for the λ7774 O I multiplet of 2.9 Å. Combined with $(b-y)_o = 0.23$ (Gray 1992)[72] derived from the spectral type, this implies an absolute magnitude $M_V = -10.5$. This is clearly incompatible with the models of the star as a post-AGB star.

5.5 Discussion

This object was observed as part of the Hipparcos programme (HIP 94496) but the derived parallax, 0.8 ± 1.12 mas, is rather uncertain. The proper motion was 1.77 ± 0.97 mas yr^{-1} in right ascension and -4.07 ± 0.74 mas yr^{-1} in declination. Translating these to a distance of 6 kpc indicate a transverse velocity of 126 ± 100 km s^{-1}. At 1 kpc this is just 21 ± 50 km s^{-1}. The total space velocities are 155 ± 100 km s^{-1} and 92 ± 100 km s^{-1} respectively. Indeed this is about the same size as one would expect from the Galactic rotation curve for the star at 6 kpc, but the direction is away from the Galactic plane rather than along it.

The distance to the star has been estimated at 6 kpc by most of the authors who favour the massive star scenario. This is purely on the basis of Zuckerman & Dyck's (1986)[222] observation that the radial velocity of the star is compatible with the rotation curve of the Galaxy at this distance. Zuckerman & Dyck themselves note that this requires a very luminous object greatly removed from the Galactic plane. The implication of this is that HD 179821 is not following disk kinematics and therefore their distance estimate is useless. However HD 179821 does present aspects that are compatible with the high mass scenario especially when examining the circumstellar environment.

Začs et al. (1996)[218] also found four absorption components to the sodium D lines (at -11.1, $+41.0$, $+68$ and $+108$ km s^{-1}) but were unsure as to whether or not the components at 68 and 108 km s^{-1} were two parts of a single line separated by an emission line at 90.2 km s^{-1}. Abundance analysis on the lowest and highest velocity components produced a result much lower than for other sodium lines and were deemed to be either circum- or interstellar.

The O-rich circumstellar environment is what would be expected from the evolution of a low mass star on the AGB. It does not have the mass to cause the efficient third dredge up required to change the surface chemistry from an oxygen to a carbon rich star.

5.6 Conclusions

HD 179821 is a semi-regular variable star with variations which are largest in the B-band. There is no discernible trend with wavelength. Periodogram analysis of the MJUO data produced a primary peak at 193 ± 6 d with secondary peaks at 102 ± 2 and 144 ± 4 d. Subjecting V-band data from Arkhipova et al. (2001)[5] to the same analysis did not produce a peak at 193 days, but the two other peaks were present. The amplitude and the period are similar to the other post-AGB stars presented in Hrivnak et al. (2001)[88].

The SED of HD 179821 showed no indications of a warm dust component between 600 and 4000 K. A more satisfactory fit was achieved by dereddening the photometry using a colour excess $E(B-V) = 0.8$ magnitudes, by assuming the star to be F8. This is independently confirmed from equivalent width measurements of diffuse interstellar bands which indicate $E(B-V) = 0.9 \pm 0.2$ mag. The stellar and dust temperatures uncovered were 5800 and 155 K respectively. At a distance of 4 kpc from the Sun this implies $0.3 M_{\odot}$ of material at around 700 $R_{\star}$ from the star.

Radial velocity analysis showed that the star is quite variable, with a peak-to-peak amplitude of about 14 km s^{-1}. Periodogram analysis uncovered a peak at 271 ± 14 d from absorption lines. The large scatter in the values does not rule out any binary companions around the star, but does indicate some strong pulsational activity.

The sodium D line profiles are very complicated and contain six components. The lowest velocity component (-11.1 km s^{-1}) is also seen in the spectrum of a nearby star, HD 179796, and its radial velocity is entirely consistent with it moving with the LSR. Other components had radial velocities compatible with them being from the Sagittarius spiral arm, and clouds at 1.2 and 2.3 kpc. The radial velocity of one of the components is a good match to that of the ejection velocities found maser emission. There is also a likely emission line from slowly outflowing material which bisects the probable stellar absorption.

HD 179821 showed an Hα profile which showed the same general characteristics as those of the other intermediate temperature stars observed in this programme. It was shown that the profile more closely resembles those of early G and late F-type than early F-type Hα profiles. This was due to the lack of an additional source for the wide emission required to accommodate those profiles.

Chapter 6

SAO 209008

6.1 Introduction & historical perspectives

SAO 209008 (= HD 159378 = IRAS 17326-3324, see Table 6.1) is also catalogued as member 102 of the Galactic cluster Trumpler 27 (= C1732-334). Moffat et al. (1977)[133] examined the properties of this cluster and estimated a distance of 2.1 kpc, a colour excess $E(B-V) = 1.40$ and an age of 6 Myr. Tr 27-102 lies 7′ from the centre of the cluster with an estimated age of 15 Myr, but they noted that not all clusters are coeval and considered it to be an older member of the group. They also pointed out that it would lie near the blue edge of the instability strip and should have a period of about 75 days.

Coordinates	α	$17^{\mathrm{h}}\ 35^{\mathrm{m}}\ 56.35^{\mathrm{s}}$
(Epoch 2000.0)	δ	$-33°\ 25'\ 56.6''$
Galactic	l	355.09
coordinates	b	-0.63
Mean Brightness	B	10.27
	V	8.61
Spectral Type		G2 Ia

Table 6.1: Basic parameters of SAO 209008.

Acting upon this information van Genderen & Thé (1978)[194] began a photometric monitoring programme which uncovered an oscillation with a period of 75 days and a variable amplitude, of at most 0.17 magnitudes. The colours changed in step with the brightness. van Genderen (1980)[193]

noted that the star's colours were unusually blue for the spectral type and claimed this was due to an unseen evolved blue companion.

Massey et al (2001)[129] examined Tr 27 spectroscopically as part of a wider survey of Galactic clusters in an effort to establish the progenitor mass of Wolf-Rayet stars. For Tr 27 they estimated the distance as 2.5 kpc and the age as 6.72 Myr. They also considered SAO 209008 to be part of the cluster and estimated its age as about 10 Myr and its mass as between 15 and 25 $M_{\odot}$ based on its position in the HR diagram.

Balona (1982)[8] obtained 25 radial velocity measures covering the interval HJD 2443941 to 2444536 (595 d) and found a mean of -15.8 ± 1.3 km s^{-1}. These velocities had an RMS of 6.2 km s^{-1} implying marked variability. But periodograms found peaks at 105, 73, 188 and 312 d which suggested no unambiguous period for the star.

Unfortunately, SAO 209008 was not part of our photometric monitoring programme, but we do have 33 high resolution spectra covering 1111 days. Spectroscopically there are a number of similarities with HD 179821, including line width and Hα shape, and it was felt instructive to compare the properties of these two stars.

6.2 Spectral energy distribution

To construct the spectral energy distribution we have used the means of the data of van den Bergh (1988, U)[189] and Dean (1980, $BVRI$)[42] to provide the optical photometry displayed in Table 6.2. These programmes were from March 1979 to July 1980 (HJD 2443954 to 2444423), and also have an overlap with the radial velocity programme of Balona (1982)[8], although not enough to explore the relationship between them. The SED is completed with the $JHKL$ and IRAS photometry listed in Table 6.3.

	U	B	V	R	I
Mean	12.23	10.37	8.44	7.24	6.08
Range	-	0.35	0.18	0.18	0.12

Table 6.2: $UBVRI$ photometry for SAO 209008. U is taken from van den Bergh (1988)[189] and $BVRI$ is the mean of the data in Dean (1980)[42].

A spectral type of G2 gives a total visual extinction of 3.2 magnitudes, from $E(B-V) = 1.1$. Assuming that all of this is due to IS dust puts SAO 209008 at ~ 2.0 kpc, if the star is a massive supergiant ($M_V = -6.30$). At

	J	H	K	L	12(Jy)	25(Jy)	60(Jy)	100(Jy)
Band	4.765	4.109	3.822	3.495	5.71:	28.76	11.17	366.00
Error	0.016	0.006	0.009	0.025	0.51	2.88	L	L

Table 6.3: Summary of the infrared photometry compiled for SAO 209008. $JHKL$ is from SAAO (1996 December 19). L denotes an upper limit for the photometry.

this distance Hakkila et al. (1997)[75] calculate an interstellar extinction of 4.1 ± 0.8 magnitudes, and within uncertainties, this is this consistent with the spectral type, and also with the earlier estimates for the distance of Tr 27.

The dereddened spectral energy distribution is displayed in Figure 6.1. There is no evidence of either hot circumstellar dust, or the hot stellar companion postulated by van Genderen (1980)[193]. Increasing the levels of extinction (from $A_v = 3.2$ to $A_v = 4.2$) revealed no additional blue flux on top of the predicted stellar curve. Indeed the dereddened U-band photometry lies below the blackbody fit. The temperatures of the fitted curves are 5100 and 185 K, with an RMS of 0.13, neglecting the uncertain 100 μm flux. The corrected stellar temperature is 5150 K.

From the 60 μm photometry and an estimated distance of 2 kpc, we predict a total mass of circumstellar material of 1.4×10^{-3} $M_\odot$ at a distance of 3.8×10^2 $R_\star$ from the central star.

6.3 Spectroscopy

The spectrum of SAO 209008 bears a striking resemblance to that of HD 179821 (Figure 6.2), particularly in the width of the lines and in the shape and behaviour of the Hα profile. The star is also listed by SIMBAD as a post-AGB star, however there is little support for this claim in the literature. The stars make an interesting pair and it is worthwhile comparing and contrasting them.

6.3.1 Radial Velocities

The radial velocity variations for a selection of lines in the spectrum of SAO 209008 are displayed in Figure 6.3 and summarized in Table 6.4. There are 28 spectra spanning 1046 days and the data from these are shown in

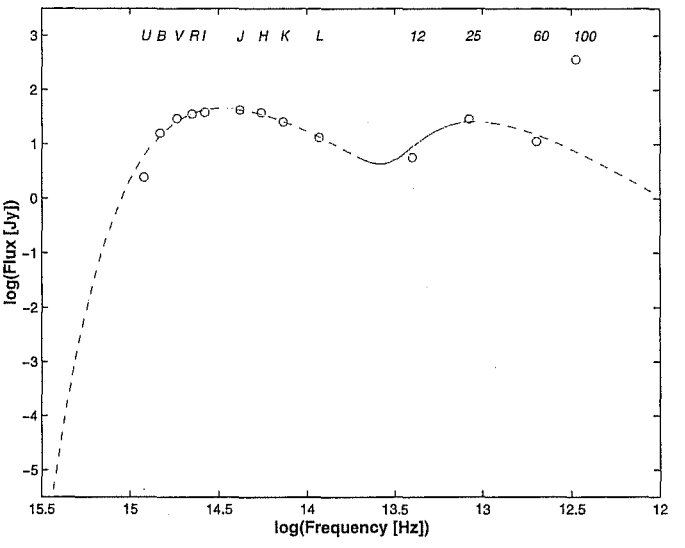

Figure 6.1: Blackbody fits to the dereddened visual and infrared photometry of SAO 209008. The fitted curves have temperatures of 5100 and 185 K. The RMS on the fits (excluding the 100 μm point) is 0.13.

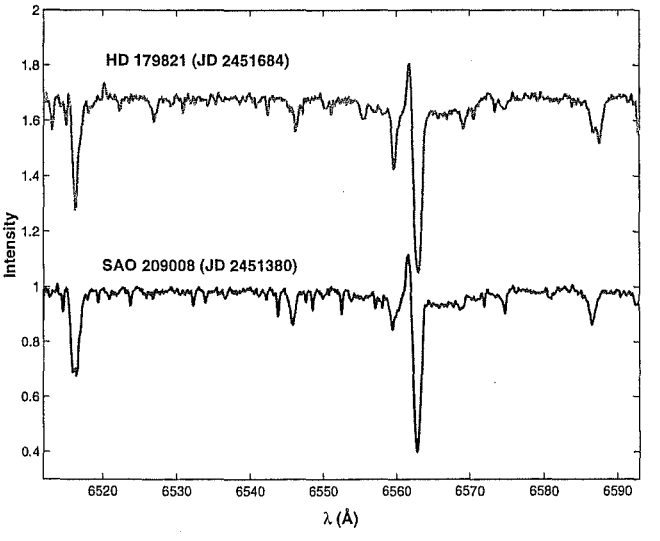

Figure 6.2: A comparison of SAO 209008 and HD 179821. The spectra have been shifted to the respective stellar rest frames.

Tables C.3 and C.4. A frequency analysis was conducted on these points and the results are shown in Figure 6.4.

The radial velocity curves show a somewhat erratic oscillation with a maximum amplitude of about 20 km s^{-1}. This was also reported by Balona (1982)[8]. This is slightly more pronounced in the lower excitation potential lines like $\lambda\lambda$5853 Ba II and 5615 Fe I. These lines show peak-to-peak variations of 22 and 24 km s^{-1}, compared to 18 km s^{-1} for the Si II and λ7442 N I lines. None of the lines show significantly different mean velocities indicating that the atmosphere is not undergoing a profound mass loss. The lower amplitude in the absorption core of the Hα lines may well be due to the underlying narrow emission. Hα also shows a lag when compared to the other lines too. None of the lines show any longer term trends which would be expected for a long period binary system, although it does not rule out the case of an eccentric orbit or a system with a low inclination.

λ_o (Å)	6347	6371	6562	7442	8446
Species	Si II	Si II	Hα	N I	O I
χ (eV)	8.12	8.12	10.19	10.33	9.52
n	29	28	29	28	24
μ_{rv} (km s^{-1})	−17.63	−16.63	−17.65	−17.16	−13.48
σ_{rv} (km s^{-1})	5.02	5.05	4.73	4.67	5.46
Δ_{rv} (km s^{-1})	0.49	0.66	0.59	0.46	0.25

λ_o (Å)	5429	5434	5572	5615	5853
Species	Fe I	Fe I	Fe I	Fe I	Ba II
χ (eV)	0.96	1.01	3.40	3.32	0.60
n	25	26	24	25	26
μ_{rv} (km s^{-1})	−16.75	−18.56	−17.35	−17.59	−17.70
σ_{rv} (km s^{-1})	6.93	6.64	6.38	5.94	6.04
Δ_{rv} (km s^{-1})	0.47	0.81	0.42	0.32	0.28

Table 6.4: Summary of the radial velocity for 10 lines in SAO 209008. μ_{rv} is the mean velocity, σ_{rv} is the standard deviation, and Δ_{rv} is the mean error, all in km s^{-1}. n is the number of measures.

The periodograms shown in Figure 6.4 for the absorption lines have their most significant peak at 161 ± 6 d (0.0062 d^{-1}). The other main peaks are listed in Table 6.5. Of the other peaks, 279 ± 19 d is probably a side lobe of the main period. The periodogram for Hα absorption velocities, on the other hand, shows its strongest peak at 25.7 ± 0.2 d (0.03896 d^{-1}) with

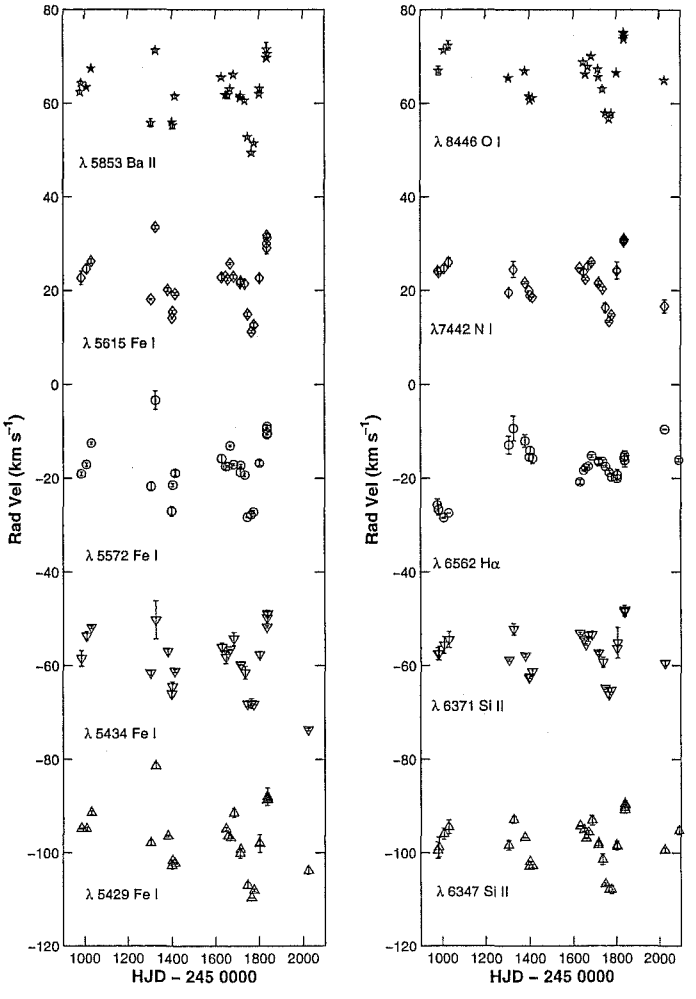

Figure 6.3: Radial velocity variations for 10 lines in the spectrum of SAO 209008. λ5572 Fe I and λ6562 Hα are shown at their correct velocities, the other curves have been offset by $\pm$20 km s^{-1}or $\pm$40 km s^{-1}.

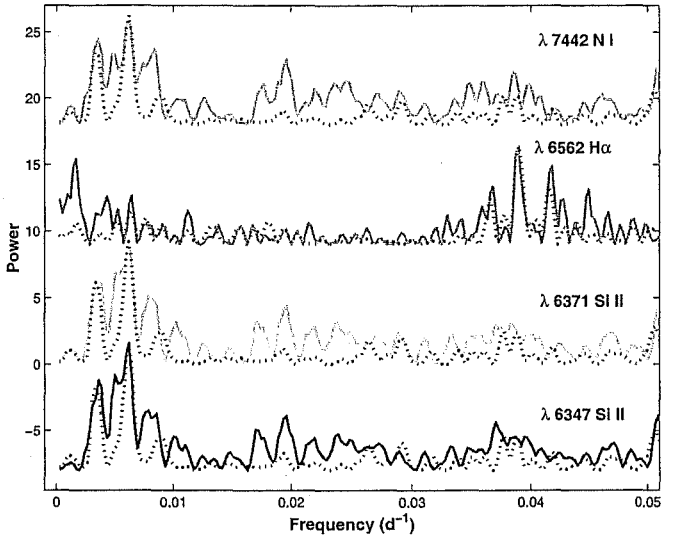

Figure 6.4: Lomb-Scargle periodograms for some radial velocity curves of SAO 209008. The periodograms are shown with the window function for 161 d, except Hα for which we use 25 d.

Frequency ($\times 10^{-3}$ d^{-1})	Power	Period (d)	ΔP (d)
0.0036	6.8	280	19
0.0050	7.2	200	10
0.0062	10.5	161	6
0.0079	4.5	127	4
0.0196	4.1	51	1

Table 6.5: Main peaks in the Lomb-Scargle power spectra of SAO 209008 Si II and N I radial velocity curves. The uncertainties in the frequencies are 0.24×10^{-3} d^{-1}.

others at 600 ± 90, 232 ± 13, 27.2 ± 0.2, 24 ± 0.1 days.

The data of Balona (1982)[8] indicated periods at 105 (0.0095 d^{-1}), 73 (0.0137 d^{-1}), 188 (0.0053 d^{-1}) and 312 days (0.0032 d^{-1}). The periodograms for the MJUO radial velocity curves do not indicate any significant power at 73, 105 or 312 d. Indeed the only the peak at 200 d is close enough to be identified with Balona's 188 d peak, and it is subordinate to the peak at 161 d.

Compared with the radial velocities of HD 179821 we find that the range of velocities of the lines is a little higher for SAO 209008 (13.7 compared with 21.4 km s^{-1}). The periodograms show that the main period of variations for the radial velocities of SAO 209008 is 161 ± 6 d. For HD 179821 this is 272 ± 14 d.

6.3.2 Hα Profile

This is very similar to HD 179821 in both appearance (Figure 6.2) and behaviour (compare Figure 6.5a, with that in Figure 5.10a). There is a sharp central absorption flanked by small variable emission features set in the middle of a wider, shallow absorption feature. This wide component is not as pronounced as it is in the F-type stars in our sample. This suggests a later spectral type.

6.3.3 Sodium D Lines

The Na D lines of SAO 209008 show more activity than those of many of the other stars in our programme. The mean échelle profile (Figure 6.5b, top) seems to consist of a saturated component flanked by two absorptions. From the rest of the residual time sequence it appears that there are shape changes in addition to those caused by a variable night sky line. In particular there appears to be a change at ~ -70 km s^{-1}, which is too far from the mean stellar velocity (~ -16 km s^{-1}) to be accounted for by photospheric velocity variations.

The HERCULES spectrum, shown in Figure 6.6, is somewhat complicated by the presence of the saturated feature. This makes it quite difficult to obtain a satisfactory fit to the profiles with Gaussians. So in this case we have just marked the positions of the various possible components. The mean radial velocity derived from 78 lines in the same spectrum (HJD 2452091) was -13.96 ± 0.05 km s^{-1} and the heliocentric correction was +6.98 km s^{-1}.

If SAO 209008 moved solely with the rotation curve of the Galaxy we

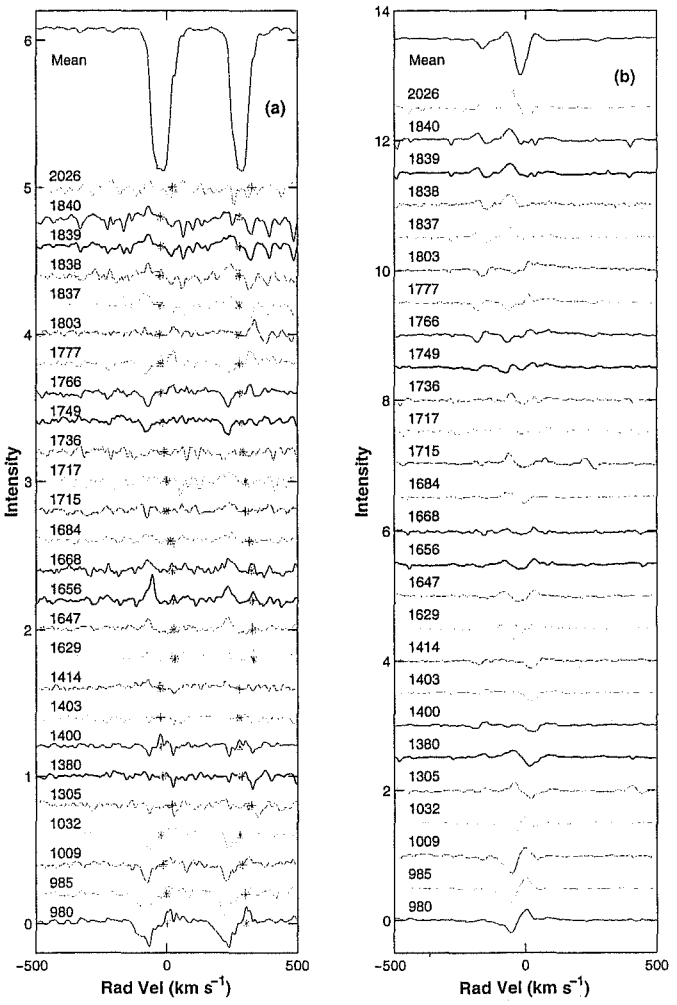

Figure 6.5: Na D (a) and Hα (b) residual line profiles of SAO 209008 over the course of our programme. The asterisks indicated the radial velocity of atmospheric features.

#	λ (Å)	Rad Vel (km s^{-1})		Notes
		$\odot$ frame	$\star$ frame	
1	5888.9310	−55.3	41.3	
2	5889.6225	−20.9	6.9	PS + Sgr
3	5889.8285	−8.1	−5.8	NS E
4	5890.2110	9.9	−23.8	
5	5890.4317	22.6	−36.5	CS E
6	5890.5494	29.3	−43.3	
1	5894.8970	−52.7	38.7	
2	5895.5885	−17.5	3.5	PS + Sgr
3	5895.7945	−7.0	−7.0	NS E
4	5896.1770	12.5	−26.4	
5	5896.3977	23.7	−37.7	CS E
6	5896.5154	29.7	−43.6	

Table 6.6: The components of the Na D lines of SAO 209008 determined from HERCULES spectra taken on the night of HJD 2452091. See Figure 6.6 for identifications. NS denotes an night sky line, CS/PS circumstellar/photospheric feature, Sgr the Sagittarius arm, and E means emission line.

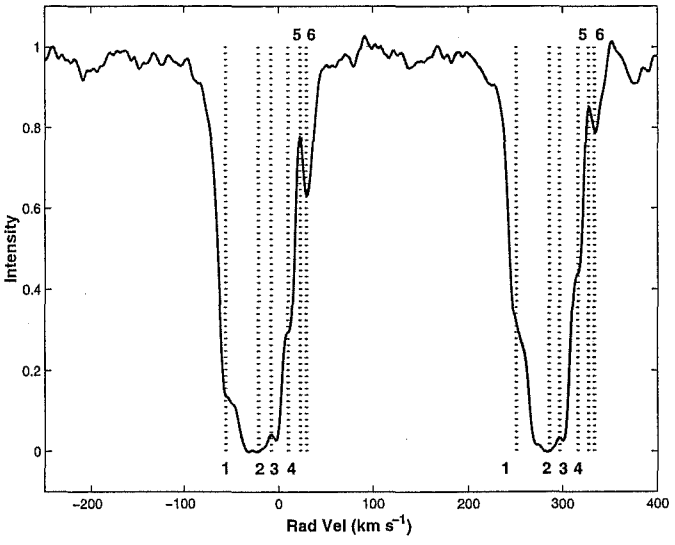

Figure 6.6: Na D line profile for SAO 209008. The components are labelled according to Table 6.6.

would find that the mean observed radial velocity, -15.3 km s^{-1}, would be achieved at 1.7 kpc, and the star would lie 19 pc below the Galactic plane. In the foreground would be the Sagittarius spiral arm ($d = 1.5$ kpc, $z = -17$ pc and $v_r = -14.5$ km s^{-1}) .

So could we identify component 1 as being due to ejected gas? The ejection velocity would be would be about 40 km s^{-1}. Component 2 is probably a combination of a photospheric and an interstellar feature associated with the Sagittarius spiral arm. This is an estimate of the mid-point of the saturated feature and is inherently more uncertain than the other features, which denote local extrema or inflections in the profile. The small emission feature matches the velocity of the heliocentric correction, which leaves us with three components to identify. These are in-falling in the stellar frame.

6.3.4 Diffuse interstellar bands

The low Galactic latitude of SAO 209008 means that there diffuse interstellar bands (DIBs) present in the spectrum. These are listed in Table 6.7 along with some derived parameters.

The mean colour excess in Table 6.7, $E(B-V) = 1.4 \pm 0.4$, translates

λ (Å)	W (Å)	$E(B-V)$	$\Delta E(B-V)$	Rad Vel (km s^{-1})
5849.78	0.08	1.59	0.26	−5.07
6196.19	0.06	0.72	0.06	−17.13
6203.19	0.13	1.20	0.18	−25.13
6270.06	0.14	1.85	0.46	−16.08
6270.36	0.00	0.00	0.00	−30.41
6376.07	0.05	1.98	0.38	−9.43
6379.27	0.12	1.48	0.46	−4.04
Mean		1.35	0.30	−15.33
σ		0.41	0.16	9.96

Table 6.7: Colour excess and radial velocity of some DIBs observed in the spectrum of SAO 209008. λ is the rest wavelength, W the equivalent width, $E(B-V)$ and $\Delta E(B-V)$ are the derived colour excess and uncertainty.

to a V-band extinction of 4.1 ± 0.9 mag. This is in good agreement with A_V quoted in §6.2. The radial velocities of the lines from 6196 to 6270 Å, as with HD 179821 (Table 5.9), are on the order of 10 km s^{-1} more blue-shifted than the other lines. Whether this is due to some unresolved stellar lines or carrier material at genuinely different radial velocities is unclear.

6.4 Comparison with HD 179821

Both HD 179821 and SAO 209008 have been shown to be photometric and radial velocity variables. These variations are semi-regular in nature. Photometrically the stars present similar amplitudes, but somewhat different periods, with HD 179821 having a principle period of 193 ± 6 d and SAO 209008 having a period of about 75 d (van Genderen, 1980). The radial velocity measurements taken as part of this project, also show that the stars have similar amplitudes but different periods. HD 179821 again having the longer principal period of 271 ± 14 d against 161 ± 4 d for SAO 209008.

If we consider these periods to be typical of the time it takes pressure waves to traverse the star then we can say that the star with shorter period variability has the higher density. Since we have derived some similar temperatures (5150 K for SAO 209008 to 5800 for HD 179821) and luminosities ($\log L/L_\odot = 4.5$ and 5.0) then we can say that HD 179821 is indeed a massive star, being about twice the mass of SAO 209008.

SAO 209008 is clearly not as evolved as the HD 179821 due to the lack of

carbon lines in the spectrum. Both stars lack the λ6708 Li I line, indicating that neither has experienced a recent third dredge up. A lack of carbon lines in the spectrum of SAO 209008, points to a star which has not experienced either the first or second dredge up. Hence SAO 209008 is quite a young star. A more quantitative justification of this assertion awaits an abundance analysis.

6.5 Conclusions

Analysing the spectral energy distribution for the star produced no evidence for either a hot stellar companion or for a warm dust component. Rather there are only two components to the SED, at 5150 and 185 K. The total reddening associated with a spectral type of G2, requires 3.2 magnitudes of visual extinction which is compatible with the star being 2 kpc away and having the extinction provided by the interstellar medium. We also estimate 1.4×10^{-3} $M_{\odot}$ at a distance of 380 $R_{\star}$ from the central star.

SAO 209008 is a radial velocity variable star which undergoes variations which cover about 20 km s^{-1} about a mean velocity of -15 km s^{-1}. A periodogram analysis uncovered a principal period of 161 ± 4 d. There were no trends over the 1111 day duration of our programme indicative of a companion star. The scale of the variations is consistent with that observed by Balona (1982)[8] but the period is different.

The Na D line profile has a saturated feature at the stellar velocity which may also be due to a foreground cloud in the Sagittarius spiral arm. This places the star is at least 1.5 kpc away. The mean radial velocity of the star is consistent with it moving with the Galactic rotation curve. The profile seems to contain three other components who's origin is undetermined.

A number of diffuse interstellar bands have been observed in the spectrum of SAO 209008. The colour excess derived from these, 1.4 ± 0.3 mag, confirm the extinction derived from the spectral type.

Most likely this is a young, massive star, not a post-AGB star. The low Galactic latitude, radial velocity, and association with a young open cluster are not indicators of an old evolved star. The spectrum is not metal poor but does lack significant carbon lines, also implying a young star. This is the main point of difference with HD 179821, suggesting that HD 179821 is a massive but more evolved star.

Chapter 7

HD 70379

7.1 Introduction & historical perspective

HD 70379 (identified with IRAS 08187-1910 and see Table 7.1) has a temperature, luminosity and an IR excess that initially hinted that it might be a post-AGB star. However, near-IR photometry (García-Lario et al. 1990)[62] and high resolution spectroscopy (Reddy & Parthasarathy 1996)[159] indicated a more mundane existence as an F6 supergiant. The latter work derived a temperature of 6300 K from a colour-temperature relationship. Combined with $BVRI$ photometry they concluded that it is an F6 supergiant at 3 kpc with a radius of 54 $R_{\odot}$.

Coordinates	α	$08^{\mathrm{h}}\ 20^{\mathrm{m}}\ 54^{\mathrm{s}}$
(Epoch 2000.0)	δ	$-19^{\circ}\ 15'\ 00''$
Galactic	l	240.57
coordinates	b	+9.76
Mean Brightness	B	9.9
	V	8.9
Spectral Type		F6Ib/II

Table 7.1: Basic parameters of HD 70379.

The results of an abundance analysis (Giridhar et al. 1997[69], listed in Table 7.2) point to a metal poor star with mild s-process enrichment. In this respect they found that it resembles the well known UU Herculis stars 89 Herculis and HD 161796.

Fujii et al. (2002)[61] modelled the dust envelope around HD 70379 using

[Fe/H]	[C/Fe]	[N/Fe]	[O/Fe]	[Mg/Fe]	[S/Fe]	[Ca/Fe]	[Y/Fe]
−0.31	+0.42	+0.38	+0.39	+0.01	+0.34	−0.17	+0.40

Table 7.2: Abundances from Giridhar et al. (1997)[69] for HD 70379.

BVRI and IRAS photometry, and derived a stellar temperature of 6630 K and dust temperature of 135 K. They also estimated the age of the dust shell to be 937 years, assuming an expansion velocity of 15 km s^{-1}. They claimed that this indicated a post-AGB star which has a low core mass of $0.55M_{\odot}$ and thus might be one of Renzini's "lazy" AGB remnants (Renzini 1981)[161].

In this chapter the photometric and spectroscopic observations of HD 70379 acquired over the period 1998 to 2001 are discussed.

7.2 Photometry

Three stars were used to calibrate the photometry. HD 70343 was used as the comparison star, HD 70441 as the primary check, and HD 70440 as the secondary check star. Their basic photometric parameters are listed in Table 7.3. They were chosen on the basis of proximity, non-variability and overall photometric similarity to the target star. Neither of the check stars have shown any variability over the course of the programme. Their RMS values are 0.007 and 0.009 magnitudes respectively.

Identifier	α(2000.0)	δ(2000.0)	B	V	SpT
HD 70343	$08^{h}\ 20^{m}\ 46.93^{s}$	$-19°\ 16'\ 38.4''$	8.96	8.52	F7V
HD 70441	$08^{h}\ 21^{m}\ 21.03^{s}$	$-19°\ 33'\ 09.3''$	8.69	8.24	F3V
HD 70440	$08^{h}\ 21^{m}\ 20.46^{s}$	$-19°\ 23'\ 38.7''$	9.80	9.36	F2/3V

Table 7.3: Basic data for the photometry calibration stars of HD 70379.

The photometric data acquired for HD 70379 consist of 70 observations over 1431 days. V and colour data are given in Table A.3 and plotted in Figure 7.1. Table 7.4 is a summary of the activity in the individual passbands which is plotted in Figure 7.2. They clearly show the star to be a variable. This propagates through all of the bands with the amplitude increasing from I to B. The star also gets bluer as it get brighter, and follows quite

well defined linear tracks on the colour-magnitude and colour-colour plots (Figure 7.3). There is no significant deviation from a straight line on these diagrams which would indicate a phase lag in one of the bands.

	B	V	R	I
Mean	9.702	9.013	8.604	8.239
Range	0.691	0.465	0.376	0.274
Error	0.002	0.001	0.002	0.002

Table 7.4: Some general properties of the $BVRI$ photometry for HD 70379. The mean magnitude for each colour is given along with the range of the change and the mean error.

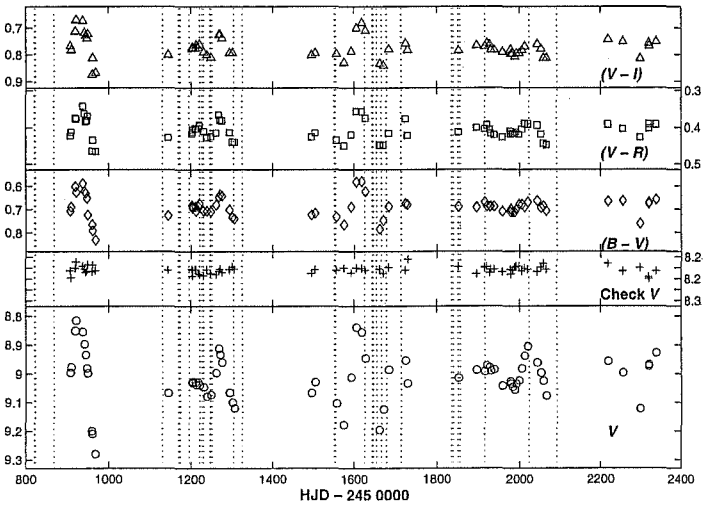

Figure 7.1: V and colour photometry of HD 70379. The vertical dotted lines indicate when échelle spectra were acquired.

The most striking feature of the oscillation is the inconsistency of the amplitude. There are groups of data which clearly show some sinusoidal variation and there appears to be a long-term periodicity which can be phased with a period of 85.2 days (see Figure 7.4). However, there are times when the oscillations (in V and the colours) disappear.

This feature is reminiscent of the UU Herculis stars. As can be seen

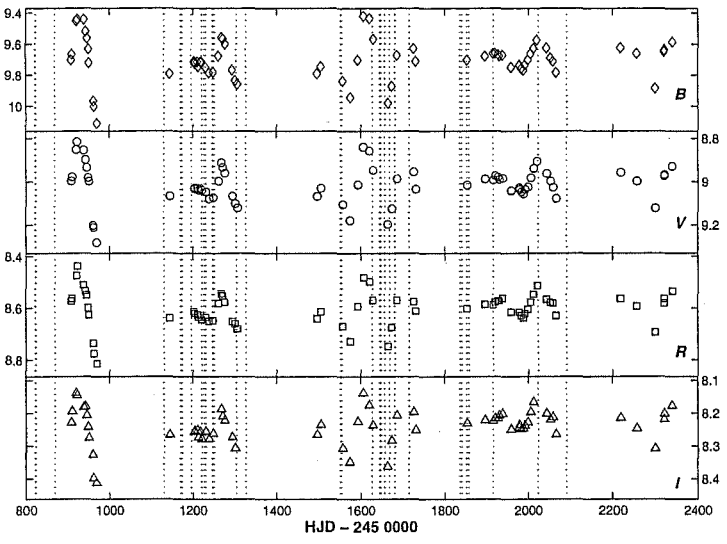

Figure 7.2: $BVRI$ photometry of HD 70379 from MJUO. The vertical dotted lines are as for Figure 7.1.

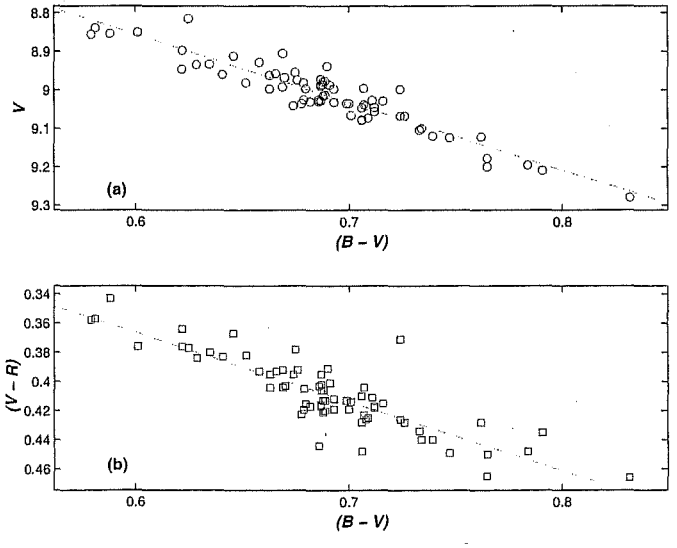

Figure 7.3: (a) Colour-magnitude and (b) colour-colour plots for HD 70379. Note the lines of best fit are included: $V = 7.814 + 1.738(B - V)$ and $(V - R) = 0.089 + 0.460(B - V)$, respectively.

from Figure 7.4, until HJD 2452000 the photometry has peaks which phase well with an 85 d period, but with the amplitude variation suggesting that perhaps there is a beat phenomenon present. Unfortunately the photometry is too patchy to allow for an accurate assessment of any beat period but an estimate of 720 ± 50d seems most likely based upon the periods of extremely low photometric variation at about HJD 2451200 and 2451900. Combined with the 85 d oscillation a beat could be due to underlying periods $T_1 = 80$d and $T_2 = 90$d, with $T_1/T_2 = 0.89$ (see §7.2.1 for more detailed analysis).

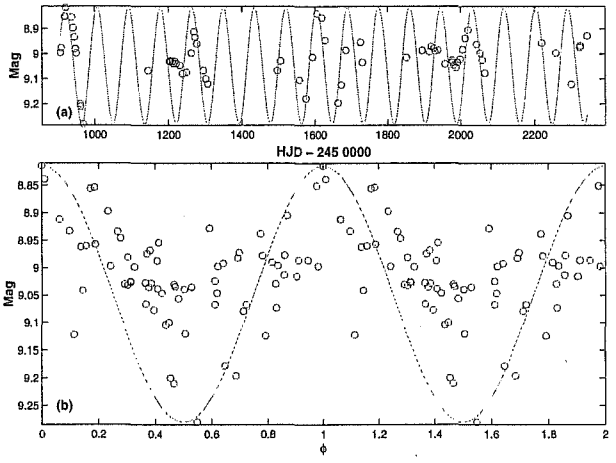

Figure 7.4: Phased photometry for HD 70379. (a) The complete range of V-band photometry with the mean oscillation of 85.2 days superimposed. (b) Phased V-band photometry using the 85.2 d period.

The photometry in 2001 (HJD $>$ 2451910) saw a resumption of the variation at a different phase (~ -0.35), which is a also feature of UU Herculis stars. Also the $(B-V)/V$ relationship changed, with the gradient in the $(B-V)$-V diagram changed from 1.7 to 2.5. In other words a smaller change in $(B-V)$ produced a larger change in V than in previous cycles.

7.2.1 Analysis of the photometry

Investigations of the MJUO photometry using Lomb-Scargle periodograms (Figure 7.5) have uncovered a principal peak at 85 ± 1 d, along with a number of others clustered between 50 and 200 days. The most significant of these are listed in Table 7.5.

To see whether or not these peaks were due to changes in the oscillation

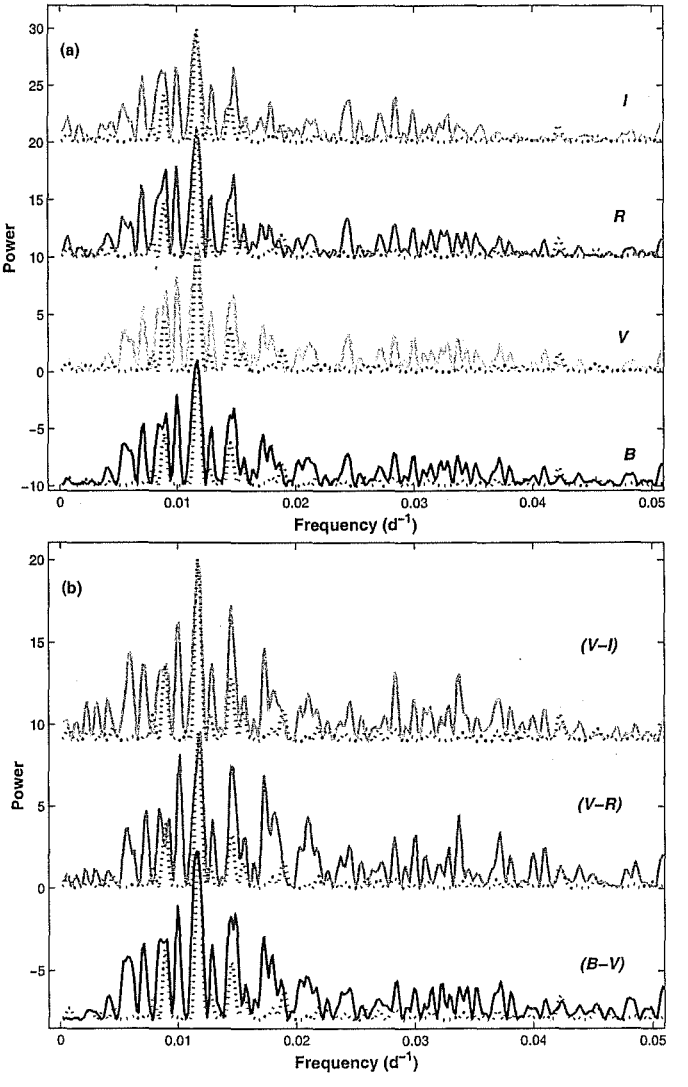

Figure 7.5: Lomb-Scargle power spectra of the MJUO photometry of HD 70379. Periodograms for (a) $BVRI$ magnitudes and (b) three colours are presented along with the window function for 85 d.

Frequency ($\times 10^{-3}$ d^{-1})	Power	Period (d)	ΔP (d)
7.16	5.6	140	3
8.39	5.5	120	2
9.08	7.0	110	2
9.96	8.2	100	2
11.70	11.1	85	1
12.92	5.3	77	1
14.85	6.7	67	1

Table 7.5: Peaks in the periodogram for the V-band photometry of HD 70379. The uncertainty in the frequencies is $\pm 0.17 \times 10^{-3}$ d^{-1} and ΔP is the uncertainty in the period.

from year to year, the photometry was broken up into the four main seasons which have been examined for periodicities. This proved to be inconclusive as the sections had 10 to 20 points per year. The principal modes for each season were 81 ± 30, 80 ± 10, 93 ± 9 and 106 ± 14 days but with no obvious evolution between the peaks.

Given the sinusoidal nature of the oscillation it was decided to investigate further and to "pre-whiten" the photometry. In this method successive Fourier components are removed from the data. The periods are found by Lomb-Scargle analysis and sine curves are fit to the data and then subtracted from the data. It was possible to identify and remove three periods from the photometry as is shown in Figure 7.6 and Table 7.6.

Fit	f (d^{-1})	P (d)	A (mag)	ϕ (d)	γ (mag)	RMS (mag)
1	0.0117	85.32	0.11	50944.8438	8.98	0.08
2	0.0103	97.37	0.10	50860.7617	0.03	0.05
3	0.0115	87.26	0.03	50865.7305	0.00	0.04

Table 7.6: Fourier fits to the V-band photometry of HD 70379.

The general form of the fits in Table 7.6 is:

$$V(t) = \gamma + A \sin\left[(2\pi(t - \phi)/P)\right]$$

where γ is the mid point of the oscillation, P is the period in days, ϕ is the

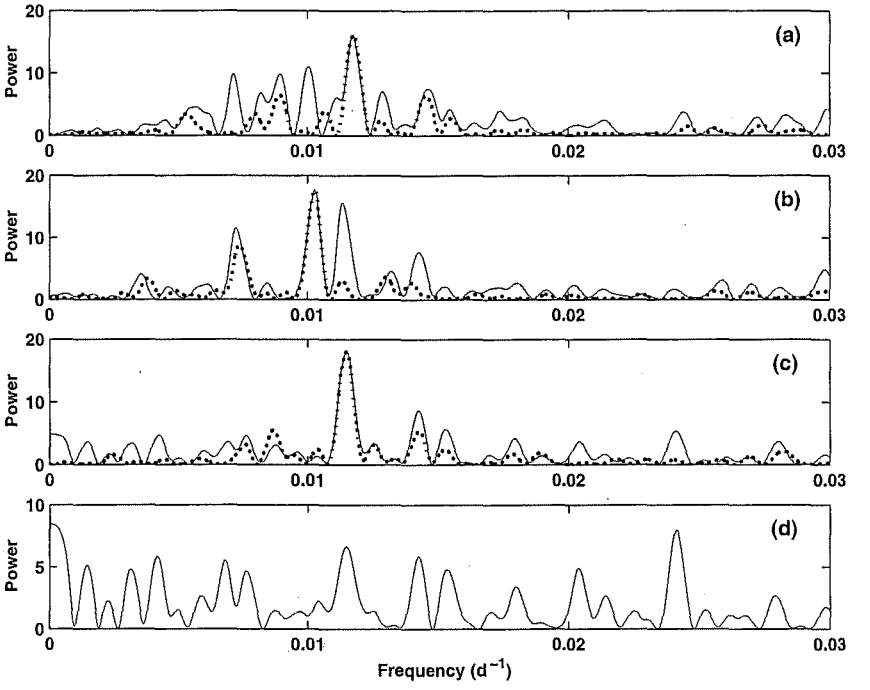

Figure 7.6: Prewhitening of the V photometry of HD 70379. (a) Lomb-Scargle power spectrum of the V photometry of HD 70379. The main peaks in the panels (a to c) are at 85 d (0.0117 d^{-1}), 97 d (0.0103 d^{-1}) and 87 d (0.0115 d^{-1}) after the data has been progressively whitened. The dotted lines are the natural window functions for each primary period.

adopted zero point in days, A is the semi-amplitude in magnitudes and $V(t)$ is the brightness as a function of time.

Using the window function for the data and these periods it is possible to reproduce all of the significant peaks in Figure 7.6a at least in position if not quite in significance. However, it should be noted that 85.32 and 87.26 days are not very different, and may well be the same frequency which has not been fully removed by the whitening, perhaps due to the oscillation not being strictly sinusoidal in shape.

The amplitude modulation may stem from the interaction of the 85.3 and 97.4 day periods. These combine to give a beat period of 689 days which lies within the uncertainty of the original beat period estimate of 720 d. In order to further investigate this hypothesis a synthetic light curve was made of two equal amplitude sine curves (periods of $T_1 = 80$ & $T_2 = 90$ days) using the sampling of the MJUO photometry to introduce an element of irregularity. Given that the oscillation amplitude appears to fall to zero it seems reasonable to have the oscillations of equal amplitude. This provides us with a nett light curve $V(t)$ about some mean light level given by:

$$\begin{aligned} V(t) &= A\cos(2\pi t/T_1) + A\cos(2\pi t/T_2) \\ &= 2A[\cos((2\pi/T_1 - 2\pi/T_2)t/2)\cos((2\pi/T_1 + 2\pi/T_2)t/2)] \\ &= 2A\cos(2\pi t/T_\mathrm{b})\cos(2\pi t/T_\mathrm{o}) \end{aligned} \tag{7.1}$$

where the beat period T_b is defined by $1/T_\mathrm{b} = 1/T_1 - 1/T_2$ and the observed frequency by, $2/T_\mathrm{o} = (1/T_1 + 1/T_2)$. So $V(t)$ can be considered as oscillation with a period of T_o which has its amplitude sinusoidally modified over a period of T_b.

All of the period-finding algorithms in the PERIOD suite found both T_1 and T_2, the two underlying periods, but *not* the resulting beat periods T_o and T_b at 85 and 720 d respectively (see Figure 7.7). This implies that the peaks found in the Lomb-Scargle periodograms are due to individual oscillations rather than interacting ones. So if the photometric variations of HD 70379 are due to underlying oscillations with periods of 85.3 and 97.4 d, they will produce amplitude modulation over 690 days, but also a shorter period oscillation at 91.0 d. However, Figure 7.4 shows that instead the V-band is best phased to 85.2 d, contradicting the results of the synthetic light curve analysis.

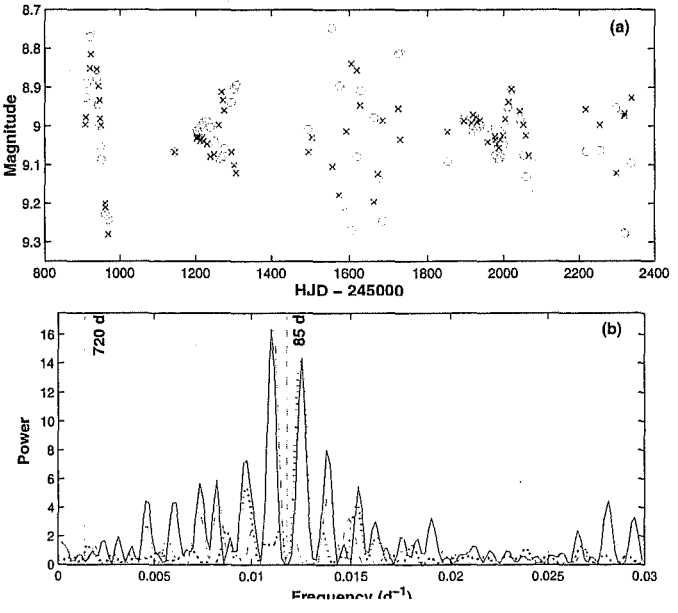

Figure 7.7: (a) A synthetic light curve (circles) and V-band photometry for HD 70379. (b) Lomb-Scargle periodogram of the synthetic data. The window functions of the two underlying periods are shown as dash-dot (90 d, 0.0111 d^{-1}) and dotted (80 d, 0.0125 d^{-1}) lines. There is a slight change in the detected periods but no significant power at the periods produced by the beat at 85 (0.0118 d^{-1}) and 720 (0.0014 d^{-1}) days.

7.3 Spectral energy distribution

In Figure 7.8 is presented the dereddened spectral energy distribution of HD 70379. The $BVRI$ data are the means of the MJUO photometry, while the $JHKL$ and IRAS photometry presented in Table 7.7 are single points.

	J	H	K	L	12	25	60	100
Band	7.689	7.395	7.259	7.100	0.71	17.62	12.31	3.68
Error	0.009	0.009	0.013	0.021	0.04	0.70	0.98	0.29

Table 7.7: Summary of the infrared photometry compiled for HD 70379. $JHKL$ is from SAAO on 1996 December 20 and the IRAS photometry is in janskys.

Comparison with the JHK photometry of García-Lario et al. (1990)[62], which was acquired between April 1988 and February 1989, does not provide any indication of variability at these wavelengths as within the quoted errors the two groups of measures are the same. Using a spectral type of F6 the colour excess is $E(B-V) = 0.3$, implying a total visual extinction of 0.9 magnitudes. The line of sight to HD 70379 is estimated to produce a peak visual extinction of 0.6 ± 0.3 magnitudes at about 3 kpc, and within the margin of error there would be negligible circumstellar extinction. The upper limit of the distance to the star is 3.4 kpc, assuming that all of this extinction is due to interstellar dust and that the star has an absolute visual magnitude of -4.6 mags.

The SED of HD 70379 shows no evidence of warm dust or cool stellar companions and has been fitted with two blackbody curves with temperatures of 7400 and 160 K and an RMS of 0.20. The former temperature translates to a stellar temperature of 6300 K. The ratio of stellar to dust flux is 6.0. An upper limit to the mass of circumstellar material, determined from the distance and the 60 μm flux, is 5.5×10^{-3} $M_{\odot}$ which is at a distance of 7.8×10^{2} $R_{\star}$ from the star. Compared with Fujii et al. (2002)[61] we derive some fairly similar parameters for the star and its environment. They derived $A_V = 0.78$, with 0.38 magnitudes due to circumstellar material. Most of the discrepancies can be accounted for by a different estimated stellar luminosity and derived total extinctions. The only major disagreement is that they claim that the circumstellar mass is 0.168 $M_{\odot}$, nearly 30 times more than our estimate. This is due to a difference in the adopted constants used to derive the dust mass from the infrared photometry, in particular from their choice of the dust emissivity, $Q(\nu)$ in equation 2.9.

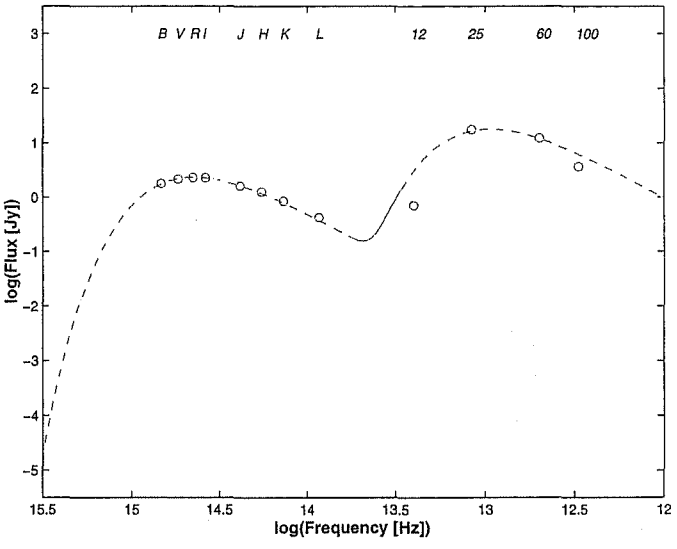

Figure 7.8: Blackbody fits to the SED of HD 70379 using the mean of the MJUO *BVRI* photometry, the *JHKL* from SAAO and IRAS fluxes. The two curves have temperatures of 7400 and 160 K.

7.4 Spectroscopy

An extensive set of 51 high resolution spectra covering almost all phases of the oscillation of this star was collected for this project. They range from 1997 October until 2001 July.

The general character of the spectrum is of a slightly metal poor F-type star. Comparisons with some F-type spectral standards (see Figure 7.12a) show that this star is noticeably different from normal F-type supergiant stars. The star is a radial velocity variable (see Figure 7.9) and also showed major line strength changes in some spectra with the neutral metal lines being much weaker than in the normal stellar profile.

No diffuse interstellar bands, including $\lambda\lambda$4430 and 6278, nor the λ6708 Li I line were detected in the spectra of this star.

7.4.1 Radial velocities

The radial velocity curves for this star, presented in Figure 7.9, are constructed from the data in Tables C.5 and C.6 and summarized in Table 7.8. The star is clearly variable, with a range of $\sim$ 6 km s^{-1} about the mean

radial velocity of +60 km s^{-1}. A frequency analysis is shown in Figure 7.10 and tabulated in Table 7.9.

λ_o (Å)	6347	6371	6562	8446	8498
Species	Si II	Si II	Hα	O I	Ca II
χ (eV)	8.12	8.12	10.19	9.52	1.69
n	35	35	38	32	32
μ_{rv} (km s^{-1})	60.28	60.73	63.96	64.97	64.22
σ_{rv} (km s^{-1})	3.17	2.96	3.66	3.31	2.56
Δ_{rv} (km s^{-1})	0.30	0.31	0.53	0.52	1.09

λ_o (Å)	5429	5434	5615	5853	6162
Species	Fe I	Fe I	Fe I	Ba II	Ca I
χ (eV)	0.96	1.01	3.32	0.60	1.90
n	33	33	19	35	22
μ_{rv} (km s^{-1})	60.80	61.42	58.78	61.75	60.38
σ_{rv} (km s^{-1})	4.03	4.03	3.58	4.54	5.99
Δ_{rv} (km s^{-1})	0.41	0.29	0.38	0.23	0.31

Table 7.8: Summary of the radial velocity for 10 lines in HD 70379. μ_{rv} is the mean velocity, σ_{rv} is the standard deviation, and Δ_{rv} is the mean error, all in km s^{-1}. n is the number of measures.

The radial velocity curves show that the behaviour of the low excitation lines is a little different to the high excitation ones. Both groups show increased velocity amplitude when the photometric amplitude increases during the period HJD 2451600 to 2451700, but only the high excitation potential lines follow the photometry during the periods of decreased amplitudes at about HJD 2451200 and HJD 2451900. There also seems to be line level effects during this period too, with the low excitation potential lines having a velocity differential about 2 km s^{-1} greater than that of the higher excitation potential lines. There is however no significant radial velocity gradient due to lines forming in different layers of an expanding atmosphere.

The radial velocity periodograms presented in Figure 7.10 roughly reproduce the main peaks of the V-band power spectrum with these peaks listed in Table 7.9. This rather suggests that the origin of the photometric variation has a common origin with the radial velocity changes.

From HJD 2451560 to 2451685 the radial velocity of all of the lines is related to the photometric changes. In Figure 7.11 is shown the variation in V, $B-V$ and radial velocity over this time period. It is also notable that

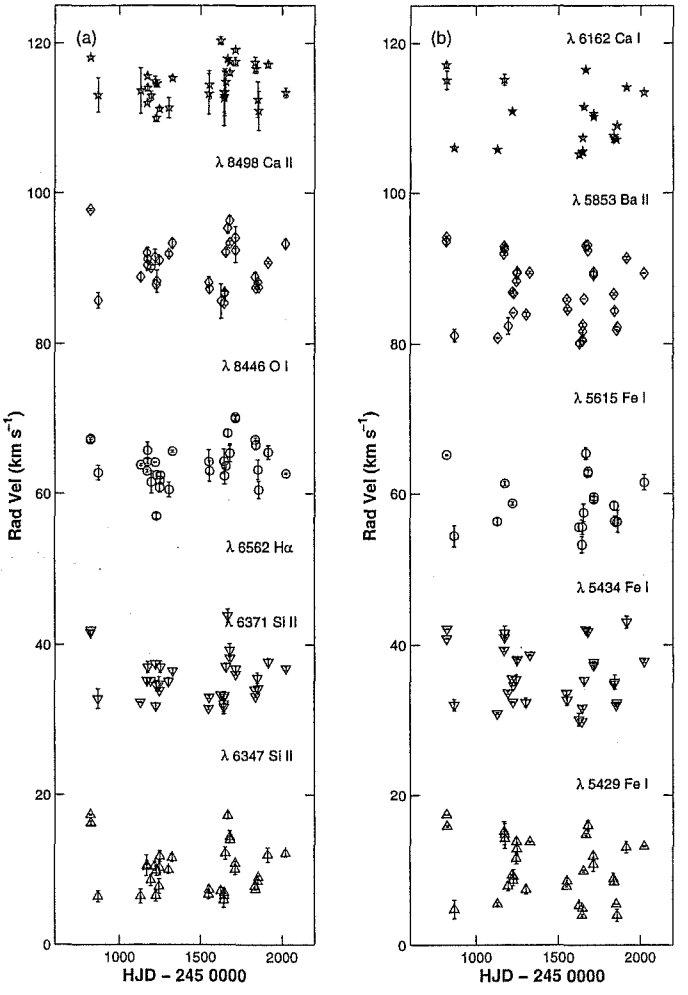

Figure 7.9: Radial velocity curves for lines in HD 70379. (a) Shows the velocities of some $\chi > 4.0$ eV lines and the Hα absorption core, while (b) shows some lines with $\chi < 4.0$ eV. λ6562 Hα and λ5615 Fe I are presented at the observed velocities while the other lines have been shifted by $\pm$12 or $\pm$24 km s^{-1}.

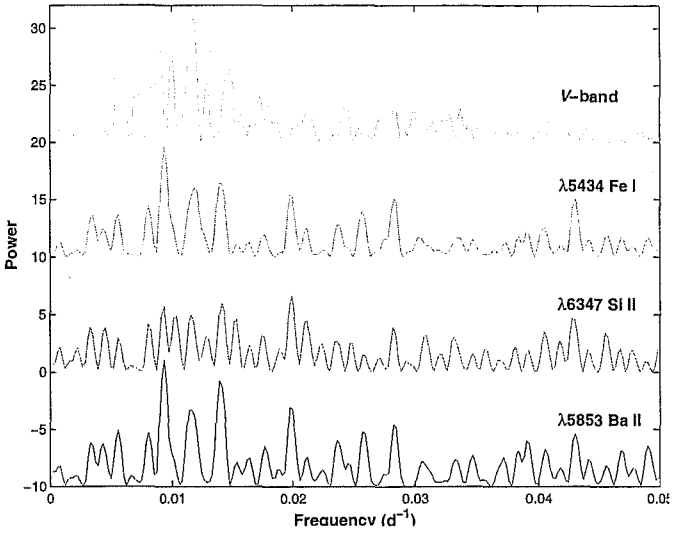

Figure 7.10: Lomb-Scargle periodograms for the radial velocity curves of HD 70379 compared with that for the V-band photometry.

Frequency ($\times 10^{-3}$ d^{-1})	Power	Period (d)	error (d)
9.35	9.6	107	2
11.85	6.0	84	2
13.93	6.5	72	1

Table 7.9: Peaks in the radial velocity periodograms of HD 70379. The uncertainty in the frequencies is 0.21×10^{-3} d^{-1}.

during this phase neutral metal line strengths, particularly those with low χ values, show an inverse relation with V magnitude (see §7.4.4, for further discussion on this point).

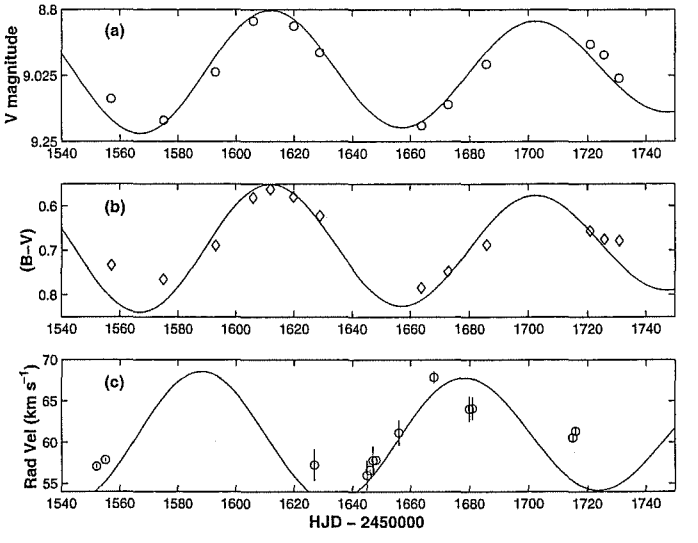

Figure 7.11: (a) V, (b) $(B-V)$ and (c) radial velocity curves, for HD 70379 from HJD 2451540 to 2451750. The solid line is the three component Fourier fit to the V data. For the radial velocity data it has been shifted by $\pi/2$ and fitted to the radial velocity amplitude and mean.

7.4.2 Hα Profile

The general appearance of the Hα profile is similar to that of 89 Herculis (Trams et al. 1989)[185] and of HD 161796 (Arellano Ferro 1985)[2]. Indeed the similarities to the latter also extend to the observed changes in line depth of HD 161796. In general there are broad absorption wings with a sharp central core. This profile is atypical of F-type supergiants (see Figure 7.12a), the transition from the wings to the core has shoulders which are not seen in more normal F-type supergiants. This seems to indicate the presence of an emission feature swamped by the absorption.

Following Arellano Ferro (1985)[2], the Hα profile of the standards have been subtracted from the mean HD 70379 spectrum (see Figure 7.12b). The resulting residual spectra feature a broad emission with central self-absorption. Compared to the two earlier type stars (α Leporis and ν Aquilae)

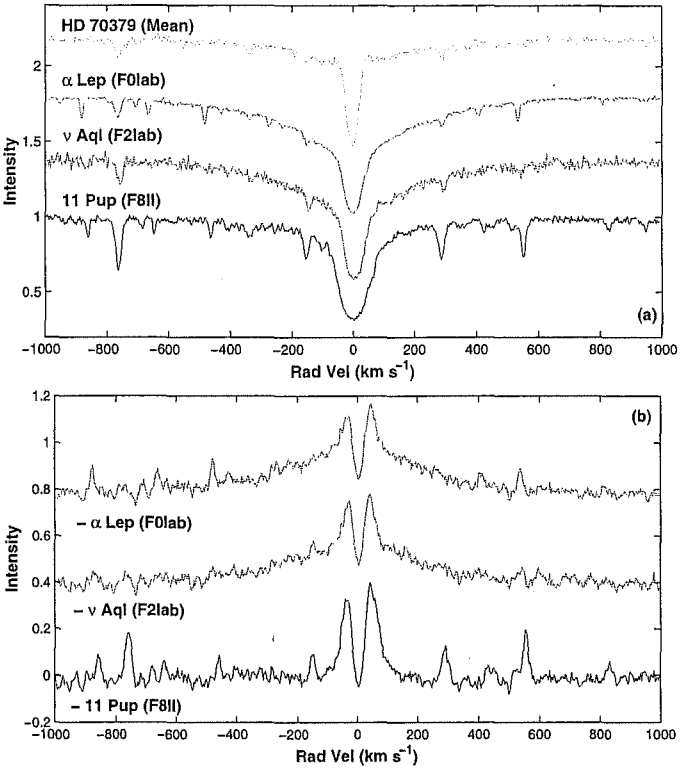

Figure 7.12: HD 70379 compared to the other F-type supergiant spectral standards. All of the spectra have been shifted onto the respective stellar frames, (a) shows the spectra directly, while (b) are the results of subtracting the standard star spectra from the mean spectrum of HD 70379.

there are wide emission wings in addition to this feature, but these are probably overstated due to the differences in spectral types of these stars (F0 and F2 compared to F6 for HD 70379) as the wings are not seen in the residual when an F8 II spectrum (11 Puppis) is subtracted. [1]

Arellano Ferro used the residual spectra to show the presence of a narrow

[1] As the radial velocity of HD 70379 is considerably higher than those of the standards the spectra first had to be moved to a common frame before performing the subtraction. The velocity differentials were determined using several lines in a number of different orders. A cross correlation involving just order 35, which contains Hα, was not considered sufficient to reflect the true velocity differences between the stars, as asymmetries within the Hα core of HD 70379 may mean that the minimum intensity points do not lie at the systemic velocity.

emission spike. The nature of this feature, which has a stellar frame velocity of -25 km s^{-1}, was claimed to be from in-falling matter. For the residuals of HD 70379 this is not so clear, as they show a strong self-absorption, but the red residual peaks are larger than the blue ones which may indicate a similar atmospheric feature.

Another feature of the residual spectra are the narrow "emission" features. These are mostly Fe I, with some Ti I and Ca I lines and they illustrate the metal-poor nature of HD 70379. Even α Leporis, the hottest standard star, has stronger metal lines than in HD 70379.

Overall the residual spectra suggest that HD 70379 has a normal supergiant Hα profile which is combined with a variable emission feature centred on the stellar velocity.

The changes of Hα can be seen in Figure 7.13a. One feature to note is the depth change in the absorption core. This is more clearly seen in Figure 7.14. From HJD 2451626 to 2451648 this averages 43% of the continuum. However, by HJD 2451714 this has changed to just 30%. Indeed the intervening spectra show a progression between these two values. This is exactly the same behaviour reported by Arellano Ferro (1985)[2] for HD 161796 where a similar sized depth change is visible in the spectra between September 1980 and April 1981. That this is observed in HD 70379 when the star is undergoing its largest photometric and radial velocity variations is worth further investigation, to check both the timescales and the onset of the increase in the line depth. That these variations are observed on timescales of a week point to a source close to the star. It could be that as the star contracts the level of emission increases in the Hα core due to an increased mass loss rate, increasing the amount of emitting material from near the star.

7.4.3 Sodium D Lines

The Na D lines of HD 70379, presented in Figure 7.15b, clearly show a multiple component structure. These seem to be slightly variable (see Figure 7.13) at times when the star is variable in other aspects, but there are no gross changes observed during the course of this programme.

In Table 7.10 are the results of fitting four Gaussians to the HERCULES spectra of HJD 2452090. The heliocentric velocity correction was $+13.3$ km s^{-1} and the mean photospheric radial velocity from 89 symmetrical lines was $+63.28 \pm 0.04$ km s^{-1}. Scenario A assumes all of the components to be absorption features does not reveal a component at the expected stellar velocity. Instead two features, 3 and 4, are approximately equidistant (± 8.4 km s^{-1}) from this velocity.

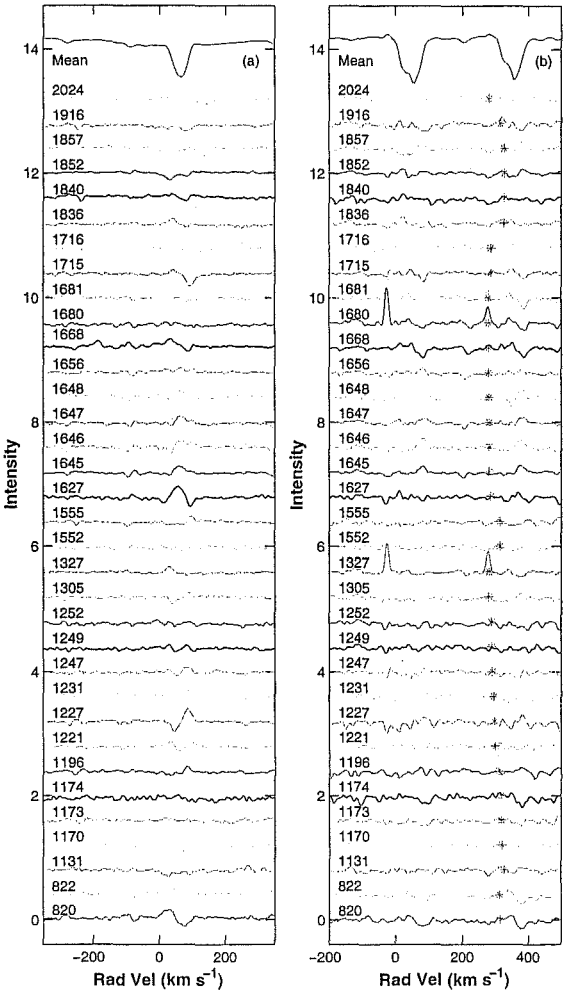

Figure 7.13: (a) Hα and (b) Na D line residual spectra of HD 70379. The mean spectra are at the top and the residuals are labelled with the Heliocentric Julian Date of observation -2450000. The asterisks in (b) denote the position of atmospheric features in the D_1 line profile.

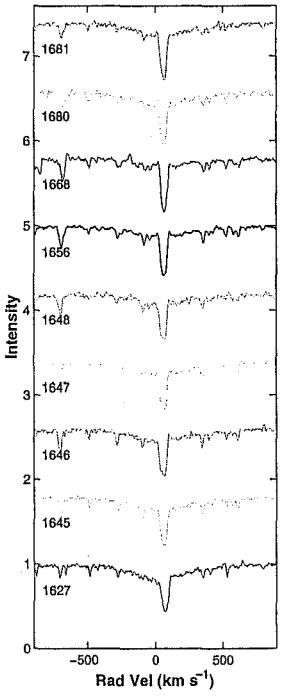

Figure 7.14: The variation in the Hα profiles of HD 70379 between HJD 2451627 and 2451681. Spectra are labelled with HJD−2450000. Note the change in the depth of the absorption feature and also the growth of a small emission peak on the blue limb of the absorption core.

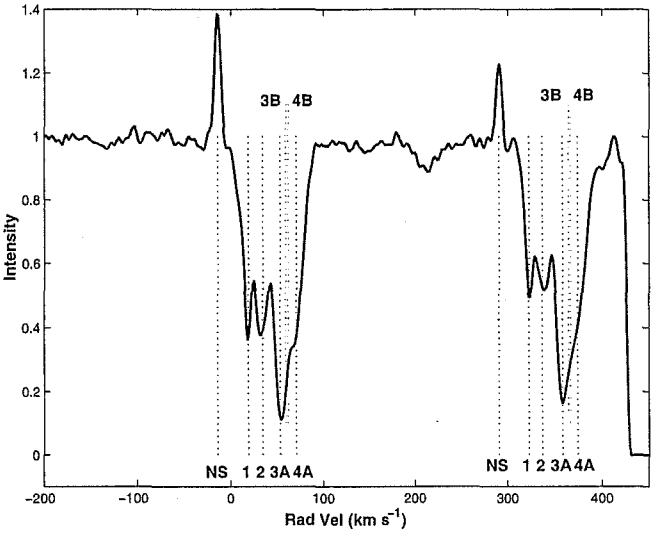

Figure 7.15: A HERCULES spectrum of the Na D lines of HD 70379 acquired on HJD 2452092. The components are labelled according to Table 7.10. NS denotes sodium emission from the night sky, and A and B differentiate between the A and B scenarios discussed in the text.

	Scenario A				Scenario B			
#	λ (Å)	W (Å)	Rad Vel (km s^{-1})	Notes	λ (Å)	W (Å)	Rad Vel (km s^{-1})	Notes
NS	5889.684	−0.069	−14.4	EM	5889.684	−0.069	−14.4	EM
1	5890.334	0.188	18.7	IS $d = 0.7$ kpc	5890.325	0.205	18.3	IS $d = 0.7$ kpc
2	5890.636	0.137	34.1	IS $d = 2.0$ kpc	5890.620	0.097	33.3	IS $d = 2.0$ kpc
3	5891.006	0.292	52.9	CS	5891.122	0.593	58.8	PS
4	5891.349	0.217	70.4	CS	5891.177	−0.054	61.6	CS EM
NS	5895.675	−0.041	−13.1	EM	5895.675	−0.041	−13.1	EM
1	5896.303	0.096	18.9	IS $d = 0.7$ kpc	5896.325	0.124	20.0	IS $d = 0.7$ kpc
2	5896.585	0.134	33.2	IS $d = 2.0$ kpc	5896.592	0.087	33.6	IS $d = 2.0$ kpc
3	5897.000	0.275	54.3	CS	5897.125	0.568	60.6	PS
4	5897.316	0.170	70.4	CS	5897.167	−0.051	62.8	CS EM

Table 7.10: The components of the Na D lines of HD 70379 from a HERCULES spectrum taken on HJD 2452092 (Figure 7.15). The resolution of the échelle is insufficient to resolve components 1 and 2. Scenario A requires all of the components to be absorptions, while scenario B has a circumstellar emission feature. For both scenarios the RMS is 0.04 Å. All velocities are heliocentric and a negative equivalent width indicates an emission feature.

It has been hypothesized that the features are circumstellar. In this scenario the star is part of a binary and has a mass loss event. This leaves an expanding shell of material which the star moves through. It is seen now through both the approaching and receding material and provides two components separated by at most twice the ejection velocity depending on where the line of sight intersects the shell. In this case the 8.4 km s^{-1} expansion velocity will have left a shell which will have grown outwards at least by about 6 AU during the 1300 days of monitoring. Over time the line of sight will encounter a different aspect of the cloud, as it expands and disperses, and as the star moves around in its orbit. However a number of post-AGB candidates show this feature and it begs the question as to how all of them could undergo such an alignment of binary orbit parameters and a discrete mass loss event in half of their orbit. In the case of HD 70379 there is also the lack of a trend in the radial velocity curves, which suggest that the orbit is either very wide and/or inclined to the line of sight.

Perhaps a more robust solution is that components 3 and 4 are due to a photospheric absorption bisected by a chromospheric emission line (scenario B). The absorption is quite strong, enough for it to reveal some chromospheric lines. The problems with this picture are that the chromospheric line is moving away from us faster than the star is, i.e., is in-falling with respect to the star, that the absorption line is very deep, too deep to be due to photospheric absorption alone and finally that the velocity of component 3 is not a particularly good match to the photospheric velocity of $+63.28 \pm 0.04$ km s^{-1}.

The line of sight to HD 70379 intercepts the Perseus arm at 3.6 kpc ($z = 611$ pc), which would provide a Na D interstellar medium radial velocity of +50 km s^{-1}. This may well account for component 3. In the stellar frame component 2 has an outward velocity of nearly +30 km s^{-1}, for component 1 this is +44 km s^{-1}. These are very high for circumstellar matter ejected from a low mass supergiant star. Instead their heliocentric radial velocities, narrow shape and consistent shape are indicative of interstellar clouds. Their radial velocities place them at distances of 0.7 and 2.0 kpc for components 1 and 2 respectively.

At 6 kpc the stellar radial velocity would be +62.2 km s^{-1} ($z = 1017$ pc) and the absolute visual magnitude would be −4.9 mag. Kinematically this is consistent with the observed radial velocity and seems to indicate that the star lies on the far side of the Perseus spiral arm.

7.4.4 Neutral metal line variability

There is a correlation between the oscillation and the strength of the neutral metal lines. The series presented in Figure 7.16 clearly shows that the strengths of the neutral metal lines increase as the star moves from photometric maximum (HJD 2451610) to minimum (HJD 2451664). However, the ionised lines remain essentially unchanged. Comparison with synthetic spectra indicates a temperature change from $\sim$ 5500 to 6250 K over the period HJD 2451656 to 2451627 respectively. These synthetic spectra were selected on the basis that they produced the lowest RMS residual for those nights.

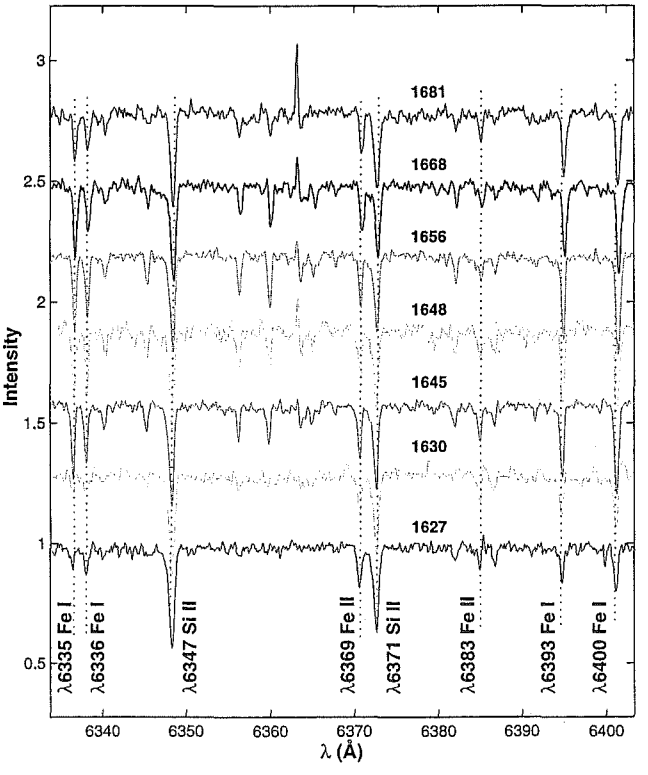

Figure 7.16: Neutral metal line variability in the spectrum of HD 70379. The spectra are labelled with the HJD -2450000 and the variable emission feature is the night sky line due to λ6363 [O I].

7.4.5 Line shape variability

Another interesting feature is best seen in the spectrum on 1998 February 24 (HJD 2450868). Many of the stronger spectral lines show a definite asymmetry favouring the blue side of the spectrum. There is a suggestion of underlying structure but the signal to noise is inadequate to clearly show this. However, the lines clearly show a strengthening of the absorption on the blue side of the line. Bisector slopes, as measured by the asymmetry parameter defined in §3.2.1, are about twice the normal value (see Table 7.11). Interestingly the average value of the asymmetry parameter for nearly all of the lines in this star is negative, i.e., the lines show more flux on the blue wing than their red. This seems to point to a current phase of mass loss. It is possible that the HJD 2450868 is showing a discrete mass-loss event and that is why the line bisectors slope towards the blue.

Line	n	A_{868} (°)	$A_{\rm ave}$ (°)	σ (°)	$A_{868}/A_{\rm ave}$
5434 Fe I	32	−11.7	−5.5	6.7	2.14
5615 Fe I	20	−18.9	−9.4	18.2	1.99
5853 Ba II	35	−15.8	−3.2	7.7	4.94
6347 Si II	31	−29.3	−18.9	8.9	1.55
6371 Si II	20	−37.5	−28.8	10.6	1.80
6562 Hα	32	−18.4	−9.4	10.3	1.96
8446 O I	30	−19.6	−8.4	10.9	2.33
8498 Ca II	32	−32.1	−11.3	20.9	2.84

Table 7.11: Asymmetry parameter for selected lines in HD 70379. n is the number of lines used, A_{868} is the asymmetry parameter on HJD 2450868, $A_{\rm ave}$ and σ are the average and standard deviation for this parameter over the rest of the spectra, and $A_{868}/A_{\rm ave}$ is the ratio of the parameters.

7.4.6 λ7774 O I triplet

Observations taken on HJD 2451306 and 2451307, see Figure 3.3, were used to obtain a total equivalent width for these oxygen lines of W(O I) = 1.37 Å. From an effective temperature of 6300 K we get $(b-y)_{\rm o} = 0.19$ from Gray's (1992) empirical relationship (Equation 3.4). Combined with W(O I) this implies an absolute visual magnitude of $M_V = -6.3$ (27000 $L_\odot$). This is similar to the luminosity of other UU Herculis stars derived from this method

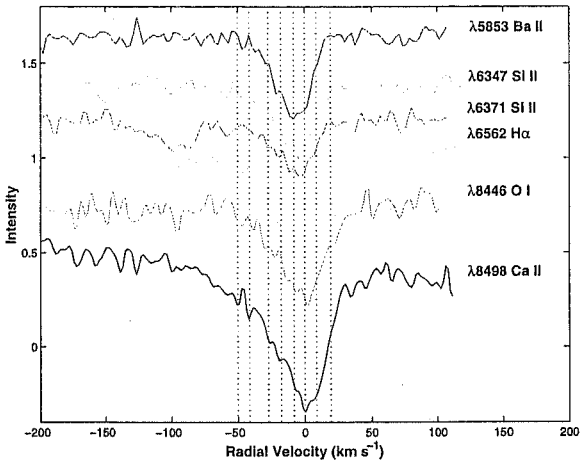

Figure 7.17: Detail from lines of the spectrum of 1998 February 24 showing "structure". The dotted lines show the position of some components at $+19.5, +8.7, 0, -8.2, -17.7, -27.2, -41.4$, and -50.1 km s^{-1} in the stellar rest frame.

by Arellano Ferro et al. 1991[3].

7.5 Discussion

From the changes in the low excitation neutral metal lines and the radial velocity changes over the period HJD 2451600 - 1700, it looks like HD 70379 has undergone a change in radius. At about HJD 2451610 this is at a minimum and the star is significantly warmer and brighter than at HJD 2451656. The transition sees the star get larger, cooler and dimmer.

The sinusoidal fit to the photometry listed in Table 7.6 shows that between the spectra of HJD 2451627 and 2451656 the star has dimmed by 0.26 magnitudes. During the same time frame the average radial velocity has changed about 13 km s^{-1}. The average expansion velocity, $v_{\rm exp}$ = 6.5 km s^{-1}. Given that the star has expanded at this rate for half of a cycle, this means the outer layers of the star have covered a distance:

$$\begin{aligned} d &= v_{\rm exp} P/2 = R_{\rm min} - R_{\rm max} \\ &= 6.5 \times 42.6 \text{ days} \\ &= 2.40 \times 10^{10} \text{ m} \\ &= 34.9 R_\odot \end{aligned}$$

where $P = 85.2$ d is the oscillation period and the subscript *min* refers to the star at *luminosity* minimum. Considering the star to be emitting radiation as a blackbody then we can relate the ratio of the luminosities to the size and temperature of the star. Since the luminosity ratio is known from the photometry we can rearrange to get the ratio of the radii:

$$\begin{aligned} \frac{L_{\rm min}}{L_{\rm max}} &= \frac{R_{\rm min}^2}{R_{\rm max}^2} \frac{T_{\rm min}^4}{T_{\rm max}^4} \\ \Rightarrow R_{\rm max} &= \sqrt{100^{(V_{\rm max}-V_{\rm min})/5} \frac{T_{\rm min}^4}{T_{\rm max}^4}}\, R_{\rm min} \\ &= 0.763\ R_{\rm min}, \end{aligned}$$

where $V_{\rm max} - V_{\rm min} = -0.38$, $T_{\rm min} = 5500$K, and $T_{\rm max} = 7070$K. $T_{\rm max}$ has been obtained by using the temperature estimates on HJDs 2451627 and 2451656, and extrapolating backwards along a cosine which peaked at the photometric maximum on HJD 2451610. What this means is that $d = (1 - 0.763) R_{\rm min}$ and so:

$$\begin{aligned} R_{\rm max} &= 0.763 d/(1 - 0.763) \\ &= 5.69 \times 10^{10} \text{ m} \\ &= 81.8\ R_\odot \Rightarrow R_{\rm min} = 113.6\ R_\odot \end{aligned}$$

The absolute magnitudes obtained are $M_{V,\rm max} = -5.63$ and $M_{V,\rm max} = -5.25$, which is lower than the estimate obtained from the λ7774 O I lines in §7.4.6.

So the model is that of a star which is radially pulsating at a variable rate. At its peak luminosity the star is also at its hottest and smallest. This is all derived from the primary cycle observed in the interval HJD 2451560 - 1730.

The comparison with UU Herculis stars is quite good. Spectroscopically the comparisons with other members of the class are quite good: low

Property	Min	Max	Mean
$L_\star$ ($L_\odot$)	10600	15100	12900
M_v	-5.25	-5.63	-5.46
T (K)	5500	7070	6300
$R_\star$ ($R_\odot$)	82	114	98
$< v_{\rm exp} >$ (km s^{-1})			6.0

Table 7.12: A summary of the physical properties of HD 70379 derived from the variations in radial velocity and V-band from HJD 2451600-1700.

metallicity ([Fe/H]= -0.31); high radial velocity ($\sim +60$ km s^{-1}); similar Hα shape and behaviour; similar luminosities from the λ7774 O I multiplet. Photometrically the fit is not so tight. Although the star displays a variable amplitude oscillation, with some indications that it undergoes sudden phase shifts, the amplitudes ($\Delta V \sim 0.5$ mag) and the periods (85 and 97 days) are significantly larger than the one would expect for a UU Herculis variable.

7.6 Conclusions

HD 70379 bears striking resemblance to other UU Herculis stars and its moderate Galactic latitude, high radial velocity and metal deficiency point to membership of Population II.

Specifically we have discovered that the star is a photometric and radial velocity variable. During time when the photometric amplitude is at its largest these changes are linked. The equivalent width of neutral metal lines is also changed during phases of enhanced photometric and radial velocity variability. These factors imply a radially pulsating star which changes the effective temperature. The observed photometric colour changes are also consistent with this model.

A curious feature, was observed in a single, somewhat noisy spectrum of HJD 2450868, in which the strongest absorption lines showed marked asymmetry to the blue, and even a hint of discrete components within this.

A period analysis of the photometry uncovered two main periods (85 ± 1 and 97 ± 2 d) which seem to interact to produce times of enhanced and suppressed variation in the manner of a beat. However, analysis of simulated photometry suggests that the underlying periods are 80 and 90 days, and this discrepancy need further investigation.

The line of sight to HD 70379 produced a total visual extinction of 0.9

magnitudes. The spectral energy distribution can be modelled with just two components at 6300 (stellar component) and 160 K (dust component). The circumstellar mass was estimated at 5.5×10^{-3} $M_{\odot}$ at 7.8×10^{2} $R_{\star}$ from the star.

The Hα profile is strikingly similar those of UU Herculis stars, even to the point of showing the same sort of variability exhibited by HD 161796. The profile can be considered to contain extra variable emission which seems to emanate from a region near the star.

The Hα profile indicates that there are 3 components:

1. The central star, providing an underlying F6 absorption profile.
2. The region around the star, producing broad (not as wide as the star though) and narrow emission features almost centred on the star, probably from the stellar wind.
3. The CS gas and dust. Providing a further core absorption.

Four components are required to account for the Na D line profile of HD 70379. The two scenarios developed to account for the Na D line structure were not particularly satisfactory, with both presenting serious flaws. The Galactic rotation curve is compatible with the mean stellar velocity ($\sim +60$ km s^{-1}) at a distance of ~ 5 kpc.

Chapter 8

HD 95767

8.1 Introduction

According to Van Winckel (1997)[198], HD 95767 (= IRAS 11000-6153, see Table 8.1) is part of a visual binary system, and appears to pulsate with a quasi-period of 103 days and an amplitude of 0.144 magnitudes. It also has an infrared excess indicating a dusty circumstellar environment (Volk & Kwok 1987)[206]. Its luminosity and temperature place it in the instability strip, but its period is too long for it to be a classical Cepheid. Van Winckel also found $T = 7500$ K, $\log g = 2.5$ and that within experimental uncertainties, the abundances for this star are approximately solar. Only oxygen is unusually low ([O/H]= -0.38) and sodium is high ([Na/H]= $+0.76$). This is typical for A-F supergiants due to nuclear processes and mixing (Venn, 1995)[203].

Coordinates	α	$11^{\mathrm{h}}\ 02^{\mathrm{m}}\ 04.32^{\mathrm{s}}$
(Epoch 2000.0)	δ	$-62°\ 09'\ 41.9''$
Galactic	l	290.54
coordinates	b	-1.95
Mean Brightness	B	9.5
	V	8.7
Spectral Type		F3II

Table 8.1: Basic parameters of HD 95767 from SIMBAD.

Pottasch & Parthasarathy (1988)[156] investigated the circumstellar environment. They assumed a distance of 2 kpc and found a cool dust shell

Identifier	α(2000.0)	δ(2000.0)	B	V	SpT
HD 95893	$11^h\ 02^m\ 48^s$	$-62°\ 28'\ 48''$	9.27	8.80	F5V
HD 95992	$11^h\ 03^m\ 17^s$	$-62°\ 27'\ 36''$	9.87	9.63	B2/B3III
HD 95393	$10^h\ 59^m\ 37^s$	$-62°\ 29'\ 03''$	8.69	7.30	G3Ib

Table 8.2: Basic data for the photometry calibration stars of HD 95767.

with a blackbody temperature of 200 K. They also mentioned the possibility that the large amount of flux in the 100 μm band could be due to old, cold dust around the star. This could also be from interstellar material because of the star's low Galactic latitude. The IRAS LRS spectra showed an unusual emission plateau from 8 to 13 μm, but provided no clear indication of the 10 μm emission one would expect from an object with a flux ratio $F_{12\ \mu\mathrm{m}}/F_{25\ \mu\mathrm{m}} = 1.41$. Van der Veen et al. (1993)[192] looked for CO emission from this star at 115 and 230 GHz but did not detect any. Based on IRAS colours Oudmaijer et al. (1996)[144] fitted a blackbody curve with a temperature of 170 K.

Using CCD imaging, Sinachopoulos (1988)[174] found four components. Two of these are more than a minute of arc away from the primary star, and are probably not physically connected to it. The remaining candidate is the 11.9 magnitude star BD-61 2910 just over 5 arc seconds away. Van Winckel (1999)[199] provides a list of binary post-AGB stars which have had their periods determined. All of these show the presence of a hot dust component. For HD 95767 he determined a period of 2050 days with an eccentricity $e = \pm 0.3$, but no other information about the system.

In this chapter we examine the results of a spectroscopic and photometric monitoring programme on this star over the period 1998 to 2002.

8.2 Photometry

Eighty five $BVRI$ data points were obtained spanning 1118 days. The V and colour data are presented in Table A.4. Basic data for the comparison and check stars are listed in Table 8.2. The comparison star was HD 95893, while HD 95992 and HD 95393 were used as the primary and secondary check stars respectively. According to SIMBAD no long-term variations have been observed in any of these stars and this is confirmed during the course of our programme. The RMS of the V-band photometry for both of the check stars is 0.009 magnitudes.

The results of the photometry are presented in Figures 8.1 and 8.2, and summarized in Table 8.3. They clearly show that the star is variable with an amplitude that peaks in the B-band. There are three epochs to the photometry. For the first 200 days of the programme HD 95767 shows a steady sinusoidal variation with a period of about 85 d and a variable amplitude. From about HJD 2451650 until HJD 2451900 the star the undergoes a decline in light level of about 0.20 magnitudes, and for the 200 days after that, they gradually return to their previous values. It is possible that the strong oscillation observed prior to this phase is not, or is only weakly present after this dip in light level. From Figure 8.3 we can see that the changes in the colours and the brightness are correlated but that this is weaker than in HD 70379. In HD 95767 the $(B-V)$ and V data have an RMS scatter of 0.04 about the mean fit compared to only 0.03 for HD 70379, which has a larger range in both.

	U	B	V	R	I
Mean	9.985	9.521	8.824	8.377	7.922
Range	-	0.313	0.235	0.199	0.201
Error	0.016	0.001	0.001	0.001	0.001

Table 8.3: A summary of the photometric data for HD 95767 acquired at MJUO. The mean brightness in each band is presented along with the peak-to-peak amplitude and the mean error. The U magnitude is a single point.

8.2.1 Analysis of the photometry

Applying the Lomb-Scargle algorithm to the photometry of HD 95767 produces a periodogram (Figure 8.4) dominated by the dip in the light curves from HJD 2451650 - 2100. The main peak at about 900 ± 150 d (see Table 8.4) is quite close to the length of the photometric programme (1118 d) and it is difficult assign any physical significance to it.

By considering only the first 190 days of the photometric monitoring programme, when the oscillation is at its most regular, we obtain a single period of 85 ± 10 d (0.0119 ± 0.0013 d^{-1}). This is slightly shorter than Van Winckel's estimate (1997)[198] of 103 ± 12 d, but within uncertainty is probably the same period. A comparison with the periodograms involving the full data set resolves this peak into a number of smaller peaks.

Looking at the star's colour-magnitude plots shows the existence of two modes. A closer look at the underlying magnitudes (Figure 8.5) reveals that

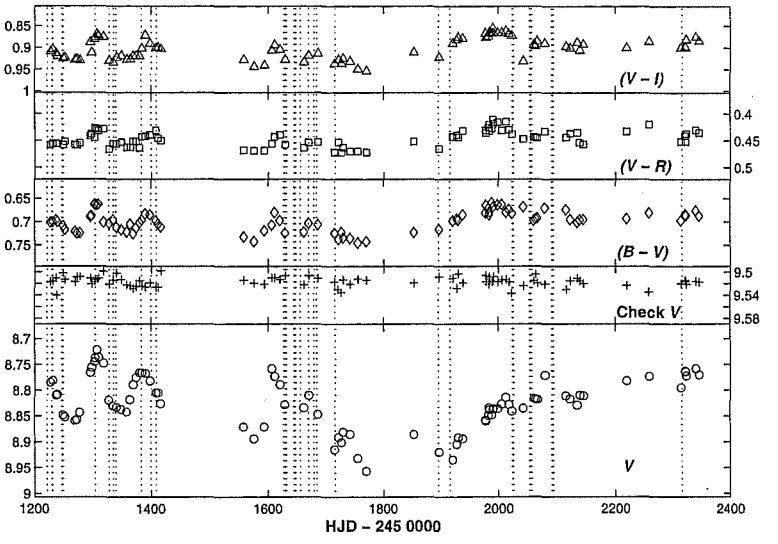

Figure 8.1: V and colour photometry of HD 95767 taken from MJUO. The dotted lines indicate times when échelle spectra were taken.

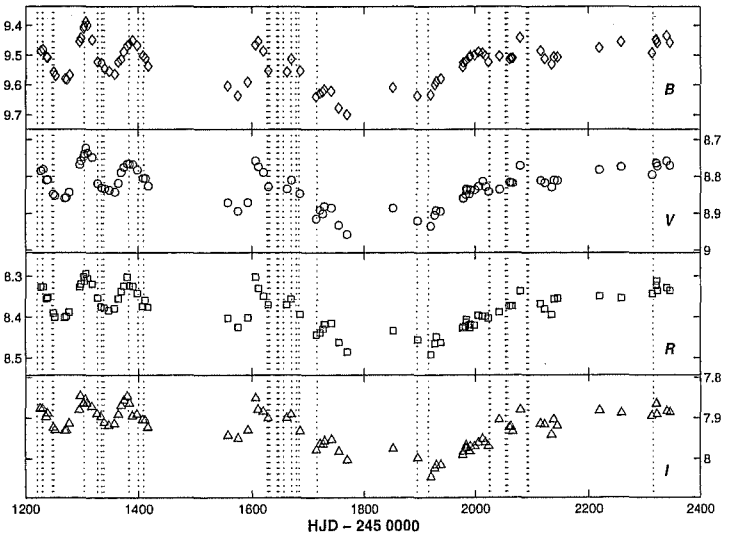

Figure 8.2: $BVRI$ photometry of HD 95767 from MJUO.

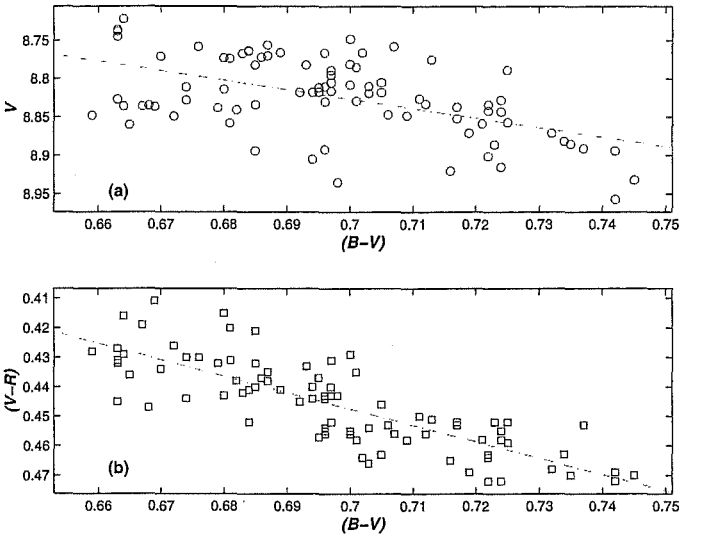

Figure 8.3: Colour magnitude (top) and colour-colour plots for HD 95767. Note the lines of best fit are included (dot-dashed lines). $V = 7.96 + 1.24(B - V)$ and $(V - R) = 0.06 + 0.56(B - V)$ respectively.

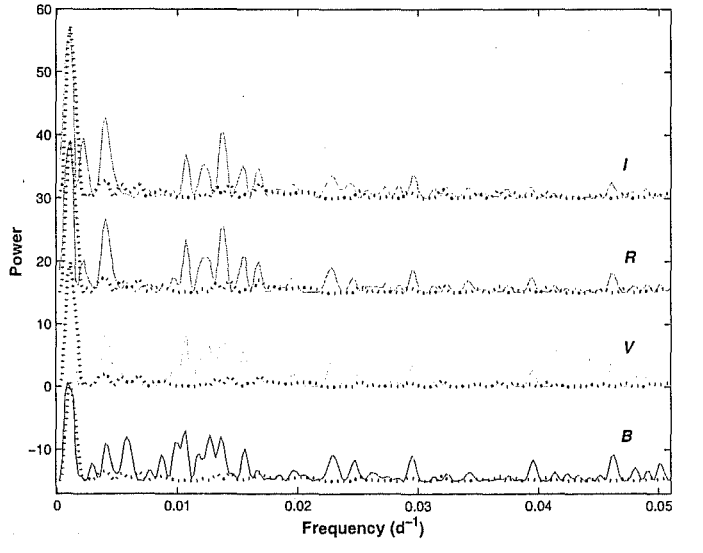

Figure 8.4: Lomb-Scargle power spectrum of the photometry of HD 95767. The window function for 894 d is the dotted line.

Frequency ($\times 10^{-3}$ d^{-1})	Power	Period (d)	ΔP (d)
1.12	19.8	900	150
2.24	9.5	450	40
4.03	8.9	250	10
5.81	4.1	170	6
10.73	8.4	93	2
12.75	6.4	79	1
13.64	8.2	73	1
15.65	5.9	64	1

Table 8.4: Main peaks in the V-band periodogram of HD 95767. The uncertainty in the frequencies is 0.22×10^{-3} d^{-1} and ΔP is the uncertainty in each of the periods.

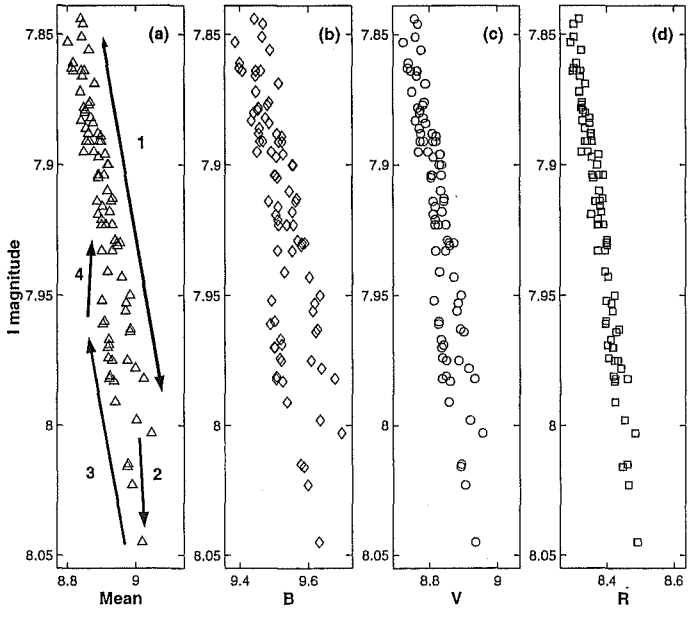

Figure 8.5: (a) Mean brightness vs I, (b) B vs I, (c) V vs I and (d) R vs I plots for HD 95767. The mean brightness is just the mean of the brightness in each of the four bands observed and is included to highlight the trends discussed in the text. Note the loop below the main line in (a), (b) and (c) but not in (d).

the change in the colours is not due to more blue light but rather a loss of red flux, particularly in I. During the normal course of the photometry the star moves along a well defined line in these plots (track 1 in Figure 8.5a). However, after the minimum, starting about HJD 2451853, the star moves at constant B to a lower value of I over the space of about 20 days (track 2 in Figure 8.5a). In the magnitude-magnitude plots this appears as a *blue loop* which lasts until about HJD 2452030. The same change can be seen in the VI and RI plots but not so clearly, as the both V and R are also diminished during this phase. For the next 100 days the star brightens along track 3 which is parallel to the track 1. This suggests that HD 95767 is behaving as normal but with a reduced level of red light. Eventually it returns to track 1 via another transition at constant B (track 4) which also lasts 20 days.

This behaviour is difficult to reconcile a model with of the star emerging from dust obscuration. This would make the colours bluer due to a proportionately greater increase in the level of blue flux. We have to find a model which has almost no influence on the B-band but increasing effect at longer wavelengths.

8.3 Spectral energy distribution and reddening

We only have MJUO $BVRI$ and IRAS photometry (Table 8.5). The dereddened blackbody fits are presented in Figure 8.6. From an estimated spectral type of F3, we derive a total colour excess of $E(B-V) = 0.44$ and a total visual extinction of 1.4 magnitudes.

	12	25	60	100
Band	22.13	15.65	10.90	58.88
Error	0.89	1.41	1.64	5.30

Table 8.5: A summary of the infrared photometric data for HD 95767. The units are janskys.

From this value a distance of 2.6 kpc is predicted from the extinction law for this line of sight (Hakkila et al. 1997)[75], but this infers an interstellar extinction of 2.2 ± 0.4 magnitudes which is significantly larger than expected total extinction from the colour excess. If we assume all of the extinction is due to interstellar material then the distance to the star is reduced to 1.7 kpc, and the absolute magnitude to -3.7 ($\sim 2500\ L_{\odot}$). We could also

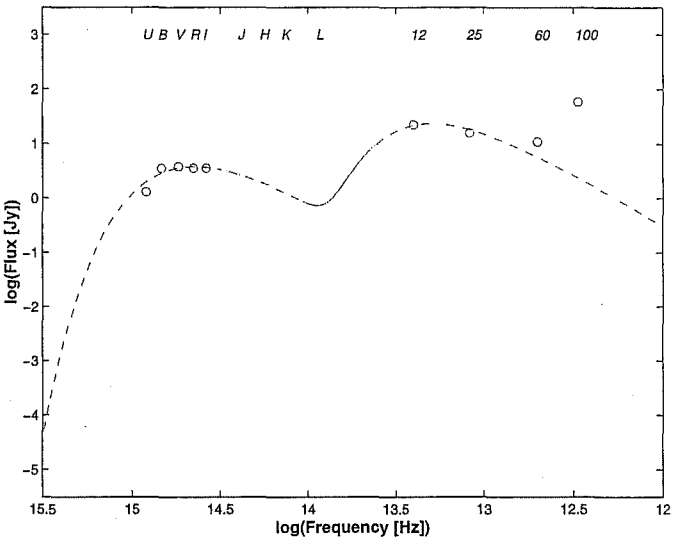

Figure 8.6: Blackbody fits to the SED of HD 95767. The fits have temperatures of 6900 and 340 K.

resolve this by assuming that the star has an earlier spectral type than F3, but this requires the star to be B8, derived by combining the mean observed $(B-V)$ and a colour excess of 0.72. This is too warm to produce the required number of neutral metal lines in the spectrum. The possibility of an anomalous extinction law on the line of sight to the star always exists, but we will not attempt to quantify this.

So using a total extinction of 1.4 magnitudes, we have fit the SED with two blackbody curves with temperatures of 6900 and 340 K, for an RMS of 0.13 and a derived stellar temperature of 6300 K. This temperature is a little more uncertain than for the other stars because we lack the near infrared photometry to fully constrain the stellar fits. The 100 μm point was not used in this fit as it could be contaminated by interstellar cirrus. The infrared profile of the star at even longer wavelengths should be examined to determine whether this point is in fact due to older ejected material from the star, which will be very cold.

From the flux at 60 μm we find a total circumstellar mass of $3.7 \times 10^{-4}\ M_{\odot}$. The radius of this shell is 340 $R_{\star}$ from the primary star.

8.4 Spectroscopy

There have been two sides to the character of HD 95767 exhibited since observations began in 1997. For the most part it resembles an F-type supergiant. But in late 2000, starting on HJD 2451896, it also showed a more explosive side during what we have labelled the outburst. This saw the appearance of numerous narrow emission features as well as extensive emission in Hα.

8.4.1 Typical Spectrum

The typical mean HD 95767 spectrum resembles an F-type supergiant. There are numerous metal absorption lines and a prominent Hα feature. The λ6708 Li I was undetected, implying that HD 95767 has not had either HBB or CPB operating in the recent past. Also there are some permanent emission lines from some low excitation potential neutral metal multiplets, e.g., Fe I RMT 15 ($\lambda\lambda$6400 and 6572) and RMT 1 of Ca I (λ6574). Some diffuse interstellar bands are visible in the spectrum of HD 95767. We have identified bands at $\lambda\lambda$5780, 5797, 6270 and 6284. However, the generally prominent band at λ4430 Å, is not present in either "blue" échelle or MRS spectra, and the line-like features at 6375 and 6379 Å are missing too.

Radial velocities

The radial velocities of HD 95767, shown in Figure 8.7, show a long term variation which has an amplitude on the order of 30 km s^{-1}. The radial velocity minimum coincides with that of the photometry. After this the radial velocity seems to return to the mean level prior to HJD 2451200 before increasing comparatively rapidly over the next 100 days.

There also appears to be a shorter period oscillation superimposed on this possibly associated with the variation seen in the first 200 days of the photometry. The velocities from HJD 2451200 to 2451800 show a variation which is larger for the lower excitation potential lines, and there is no indication of significant differences between the mean radial velocities of lines formed at different levels in the atmosphere, indicating a lack of expansion.

A periodogram analysis of these curves are presented for four prominent absorption lines in Figure 8.8. The main peak at 1400$\pm$280 d is, within error, at the length of the monitoring programme (1388 d). There are ancillary peaks at 280 ± 15, 500 ± 40 and 150 ± 4 days. Only Hα shows any sign of the 85 d variation detected in the early stages of the photometric monitoring programme.

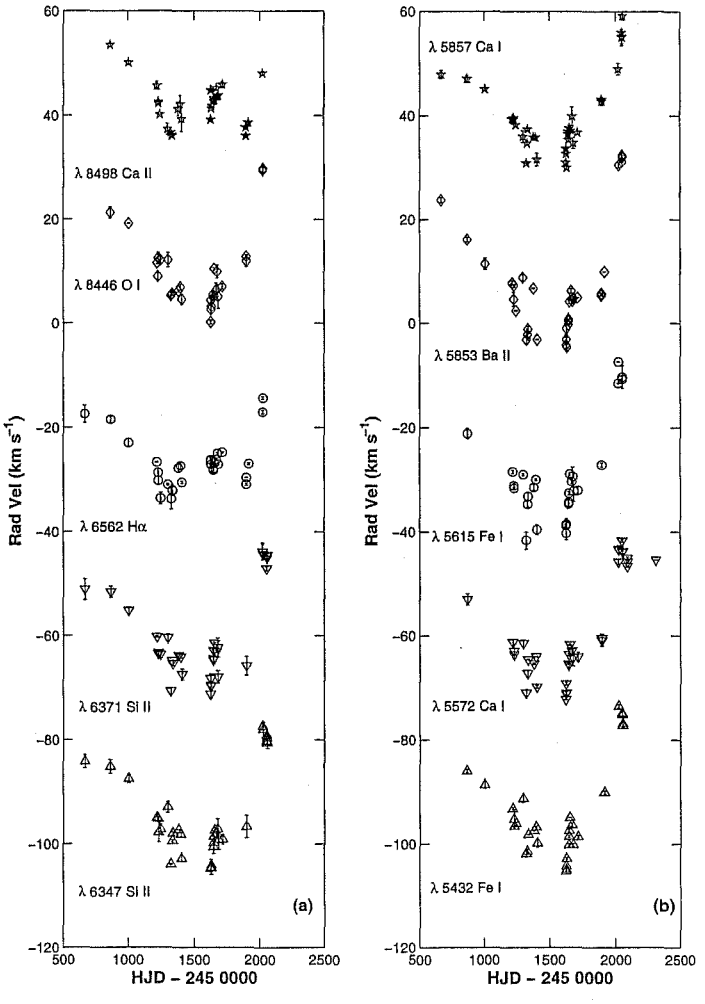

Figure 8.7: Radial velocities for HD 95767. High χ lines are displayed in (a) while lower excitation potential lines are displayed in (b). The middle group of points, marked with circles, are unshifted, all the other curves are displaced by multiples of ± 16 km s^{-1}.

λ_o (Å)	6347	6371	6562	8446	8498
Species	Si II	Si II	Hα	O I	Ca II
χ (eV)	8.12	8.12	10.19	9.52	1.69
n	35	33	31	28	29
μ_{rv} (km s^{-1})	−26.31	−26.07	−26.82	−23.76	−25.10
σ_{rv} (km s^{-1})	9.11	9.07	4.68	7.32	4.20
Δ_{rv} (km s^{-1})	0.56	0.50	0.48	0.48	0.53

λ_o (Å)	5432	5572	5615	5853	5857
Species	Fe I	Fe I	Fe I	Ba II	Ca I
χ (eV)	4.45	3.40	3.32	0.60	2.93
n	32	36	29	35	34
μ_{rv} (km s^{-1})	−25.38	−24.37	−28.96	−24.06	−26.62
σ_{rv} (km s^{-1})	10.24	10.56	9.83	12.62	8.33
Δ_{rv} (km s^{-1})	0.37	0.40	0.58	0.41	0.46

Table 8.6: Summary of the radial velocity for 10 lines in HD 95767. μ_{rv} is the mean velocity, σ_{rv} is the standard deviation, and Δ_{rv} is the mean error, all in km s^{-1}. n is the number of measures.

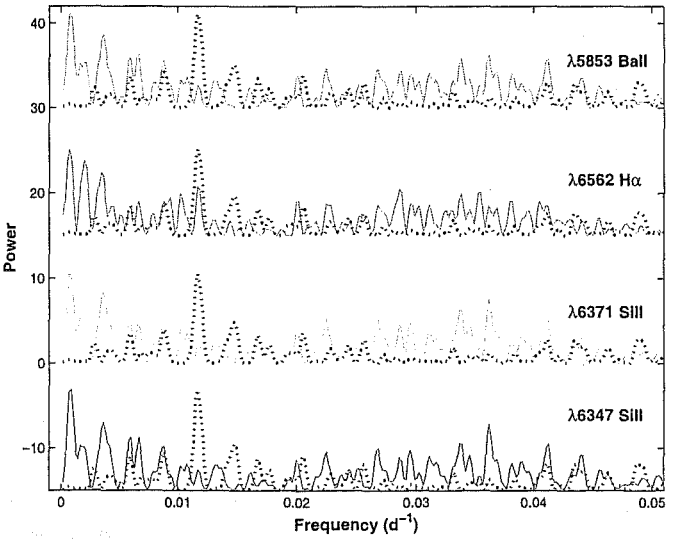

Figure 8.8: Lomb-Scargle periodograms of the radial velocities of HD 95767 shown with the window function for 85 d.

Na D lines

Multiple component fitting of absorption profiles to a normal Na D profiles is summarized in Table 8.7 (see also Figures 8.9 and 8.11a). This is from a HERCULES spectrum acquired on the night of HJD 2452315. The photospheric velocity from 104 neutral metal lines was -11.22 ± 0.08 km s^{-1} and a heliocentric velocity correction of -14.4 km s^{-1} was made. Overall there seem to be five components. An attempt was made to fit the profile assuming an emission line between components 4 and 5, but it proved impossible to obtain a satisfactory fit. Thus we believe all of the individual components are absorption features.

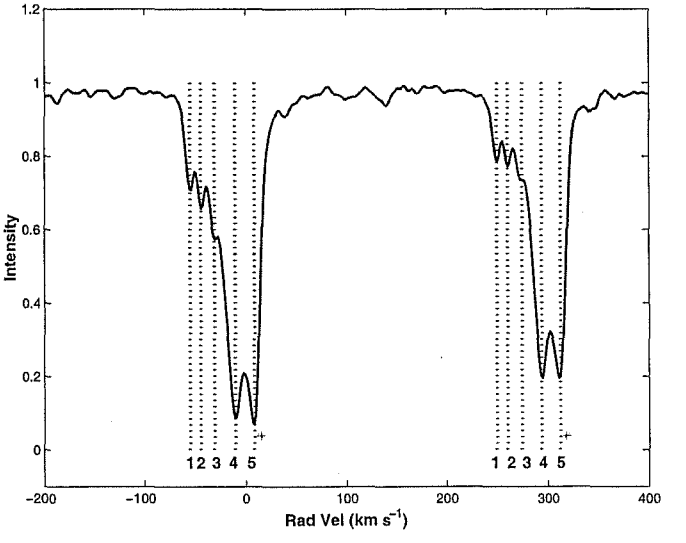

Figure 8.9: Components of the Na D lines for HD 95767. The positions of the fitted components are marked by the dotted lines and the details are listed in Table 8.7. The asterisks indicate the positions of any night sky lines.

The radial velocity along the line of sight due to the Galactic rotation curve is at its most blue-shifted, -16.2 km s^{-1} at about 3 kpc. The Sagittarius arm lies at 1.9 kpc ($z = -65$ pc) and we predict a heliocentric radial velocity of -13.7 km s^{-1}. This is a reasonable match to component 4. It is also a match to the stellar velocity on this night, but as we have seen in §8.4.1 the velocity of the star changes considerably. The shape of the HERCULES D lines is almost the same as the mean échelle profile, with

#	λ (Å)	W (Å)	Rad Vel (km s^{-1})		Notes
			$\odot$ frame	$\star$ frame	
1	5888.884	0.066	−55.1	43.9	CS?
2	5889.094	0.039	−44.4	33.2	CS?
3	5889.359	0.122	−30.9	19.7	CS?
4	5889.762	0.363	−10.4	−0.8	IS Sgr
5	5890.131	0.260	8.4	−19.6	IS?
1	5894.861	0.039	−54.5	43.3	CS?
2	5895.068	0.025	−43.9	32.7	CS?
3	5895.351	0.061	−29.5	18.3	CS?
4	5895.733	0.330	−10.1	−1.1	IS Sgr
5	5896.106	0.230	8.8	−20.0	IS?

Table 8.7: The components of the Na D lines of HD 95767. The RMS on the fit is 0.037 Å. CS indicates circumstellar material, IS interstellar, Sgr Sagittarius arm and ? marks an uncertain identification.

components 4 and 5 clearly visible and in the same position and features 1-3 unresolved. The only difference is that components 2-3 are higher, and 4 and 5 are lower, as if an absorption feature has moved from behind the former group to a higher radial velocity. Subtracting the two spectra and measuring the respective areas did not find them to be equal and opposite, the additional absorption required behind components 4 and 5 was 0.03 Å too weak. However, the presence of emission in other low excitation potential lines in the HERCULES spectra may account for the discrepancy.

Because component 4 is visible in the échelle spectra we will not assign it to the star and will instead suggest that it is part of the Sagittarius spiral arm. In the stellar frame components 1 and 2 have quite high velocities for ejected material, but as is seen in §8.4.3, the star does have periods of enhanced mass-loss and these features could be due to past eruptions.

The radial velocity of component 5 in the stellar frame pairs it with component 3. They could be represent two sides of an expanding asymmetric, shell of material as described in scenario B in §7.4.3 for HD 70379. Or it could be a local gas cloud.

Hα Profile

Like most of the stars in this programme the structure of the Hα line is abnormal for F-type supergiants (see Figure 8.10). Prior to the outburst the variations on the Hα profile were subtle and almost exclusively confined to the core and the flanking emission features, just as in our other F and G-type programme stars (see Figure 8.11b). The main change is in the height of the two small peaks that demarcate the boundary between the core and wings. Compared to normal late F-type supergiants the profile shows clear differences around the absorption core. The broad absorption wings are still present, but the core is different being both narrower and showing signs of emission.

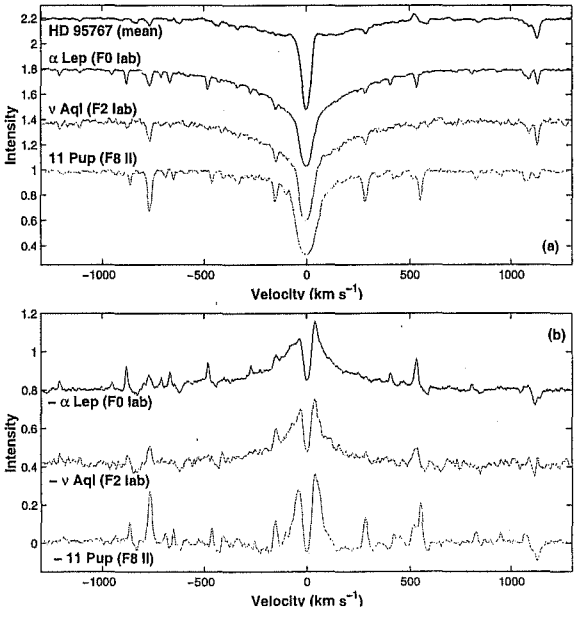

Figure 8.10: (a) A comparison of the typical spectrum of HD 95767 with three F-type standard stars. (b) The residual spectrum after each of the standard spectra have subtracted from the spectrum of HD 95767.

As has been shown by Dupree, Hartmann and Avrett (1984)[46], it is possible for luminous stars ($\log L/L_{\odot} > 2.7$) to generate significant emission wings in their chromospheres. The Hα profile for HD 95767 changes over the course of weeks indicating that it forms close to the star. It could be associated with the dissipation of shock wave energy, which heats the

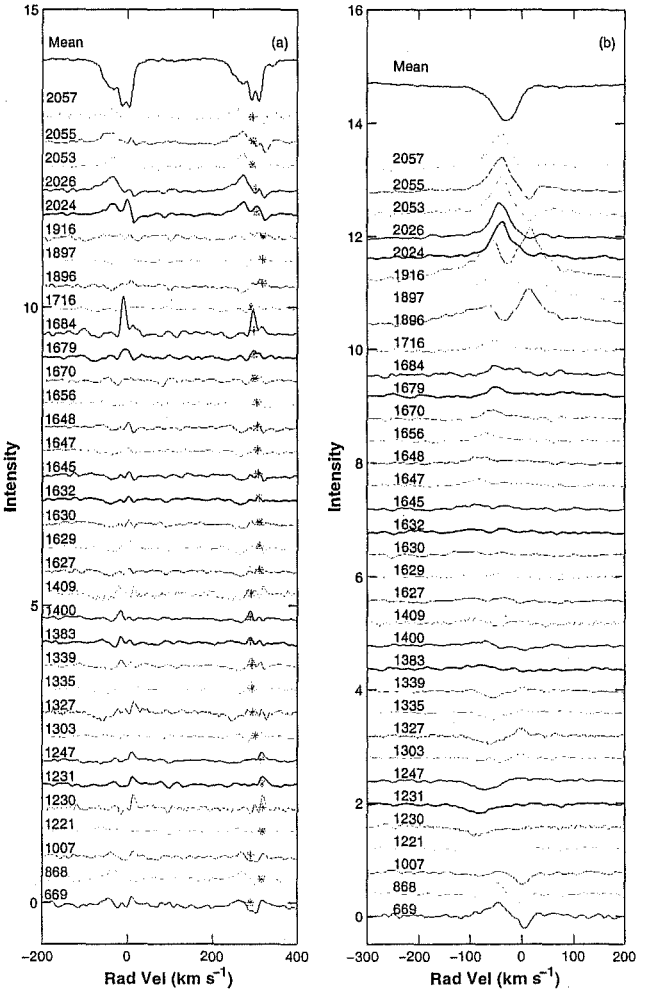

Figure 8.11: (a) Na D and (b) Hα residuals for HD 95767. The residuals are labelled with HJD−2450000 and the asterisks in (a) indicate the position of atmospheric features in the D_1 line.

chromospheres, generating the Hα emission wings via thermal electron scattering.

The displacement of the absorption core bluewards of the emission centre indicates that the star is undergoing mass loss. This is also indicated by negative asymmetry parameters for Hα and some of the strongest lines in the spectrum. Assuming the emission originates in an expanding, optically thin circumstellar shell, and that the emission is generated by recombination of H I (Cohen, 1976)[35] we can use the mass loss formula of Mallia & Pagel (1978)[126]:

$$\begin{aligned} \dot{M} &= 2.76 \times 10^{-4} V_{exp} R_{\star} (R_s W_{\lambda})^{1/2} \\ &\quad \times \exp(-1.1/T_4)\ M_{\odot}\ \mathrm{yr}^{-1} \end{aligned} \tag{8.1}$$

where V_{exp} is the expansion velocity in km s^{-1}, $R_{\star}$ the stellar radius in R$_{\odot}$, $R_s = 2R_{\star}$ is the estimated inner radius of the emission shell, W_{λ} the equivalent width of the emission in Å and T_4 is the brightness temperature of the star at Hα in units of 10^4 K. For the expansion velocity we take the mean difference between the absorption core and the red and blue emission peaks, 64 km s^{-1}, with an equivalent width of 4.3 Å of emission. $R_{\star}$ is taken as 90 R$_{\odot}$, typical for F-type supergiants and T_4 is taken as 0.058. The resulting mass loss rate is $2.6 \times 10^{-7} M_{\odot}$ yr^{-1}.

8.4.2 λ7774 O I triplet

Based upon three échelle spectra acquired prior to the outburst, the total equivalent width of this feature is 1.9 Å. Combined with $(b-y)_o = 0.204$, estimated from the spectral type (Gray 1992)[72], this gives an absolute magnitude of $M_V = -8.2$. This rather suggests HD 95767 is an extremely luminous star, about 150000 $L_{\odot}$, but this is at odds with earlier estimates of 2500 $L_{\odot}$.

8.4.3 The outburst of 2000/01

Starting on HJD 2451716, a series of dramatic changes occurred in the spectrum of HD 95767 (see Figure 8.12 for some examples). The first change was that the narrow Hα core became shallower. The following spectrum saw the steepening of the red wings of many low excitation absorption lines. Eventually this would develop into overt emission. By this time the Hα and Ca II triplet profiles had developed two emission peaks around their central absorptions with the red emission being stronger. As the outburst evolved

the blue peak becoming the stronger. This is reflected in the position of the emission in the other lines which migrate from the red wing to the blue, still growing in intensity. At about this time we also saw the progression of the absorption lines towards the red. After 340 days only a few of the emission peaks are visible and the absorption features are moving back to the blue.

There are four principal classes into which the line profiles can be categorized during this episode:

1. *P Cygni-like* (Figure 8.12a). Show both absorption and emission components. Restricted to low excitation ($\chi \leq 3$ eV) lines of Fe I, Fe II, Ca I and Ba II.

2. *Strong emission* (Figure 8.12c). Similar to the P Cygni-like lines but with a stronger emission feature that produces peaks on both sides of the narrow central absorption. Applies specifically to Hα and the Ca II triplet lines.

3. *Permanent absorption* (Figure 8.12b). These lines show no emission at all at any stage during the event. Some lines may weaken slightly but generally remain visible. Includes the higher excitation potential lines like $\lambda\lambda$6347 and 6371 Si II.

4. *Permanent Emission* (Figure 8.12c). Show no absorption at any time. Examples are Fe I multiplets 12, 14 and 15 (but not 13, which belong to type 1). There are no radial velocity variations and no absorption components either.

There are 2 key dates in the outburst as far as radial velocity behaviour is concerned, HJD 2451896 and 2451916. At the first date we start to see the absorption features move to the red. The second sees the emission features moving in the opposite direction. This is also the date of the emission intensity maximum for Hα.

By HJD 2451896, many of the neutral metal line profiles had developed steep red edges. Over the course of the event these peaks not only grow in intensity but also become blue-shifted. Initially there was filling in of the absorption, but ultimately it moved to the blue side of the absorption profiles. In many cases it appeared as small emission peaks on the blue edge of the absorption. This is exactly the kind of behaviour seen over a longer timescale in the luminous blue variable S Doradus during its 1989 outburst (Wolf & Stahl, 1990)[216].

Using λ5853 Ba II (see Figure 8.12a)as our sample neutral metal line we find that the emission peak shifts from -3.5 km s^{-1} on HJD 2451897

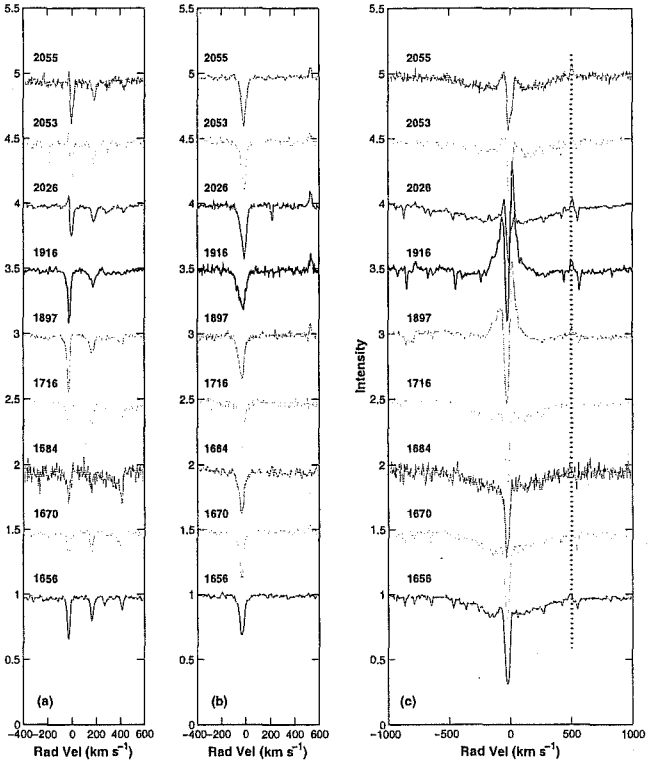

Figure 8.12: Line morphology, showing some examples of the basic line types exhibited by HD 95767 over the course of its outburst. From left to right we have: (a) P Cygni-like line (λ5853 Ba II); (b) permanent absorption line (λ6347 SiII) and (c) a strong emission feature (Hα) as well as a permanent emission line (λ6574 Fe I) indicated by the dotted line.

to -29 km s^{-1} on HJD 2452026. The spectrum from HJD 2451916 does not show the presence of any emission at all. If we relate these to the stellar frame, which we take to be given by the position of the absorption component, then the material responsible for the emission is moving towards the star at 27 km s^{-1} before moving away from it at 27 km s^{-1}. So in the space of 129 days this material is subject to an outward acceleration which turns inflow into outflow.

8.5 Discussion

To account for the observed changes in colour there are three possibilities for HD 95767. It either:

1. has a reduction on the level of obscuration by circumstellar dust;
2. undergoes a temperature change, or;
3. exists in a binary system.

The first model suggests itself due to the bluing of the colours. However, we have seen that this is due to a loss of red flux, which is the inverse of what a reduction in the level of obscuring dust would do.

A temperature change of +250 K at 7000 K would reduce $V-I$ by 0.05. However, it would also produce changes in other bands incompatible with a static B magnitude.

This leaves us with the binary scenario. In this case the sudden change in the red flux would be due to a cool, dim companion being eclipsed. In column 5 of Table 8.8 we estimate the brightness of this companion in various bands based upon the photometry acquired before (HJD 2451897) and during the eclipse (HJD 2451921).

From the derived $V-R$ and $V-I$ colours, and comparing them with those calculated from Kurucz model atmospheres, the best model candidates have the characteristics displayed in Table 8.9. The surface gravity does not provide a particularly definitive characteristic, so given the differential in V-band magnitude between the companion and primary of 4.64 magnitudes, means that the companion is much less luminous, probably a red giant.

The binary scenario can also help explain the radial velocity curve. This requires a rather eccentric orbit and the system would have to be in quite close alignment with the line of sight and have periastron occurring just after the observed changes in colour.

Band	$m_{1897} - m_{1921}$	f_{1897}/f_{1921}	Δm	m
B	0.003	99.72	6.36	16.02
V	-0.015	101.39	4.64	13.56
R	-0.037	103.47	3.65	12.10
I	-0.047	104.42	3.39	11.38

Table 8.8: HD 95767 estimated companion magnitude characteristics, derived from the observed magnitudes on HJD 2451897 (m_{1897}, before) and HJD 2451921 (m_{1921}, during) a purported eclipse. f_{1897}/f_{1921} is the flux ratio, Δm is the difference in magnitudes between the primary and secondary and m is the brightness of the secondary.

Colour	Value	T_{eff} (K)	$E(B-V)$
$V-R$	1.46	3500, 3750	0.8
$V-I$	2.18	3750	0.1

Table 8.9: HD 95767 estimated companion physical parameters, from Kurucz model atmospheres using the colours as a characteristic. $\log g$ is not included as it does not constrain the model.

It may also account for the outburst occurring at this time. In 2000, δ Scorpii was observed to undergo a radical spectral change associated with the periastron passage of an unseen companion (Miroschnichenko et al. 2001)[132]. The spectrum changed from a B-type to Be, as the companion induced strong mass loss from the primary producing a circumstellar disk which provides significant amounts of emission.

An alternative scenario to account for the outburst event is that of a collapsing false photosphere. The behaviour of the emission peaks during the outburst has been observed in the luminous blue variable S Doradus during its 1989 outburst (Wolf & Stahl 1990)[216]. As it collapses the false photosphere will move away from us and we see red shifted absorption lines compared to the normal systemic velocity. But then it re-establishes itself and the lines slow down and return to rest in the systemic frame.

The question is just how such a structure could form in this star. Is it likely that it could collapse and then reform in 12 months? In a star which is not particularly luminous or massive? There are also some very large distances involved. From HJD 2451716 to 2452026 we find that the velocity of the absorption lines changes from -32 to -12 km s^{-1}. Using a primitive Simpsons integration and the average velocities of the absorption lines over this time, this implies a distance change of 137 million km, i.e., 197 $R_{\odot}$. These changes are surely more indicative of a binary orbit than moving matter attached to a supergiant.

Fitting a binary orbit to the radial velocity curves requires six parameters: the inclination of the orbit, i; the argument of periastron, ω; the eccentricity, e; the systemic velocity, γ; the Period, P; and the semi-amplitude of the velocity, K. We have to find a fit in the 6-dimensional parameter space. In this case the orbit is oriented so that the stars eclipse and so $i = 90°$. Unfortunately because we have only sampled part of the orbit there is a whole family of orbits which fit our data. The results presented in Figure 8.13 shows the result of two fits with eccentricities of 0.5 and 0.7. The corresponding periods are 1600 and 3400 days respectively, but orbits with higher eccentricities and longer periods are also compatible with the radial velocity data. An additional complication is the semi-regular pulsation of the primary which obscures the position of the mean velocities.

Other issues to explain include the lack of titanium and nickel lines which seems incongruous for a star which does not appear to be iron deficient. The permanent stationary emission features may be due to a static shock as the stellar wind encounters some slower moving material (de Jager, 1998)[40]. This will occur at some distance from the star and will thus not be affected by any surface pulsations, nor even the motions of the binary. Such lines

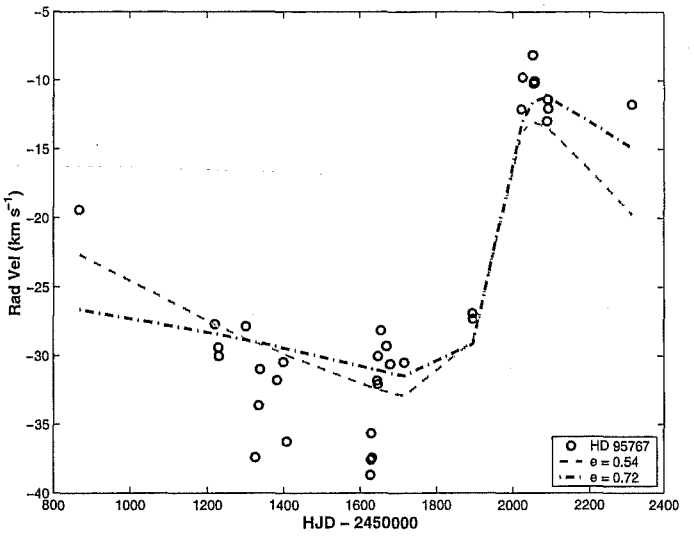

Figure 8.13: Two fits to the radial velocity curve of HD 95767.

have been detected in the spectrum of 89 Herculis (see Waters et al. 1993[212] and references therein), which have been assigned an origin outside of the binary system.

8.6 Conclusions

The results of our programme uncovered an unexpected side to HD 95767. Prior to about HJD 2451700 it showed many properties of the other stars in this programme. The photometry showed a variable amplitude oscillation with a period of 84 ± 8 d.

Assuming that HD 95767 is a supergiant means that the amount of extinction expected from the interstellar medium is considerably more than that derived from the spectral type. If the star has a luminosity $L = 2500\ L_{\odot}$ ($M_V = -3.7$), then we find that the visual extinction ($A_V = 1.4$) is at a level consistent with the spectral type. In this instance the star is 1.7 kpc distant. The circumstellar material has a temperature of 340 K and lies at 340 $R_{\star}$ with a mass of $3.7 \times 10^{-4}\ M_{\odot}$.

The spectrum had a multiple component Na D line profile consisting of 5 absorptions. Hα exhibited variable emission peaks adjacent to the absorption core. This could be generated by a mass loss of $2.6 \times 10^{-7}\ M_{\odot}\ \mathrm{yr}^{-1}$.

However, after the first 200 days of our monitoring the star began to dim and the radial velocities became more blue-shifted. But the most startling change began on HJD 2451716 when the Hα profile began to change producing large amounts of self-absorbed emission. At about this time a loss of long wavelength flux caused the colours to become bluer.

To account for this we developed a binary scenario in which the F-type primary is in orbit around a cooler dimmer star, probably an M-giant. The orbit is highly eccentric and with a period possibly several times the length of our observing programme. As the companion approaches periastron the tidal forces induce mass loss in the primary which we see as emission in Hα and other lines, as well as the rapid radial velocity changes around the time of periastron.

Chapter 9

HD 172481

9.1 Introduction

Until quite recently HD 172481 (= IRAS 18384-2800, and see Table 9.1) had been examined very sparingly. The most extensive list of properties was compiled by Odenwald (1986)[140] by considering IRAS fluxes and the observed spectral type. He found a star 6 kpc away with a surface temperature of 7200 K surrounded by a dust shell at 630 K.

Coordinates	α	$18^{\mathrm{h}}\ 41^{\mathrm{m}}\ 36.85^{\mathrm{s}}$
(Epoch 2000.0)	δ	$-27°\ 57'\ 00.6''$
Galactic	l	6.72
coordinates	b	-10.37
Mean Brightness	B	9.2
	V	8.3
Spectral Type		F2Ia0

Table 9.1: Basic parameters of HD 172481.

Oudmiajer et al. (1996)[144] also examined the IRAS data, but derived a dust temperature of 430 K. Eggen (1991, 1992)[49][50] and Gray (1991)[73] collected Strömgren photometry as part of their surveys of F- and G-type supergiant stars. Their observations are summarized in Table 9.2.

Bersier (1996)[15] calculated a colour excess of $E(B-V) = 0.271$, based upon a spectral type of F2/3Ia and a calibration of $E(B-V)$ in terms of two colour indices from the Geneva photometric system.

Reyniers & Van Winckel (2001, RVW hereafter)[162] and Whitelock &

v	$b-y$	m_1	c_o	β	Ref
8.968(7)	0.393(4)	0.017(6)	1.346(6)		Gray (1991)[73]
			[1.518]	2.650	Eggen (1991)[49]
9.05	0.292	0.063	1.576	2.656	Eggen (1992)[50]

Table 9.2: Strömgren photometry of HD 172481.

Marang (2001)[213] both agree that the system is a binary in which the secondary is a Mira variable. However, the nature of the primary is disputed. RVW identified it as a post-AGB star on the basis of the moderate metal deficiency ([Fe/H]= -0.55), high Galactic latitude, high radial velocity and slight s-process overabundances, indicative of third dredge-up.

Whitelock & Marang (2001) based their conclusions on $JHKL$ photometry which showed a clear pulsation period of 312 days. They noted that the pulsation amplitude is unusually high for a Mira variable, but that this is somewhat confused by the presence of the F-star which has a small, but significant, contribution to the flux at these wavelengths. They claim that the F-star is a product of mass accretion and subsequent hydrogen shell burning by a white dwarf companion to the Mira in a wide binary system with an orbital period exceeding a decade.

Giridhar et al. (2001)[68] described an abundance analysis which found an overabundance of lithium ([Li/H]= $+0.39$) and a carbon to oxygen ratio (C/O ~ 0.4) which indicates that the star has gone through the third dredge-up phase (Lattanizio, 1997)[112]. They also estimated the star's luminosity $L = 32000$ $L_\odot$ using the λ7774 O I triplet. The λ6708 Li I line was found to have a variable profile.

In this chapter we present the results of our spectroscopic and photometric monitoring of HD 172481 taken during the period 1997-2002.

9.2 Photometry

Fifty three $BVRI$ data points from MJUO covering 1032 days were obtained for HD 172481 (see Table A.5). The three stars used to calibrate the photometry are listed in Table 9.3: HD 172534 was the comparison, HD 172388 and HD 172794 were the primary and secondary check stars respectively. The RMS for the V-band magnitudes of the two check stars were 0.010 and 0.007 magnitudes respectively. No significant variations of the calibration stars was detected during the course of our programme.

Identifier	α (2000.0)	δ (2000.0)	B	V	SpT
HD 172534	$18^{\rm h}\ 41^{\rm m}\ 54.18^{\rm s}$	$-28°\ 19'\ 28.3''$	10.27	9.68	G2V
HD 172388	$18^{\rm h}\ 41^{\rm m}\ 05.03^{\rm s}$	$-28°\ 15'\ 19.7''$	9.11	7.96	K0III
HD 172794	$18^{\rm h}\ 43^{\rm m}\ 19.62^{\rm s}$	$-28°\ 26'\ 59.7''$	9.36	8.18	K1III

Table 9.3: Basic data for the photometry calibration stars of HD 172481.

From Figures 9.1 and 9.2, and from Table 9.4, it can be seen that the star varies in flux across all of the colours and passbands observed. Initially there is also a slight phase shift between the bands, with B leading V and R by about 19 d, and I by about 39 d, and the amplitude increases from B to I. However, this is not maintained. After HJD 2451200 the oscillation in BVR is not closely linked to the change in I, which remains very consistent throughout our programme. The colour-magnitude plot (Figure 9.3a) shows a different pattern to most of our other F-type stars because of this. Overall there is not such a strong correlation between the changes in V and those in $B-V$ and so the star follows no clear path on the diagram.

	U	B	V	R	I
Mean	9.854	9.729	9.111	8.739	8.125
Range	-	0.368	0.298	0.336	0.551
Error	0.010	0.002	0.001	0.002	0.002

Table 9.4: Some general properties of the $BVRI$ photometry for HD 172481. The mean magnitude for each colour is given along with the range of the change and the mean error. The U-band value is a single measure from the night of HJD 2451400.

9.2.1 Analysis of the photometry

The photometry can be broken into three sections, selected on the basis of how the variability in V reflects that in I:

1. HJD 2450910 to 2451045, spanning 135 days and containing 15 points. There appears to be an oscillation common to all of the photometric bands;

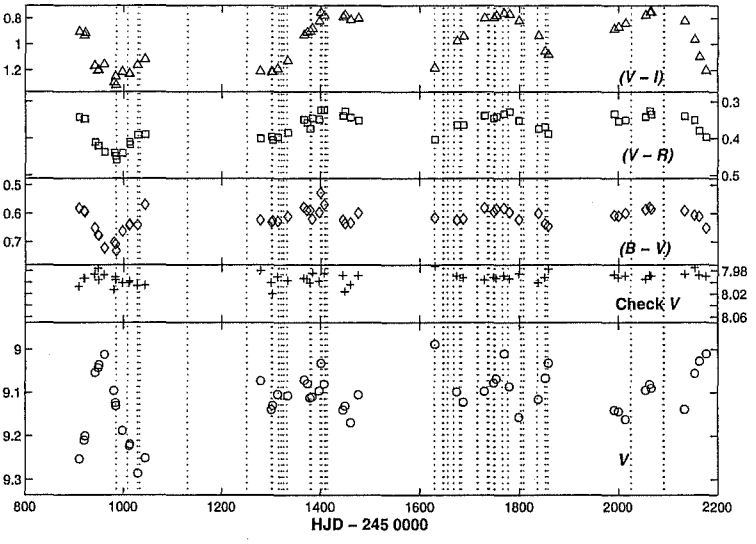

Figure 9.1: V and colour photometry of HD 172481 taken from MJUO. The dotted lines indicate when échelle spectra were taken.

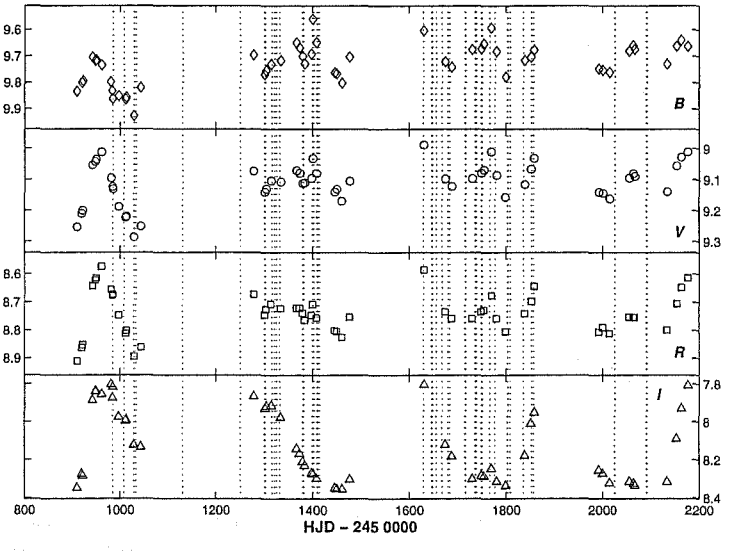

Figure 9.2: $BVRI$ photometry of HD 172481 from MJUO. Notice how consistent the I variation is compared to that in other passbands.

2. HJD 2451280 to 2451800, covering 520 days and containing 24 points. Only I behaves in a similar manner to before. The variation in R follows it but with a much reduced amplitude. In B and V it appears as though the star is following a shorter and very much smaller variation;

3. HJD 2451800 to 2452177, 14 points over 377 days. The trends in I are reflected in R and V but less strongly than in section 1.

The first and third sections follow quite similar tracks in the colour-magnitude diagram, with increases in brightness causing $(B-V)$ to become redder. This is not like the photometry for the other F-type star in our sample which become bluer when brighter, but rather it resembles the behaviour of the cooler variable, AI CMi. However, in the second section HD 172481 follows the pattern exhibited in the colour-magnitude diagrams of the other F-type stars, indicating that the photometric changes in B and V are driven by the F-component. The slope of the change in this section, 1.04 ± 0.04 is more like those measured for the F-stars HD 70379 and HD 95767 which have gradients of 1.736 ± 0.003 and 1.235 ± 0.002 respectively.

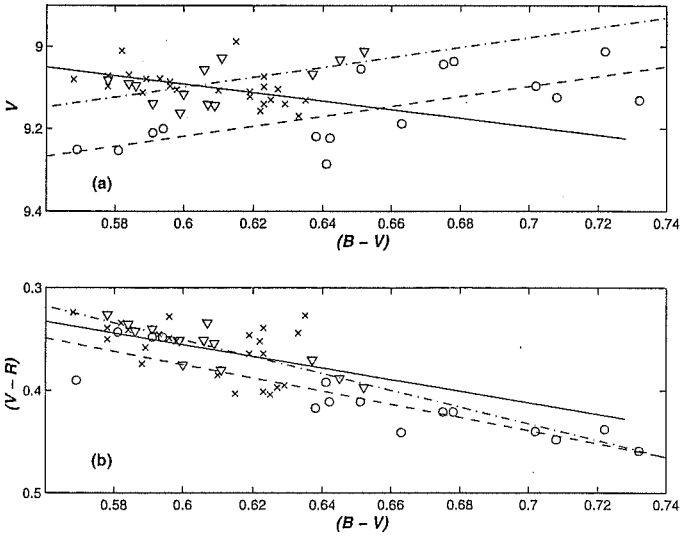

Figure 9.3: (a) Colour-magnitude and (b) colour-colour plots for HD 172481. The data have been divided up into the three sections indicated in §9.2. Section 1 is represented by the circles and a dashed line; section 2 by crosses and a solid line; and section 3 by the triangles and the dash-dot line.

Lomb-Scargle periodograms of the brightness in each passband and colour are presented in Figure 9.4. At the top are the power spectra for the whole dataset. The next three rows represent the three sections outlined above to check for seasonal variations in the periodicities at somewhat reduced resolution.

Examination of the whole data set by a number of period finding algorithms uncovered an extremely significant peak in I and the three colour indices at 310 ± 20 d (0.0032 d^{-1}). It is also present in the full R spectra, but with a lower level of significance. In the R-band there are two peaks which are more significant: at 130 ± 10 d (0.0075 d^{-1}) and 110 ± 10 d (0.0091 d^{-1}) and these are also the most significant periods in the V-band. Indeed, the V-band lacks any notable peaks at about 300 d. While the B power spectrum does show at peak at 300 d, it is part of a cluster of similar peaks and the interpretation is not so clear.

The periodograms in the first section of the photometry (HJD 2450910 to 2451045) are quite different to those in the other subsections and in the whole set. The most prominent peak in BVR is at 130 ± 10 d (0.0075 d^{-1}). The I spectrum has two peaks (0.0054 and 0.0102 d^{-1}) which have a mean of 140 ± 40 d. The colours also show the same twin peaked structure.

The second section sees the emergence of prominent 330 ± 40 d peak in R, I and their associated colours. $B - V$ shows no significant period, while B and V have their most significant peaks at 120 ± 10 d. The final section sees the I spectrum with the same dominant peak (270 ± 30 d). The colours exhibit two strong peaks at 310 ± 40 d (0.0032 d^{-1}) and 170 ± 10 d (0.0059 d^{-1}). R shows traces of the 300 d peak but like B and V shows clear peaks at 0.0069, 0.0096 and 0.0151 d^{-1} (145 ± 10, 105 ± 5, 66 ± 2 d).

Given how closely the I-band matches the period derived by Whitelock & Marang (2001)[213] from their $JHKL$ photometry, it is clear that this is due to the oscillation of the cooler component. In the first section it is causing the changes in all of the photometric bands. The fact that the peak of the power spectra is at 133 d is due to the length of the observing season (135 days), which includes only the part of the cycle where the Mira is bright enough to cause the changes, and not the remainder where the F-star dominates the photometry. For section 1 of the photometry it would appear that it is driving the changes in all of the bands. In section 2 the changes in B and V do not correlate as strongly with those in I and this is reflected in the periodograms, which show a main period of 121 ± 6 d (0.0082 d^{-1}), and it has a much lower level of significance. Even in R the patterns seen in I are much weaker than they were in section 1. Section 3 seems to have at least V, R and I following the same trends.

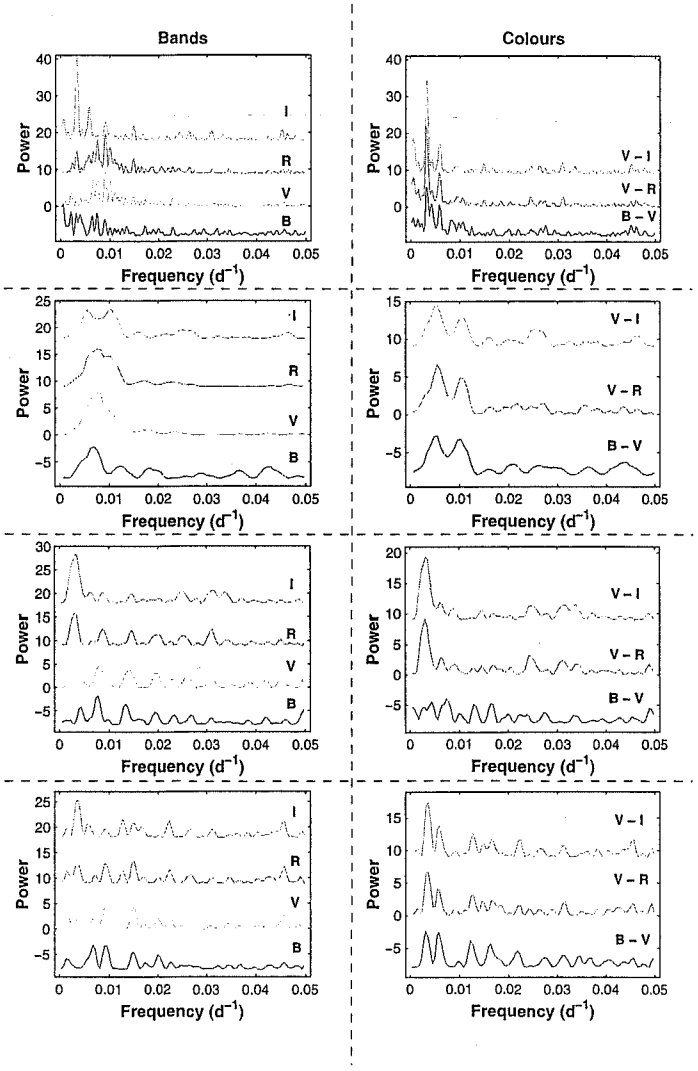

Figure 9.4: Lomb-Scargle periodograms for $BVRI$ photometry of HD 172481. The top row is the power spectra using the full data set, while rows 2-4 cover the three subsections of the photometry. On the left are periodograms from each of the bands (from top to bottom the order is I, R, V, B) and on the right, the transformed colours ($B-V$, $V-R$ to $V-I$ at the top). The periodograms have been offset.

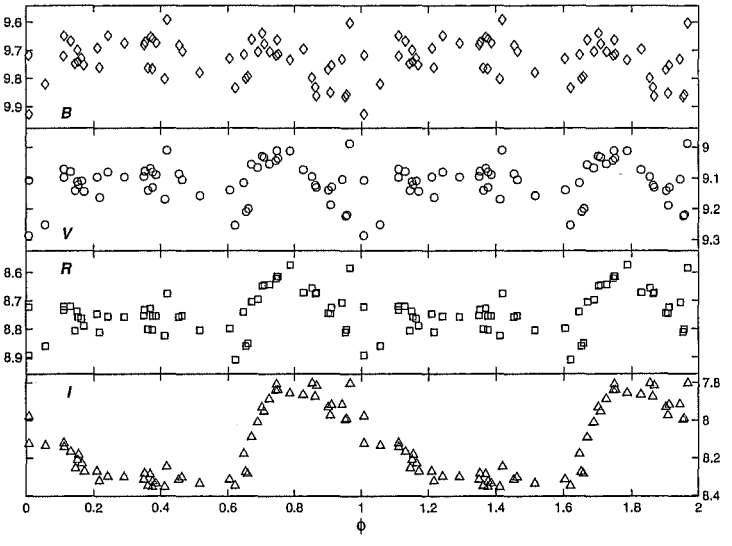

Figure 9.5: MJUO $BVRI$ photometry of HD 172481 phased to 307 days.

RVW estimated that HD 172481 was a semi-regular variable with a period about 100 d, based upon observations with the Geneva photometric system. In the power spectra from the entirety of the MJUO photometry this is what is seen in the V and R-bands. Both show a clustering of peaks centred around 120 d.

Further investigations were conducted with a simulated system consisting of an F2 supergiant and a Mira variable to see how the two might combine to produce a light curve which has a pronounced oscillation in all bands before HJD 2451100, but maintains this only in I subsequently. The standard F-supergiant colours were taken from Cox (2000)[38]. The synthetic Mira was given a period of 312 days and photometric colours and amplitudes which are averages of the variations of RR Telescopii, R Horologii, R Carinae and T Columbae provided in Eggen (1975)[47]. Although Mira variables peak in the B-band shortly before they peak in V and have neither strictly periodic nor sinusoidal light curves, for the purposes of this simulation these features were ignored. The aim was to reproduce the main features of the light curve (Figure 9.6 lower panel). To simulate the variability in the F-star random noise was added to the light curve with a peak-to-peak amplitude of about 0.1 mag. The mean V magnitude of each star was then fixed and the resulting combined flux was reddened with $E(B-V) = 0.43$. The synthetic light curve was sampled at the same dates as the observations.

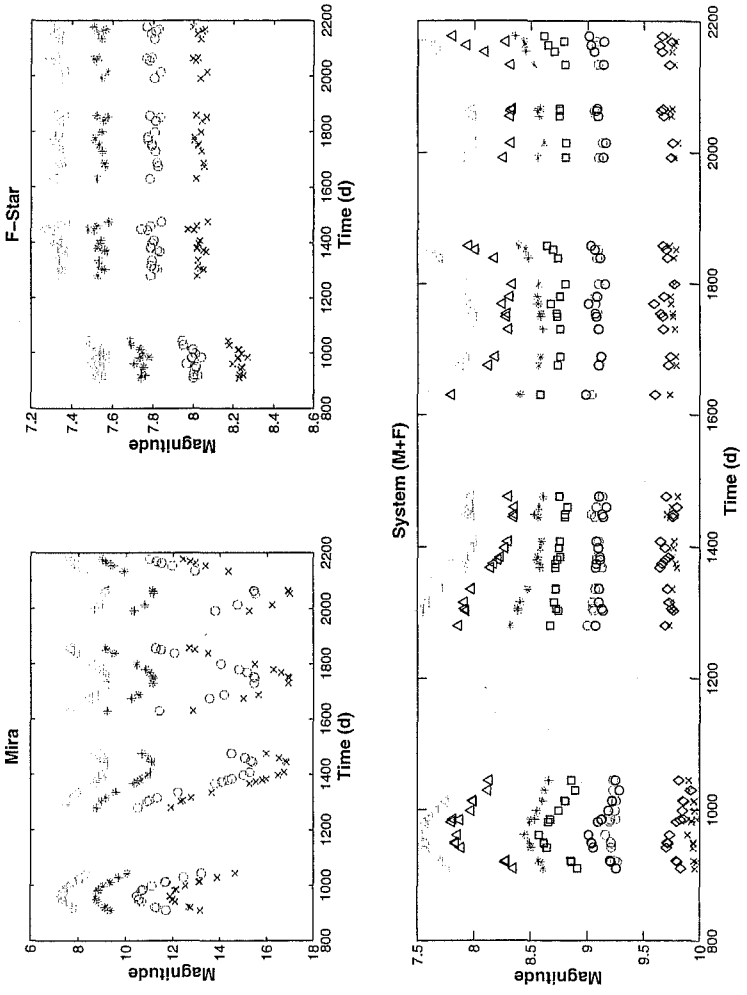

Figure 9.6: Synthetic light curves for an F star and a Mira variable. The upper panels show the variations for the components and the lower one shows the combined synthetic light curves along with our photometric measurements. B is at the bottom and I at the top, with the real photometry represented by the same markers as in Figure 9.2 and the synthetic data by the lighter symbols.

	Mira			F-Star	M+F
	Ampl	Colour			
B	5.09	$B-V$	1.45	0.23	0.69
V	5.04	$V-R$	2.98	0.26	0.60
R	2.41				
I	1.83	$V-I$	4.67	0.47	1.35

Table 9.5: Adopted values of the photometric properties of the Mira and F-star for the synthetic photometry. All values are given in magnitudes and Ampl is the semi-amplitude.

After adjusting the relative brightness of the components it was possible to achieve a satisfactory approximation to the actual light curve. Changing the brightness of the Mira causes a change in the maximum brightness reached by the system; altering the amount of F-star flux determines the lower limit of the flux as it provides almost all of the photons when the Mira is at minimum light.

The only modification to match the synthetic and observed light curves, was that for the first 320 days, the F-star was 0.15 magnitudes dimmer in V than during the rest of the simulation. This was necessary as HD 172481 is dimmer in almost all bands than the mean light level in later sections. This could be due to a dust obscuration event and futher monitoring is required to confirm this. It also allows the Mira to drive the changes observed in the photometry. The resulting mean unreddened magnitudes are $V = 7.8$ for the F-star and $V = 13.0$ for the Mira, a flux ratio of 91:1. Compared with RVW, who predicted a 1:24 flux ratio at V, it would appear that we have underestimated the V-band brightness of the Mira. But RVW's infrared photometry was taken on 1992/6/15-16 (~HJD 2448788-9), and the infrared data in Whitelock & Marang (2001) confirms that the Mira was at its brightest at that time. So they will have over estimated the contribution of the Mira to the SED. This is shown in Figure 9.7 which has the MJUO $BVRI$ and $JHKL$ from Whitelock & Marang (2001) acquired at the two extremes of the Mira's light cycle. The data are not contemporaneous but are separated by about a light cycle they are combined to show the changes the variations can bring.

The lack of variation in the photometry, especially the B and V-bands, appears to be due to an alias with the light cycle of the Mira. At these phases the F-star provides the flux, which gives rise to a flat light curve.

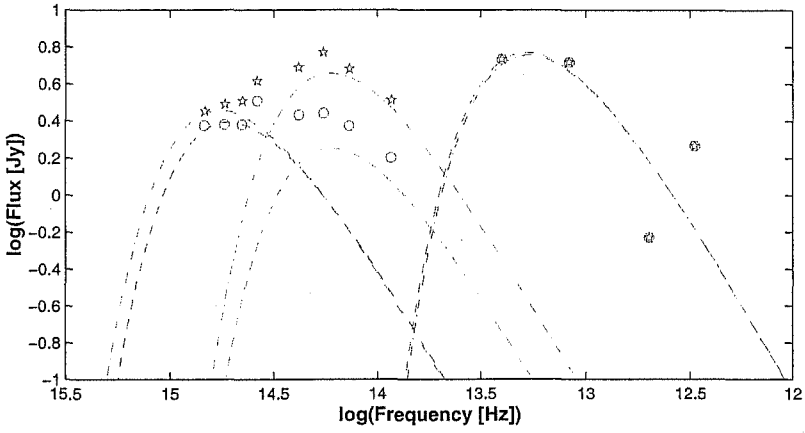

Figure 9.7: Changes in the SED of HD 172481 due to the variation of the cool component. The darker dashed lines are the three blackbodies fitted to the circles, denoting the Miras minimum, while the dash-dot lines fit the photometry at maximum marked by stars.

The fake R and I-bands do show the same pattern of increasing amplitude as the real data but they are a little bit too bright, seemingly due to our adopted mira colours and pulsation amplitudes.

9.3 Spectral energy distribution and reddening

The dereddened SED, shown in Figure 9.8, clearly shows the star to have at least three components: 7700, 2700 and 320 K, with an RMS of 0.14. The stellar component temperature is corrected to 7100 K. The fit neglects the R and I-band photometry, as they contain significant contributions from the cooler component, which cause the photometry of the primary to be fit with blackbodies at 9000 K. A total V-band extinction of $A_V = 1.5$ was derived from a colour excess of $E(B-V) = 0.47$. This compares well with $E(B-V) = 0.44$ derived by RVW. No new infrared photometry was acquired for this star as part of this project and the $JHKL$ photometry presented here has been acquired at the SAAO as part of a separate project (Whitelock, private communication).

The line of sight through the Galaxy to HD 172481 has an extinction curve that has a plateau at 0.9 ± 0.3 magnitudes in V for distances greater

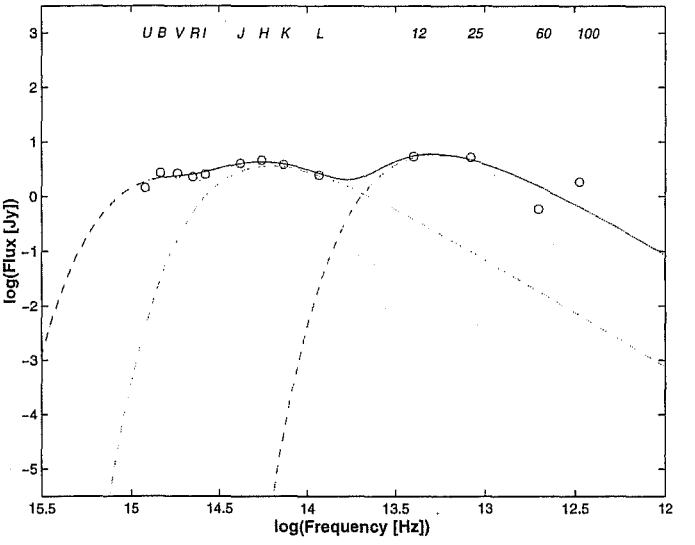

Figure 9.8: The blackbody fits for HD 172481 using the mean of the MJUO $UBVRI$ photometry, the $JHKL$ from SAAO and IRAS fluxes. The three curves have temperatures of 7700 K, 2700 K and 320 K.

	J	H	K	L	12	25	60	100
Band	6.808	6.054	5.67	5.211	5.41	5.22	0.59	1.85
Error	0.03	0.03	0.03	0.05	0.27	0.68	0.06	L

Table 9.6: Summary of the infrared photometry compiled for this star. $JHKL$ is from SAAO (Whitelock, private communication) and the IRAS photometry is in janskys.

than 2 kpc (Hakkila et al. 1997)[75]. So for HD 172481 the extinction requires a circumstellar contribution of at least 0.6 ± 0.3 mag. Assuming $M_V = -4.6$ for a post-AGB star, the observed brightness and colour excess imply a distance of 3.1 kpc and a circumstellar extinction of 0.5 mag. The 60 μm flux predicts 7.1×10^{-5} $M_\odot$ of circumstellar material at a distance of 2.5×10^2 $R_\star$ from the star.

9.4 Spectroscopy

The spectra of this star are unusual. In general they have most of the features of the other F-type stars in the programme but they also include some narrow emission lines as well as some molecular band heads which are visible in the redder parts of our spectra during certain phases of the photometry.

Only a few diffuse interstellar bands can be seen in the spectrum of HD 172481: $\lambda\lambda$5870, 5802 and 6428. Other normally prominent features, including those at $\lambda\lambda$4430, 5849, 6376 and 6379, are not present and those at $\lambda\lambda$6196 and 6203 may be weakly visible but are subject to interference from molecular features.

9.4.1 Radial Velocities

One of the goals in observing this star was to try and get some information which will constrain the period of the binary system. Unfortunately many of the lines observed in the spectrum are not suitable as they show significant profile changes, like λ5853 Ba II (see Figure 9.15b). The radial velocities have been derived from lines which are relatively free from interference from underlying emission lines, molecular bands or other sources of uncertainty (e,g., non-LTE effects) and are believed to be associated with the F-star. Suitable lines include high excitation lines ($\chi > 8$ eV): $\lambda\lambda$6347 and 6471 Si II, λ8446 O I and the Hα absorption core, as well as some moderate excitation potential lines ($2 < \chi < 4$ eV). These latter lines show no sign of the emission distortion which affect the line profiles of the low excitation potential lines to be discussed in §9.4.5. There is a summary of the data in Table 9.7 and the radial velocity data are presented in Tables C.9 and C.10 of Appendix C.

Figure 9.9 shows the velocity curves for the ten lines in the above categories. The mean velocity is -83.5 km s^{-1} with a standard deviation 2.9 km s^{-1}. They show a smaller amplitude variation about the mean than

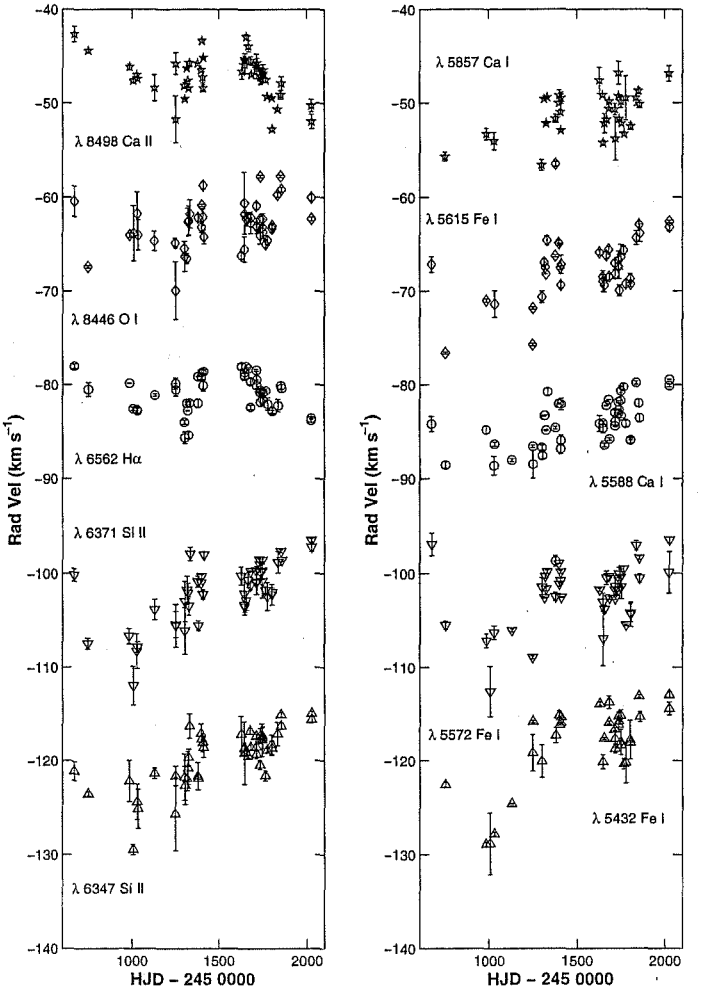

Figure 9.9: Radial velocity curve for 10 lines in the spectrum of HD 172481. λ6562 Hα and 5588 Ca I are plotted at their correct velocities. The other lines have been offset by $\pm$20 or $\pm$40 km s^{-1}.

is observed for other stars in this programme, which have standard deviations in the range of 3.6 to 7.9 km s^{-1}. There are some indications of a trend in the velocities of $\lambda\lambda$6347, 6371, and all of the intermediate excitation potential lines, between about HJD 2451000 and HJD 2452200, and it is this which contributed most to the standard deviation. HD 172481 lacks substantial radial velocity variations over time scales measured in months. The λ8446 O I line shows little evidence of a trend in radial velocity but has some scatter about the mean. Hα and λ8498 Ca II hint at a variation with a period roughly the length of our programme.

λ_o (Å)	6347	6371	6562	8446	8498
Species	Si II	Si II	Hα	O I	Ca II
χ (eV)	8.12	8.12	10.19	9.52	1.69
n	45	45	48	38	47
μ_{rv} (km s^{-1})	−85.83	−84.99	−80.90	−79.33	−80.72
σ_{rv} (km s^{-1})	2.90	3.17	1.92	2.30	2.20
Δ_{rv} (km s^{-1})	0.81	0.64	0.22	0.58	0.45

λ_o (Å)	5432	5572	5588	5615	5857
Species	Fe I	Fe I	Ca I	Fe I	Ca I
χ (eV)	4.45	3.40	2.53	3.32	2.93
n	35	41	45	39	34
μ_{rv} (km s^{-1})	−84.49	−85.10	−84.02	−84.28	−84.66
σ_{rv} (km s^{-1})	4.13	2.83	2.48	2.76	2.34
Δ_{rv} (km s^{-1})	0.75	0.59	0.35	0.37	0.56

Table 9.7: Summary of the radial velocity for 10 lines in HD 172481. μ_{rv} is the mean velocity, σ_{rv} is the standard deviation, and Δ_{rv} is the mean error, all in km s^{-1}. n is the number of measures.

The lack of scatter about these trend lines suggests, at most, a weak pulsation in the F-star, with a peak-to-peak amplitude of less than 10 km s^{-1}.

The Si II lines show a long term trend with some significant scatter, the Ca II and Hα lines have a different pattern which peaks at about HJD 2451500. These changes are not due to either line level effects or to a nett shift in stellar velocity. For the latter lines the changes seem to be linked to changes in the line shape. The scatter in the data could be due to pulsations associated with photometric variations of the F-star.

RVW have CORALIE and CORAVEL radial velocities spanning about 7000 d, and report a peak-to-peak variation of 17 km s^{-1} but no long-term

trend indicative of a binary companion. Rather arbitrarily they assume an inclination of 60° and a velocity amplitude of 5 km s^{-1}, deriving a period of 51 years. However, this is a very speculative estimate and should be treated with caution. Our programme confirms that HD 172481 is not a significant radial velocity variable, either due to the influence of the secondary, or to pulsational motion within the atmosphere of the primary.

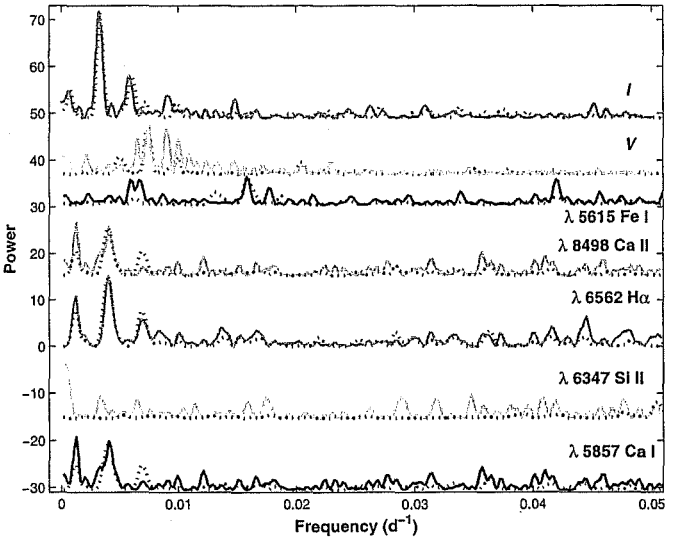

Figure 9.10: Lomb Scargle periodograms for the radial velocities of HD 172481. Also included are the periodograms for the V and I-band photometry which reflect the variations in the F-star and Mira components respectively.

The periodogram analysis of these radial velocity curves is presented in Figure 9.10 along with periodograms for the V and I band photometry and the respective window functions. The strongest peak in three of the periodograms (λ5857 Ca I, λ6562 Hα, λ8498 Ca II) occurs at 250 ± 10 d which is most likely a reflection of the influence of the variability of the Mira, as can be seen in how close it is to the peak in the I-band power spectrum.

9.4.2 Hα Profile

This feature presents the typical profile of post-AGB stars: wide absorption wings, sharp central absorption, with variable emission peaks as can be seen in Figure 9.11a.

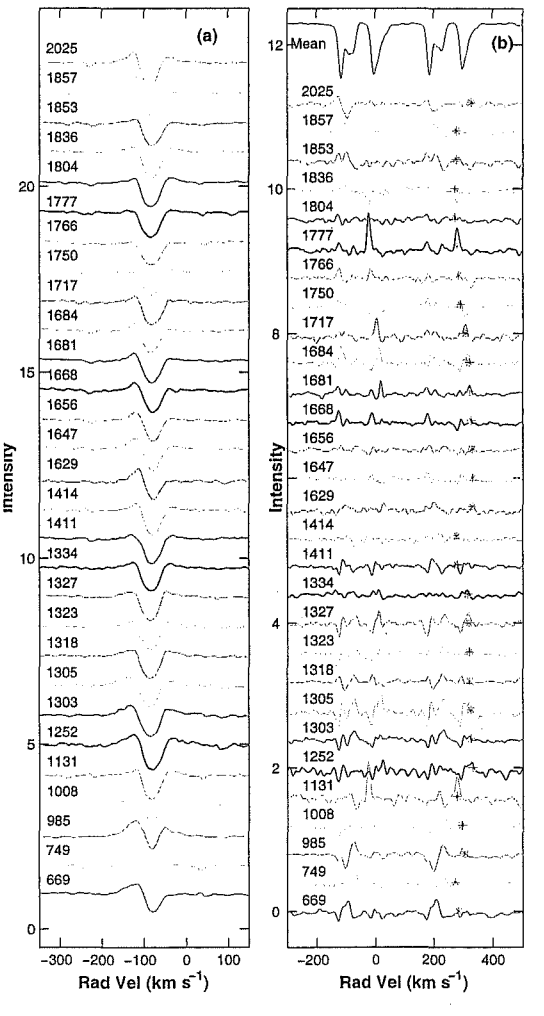

Figure 9.11: (a) Hα line profile and (b) Na D residuals of HD 172481 over time. The asterisks in (b) mark the position of night sky emission lines in the Na D_1 profile.

RVW Figure 6 shows a stack of four Hα profiles spread over a period of about 4.5 years. Our spectra confirm that the Hα profile undergoes changes in the relative intensity of the emission surrounding the absorption core as shown by RVW, but in months rather than years. This is also in line with Hα profile changes observed in the other stars in our programme.

9.4.3 Sodium D Lines

The Na D line profiles for this star are quite complicated. They form two distinct groups comprising at least seven separate components. Assuming all of the components to be due to absorption, an identification from a HERCULES spectrum (Figure 9.12) is presented in Table 9.8.

#	λ (Å)	W (Å)	Rad Vel (km s^{-1})		Notes
			$\odot$ frame	$\star$ frame	
1	5887.6925	0.308	-115.8	34.1	CS
2	5888.1730	0.161	-91.3	9.6	CS?
3	5888.5475	0.180	-72.3	-9.5	CS?
4	5889.8465	0.232	-6.1	-75.7	IS Sgr
5	5890.1485	0.105	9.3	-91.0	IS Sct
6	5890.4245	0.154	23.3	-105.1	IS Nrm
7	5890.8145	0.033	43.2	-125.0	IS
1	5893.6545	0.265	-115.9	34.1	CS
2	5894.1045	0.099	-93.0	11.2	CS?
3	5894.4890	0.194	-73.4	-8.3	CS?
4	5895.8390	0.219	-4.7	-77.0	IS Sgr
5	5896.1270	0.089	9.9	-91.7	IS Sct
6	5896.4145	0.092	24.5	-106.3	IS Nrm
7	5896.7700	0.033	42.6	-124.4	IS

Table 9.8: The components of the Na D lines of HD 172481 determined from HERCULES spectra taken on the night of HJD 2452090. See Figure 9.12 for identifications. The RMS of the fits is 0.02 Å. CS identifies the line as circumstellar, IS interstellar, ? indicates an uncertain designation, and Sgr, Sct, and Nrm refer to spiral arms.

The heliocentric correction was -0.3 km s^{-1} and the radial velocity of the star on HJD 2452090 was -81.75 ± 0.03 km s^{-1} from 236 lines. This velocity has been used to convert from heliocentric to the stellar rest frame

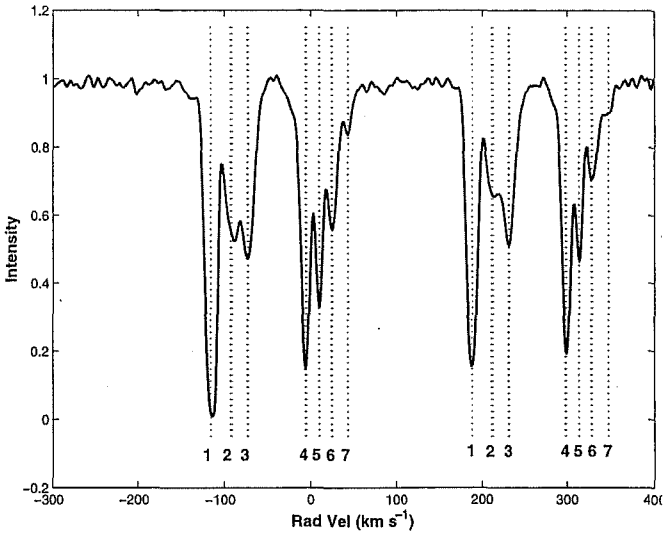

Figure 9.12: Na D line profile for HD 172481. The components are labelled according to Table 9.8.

in column 5 of Table 9.8, and using these values components 1, 2 and 3 can be assigned to the star and its environs and components 4-7 to the interstellar medium. The variations seen in this second group (see Figure 9.11b) are mostly due to interference from night sky emission.

To help identify the components, and to investigate the distance to the star, spectra were also acquired of two stars with similar lines of sight. HD 172440 (HIP 91650, $V = 7.2$, K2) lies $2.8'$ away from HD 172481 with a parallax of 0.7 to 3.5 mas (Perryman et al. 1997)[150], implying a distance of 474 pc although this is quite uncertain and could be as far as 1400 pc. As can be seen from Figure 9.12 there are two components to its D lines with associated heliocentric radial velocities of -4.3 and $+46$ km s^{-1}. The shape and radial velocity of the former, clearly denote it as due to the same cloud responsible for component 4. The stellar nature of the other larger component is confirmed by the radial velocity of 42 other spectral lines $+46.82 \pm 0.06$ km s^{-1}.

Coincidentally spectra were taken of Nova Sagittarius 1999 which lay about 7.5° away. It shows both components 5 and 6. Work carried out in this department by Ceridwen Livingstone (2000)[119] on this nova placed it at 4100 ± 1200 pc, which suggests that these two features are from gas that lie within this range.

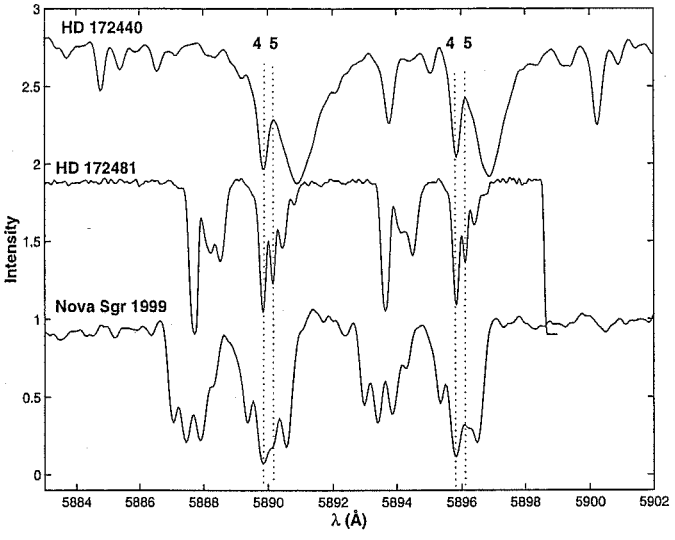

Figure 9.13: The HERCULES version of the sodium D lines. The components are labelled according to Table 9.8. Also displayed are the spectra of Nova Sgr 1999 and HD 172440.

To investigate this further the radial velocities of components 4-7 have been compared with velocities one would expect along the line of sight due to the Galactic rotation curve. Using the position of the main spiral arms given in Taylor & Cordes (1993)[181], component 4 was found to have a radial velocity compatible with it being part of the Sagittarius arm at 1.9 kpc ($z = -340$ pc). The Galactic rotation curve predicts a radial velocity of -2 km s^{-1} at this distance. Further along the line of sight it intercepts the Scutum-Crux and Norma spiral arms at distances of 3.5 and 5.1 kpc, with corresponding radial velocities of $+9$ and $+23$ km s^{-1} respectively. The Scutum-Crux arm provides a match to component 5 and Norma to component 6.

The fit presents one problem and that is the lack of a component at the stellar velocity. Components 2 and 3 have an average velocity similar to the systemic velocity. An alternative fit to components 1-3, in which component 2 is an emission line, and 3 becomes a large wide absorption proved unsatisfactory as they were unable to provide a reasonable fit to the line profile along the wings of the revised component 3. The interpretation of these lines is also confused further by variability, probably associated with the contribution of the Mira to the profile (See Figure 9.13b).

If HD 172481 was itself following the Galactic rotation curve it would have a red-shift for all points along its line of sight. Clearly the heliocentric radial velocity is not compatible with this model. Minniti et al. (1996)[131] used the metallicities and radial velocities of K giants to explore the kinematics of the Galactic bulge. They found that the lower the metallicity the higher the blue-shift, but also that the radial velocities had a higher dispersion. Their paper was based upon a field at Galactic coordinates $l, b = (9.9°, -7.6°)$, close to the line of sight to HD 172841. The radial velocities for metal weak stars, [Fe/H]=−1.0 to 0.0, indicate that HD 172481 is moving towards us with a velocity slightly greater than measured for the bulge stars. Although the dispersions are very large, $\sim$ 50 to 70 km s^{-1} about a mean velocity of 0 km s^{-1}, that it is possible that HD 172481 is a bulge star, but is more likely to belong to the Galactic Halo. This region is populated by objects with eccentric orbits, and would account for the radial velocity of HD 172481 quite readily.

9.4.4 Molecular band heads

Compared to AI CMi (see §4.4.4), HD 172481 has only a few molecular band heads and most of these are found in the red parts of our spectra. Table 9.9 is a list of the band heads found. These have been identified from the échelle spectra of HJD 2450985 and HJD 2451306 which have the clearest examples of molecular bands. The majority of these belong to titanium oxide, but there is one due to zirconium oxide and two due to vanadium oxide.

The behaviour of one of the bands is shown in Figure 9.14. It can be seen that the band is most easily seen in spectra taken between phases 0.72 and 0.91 when the star is brighter than about $I = 8.25$.

9.4.5 Metal line profiles

The profiles of many metal lines are unusual and change significantly over time. Examples of these changes are presented in Figure 9.15.

For low excitation potential neutral metal lines there is a distinct lack of symmetry to the observed profiles. This makes them unsuitable for use in determining radial velocities. The line shapes vary from subtle distortions to overt emission. It is this feature which tells us that we are not seeing "doubled" absorption lines due to shock wave propagation within the atmosphere according to the scenario developed by Schwarzschild (1952)[172] in the context of W Virginis variables. Lines which show this emission are listed in Table 9.10. For higher excitation lines there is only a change in

Molecule	System	λ (Å)	Notes
TiO	Blue-Green(1,0)	5448.3	
TiO	Orange(0,0)	5597.6	
TiO	Orange(3,1)	5615	
ZrO	Yellow(0,0)	5718.1	
TiO	Red (0,1)	6714.4	
		6782	
VO	Red (0,3)	6919.0	
		6950	
TiO	Red (0,0)	7054.5	
TiO	Red (0,0)	7087.9	
TiO	Red (0,0)	7125.6	
TiO	Red (1,1)	7159.0	
VO	Extr. Red (1,0)	7372.4	
TiO	Red (0,1)	7589.6	
TiO	Red (1,2)	7666.4	A-band
TiO	Red (0,1)	7672.1	A-band
TiO	Red (2,3)	7782.8	
TiO	Orange-Red(1,0)	7826	
TiO	Red (2,3)R_c	7828.0	
TiO	Red (3,4)Q_a	7828.0	
TiO	Red (3,4)	7861.0	
TiO	Orange-Red(2,1)	7907	Unres.
TiO	Red (4,5)Q_a	7907.3	Unres.
TiO	Red (3,4)R_c	7907.3	Unres.
TiO	Red	8386	
TiO	Red	8420	
TiO	Orange-Red(0,0)	8432	
TiO	Orange-Red(0,0)	8442	
TiO	Orange-Red(0,0)	8452	
TiO	Orange-Red(1,1)	8495	Ca II
TiO	Orange-Red(1,1)	8516	

Table 9.9: Molecular bands identified in the spectrum of HD 172481. A-band and Ca II in the notes column means that the band is subject to interference from those features. Unres. means unresolved as to which is the main band.

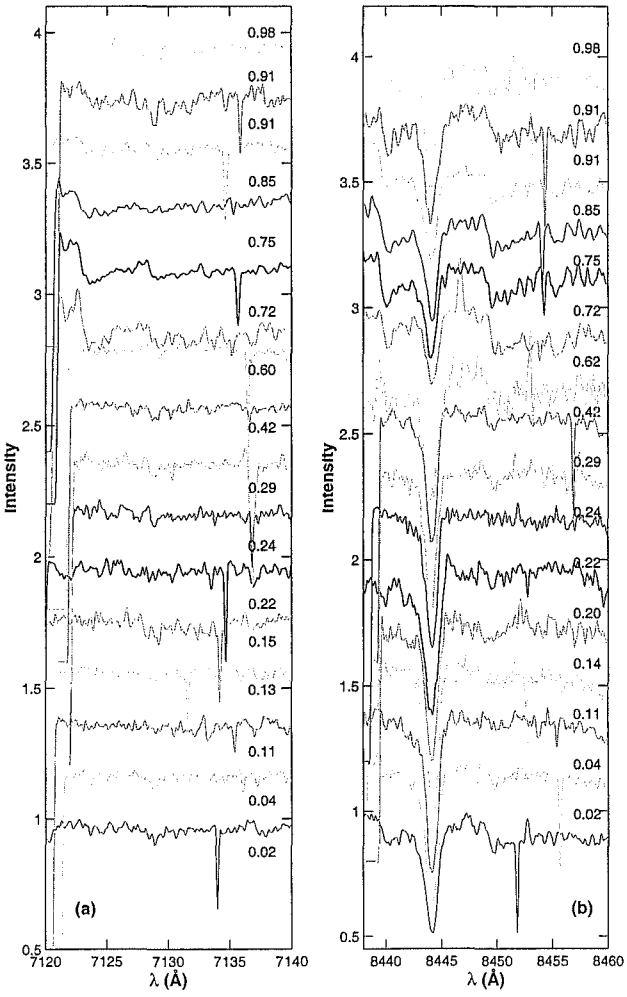

Figure 9.14: Phased variation of two TiO band heads in HD 172481. (a) The λ7125 TiO $\gamma(0,0)$ band. (b) The $\lambda\lambda$8442 and 8452 TiO $\gamma'(0,0)$. The deep persistent feature is from O I at 8446 Å. The narrow absorption feature in both panels is due to the bad row of the detector.

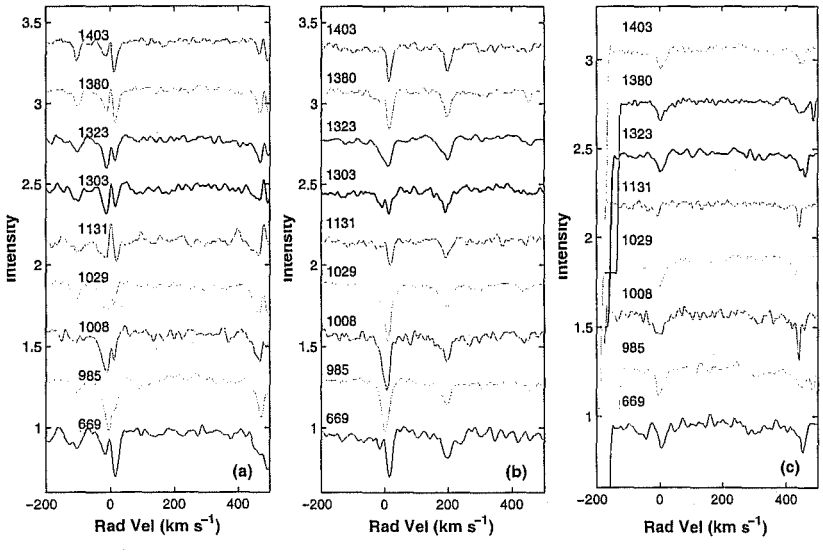

Figure 9.15: Examples of the neutral metal line profiles observed in HD 172481: (a) $\lambda\lambda$5445, 5446 and 5455 Fe I; (b) $\lambda\lambda$5853 Ba II and 5857 Ca I; and (c) λ6708 Li I doublet. The spectra have been red-shifted by +90 km s^{-1} to the mean stellar rest frame.

the strength of the line. This is most prominent in the spectrum taken on HJD 2451131. It would appear that these are linked to the photometry and possible diminishment of the F-star photosphere.

The emission components were examined for radial velocity variations using the interactive FIGARO routine GAUSS. By considering the low excitation Fe I (RMT 15) lines $\lambda\lambda$5446.9 and 5455.6 to be due to two components: one in absorption and the other narrower and in emission, velocity changes were looked for. The absorption components produced mean velocities of -86 ± 2 and -86 ± 3 km s^{-1}. The emission features were slightly blue-shifted with respect to the absorption, to -88 ± 6 and -88 ± 5 km s^{-1}. Within the quoted RMS uncertainties there is no variation in the velocities.

This phenomenon is not due to ballistic motions within the Mira atmosphere. Gillet et al. (1993)[67] observed central emission in a number of neutral metal lines extending into the near infrared for the star S Car. They also found that the emission moved and attributed it to motion of the emitting material within the atmosphere of the star, moving outward with the shock, providing a blue-shifted line and then subsequently in-falling material moving the line to the red. There are several reasons for the neutral metal emission lines not being due to such a phenomenon. First of all the lines are static. Over the course of this programme they have not been seen to change velocity. Second, it is most strongly visible in the spectrum on HJD 2451131 which is when the Mira is quite dim in all the photometric bands. Third, this is not seen in the infrared, where the Mira's imprint on the spectrum is stronger.

Other F-type post-AGB candidates in our programme show exactly this type of stationary emission in low excitation potential neutral metal lines. For example, HD 95767 (§8.4.3) shows permanent stationary emission at 6400 and 6574 Å due to Fe I (RMT 13). This is also seen in HD 108015 in spectra taken during the course of this project.

Observed	Type	Identification			Notes
λ(Å)		Species	λ(Å)	RMT	
5430.5	CE	Fe I	5429.7055	15	E
		Fe I	5429.8394	1062	A
5430.5	CE	Fe I	5434.5315	15	E
5447.8	CE	Fe I	5446.9238	15	
5456.1	CE	Fe I	5455.4666	1145	A
		Fe I	5455.6178	15	A?E
5577.8	IPC	[O I]	5577.350	3F	E, NS
5867	IPC	Ba II	5853.6829	2	
5891	CE	Na I	5889.9661	1	
5897	CE	Na I	5895.9321	1	
6357	E	Fe I	6358.6985	13	E
6363	E	[O I]	6363.776		E, NS
6401	IPC	Fe I	6400.0101	816	?
		Fe I	6400.3240	13	?
6547	IPC	Ti I	6546.2790	102	E
		Fe I	6546.2479	268	A?
6563.2	IPC	H I	6562.8163	1	
6573.9	E	Ca I	6572.7842	1	?
6575	E	Fe I	6574.2325	13	?
6576	E	Ti I	6575.1800		?
6706	E	Li I	6707.76		
6744.1	E	Ti I	6743.1289	48	
	A	S I	6741.2		A
7666	E	K I	7664.9110	1	
7860.5	E	Mol			B
7910.5	E	Fe I	7912.8713	12	
7914.1	E				
7920.6	AE				
8436	CE	Ti I	8434.9718	33	
8437	CE	Ti I	8435.6633	33	
8439.5	PC	Ti I	8436.9279	224	E

Observed λ(Å)	Type	Identification Species	λ(Å)	RMT	Notes
		Fe I	8439.5798	1172	A
8452	E	Ti I	8450.8979	224	B
8458.3	E	Ti I	8457.1		B
8466	E				
8469.5	PC	Fe I	8468.4174	60	?
	??	Ti I	8467.1551	182	?
8497.1	E	Ca II	8498.0524	2	B
8498	CE	Ca II	8498.0524	2	B
8515.2	E	Fe I	8514.0826	60	
8519.6	E	Ti I	8518.3942	150	
		Ti I	8518.0221	182	?
8540.7	E	Ti I	8539.3760		
8543.1	CE	Ca II	8542.1261	2	
8548	E	Ti I	8546.0926	150	

Table 9.10: Identified emission lines for a range of metal lines in the spectrum of HD 172481. The line types are: IPC denoting an inverse P Cygni-like profile; CE central emission; E just emission; night sky lines are designated NS; while B means an uncertain identification due to interference from molecular bands. A and E in the notes mean an absorption and emission component. AE is for lines which show both at different times.

As noted by Giridhar et al. (2001)[68] the λ6708 Li I line shows variation in its shape and equivalent width (see the profile sequence in Figure 9.15c). The profiles vary considerably, with no apparent dependence upon the photometric brightness. Overall it would seem that these are produced by a kind of chromospheric emission which moves with respect to the photospheric spectrum.

9.4.6 λ7774 O I triplet

Two spectra of HD 172481 were acquired from which the equivalent width of the O I 7774 feature was measured. The first, acquired on HJD 2451306, yielded a feature with $W_\lambda = 1.03 \pm 0.05$ Å. This value is subject to a large degree of uncertainty as there is significant interference from molecular bands. From the second spectrum, taken on HJD 2451385 (see Figure 3.3), has a considerably larger equivalent width of 1.62 Å. The placement of the continuum on this date is more certain as the bands have become much less significant. This is not too surprising as the I-band photometry, which

is dominated by the secondary star, is 7.9 on HJD 2451306 and 8.2 on HJD 2451384. A spectral type of F0 for the star implies $(b-y)_o = 0.08$ (Gray 1992)[72] and, coupled with the equivalent width, means an absolute magnitude of -6.8, or a luminosity of $45000L_\odot$. The equivalent width from HJD 2451305 reduces this to -4.4 ($5000L_\odot$). Compared with the estimate of Giridhar et al. (2001))[68] the value from HJD 2451384 is very much in agreement.

9.5 Discussion and conclusion

HD 172481 is an unusual star system, consisting of a metal deficient F-supergiant and a Mira variable. MJUO I-band photometry confirms the $\sim$ 300 d period uncovered by Whitelock & Marang (2001)[213]. Using this period and a simulation of the Mira based on a composite variation, reveal that the sampling of the light curve is responsible for the lack of variation seen in BVR-bands in some seasons. The ratio of the stellar contributions to the V-band was found to be 1:91. Between our first and second observing seasons the F-star increased in brightness by $\Delta V = +0.15$ magnitudes. There is some variability associated with these times, which has a much shorter period and smaller amplitude than for the first section. The V-band periodogram for the whole dataset shows the presence of a group of peaks around 0.01 d^{-1}, that is also present in the V-band periodograms of the other F-type stars. Radial velocity observations with a time resolution of days to weeks do not show large scale variations indicative of pulsations associated with these shorter period variations.

The star also proved to have a variable spectrum. TiO, VO and ZrO bands were seen to correlate with the brightness in the I-band, which measures the contribution of the Mira. There are more of these bands in the red part of the spectrum, where the imprint of the Mira is expected to be stronger. Additional variability was seen in the absorption lines of some neutral metal species, particularly those with low excitation potentials. These lines exhibit an asymmetric line profile, or in the more extreme cases, actually showed the presence of a blue-shifted narrow emission line. A key feature of the emission is that it is static, remaining at the same radial velocity irrespective of what the corresponding absorption is doing. Most likely this is due to a circumstellar shock wave generated by gas slowing down as it encounters slower moving material, perhaps as part of a circumbinary disk.

HD 172481 also displayed a general lack of radial velocity variation. The star has longer term velocity trends but no changes of about $10-20$ km s^{-1}

over time spans of months as seen in other stars in this programme.

Using the λ7774 O I multiplet the estimated stellar luminosity was 45000 $L_{\odot}$. However, this is complicated by the variable strength of the feature, which was smaller when the Mira was brighter. The distance associated with this is 7.9 kpc, using the mean observed visual magnitude and $A_V = 1.5$.

From spectroscopic observations of the sodium D lines there were at least 7 components, which are organized into 2 groups. One of the interstellar group is seen in the spectrum of HD 172440, which is only 474 pc away, indicating that it is due to a foreground cloud. Three of the other lines can be linked to other spiral arms, implying a distance of at least 3.5 kpc.

The mean radial velocity of the star is not consistent with that due to the Galactic disk rotation curve, and given the low metallicity and high radial velocity is probably Galactic halo.

The total visual extinction, 1.5 mag, contains at least 0.5 mag of circumstellar extinction, as the line of sight provides at most 0.9 ± 0.3 mag of interstellar extinction. This is due to 7.1×10^{-5} $M_{\odot}$ of material predicted to exist around the star from the 60 μm flux, at a distance of 250 $R_{\star}$. Associating this with Na D line component 1 implies an expansion velocity of 34 km s^{-1}, and this in turn implies a dynamical age on the order of 45 years for this shell.

Chapter 10

HD 168625 & HD 168607

10.1 Introduction & historical background

Much of the work to date on HD 168625 (see Table 10.1) has assumed that it is part of the open cluster M 17 (= C 1817-162), which also contains the Omega Nebula, and is part of the Sgr OB-1 complex. It has a significant infrared excess and was detected by IRAS as the point source 18184-1623. It is also a variable star (= V4030 Sgr). Coincidentally it lies about 1 arc minute from HD 168607 (= V4029 Sgr), another B-type supergiant also believed to lie near M 17. The two stars are often studied in tandem. In this chapter we present the results of a programme of photometric and spectroscopic observations of HD 168625. A smaller number of similar data were also collected for HD 168607 and we shall contrast and compare the two stars.

Star		HD 168625	HD 168607
Coordinates	α	$18^{\rm h}\ 21^{\rm m}\ 19.46^{\rm s}$	$18^{\rm h}\ 21^{\rm m}\ 14.89^{\rm s}$
(Epoch 2000.0)	δ	$-16°\ 22'\ 26.0''$	$-16°\ 22'\ 31.8''$
Galactic	l	14.98	14.97
coordinates	b	-0.96	-0.94
Mean Brightness	B	9.87	9.60
	V	8.41	8.25
Spectral Type		O+	O+

Table 10.1: Basic parameters of HD 168625 and HD 168607.

Photometric monitoring of the stars was undertaken by Sterken (1977)[178]

and was the start of 27 years of observations (Sterken et al. 1999)[179]. HD 168607 was the more active of the two stars and also showed an increase in brightness of 0.0045 mag yr^{-1} in the Strömgren y-band, with shorter period variability (with periods of 35.7 and 62 d) superimposed on this. HD 168625 showed a slight decrease in brightness over this time period ($\Delta y = -0.0025$ mag yr^{-1}) but no really significant period. They suggested that the 35 d period of HD 168625 found by van Genderen et al. (1992)[195] and van Leeuwen et al. (1998)[197], from Walraven and Hipparcos photometry respectively, is not a long-term feature of the star. van Genderen et al. (1992)[195] also noted that there was no difference between their photometry and that of Hiltner (1956)[83] acquired in the early 1950s, implying that the photometry had been stable over that time.

As well being in a field which contains a great deal of nebulosity associated with M 17 (Hobbs 1961)[84], HD 168625 is surrounded by a fairly complex nebula of its own. This was first described by Hutsemékers et al. (1994)[91]. Nota et al. (1996)[138] imaged the nebula in Hα and $\lambda\lambda$6548 and 6584 [N II] and acquired spectroscopy of the star. The overall morphology was reckoned to be bipolar with the inner nebula ($12'' \times 16''$) surrounded by fainter arcs and loops further out. Hutsemékers et al. (1994)[91] estimated a distance of 2.2 kpc which is consistent with membership of M 17. The dynamical age of the nebula was 3000 years based upon an expansion velocity of 20 ± 2 km s^{-1}. More recently Robberto & Herbst (1998)[163] looked at the star in mid-infrared wavelengths and found it to be surrounded by cold dust at 135 K. However by considering the reddening of the mean stellar model proposed by Nota et al. ($T = 14000$ K, $R_\star = 70 R_\odot$) they revised the distance to the star down to 1.2 kpc. The dynamical age of the nebula at this distance is only 1100 years.

Hutsemékers et al. (1994)[91] also searched for nebulosity around HD 168607 but found nothing, confirming the non-detection by IRAS.

They also pointed out that the spectral type of HD 168625 has varied widely over the last 60 years: from B2 (Popper & Seyfert 1940)[155] through B5.6 (Chentsov & Luud 1989)[34] to B8 (Morgan et al. 1955)[135] (i.e., 17400 to 10100 K using the spectral type-effective temperature calibration of de Jager & Nieuwenhuijzen 1987[41]). The same authors find only a range B8 (11100 K) to B9.4 (10000 K) for HD 168607. Such changes were detected between between May and October of 1995 by Nota et al. In this time the temperature of HD 168625 decreased by 3000 K to 12000 K.

Chentsov & Luud (1989)[34] examined the stars spectroscopically and found that HD 168607 showed P Cygni profiles in Balmer lines down to Hδ, in λ4481 Mg II and the strongest He I lines. They also uncovered Fe

II absorption lines which split into two components. Na D line absorption gives a distance of 1.8 kpc but this is inconsistent with the star as a luminous blue variable star (LBV).

García-Lario et al. (2001)[63] performed an abundance analysis on HD 168625 using a model atmosphere with the parameters $T = 15000$K, $\log g = 2.5$ and $\xi_t = 6$ km s^{-1}. They found a star which was overabundant in N ([N/H]= $+0.5 \pm 0.1$) and Ne ([Ne/H]= $+0.8 \pm 0.2$), had solar O levels ([O/H]= 0.0 ± 0.1) and was slightly underabundant in C ([C/H]= -0.3 ± 0.1). These point to a star which has had the products of CNO burning mixed to the surface but they could not say whether this was as part of its evolution as a high-mass or low-mass star. The N overabundance is consistent with that found for the nebula. Using the Hipparcos parallax and B and V-band photometry they estimate a spectral type of B5II and an absolute magnitude of $M_V = -4.1$.

10.2 Photometry

The photometry of these stars was carried out using the stars listed in Table 10.2. HD 168816 was the comparison, and HD 168521 the check star. A reference check with SIMBAD did not indicate any variability of these stars and the check star had a V-band RMS of 0.019 magnitudes.

Identifier	α(2000.0)	δ(2000.0)	B	V	SpT
HD 168816	$18^{\rm h}\ 22^{\rm m}\ 21.99^{\rm s}$	$-16°\ 04'\ 17.5''$	10.19	8.98	K0/K1III
HD 168521	$18^{\rm h}\ 20^{\rm m}\ 47.98^{\rm s}$	$-16°\ 17'\ 31.0''$	10.8	9.43	K5

Table 10.2: SIMBAD data for the photometry calibration stars of HD 168625 and 168607.

The resulting photometry for HD 168625 (See Table A.6) is displayed in Figures 10.1 and 10.3. Figures 10.2 and 10.4 show the photometry for HD 168607 which is collated in Table A.7. A summary of the $BVRI$ photometry for both stars is presented in Table 10.3. For HD 168625 there are 35 data points spanning 1574 days, while HD 168607 has 34 over the same period.

HD 168625 is a variable with an oscillation which has a peak amplitude of 0.32 magnitudes in B. HD 168607 has a larger amplitude in all of the bands observed and this has the largest amplitude in the I-band.

It is difficult to detect trends in the colour-colour and colour-magnitude plots, but there is a suggestion that both stars are redder in the three main

	B	V	R	I
HD 168625	9.869	8.371	7.487	6.529
Range	0.118	0.118	0.105	0.125
Error	0.003	0.001	0.002	0.002
HD 168607	9.836	8.187	7.180	6.131
Range	0.258	0.267	0.283	0.295
Error	0.007	0.006	0.006	0.005

Table 10.3: The means, ranges and mean errors of the $BVRI$ photometry for HD 168625 (top) and 168607.

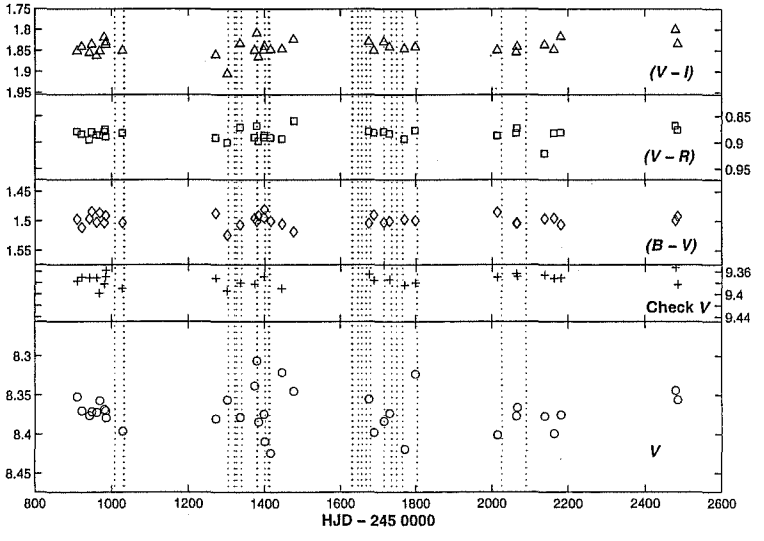

Figure 10.1: V and colour photometry of HD 168625 taken from MJUO. The dotted lines indicate the times when échelle spectra were taken.

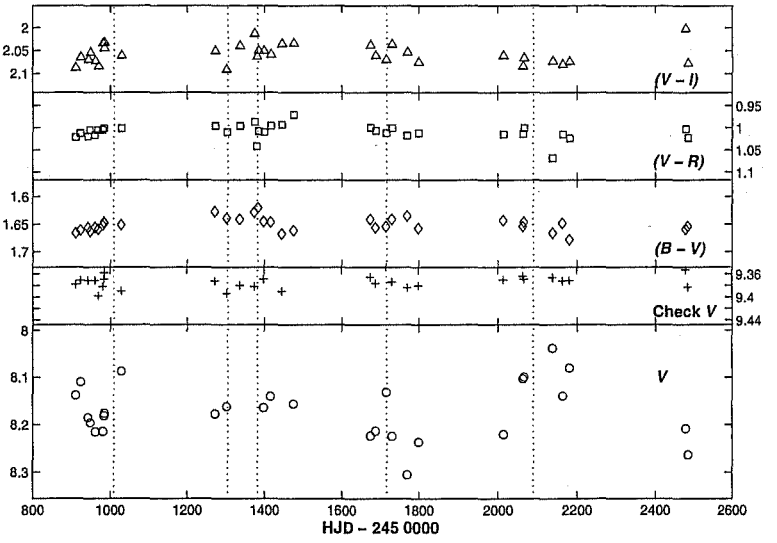

Figure 10.2: V and colour photometry of HD 168607 taken from MJUO. The dotted lines indicate the times when échelle spectra were taken.

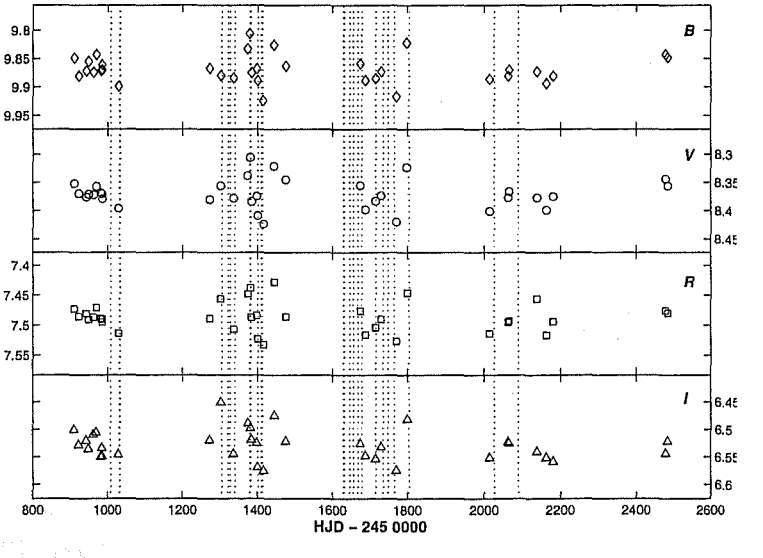

Figure 10.3: $BVRI$ photometry of HD 168625 from MJUO.

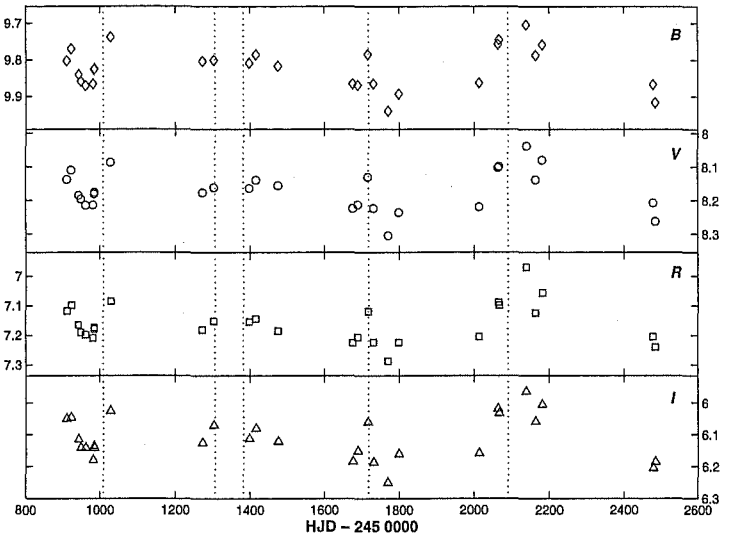

Figure 10.4: $BVRI$ photometry of HD 168607 from MJUO.

colour indices when they are brighter.

10.2.1 Analysis of the photometry

The periodograms for the photometry of HD 168625 are displayed in Figure 10.5 along with a window function with a period of 68.4 d (0.015 d^{-1}). This would appear to be the main period of oscillation in both the V and R-bands and it appears to be present in B and I, but not with the same level of significance. The main peaks in the V-band power spectrum are presented in Table 10.4.

Figure 10.6 shows the Lomb-Scargle periodograms for HD 168607 and the principal peaks in the V-band power spectrum are listed in Table 10.5. 39.6 ± 0.2 d would appear to be the main period of oscillation in both the V and R-bands and it appears to be present in B and I, but not with the same level of significance.

HD 168625 present a cluster of peaks between 180 (0.0056 d^{-1}) and 59 d (0.0169 d^{-1}), the most significant of which is at 68 ± 1 d. This is in contrast to the 35 d period estimated by van Genderen et al. (1992)[195] and van Leeuwen et al. (1998)[197]. However, Sterken et al. (1999)[179] pointed out that this period is probably a temporary feature and it is possible that we are sampling the star when it is no longer present.

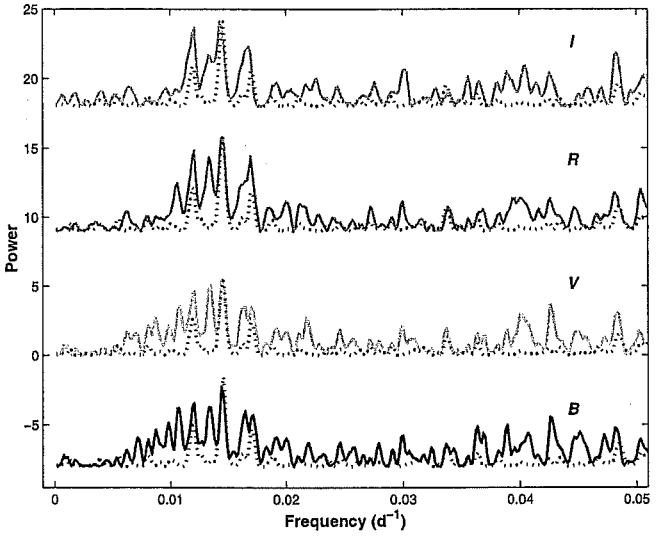

Figure 10.5: Lomb-Scargle periodograms for $BVRI$ photometry of HD 168625. The window function for a 68.4 d (0.0146 d^{-1}) period is shown as a dotted line.

Frequency ($\times 10^{-3}$ d^{-1})	Power	Period (d)	Error (d)
10.64	3.5	94	1
12.07	5.8	83	1
13.34	5.4	75	1
14.61	6.8	68	1
17.00	5.4	59	1

Table 10.4: Peaks in the periodogram for the V-band photometry of HD 168625. The uncertainty in the periods is 0.16×10^{-3} d^{-1}.

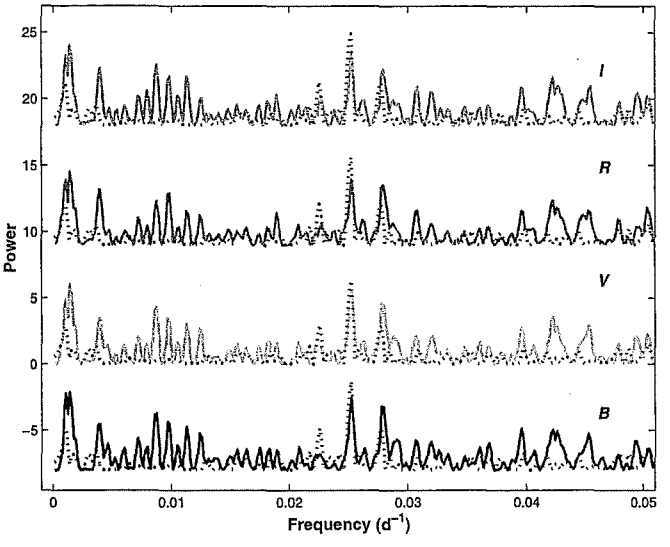

Figure 10.6: Lomb-Scargle periodograms for $BVRI$ photometry of HD 168607. The window function for a 39.6 d (0.0278 d^{-1}) period is shown as a dotted line.

Frequency ($\times 10^{-3}$ d^{-1})	Power	Period (d)	Error (d)
1.43	6.1	700	70
3.97	3.5	250	10
8.74	4.4	114	2
9.69	3.5	103	2
25.26	5.5	39.6	0.2
27.80	4.7	36.0	0.2

Table 10.5: Peaks in the periodogram for the V-band photometry of HD 168607.

The two main peaks found in the photometry of HD 168607 presented in Sterken et al. (1999)[179] were at 62 (0.016 d^{-1}) and 35.7 d (0.028 d^{-1}). There are no significant peaks at the first frequency and two peaks near the latter. Indeed 36.0 d is a match to their period. To account for lack of signal at 62 d it could be possible that this oscillation has diminished in significance during the course of our monitoring, from reasonably significant levels during the 27 years of Sterken's programme. The overlap between the two programmes is about 500 days. Our peak at 700 ± 70 d, within error, matches the 640 d (0.0016 d^{-1}) peak noted by Sterken et al., which they claimed was probably an artefact. It is quite interesting that the same artefact is present in two independent datasets.

10.3 Spectral energy distribution

The SED of HD 168625 presented in Figure 10.7 is derived from the dereddened MJUO *BVRI*, *JHKL* (Manchado et al. 1989)[127] and IRAS photometry. The infrared data is summarized and presented in Table 10.6 along with the *JHKL* photometry of HD 168607 (Whittet & Van Breda 1980)[214]. No IRAS photometry was acquired for this star.

HD 168625	*J*	*H*	*K*	*L*	12	25	60	100
Band	5.08	4.52	4.16	3.71	69.97	325.40	116.90:	583.70
Error	0.01	0.01	0.01	0.01	4.20	13.02	12.86	L

HD 168607	*J*	*H*	*K*	*L*
Band	4.41	3.82	3.39	2.99
Error	0.01	0.01	0.01	0.01

Table 10.6: Summary of the infrared photometry compiled for HD 168625 and HD 168607. The 100 μm flux is an upper limit as indicated by the L.

An assumed spectral type of B5 implies a total visual extinction $A_V = 4.9$, from a colour excess $E(B-V) = 1.6$, for HD 168625, which implies that the star would be visible to the naked eye if not for the dust in the line of sight. Interstellar extinction in the direction of HD 168625 increases steadily, reaching 4.8 ± 0.9 magnitudes at 3.6 kpc (Hakkila et al. 1997)[75]. Working backwards from this distance and extinction assuming that it is entirely due to interstellar material places the upper limit to the absolute magnitude for the star of $M_V = -9.3$, which is consistent with the interpretation of the star as a hypergiant. At supergiant luminosities ($M_V = -6.2$) the distance

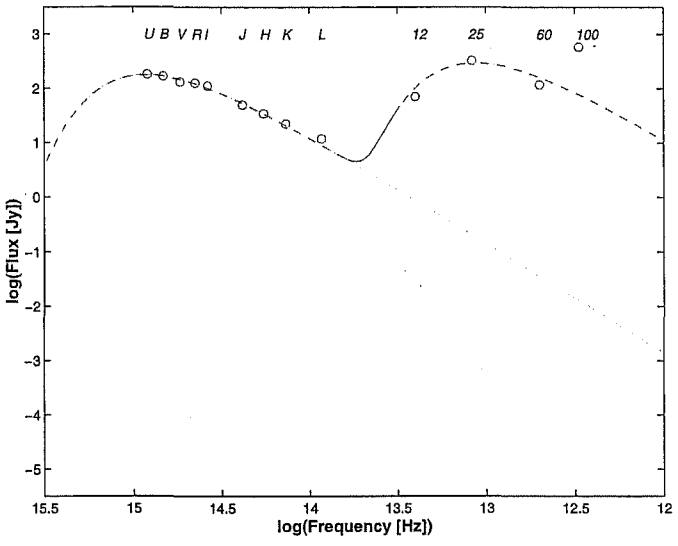

Figure 10.7: The SED for HD 168625 constructed from the mean $BVRI$ photometry, plus one off measures in U and $JHKL$ and IRAS photometry. The temperatures of the fitted curves are 14300 and 190 K.

to the star is 960 pc, or just 380 pc if we adopt post-AGB star luminosities. This also has the effect of requiring a considerable amount of extinction due to circumstellar material as the interstellar environment produces between 0.4 ± 0.3 to 1.2 ± 0.5 magnitudes of extinction.

The estimated stellar temperature is 13500 K from the fitted blackbody temperature of 14300 K. The dust is best fitted by a curve at 190 K, neglecting the 100 μm photometry which is rather uncertain. The RMS error on these fits is 0.08.

The anomalous value of the 100 μm point could be due to interstellar cirrus or to an old cold dust shell from a previous mass loss episode. The mass of the circumstellar envelope predicted from the 60 μm flux ranges from $5.2 \times 10^{-4} M_{\odot}$ at 400 pc to $4.2 \times 10^{-2} M_{\odot}$ at 3.6 kpc, with a radius of 2500 $R_{\star}$.

HD 168607 has a higher level of total visual extinction, $A_V = 5.1$, which is the predicted extinction from the ISM at 3.7 kpc. Only one blackbody is required to fit the SED and the derived stellar temperature is 11600 K. The star would have to be extremely luminous, $M_V = -9.1$, to produce the observed m_V. For supergiant luminosities, HD 168607 would have a distance of 1.7 kpc. This however means that there is only 2.0 ± 0.6 magnitudes of inter-

stellar extinction, requiring a considerable circumstellar contribution from a star which lacks an infrared excess. It is quite interesting that HD 168607 has been observed with prominent P Cygni profiles in a number of lines for many years, indicating strong, persistent mass loss, but does not have any indications of circumstellar material.

10.4 Spectroscopy

As one would expect from a B-type star, the spectrum of HD 168625 is relatively featureless. However it does display some absorption lines, including DIBs, and emission from Hα and $\lambda\lambda$ 6548 and 6584 [N II]. This is also visible in our échelle spectra as emission extending from the stellar spectrum (see §10.4.5). During the course of this programme 24 high resolution spectra of HD 168625 were acquired, which will be discussed below.

For HD 168607 only 5 spectra were obtained. The main feature of these is a large P Cygni profile in Hα. Emission is also observed in the lines of certain Fe II multiplets. Indeed, the emission patterns are similar to those observed in LBVs.

10.4.1 Radial velocities

Radial velocities for HD 168625 were obtained from various absorption lines observed in the spectra. Some of the radial velocity curves are displayed in Figure 10.8 and summarized in Table 10.7. The λ6582 C II line was not deemed to be useful due to interference from λ6584 [N II] emission.

λ_o (Å)	6347	6371	5453	5875	6578
Species	Si II	Si II	S II	He I	C II
χ (eV)	8.12	8.12	13.67	20.96	20.70
n	17	19	13	23	21
μ_{rv} (km s^{-1})	3.78	3.88	9.04	15.05	11.03
σ_{rv} (km s^{-1})	4.83	4.76	3.10	3.59	3.89
Δ_{rv} (km s^{-1})	0.75	0.73	1.08	0.56	0.66

Table 10.7: Summary of the radial velocity for five lines in HD 168625. μ_{rv} is the mean velocity, σ_{rv} is the standard deviation, and Δ_{rv} is the mean error, all in km s^{-1}. n is the number of measures.

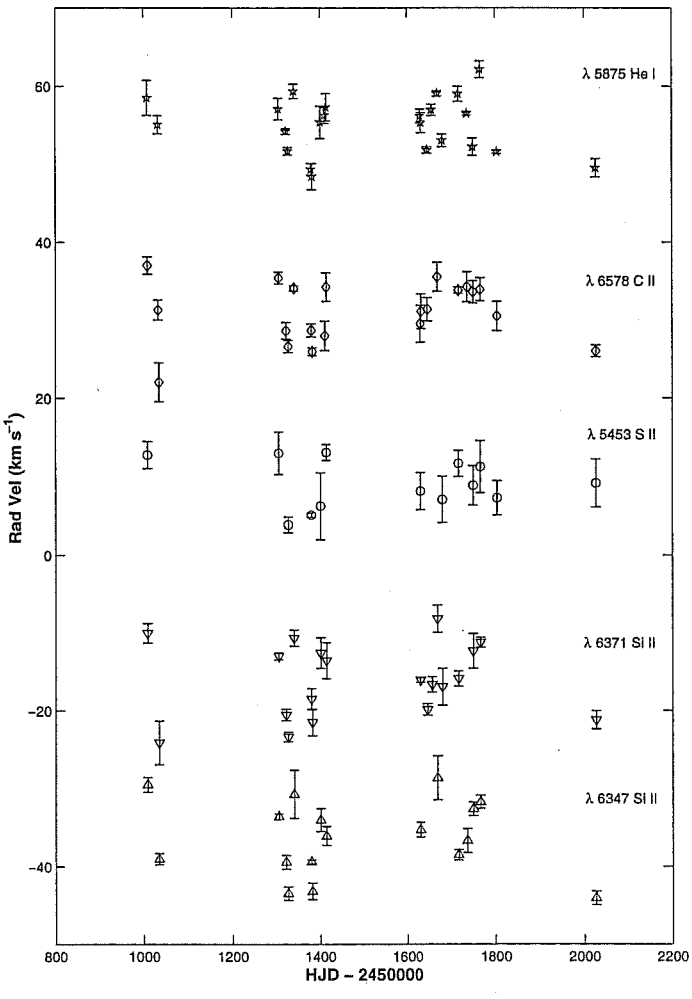

Figure 10.8: The radial velocity variation for five lines in the spectrum of HD 168625. The λ5453 S II lines are shown at the correct heliocentric velocity while the other groups have been shifted by $\pm$20 or $\pm$40 km s^{-1}.

There is a gradient observed in the lines of HD 168625. The lines with higher excitation potentials have greater red-shifts. This is due to an expanding atmosphere, in which the different layers are moving away from the central star at greater velocities further out. The mean velocities of the lines and the range of velocities they are subject to is very similar to those observed in CPD-59 6723 (see §11.4.1), although the circumstellar environment is quite different for HD 168625. HD 168607 shows the same pattern, with a slightly greater range. For example the difference between the mean velocities of the λ5875 He I ($\chi = 20.96$ eV) line and the λ6347 Si II ($\chi = 8.12$ eV) line is 18.8 km s^{-1} in HD 168607 and 11.3 km s^{-1} in HD 168625. The velocities of the absorption lines are quite variable, having ranges of 10 to 15 km s^{-1}.

A periodogram analysis (Figure 10.9) of the radial velocities for HD 168625 did not uncover a clear period although there is a peak at 0.0400 d^{-1}, or 25.0 ± 0.2 d^{-1} in the periodograms, most clearly visible for λ5875 He I.

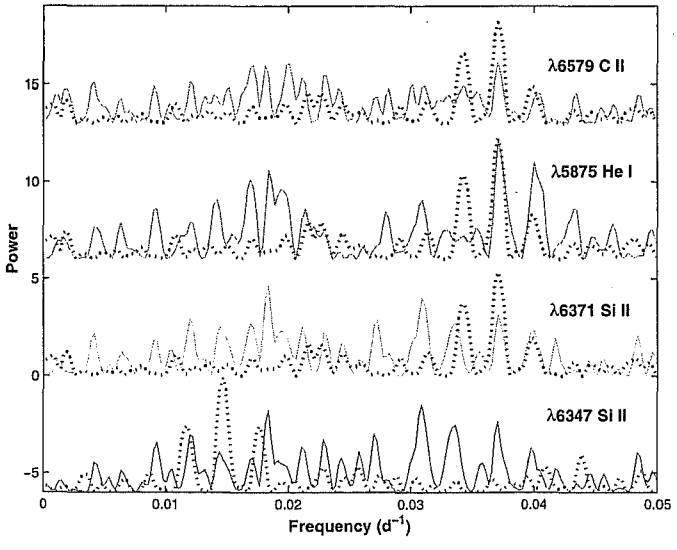

Figure 10.9: Periodograms of the radial velocity variations of some lines in the spectrum of HD 168625.

10.4.2 Hα Profile

The profiles of the Hα lines for both stars are quite striking, showing considerable amounts of emission. HD 168607 (Figure 10.12) shows a well de-

veloped P Cygni profile at all times which varies only slightly over time. For HD 168625 the profile is made up of many components which vary in intensity. Large profile changes are observed on weekly timescales. For example, the nights labelled 1630 and 1632 in Figure 10.10a clearly show a prominent blue-shifted absorption feature, but in the spectrum 14 nights later it has disappeared and the emission component has grown. Smaller changes are also visible between spectra taken a couple of nights apart, as can be seen in the increase in Hα emission from the spectrum of HJD 2451411 and to that of HJD 2451414.

In general there seem to be four main components in the Hα profile as can be seen in Figure 10.11:

1. Blue-shifted absorption profile.
2. Blue-shifted emission.
3. Emission associated with the extended (nebula) emission.
4. Higher velocity red-shifted emission.

From Figure 10.10 we can see that all of these features are variable in strength. It should also be noted that emission features 3 and 4 appear to consist of two further emission peaks separated by 25 and 27 km s^{-1} respectively. It is possible that there is even more structure than this but the resolution of the observations is not sufficient to investigate this further. From §10.4.5 it is clear that the circumstellar lines are single peaked.

In some of the spectra of HD 168625 the Hα profile presents a detectable blue-shifted absorption feature in addition to the emission. Table 10.8 presents the velocities of the most blue-shifted point of this component. This point marks the maximum outward velocity of the expanding shell of material responsible for the absorption. The derived velocities are subject to uncertainties in the placement of the continuum and also to the variable presence of some telluric lines. The telluric lines are on the order of 20 km s^{-1} wide at the continuum, and combined with the uncertainty on the position of the continuum itself, the estimated an error is about $\pm$40 km s^{-1} on the absolute values of the velocities. However the relative positions are reasonably secure.

There is the possibility that there are discrete absorption components, or DACs, in the Hα profile. These have been observed in a number of LBV stars and also in a variety of lines in the stellar spectra (Markova 2000)[128]. But the time resolution of the spectra is not sufficient to follow the motion of such features through the atmosphere.

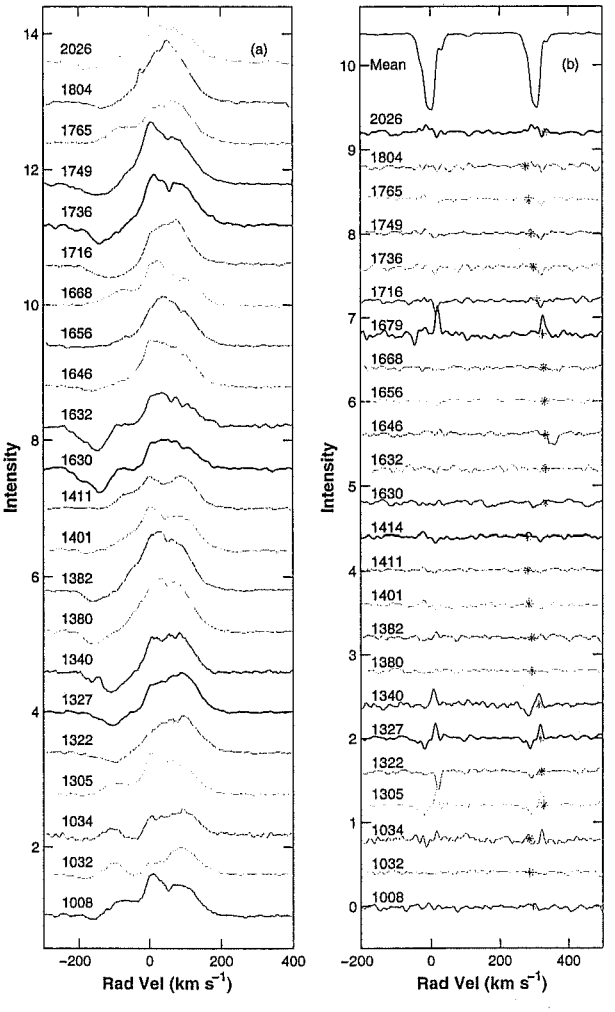

Figure 10.10: The variations of (a) Hα profile and (b) the residual Na D lines of HD 168625. The spectra are labelled with the Heliocentric Julian Date (-2450000) of observation. The asterisk in (b) marks the position of terrestrial features in the Na D_1 profile.

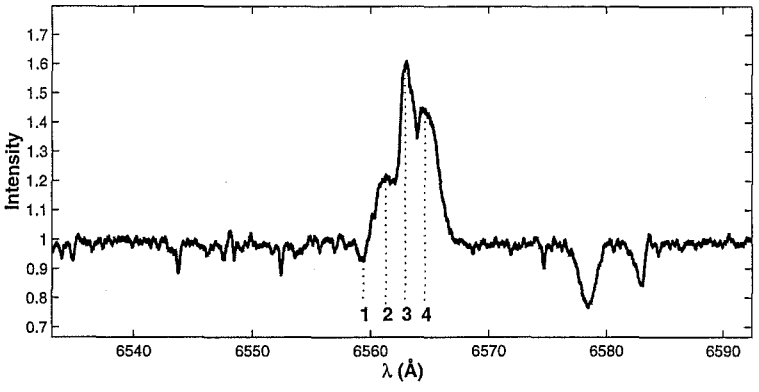

Figure 10.11: Features of the Hα lines of HD 168625 as listed in the text.

HJD - 2450000	λ (Å)	Rad Vel (km s^{-1})
1008	6586.201	−192
1032	6574.423	−245
1034	6573.730	−249
1305	6579.966	−220
1322	6577.768	−219
1327	6579.316	−220
1340	6584.735	−196
1380	6582.025	−223
1382	6580.477	−224
1630	6572.426	−249
1632	6574.987	−241
1716	6585.232	−196
1736	6574.134	−238
1804	6575.841	−216
2026	6569.865	−266
Mean	6578.100	−226
σ	4.998	22

Table 10.8: Blue limit of the absorption feature in the Hα profile of HD 168625.

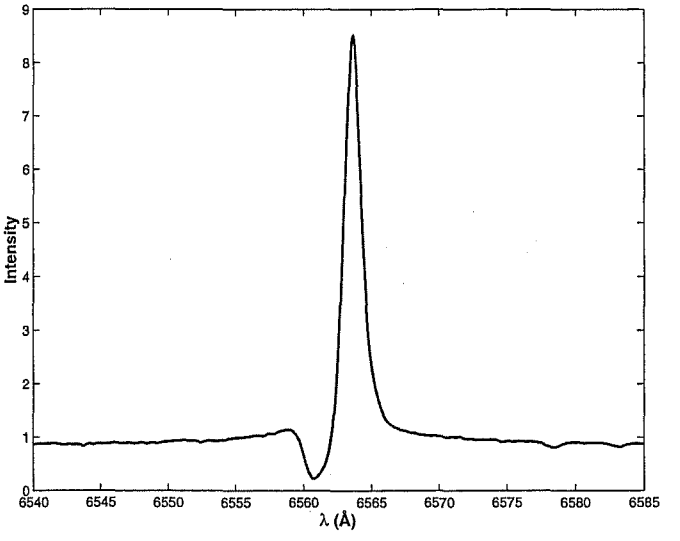

Figure 10.12: Hα profile of HD 168607.

HD 168607 presents a prominent P Cygni profile in Hα in all of our spectra. The emission wings extend out to about $\pm$800 km s^{-1}. There are three signs of variability. The first is the main emission peak in the spectrum of HJD 2452026 which is about 20% larger than for the previous spectrum acquired on HJD 2451737. Another variable feature appears to be in the blue-shifted absorption, where there may be a discrete absorption in the spectra HJD 2451305 and 2451632 near 6560Å.

10.4.3 Sodium D Lines

The Na D line structure for both HD 168625 and 168607 have a much in common. Both sets show very little variation over time (see Figure 10.10b, for HD 168625) and have a number of components in common.

From higher resolution HERCULES spectra of the Na D lines on HJD 2452090 we have measured up to five Gaussian components listed in Table 10.9. The heliocentric correction was +1.3 km s^{-1} and the systemic velocities are $+18\pm2$ km s^{-1} (HD 168625) and $+32\pm$ km s^{-1} (HD 168607) taken from four lines. The radial velocities of HD 168607 are complicated by the appearance of inverse P Cygni profiles in a number of lines, and other lines which are more red-shifted when compared with the average of their velocities from our échelle spectra. These indicate an influx of matter onto the

	HD 168625				HD 168607			
#	λ (Å)	W (Å)	Rad Vel (km s^{-1})	Notes	λ (Å)	W (Å)	Rad Vel (km s^{-1})	Notes
1	5889.377	0.076	-30.0		5889.405	0.096	-28.6	
2	5889.763	0.342	-10.3	IS? + NS?	5889.777	0.270	-9.6	IS? + NS?
3	5890.116	0.301	7.6	IS? + NS?	5890.110	0.378	7.3	IS? + NS?
4	5890.604	0.063	32.5		5890.554	0.018	29.9	PS
5					5890.792	0.024	42.0	
1	5895.354	0.049	-29.4		5895.385	0.063	-27.8	
2	5895.756	0.309	-9.0	IS? + NS?	5895.759	0.230	-8.8	IS? + NS?
3	5896.084	0.273	7.7	IS? + NS?	5896.068	0.349	6.9	IS? + NS?
4	5896.585	0.043	33.2		5896.462	0.009	26.9	PS
5					5896.710	0.019	39.6	

Table 10.9: The components of the Na D lines of HD 168625 and HD 168607 determined from HERCULES spectra taken on the night of HJD 2452090. See Figure 10.13 for identifications. In the notes IS is a contraction of interstellar, NS for night sky, PS photospheric. ? denotes an uncertain designation.

star and are thus not representative of the stars motion through space, and they could account for components 4 and 5. RMS errors on the Gaussian fits are approximately 0.01 Å. There is a possibility that components 2 and 3 are in fact part of a single large absorption bisected by a night sky emission line, but on the basis of the one spectrum there is no way of verifying this. A second spectrum taken at a different time of year is needed to settle this matter. In either case the two stars have very similar Na D lines profiles.

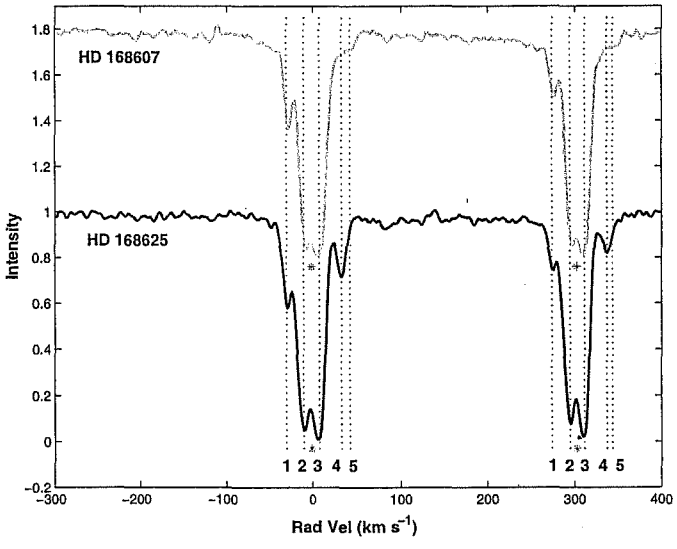

Figure 10.13: Na D line profile for HD 168625 and HD 168607. These normalized HERCULES spectra were taken on the night of HJD 2452090. The components are labelled according to Table 10.9. The asterisk marks the position of any night sky lines.

By comparing the Na D lines profiles of HD 168625 and 168607, shown Figure 10.13, the fact that components 1,2 and 3 have the same shape and positions in both stars suggests a common origin, most likely from interstellar space. Component 4 however is much more clearly defined in HD 168625 and this may be a feature native to this star.

A spectrum in the blue échelle region was acquired on HJD 2451384 for HD 168625. It shows narrow Ca II H and K lines (FWHM = 0.74 Å for the K line) with radial velocities of -8.38 and -9.16 km s^{-1} respectively. This would seem to suggest that the component 2 is interstellar. However, synthetic spectra based on the models listed in the introduction to this chapter produce quite distinctive H and K lines, and as seen in Table 10.7,

lines formed by lower extinction potential multiplets have greater blue-shifts due to the expanding nature of the atmosphere. So it is more likely that these are seeing stellar H and K lines, not interstellar ones at these velocities. Follow up observations are needed to see whether these lines are as variable as the other stellar lines to confirm this.

For the given Galactic coordinates of this star the line of sight will intersect the Sagittarius arm at a distance of 1.9 kpc ($z = -32$ pc) and also for the cloud to have a radial velocity of about +8 km s^{-1}. The stellar velocity due to Galactic rotation will vary from -7.5 km s^{-1} at 412 pc, through +0.5 km s^{-1} at 1.2 kpc to +29.5 km s^{-1} at 3.6 kpc. At the distance predicted for M 17, 2.2 kpc, the radial velocity is +11 km s^{-1}, which is very close to the systemic velocities of the two stars.

10.4.4 Diffuse interstellar bands

A number of diffuse interstellar bands are visible in the spectra of both HD 168625 and 168607. In Table 10.10 is a list of these lines along with their equivalent width, estimated colour excess and the radial velocity. The colour excesses are calculated from the equivalent width-colour excess relations given in Jenniskens & Désert (1994)[95]. Note that HD 168607 has not been observed in either the "blue" or "red minus" spectral regions and so the number of DIBs identified in its spectrum is lower.

Despite the large scatter in the estimated colour excesses, the most interesting feature about the DIBs observed in the spectra of these two stars is that they are very similar, to the point that the equivalent widths of the bands are the same to within a few hundredths of an angstrom. Even the Na D line structure is largely the same. This indicates a similar distance for the stars. If one was significantly further away then one would expect to find that the strength of the DIBs would be greater, due to the increased amount of the carrier material along the line of sight. The very small Galactic latitude is such that the line of sight will remain in the thin disk for about 15 kpc.

Consequently the derived colour excesses are also quite similar. There are two incongruous values from lines at 6270 and 6376 Å. The latter may be blended with an unidentified stellar feature. Ignoring these then the derived colour excess and associated errors translate to visual extinctions of 5.7 ± 1.0, which within error agree with the extinctions derived in §10.3. This is strongly suggestive of the reddenings being entirely due to interstellar material.

Some of the radial velocities are inconsistent. Apart from λ5780, which

λ (Å)	HD 168625				HD 168607			
	W (Å)	$E(B-V)$	$\Delta E(B-V)$	Rad Vel (km s^{-1})	W (Å)	$E(B-V)$	$\Delta E(B-V)$	Rad Vel (km s^{-1})
4428.88	5.15	2.31	0.62	5.9	5.34	2.39	0.64	15.3
5780.59	0.95	1.64	–	15.7				
5849.78	0.10	2.08	0.35	4.43	0.15	3.12	0.52	8.3
6196.19	0.10	1.64	0.13	−4.5	0.09	1.48	0.12	−3.2
6203.19	0.12	1.12	0.17	−5.8	0.10	0.93	0.14	−4.4
6270.06	0.08	1.05	0.26	−12.6	0.07	0.92	0.23	−12.5
6270.36	0.27	4.43	1.16	−14.7	0.26	4.26	1.12	−4.6
6376.07	0.10	3.85	0.74	4.0	0.10	3.85	0.74	6.5
6379.27	0.19	2.44	0.75	6.5	0.15	1.92	0.59	6.7
6993.18	0.18	1.55	0.27	3.1	0.15	1.29	0.22	2.4
Mean		2.26	0.44	0.2		2.24	0.48	1.6
σ		1.07	0.34	9.4		1.25	0.33	8.5

Table 10.10: Properties from DIBs observed in the spectrum of HD 168625 and HD 168607. λ is the rest wavelength, W the equivalent width, $E(B-V)$ and $\Delta E(B-V)$ are the derived colour excess and uncertainty. Blanks indicate an unobserved feature.

has a high radial velocity due to a pronounced asymmetry to the red, they fall into two main camps: $\lambda\lambda$4428.88, 5849.78, 6376.07, 6379.27 and 6993.18 which have a slight red-shift, and $\lambda\lambda$6196.19, 6203.19, 6270.06 and 6270.36, which are blue-shifted.

10.4.5 Nebular spectra

The nebula imaged in Hutsemékers et al. (1994)[91], Nota et al. (1996)[138] and Robberto & Herbst (1998)[163] is also visible in our long slit échelle spectra due to various extended emission lines, especially Hα and $\lambda\lambda$6548 and 6584 [N II]. Other visible lines include $\lambda\lambda$6717 and 6731 [S II], $\lambda\lambda$7377 and 7411 [Ni II] and 8446 O I. A sample spectrum image (from HJD 2452026) is displayed in Figure 10.14.

The majority of the extended emission lines are so weak that they are not very visible in the extracted stellar spectra, the notable exception being the Hα profile, although most of the emission in this line is due to a variable stellar wind. The [N II] features in the same order are visible in some spectra but are subject to strong interference from telluric lines ($\lambda\lambda$6548) or the $\lambda\lambda$6582 C II line ($\lambda\lambda$6584).

The échelle is set up so that the slit lies on the east-west line. It has an angular resolution of 0.345″ per pixel. Thus the Hα lines which extend 17$\pm$2 pixels from the centre of the stellar spectrum is from a region 5.9$\pm$0.7″ across east to west. This is approximately equivalent to the region of Hα emission found by Nota et al. (1996)[138].

To probe the structure of the material responsible for these lines, spectra were extracted from beside the stellar spectrum. The lines in Figure 10.15 are single peaked and have a low S/N. Both sides of the stellar spectrum were extracted in this way, but there is no conclusive evidence of an east-west velocity gradient or temporal changes. The radial velocity of the Hα and [N II] lines on both sides of the stellar spectrum is about 4.5 km s^{-1}.

Again this compares well with the nebula spectra obtained by Nota et al. with the slit oriented east-west which also show single peaks but they don't give a radial velocity.

No extended emission is found around HD 168607 in our high resolution spectra.

10.5 Discussion

Hipparcos also obtained parallaxes for both stars: 2.02 $\pm$ 1.16 mas for HD 168607 (HIP 89956) and 2.43 $\pm$ 1.20 mas for HD 168625 (HIP 89963). The

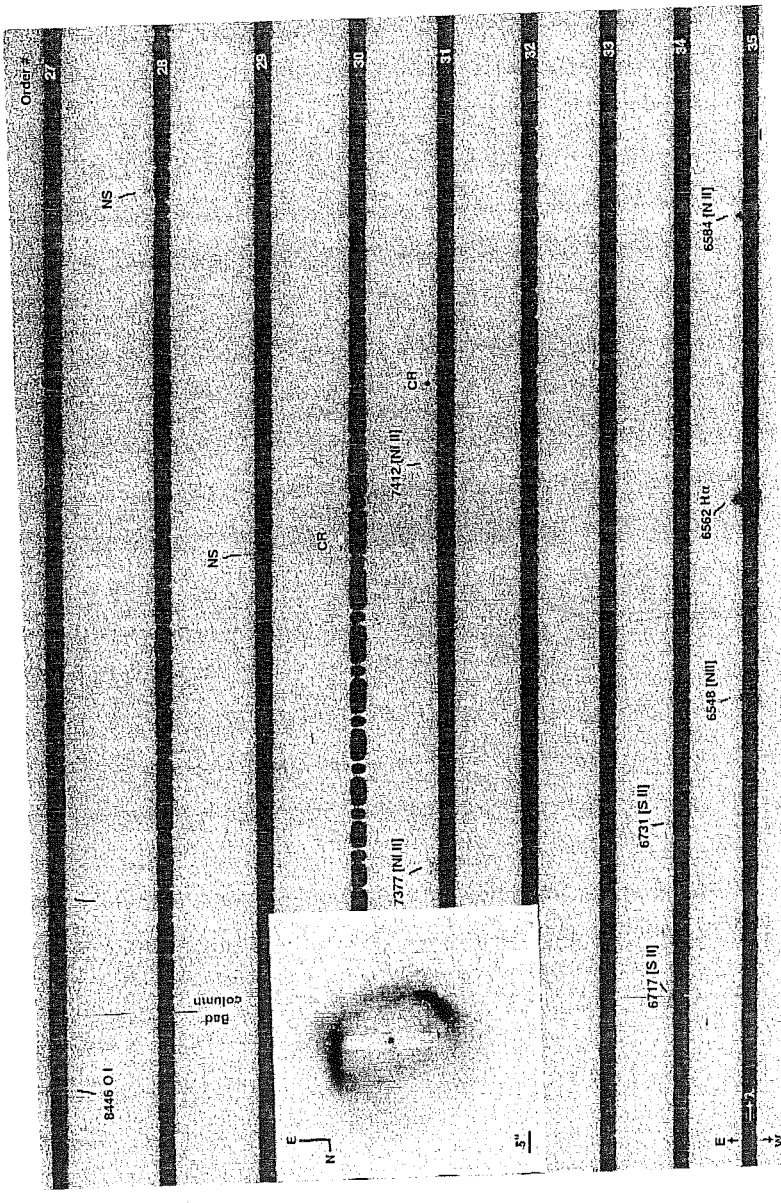

Figure 10.14: Extended emission lines in the spectrum of HD 168625. CR denotes cosmic ray, NS night sky emission lines. The insert shows Figure 2 from Robberto & Herbst (1998)[163] with the lighter area denoting the échelle slit position.

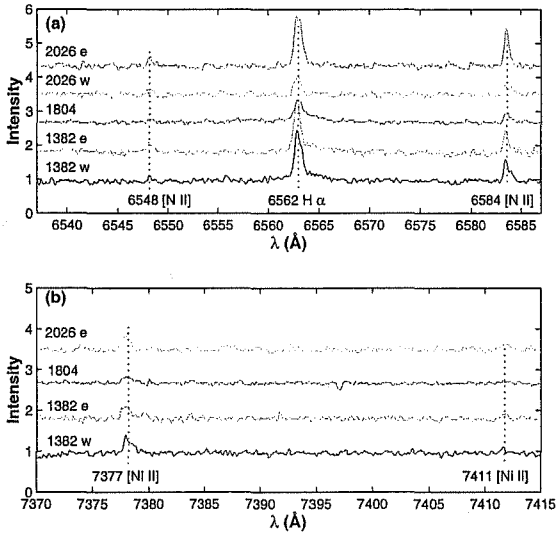

Figure 10.15: Extracted nebular spectrum of HD 168625. The top panel is the region around Hα and the bottom is the spectrum near the [Ni II] emission. The spectra are labelled with the HJD (-245000), **e** denotes from east of the star **w** west. 1804 combines both east and west sides.

corresponding distances range from 315 to 1162 pc with an estimate of 495 pc for HD 168607 and 276 to 813 pc with a mean of 412 pc for HD 168625. These results are at odds with the 2.2 kpc estimated for the stars as part of M 17. The dynamics of the nebula would have to be revised from a dynamic age of $\sim 1 - 3 \times 10^3$ years to around 600 years (585 years at 411.25 pc at 20 km s^{-1}) if the Hipparcos parallaxes are correct. However it is possible that the nebulosity around HD 168625 may also affect the Hipparcos parallax, as it gives the star a finite angular extent and thus the measurement of its position may not be as accurate.

Their proper motions are slightly different but quite uncertain. For HD 168625 (μ_α, μ_δ) = (0.95 ± 1.23, $+0.04 \pm 0.84$) mas, and for HD 168607 (μ_α, μ_δ) = (1.18 ± 1.24, -1.16 ± 0.81) mas. The size of the errors is such that within the uncertainties the proper motions are the same. Definitive parallaxes and proper motions will have to wait until higher precision astrometry is available.

There is an interesting point in Pasquali et al. (2002)[148] regarding the spectra acquired of HD 168625 they acquired in 1995 and 1999. They claim to have found discrete absorption components which are very much narrower than the other absorption lines in the spectrum (FWHM of 10 km s^{-1} compared to 69 km s^{-1}). In Figure 10.16 is shown an MJUO spectrum of HD 168625 around Hα which bears a striking resemblence that to their Figure 9. Below this is a synthetic telluric spectrum which has been broadened using the instrumental profile and shifted to compensate for the heliocentric radial velocity correction (-25.4 km s^{-1}). The dashed lines indicate those lines identified in Pasquali et al. as metal lines from a shell ejection. The alignment of the synthetic spectrum and our stellar spectrum is very good, in both the positions of the narrow lines and also in their relative strengths. Further than this, the radial velocities of the narrow features during the course of our programme clearly show an annual variation consistent with the changing heliocentric correction.

The majority of the lines in the telluric spectrum are due to water vapour, which unlike O_2, is a variable constituent of the atmosphere. Thus it is possible for the discrete absorptions to be present in one spectrum and absent in another. That their two spectra which show these narrow lines also have a P Cygni profile for Hα is most likely a coincidence. Given the variability of the absorption component of the Hα feature, HD 168625 is undergoing variable mass loss, but these narrow lines are not part of this behaviour.

The blue limit of the absorption variable feature in Hα, which is part of a P Cygni profile, is considerably larger than for CPD-59 6723. Indeed it

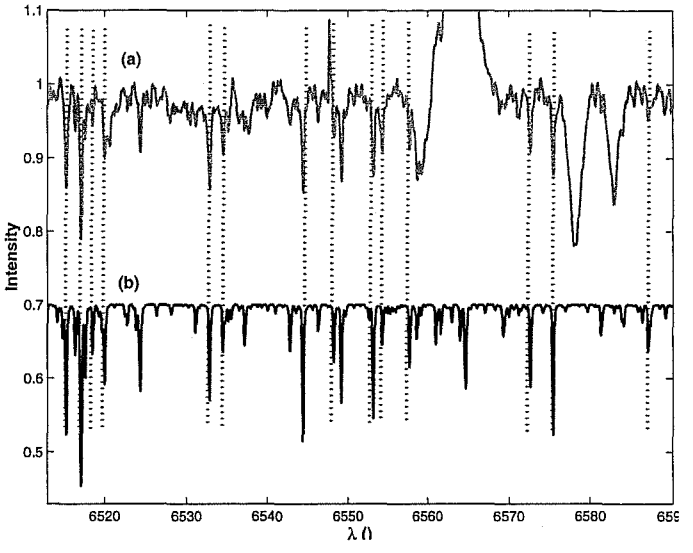

Figure 10.16: (a) HD 168625 order 35 compared with (b) a synthetic telluric spectrum. The vertical dotted lines represent lines identified by Pasqualli et al. (2002).

is more consistent with those observed in HR Carinae and other luminous blue variables.

10.6 Conclusions

MJUO photometry found that HD 168607 is the more variable of the two stars, with a peak amplitude of 0.317 magnitudes in R. HD 168625 has its largest variation in the B and V-bands. The observed periods were 35.4 and 67.3 days respectively.

From the spectral energy distributions the stellar temperatures were 13500 (HD 168625) and 11000 K (HD 168607), with an additional cool dust component around HD 168625 at 190 K. Estimates of the reddening are consistent with being due to the ISM if the stars are both hypergiants. The mass of circumstellar material around HD 168625 was estimated at $4.2 \times 10^{-2} M_{\odot}$ at a distance 3.6 kpc. This material has a radius 2500 $R_{\star}$ Neither star showed evidence of hot dust.

The radial velocities showed variability and gradients within the atmospheres of both stars. No clear period was found. HD 168625 has a variable

Hα profile which consists of four main components. HD 168607 displays a P Cygni profile at all times, but does show subtle deviations from this. No narrow metal absorption lines were found during periods when HD 168625 showed a P Cygni profile in Hα, as indicated by Pasquali et al. (2002)[148]. There are hints of DACs in the Hα line profile of HD 168625, but the time resolution of our observations was not enough to confirm this.

The Na D lines and DIBs proved to be virtually identical, which rather suggests that the stars do in fact lie at the same distance. The interstellar extinction derived from the diffuse interstellar bands for both stars was was 5.7 ± 1.0 mag, and is consistent with the values derived in §10.3.

Extended emission spectra did not clearly indicate the presence of any structure or asymmetry but rather maintained a radial velocity of 4.5 km s^{-1} on the east and west sides of the spectra. There was also no indication of structure from either Hα or the two [N II] lines.

Chapter 11

CPD-59 6723

11.1 Introduction

Over the last 20 years CPD-59 6723 (= SAO 243756 = IRAS 16206-5956, see Table 11.1) has undergone a significant spectral shift. Spectroscopic and photometric observations acquired in the late 1960's and early 1970's showed a 10th magnitude star with weak Hβ absorption (Hill et al. 1974)[82]. But Oudmiajer (1996)[144] reported that the star showed significant emission at Hβ by the early nineties.

Coordinates	α	$16^{\rm h}\ 25^{\rm m}\ 02.61^{\rm s}$
(Epoch 2000.0)	δ	$-60°\ 03'\ 32.3''$
Galactic	l	326.77
coordinates	b	-7.49
Mean Brightness	B	10.13
	V	9.89
Spectral Type		A3Iab:e

Table 11.1: Basic parameters of CPD-59 6723.

Most of the work done on this star has been photometric, often supplemented with spectral typing. The results of some of these programmes are shown in Table 11.2.

Kozok (1985)[108] used UBV photometry in conjunction with intrinsic star colours and a mean Galactic reddening law to derive a distance to the star of 1.02 kpc, assuming the star to be a giant with $M_V = -1.77$ and $E(B-V) = 0.47$. Kilkenny & Hill (1975)[104] obtained spectra and derived

V	$(B-V)$	$(U-B)$	Spectral Type	Reference
9.75	0.30	−0.22	B5p	Hill et al (1974)[82]
9.74				Kilkenny et al. (1975)[105]
9.79	0.31	−0.17	A3Iab:	Humphreys (1975)[89]
9.94	0.32	−0.14	A0Iae	Schild et al. (1983a)[168]
9.79	0.32	−0.26		Kozok (1985)[108]

Table 11.2: Previous photometric studies and spectral typing of CPD-59 6723.

a stellar radial velocity of -9 ± 3 km s^{-1}. They also measured the average velocity of the Ca II H and K lines to be -19 ± 5 km s^{-1}.

Oudmaijer (1996)[144] searched for hot post-AGB stars in the IRAS point source catalogue. CPD-59 6723 did not show extended emission in any of the IRAS photometric bands. However he fitted synthetic spectra to the UV, optical, and near infrared photometry obtaining $T = 11000$ K and $\log g = 2.0$. If the star is assumed to be a massive supergiant then it lies at 14.9 kpc from the Sun, and 1.9 kpc below the Galactic plane. This is over 16 times the 120 pc scale height for massive supergiants (Mihalas & Binney 1981)[130]. Additionally he tried to fit the IRAS photometry but was not very successful due to the star's rather low 12:25 μm ratio. The derived parameters assumed a distance of 1 kpc and a mass loss rate of 5.1×10^{-9} $M_{\odot}$ yr^{-1}, and a total dust mass of 8.2×10^{-5} $M_{\odot}$ at a distance of 39000 to 50000 $R_{\star}$ from the star.

Venn et al. (1998)[205] followed this up with a single spectrum that they analysed for abundances. They used model parameters of $T = 8500 \pm 200$K, $\log g = 0.9 \pm 0.2$ and $\xi_t = 7 \pm 1$ km s^{-1}. The derived abundances showed that the iron-group elements were deficient by about 1 dex but approximately solar levels of O and N ([O/Fe]= +1.4, [N/Fe]= +1.0). These abundances are typical of post-AGB stars (Van Winckel et al. 1996)[201]. They also found many lines in emission. The Balmer lines down to Hδ and many Fe II lines had clear P Cygni profiles indicating on-going mass loss.

More recently low resolution spectroscopy (Parthasarathy et al. 2000)[147] reveals that Hβ is still in emission and a spectral type of A3Ie.

11.2 Photometry

Fifty four $BVRI$ data points covering 1165 days were collected from MJUO. These are presented in Table A.8. The details for the three stars used in the differential photometry of CPD-59 6723 are listed in Table 11.3. HD 147304 was the comparison, HD 147129 was the primary check and HD 147566 the secondary check star. Neither of the two check stars have shown any significant variations over the course of the programme. The RMS errors for the V-band photometry for both of the check stars was 0.010 magnitudes.

Identifier	α(2000.0)	δ(2000.0)	B	V	SpT
HD 147304	$16^{\rm h}\ 24^{\rm m}\ 37.58^{\rm s}$	$-59°\ 45'\ 11.1''$	9.89	9.88	B8III
HD 147129	$16^{\rm h}\ 23^{\rm m}\ 24.22^{\rm s}$	$-59°\ 37'\ 03.3''$	9.95	9.89	B8/B9
HD 147566	$16^{\rm h}\ 26^{\rm m}\ 04.08^{\rm s}$	$-59°\ 43'\ 45.0''$	10.09	9.93	A1IV/V

Table 11.3: Photometry calibration stars of CPD-59 6723 (SIMBAD).

As can be seen in Figures 11.1 and 11.2, and from Table 11.4, CPD-59 6723 is indeed variable but shows no obvious signs of periodicity. The variation is observed in all bands with the greatest range observed in I. The size of the variations show no distinctive trend with wavelength and the colour-magnitude and colour-colour plots show no discernible patterns either.

	B	V	R	I
Mean	10.214	9.914	9.674	9.434
Range	0.245	0.238	0.258	0.277
Error	0.002	0.001	0.002	0.003

Table 11.4: The means, ranges and mean error of the $BVRI$ photometry for CPD-59 6723.

11.2.1 Analysis of the photometry

The photometry of CPD-59 6723 shows quite a large amount of scatter about the mean level and it was investigated as if this was due to a variation with a period of a few days.

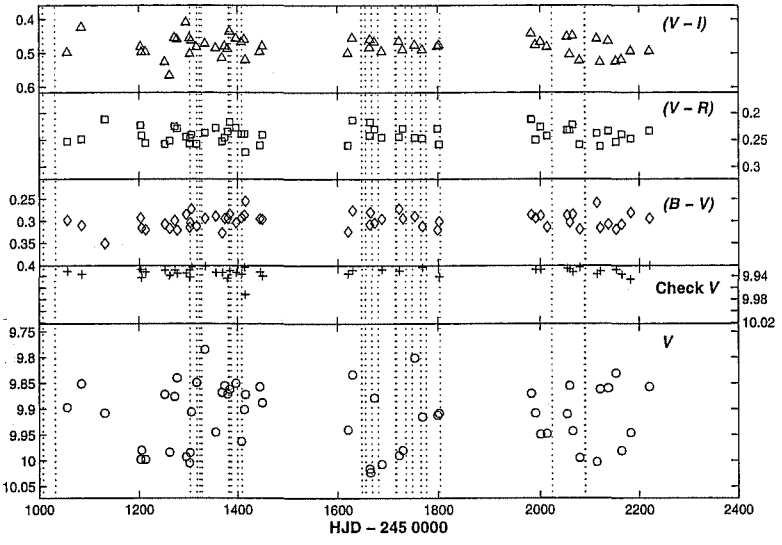

Figure 11.1: V and colour photometry of CPD-59 6723 taken from MJUO. The dotted lines indicate when échelle spectra were taken.

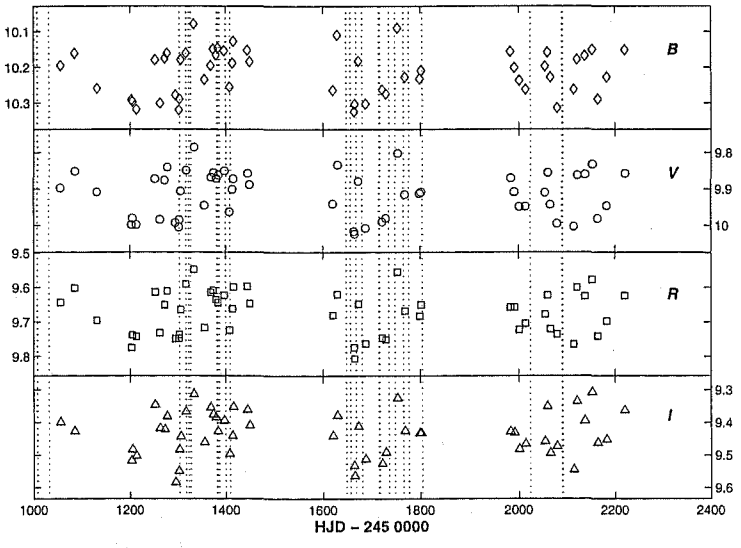

Figure 11.2: $BVRI$ photometry of CPD-59 6723 from MJUO.

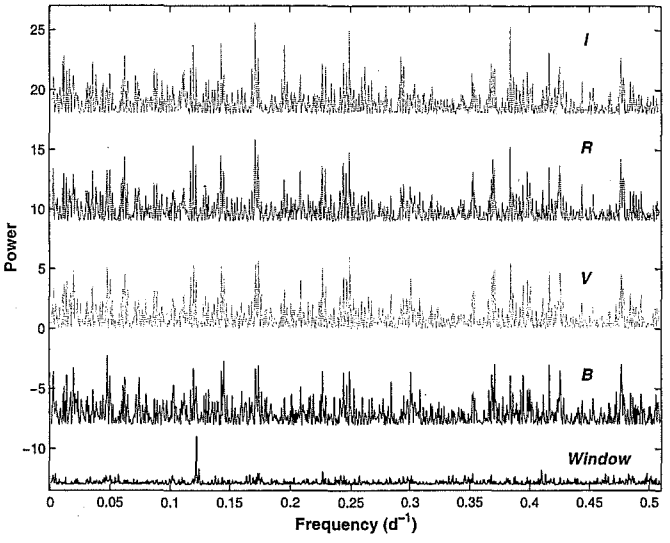

Figure 11.3: Lomb-Scargle periodograms for $BVRI$ photometry of CPD-59 6723. The window function for a 8.2 d (0.1218 d^{-1}) period is shown at the bottom.

Frequency (d^{-1})	Power	Period (d)	Error (d)	P/P_0	Error
0.0624	4.6	16.01	0.06	3.98	0.07
0.1219	4.1	8.20	0.01	2.04	0.02
0.1429	5.3	7.00	0.01	1.74	0.02
0.1713	5.3	5.839	0.007	1.45	0.01
0.1736	5.8	5.760	0.007	1.43	0.01
0.2487	6.1	4.021	0.003	1.000	0.006
0.3693	4.8	2.708	0.002	0.674	0.004
0.3837	5.5	2.606	0.001	0.648	0.003
0.4165	4.8	2.401	0.001	0.597	0.003
0.4253	4.6	2.351	0.001	0.585	0.003
0.4762	4.5	2.100	0.001	0.522	0.003

Table 11.5: Main peaks in the $BVRI$-band periodograms of CPD-59 6723. The uncertainty in each of the frequencies is $\pm 2 \times 10^{-4}$ d^{-1}. $P_0 = 4.021$ d, and is used to look for aliases in the peaks.

Lomb-Scargle periodogram analysis of the photometry in each of the four photometric bands are displayed in Figure 11.3. The frequency scale is compressed compared to similar plots for the other stars in our sample, running from 0 to 0.5 d^{-1} instead of to 0.05 d^{-1}. No clear period stands out although there are a number of peaks common to all, which are listed in Table 11.5. The main periods are considerably shorter and less significant than for most of the other stars in this programme. The most significant period here is at 4.021 ± 0.003 d, and this may be aliased with some of the other peaks in Figure 11.3. Peak 1 is the most notable of these being exactly one quarter of the frequency of the principal.

11.3 Spectral energy distribution

The dereddened spectral energy distribution for CPD-59 6723 is displayed in Figure 11.4, incorporating MJUO optical photometry with infrared measurements from Oudmaijer (1996)[144] and IRAS. The infrared measures are summarized in Table 11.6.

	J	H	K	L	12	25	60	100
Band	9.11	8.91	8.77	8.59	0.36	11.04	12.30	4.83
Error					L	0.44	0.74	0.34

Table 11.6: Infrared and IRAS photometry for CPD-59 6723. The near infrared photometry is from Oudmaijer (1996)[144].

It has been assumed that the spectral type was B8, approximately the middle of the spectral type range for the star, which implies a total colour excess $E(B-V) = 0.34$ and a visual extinction of ~ 1 magnitudes. An A3 classification (Parthasarathy et al. 2000)[147] requires $E(B-V) = 0.26$ and a total visual extinction of 0.78 magnitudes. For both cases the predicted interstellar extinction is 0.8 ± 0.2 mag, which means that within the uncertainties there is not a significant circumstellar contribution.

The blackbody fits to the SED are more consistent with the B8 spectral type, as the fits to the two sets of dereddened photometry model the stellar contribution with blackbodies at about 11100 and 10400 K. The calibrated temperatures are 10600 and 9100 K respectively. There is no indication of a hot dust component to either fit and a second more prominent cool component at 135 K is needed which has about 16% of the stellar flux. The RMS error for the 2 curve fit at is 0.13. The stellar temperatures and total

colour excess agree with Oudmaijer (1996)[144].

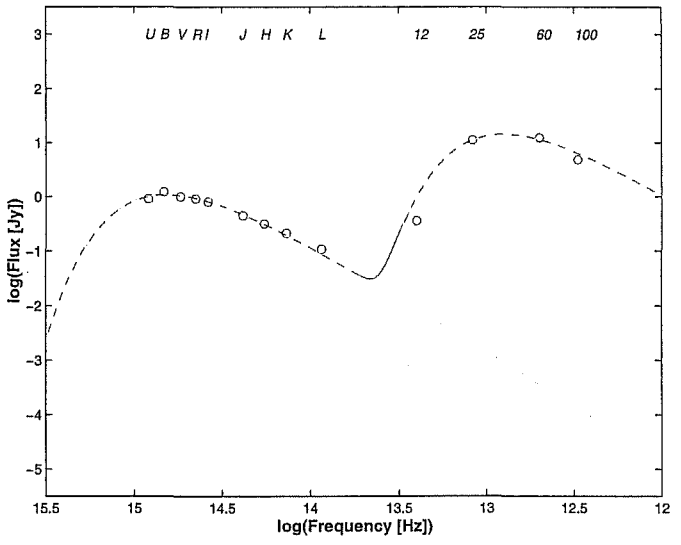

Figure 11.4: The blackbody fits to the SED of CPD-59 6723. The temperatures used in the fits are 11100 and 135 K.

Supergiant luminosities require the star to have a distance of 10.4 kpc. At more typical post-AGB luminosities, say 4000 $L_{\odot}$, the star would be placed at only 4.1 kpc. From the 60 μm flux we infer 0.01 $M_{\odot}$ of gas and dust around the star, since $M_{\rm d}/D^2 = 6.8 \times 10^{-6}$ $\rm M_{\odot}$ $\rm kpc^{-2}$, at a distance of 3.1×10^3 $R_{\star}$ from the star.

To estimate the angular extent of the dust shell it is necessary to calculate the stellar radius. This can be done through the luminosity and temperature from above and implies that the radius of the dust shell is 5.0×10^{13} m. The angle subtended by the shell at 4.1 kpc is 0.08″, considerably smaller than the 45″ resolution for the 60 μm images presented in Oudmaijer (1996)[144]. So the values obtained here for the size and distance of the shell around CPD-59 6723 are consistent with it being an unresolved point source.

11.4 Spectroscopy

As a relatively hot, and somewhat metal deficient star, there are comparatively few lines visible in the spectrum of CPD-59 6723. However the lines that are observed point to a star undergoing significant mass loss. One

of the main features is the prominent P Cygni profile in Hα. Apart from the height of the peak and the shape of the absorption component it has remained quite constant over the course of this programme ($\sim$ 1100 d).

CPD-59 6723 was the faintest star that was regularly observed during this campaign. As such the spectra have lower S/N than for our other objects. They are also subject to more interference from night sky emission lines, especially from OH in the near infrared (Osterbrock et al. 1996)[143].

There are a number of other emission features in the spectrum, often in conjunction with absorption features. HERCULES spectra uncovered a range of Fe II multiplets (RMT 42, 48 and 49) showing combined emission and absorption features. Fe II emission is seen in the near-infrared at $\lambda\lambda$8451, 8490 and 8499. These are all from the same Fe II multiplet, 5s^{6}D - 5p^{6}F (Johansson 1978)[96], and they are also present in many LBV star spectra. Emission is also seen in $\lambda\lambda$7877 and 7896 Mg II, Paschen 11 to 13 and $\lambda\lambda$8498 and 8542 Ca II. Notable absorption lines belong to high excitation potential multiplets: λ5875 He I (RMT 11), λ6402 Ne I (RMT 1), $\lambda\lambda$6347 and 6371 Si II (RMT 2), $\lambda\lambda$7423 and 7442 N I (RMT 3), $\lambda\lambda$6578 and 6583 C II (RMT 2) and λ8446 O I (RMT 4). It should be noted that the O I line is quite variable, with the equivalent width ranging from 0.45 to 1.34 Å.

There are no diffuse interstellar bands observed in the spectrum of CPD-59 6723. Even the λ4430 feature is not visible in the spectra.

11.4.1 Radial velocities

The radial velocity curves for CPD-59 6723 from various absorption lines are displayed in Figure 11.5 and consist of between 13 and 24 points spread over 1044 days. The data used in this section is given in Table C.12 and summarized in Table 11.7.

The Hα absorption feature is probably not associated with any variations in the stellar photospheric velocity as it arises in the stellar wind (see §11.4.2 for a more detailed investigation). The Si II lines however, show a tendency to be anti-phased to the variation in the Hα profile.

As with the other B-stars in this programme, CPD-59 6723 shows a wide range of radial velocities for a given night. The mean velocity of each group of lines depends upon the excitation potential, with the highest potential lines also being the most red-shifted. This can be accounted for if we consider CPD-59 6723 to have an expanding atomsphere. In this case lines are forming at different levels in the atmosphere which is expanding under the influence of radiation pressure. This accelerates the gas, so that higher

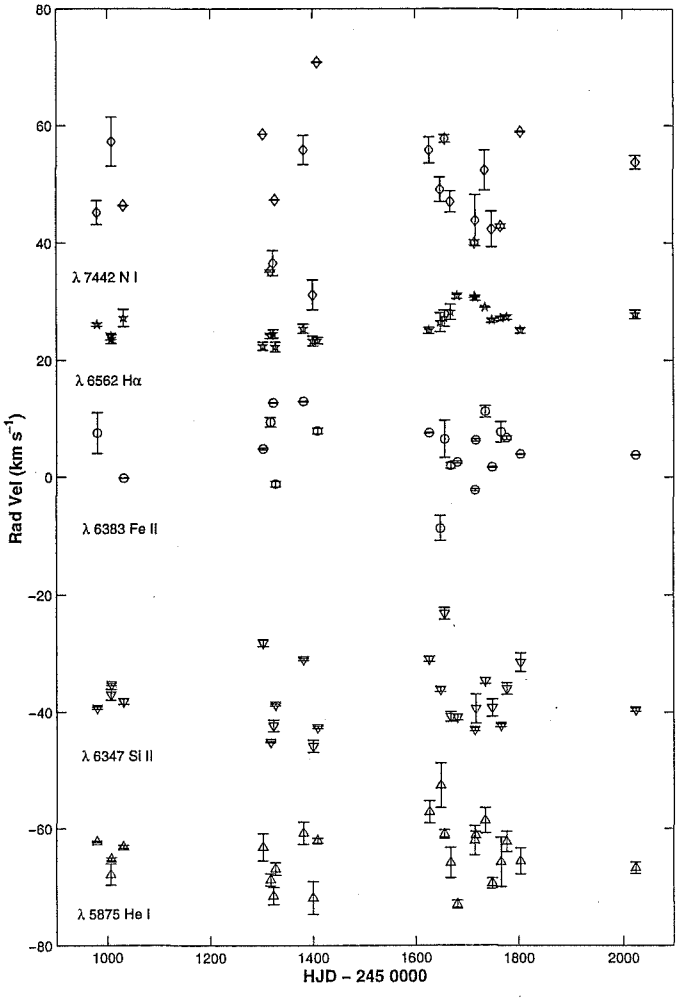

Figure 11.5: The radial velocity variation for five lines in the spectrum of CPD-59 6723. The λ6383 Fe I line is at the observed heliocentric values while the rest of the lines have been offset by $\pm$20 or $\pm$40 km s^{-1}.

λ_o (Å)	6562	6383	6347	7442	5453	5875
Species	Hα	Fe II	Si II	N I	S II	He I
χ (eV)	10.19	5.55	8.12	10.33	13.67	20.96
n	24	13	24	13	11	15
μ_{rv} (km s^{-1})	-53.78	4.48	2.46	9.51	10.07	15.35
σ_{rv} (km s^{-1})	2.55	3.76	5.52	9.32	5.41	4.58
Δ_{rv} (km s^{-1})	0.41	0.84	0.58	1.18	1.06	0.80

Table 11.7: Summary of the radial velocity for five lines in CPD-59 6723. μ_{rv} is the mean velocity, σ_{rv} is the standard deviation, and Δ_{rv} is the mean error, all in km s^{-1}. n is the number of measures. Note that the Fe II line is in emission.

excitation potential lines, such as λ5875 He I, which form lower down in the atmosphere than lower excitation potential lines, like the Si II (RMT 2) lines, are moving towards us at lower velocities. Hα notwithstanding, this reaches a peak in the H and K lines of Ca II ($\chi = 0.0$ eV), which were measured with a mean radial velocity of -8.2 km s^{-1} (see §11.4.3).

As with the photometry, there is no obvious period in the radial velocity curves (compare Figures 11.5 and 11.6). There is a hint of periodicity in the Hα curve between HJD 2451600 and 2451800, but in the other lines there is no such indication. The frequency spectra displayed in Figure 11.6 do not show any distinctive peaks. The Hα spectrum shows a peak at 260 ± 20 d, which is probably due to the sinusoidal variation during the observing season mentioned earlier. The other lines exhibit a peak at ~ 40 d which is absent from both the V-band and Hα periodograms.

11.4.2 Balmer line profiles

CPD-59 6723 presents a very consistent Hα profile. The feature consists of a large emission spike and wings (out to $\pm$350 km s^{-1}) and a narrow blue-shifted absorption component. It resembles a smaller version of what was seen in HD 168607. As changes are not immediately obvious between the spectra, what is presented in Figure 11.7 (a) is the time evolution of the residuals of the observed spectrum minus the mean spectrum.

Prior to HJD 2451303 the peak of the emission is lower than average. The spectrum of HJD 2450980 has the lowest intensity of all (6 times the continuum) and reaches a maximum on HJD 2451668 (10 times). The peak grows from HJD 2451626 until 2451668 and then shrinks to a new observed low

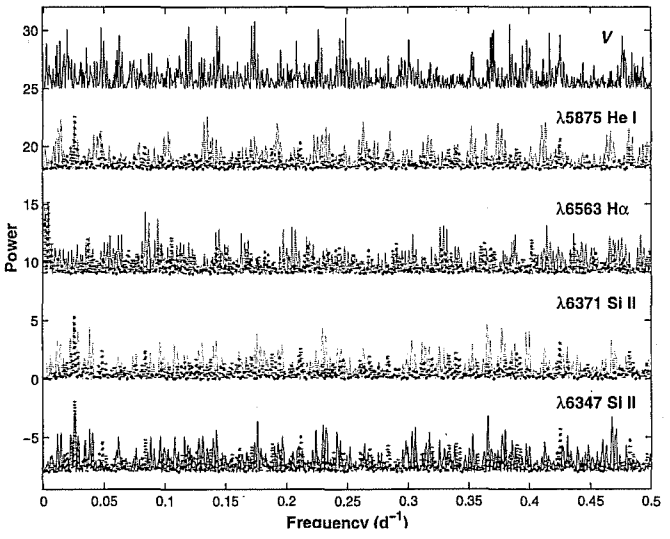

Figure 11.6: Periodogram analysis of some radial velocities of absorption lines in the spectrum of CPD-59 6723 compared with the V-band frequency spectrum. The uncertainty in the frequencies is $\pm 0.24 \times 10^{-3}$ d^{-1}. Hα is shown with a window function at 260 d (0.0038 d^{-1}) while the other lines have a window function at 39.4 d (0.0254 d^{-1}).

on HJD 2451736. During this time there is extra absorption near 0 km s^{-1}. This could be the reason why the Hα absorption velocity (Figure 11.5) becomes more positive over the same period, as this moves the bisector average to higher values. This is not due to the profile undergoing a systematic shift in velocity compared to the mean profile. If this were the case then the whole profile would be affected and there would be significant residuals across the whole feature not just at the centre. Plots of the spectra, not the residuals, show that the emission peak is indeed higher during this time than for others. The wings in subsequent spectra may also be enhanced.

This suggests that the Hα profile during this phase consists of the mean P Cygni profile plus a smaller one, which grows and recedes in the space of 250 d. The most likely explanation for this is a sudden increase in the density of the wind responsible for the line profile, due perhaps to an increase in the mass loss rate or to a shock wave in the circumstellar medium.

From spectra at shorter wavelengths hydrogen emission can be seen down to Hδ. The Hβ emission on HJD 2452090 had an equivalent width of 1.2Å, is higher than the emission equivalent widths found by Oudmaijer (1996)[144] and by Venn et al. (1998)[205]. Oudmaijer's spectrum was taken prior to 1995 June 7, HJD 2449875. Venn et al. acquired their spectra on the nights of 1995 July 7-9, HJD 2449905-7. This means that there is at least 2200 days, or $\sim$ 6 years, between the MJUO Hβ observation and those of other researchers. Going back even further, Hill et al. (1974)[82] reported that the Hβ absorption was quite weak and that it was probably partially filled in by emission. Connecting these values together would suggest that there has been an on-going increase in the mass loss rate over the last 30 years, in line with the evolution of a post-AGB star. However, the gaps in coverage can not rule out the effects of the current erratic mass loss phase.

By examining the position of the blue-most wing of the Hα absorption feature (see Figure 11.8) it would appear that the mass loss responsible for the P Cygni profile has been quite stable over the course of this programme. The velocities listed in Table 11.8, have been obtained by visually estimating where the point of transition between the absorption and the blue emission wing lies. This will give us the value of the highest speed absorption material and thus an estimate of the terminal velocity of the stellar wind. The standard deviation of these values, 4.6 km s^{-1}, is about the order of magnitude of the error one would expect given the noise in the spectra ($\sim$ 3%) and intermittent interference from telluric lines. Converting this heliocentric value to a the stellar frame using the mean velocity of the λ5875 He I absorption lines, $+15 \pm 5$ km s^{-1}, gives an outward velocity of $+119 \pm 9$ km s^{-1}.

Applying similar techniques to the Hβ and Hγ profiles found a blue

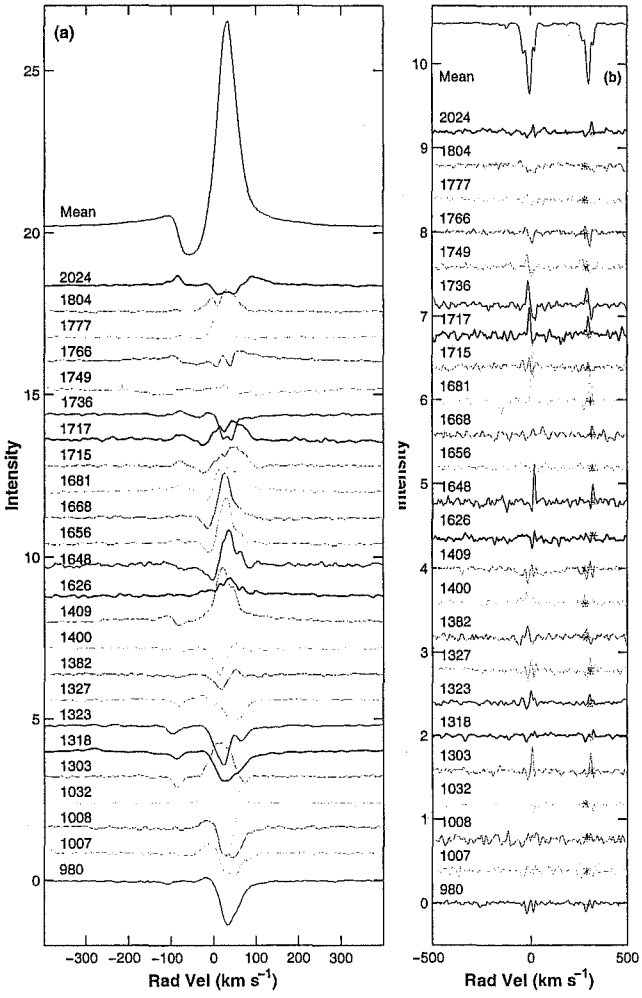

Figure 11.7: The residual profile variations of (a) Hα and (b) Na D profiles of CPD-59 6723. The residuals are labelled with the Heliocentric Julian Date of observation -2450000. The asterisks in (b) denote the radial velocity of night sky features on the Na D_1 lines.

HJD −2450000	λ (Å)	Rad Vel (km s^{-1})
0980	6560.658	−98.6
1007	6560.658	−98.6
1008	6560.541	−103.9
1032	6560.686	−97.3
1303	6560.482	−106.6
1318	6560.475	−106.9
1323	6560.356	−112.4
1327	6560.435	−108.8
1382	6560.554	−103.3
1400	6560.554	−103.3
1409	6560.492	−106.2
1626	6560.492	−106.2
1648	6560.303	−114.8
1656	6560.586	−101.9
1668	6560.492	−106.2
1681	6560.670	−98.0
1715	6560.670	−98.0
1717	6560.615	−100.5
1736	6560.615	−100.5
1749	6560.615	−100.5
1766	6560.614	−100.6
1777	6560.614	−100.6
1804	6560.555	−103.3
2024	6560.495	−106.0
Ave	6560.551	−103.5
σ	0.100	4.6

Table 11.8: Measured wavelength and radial velocity of the blue limit of the absorption feature in the Hα profile of CPD-59 6723.

absorption limit of about -80 ± 6 and -104 ± 10 km s^{-1} respectively (see Figure 11.8). These are taken from single spectra acquired with HERCULES on HJD 2452090, for Hβ, and with the échelle spectrograph in the case of Hγ on HJD 2451384. The échelle spectrum has lower signal-to-noise and is subject to an even greater degree of uncertainty in the position of the blue wing due to a bad column on the CCD. This produces the narrow absorption-like feature at about -90 km s^{-1}.

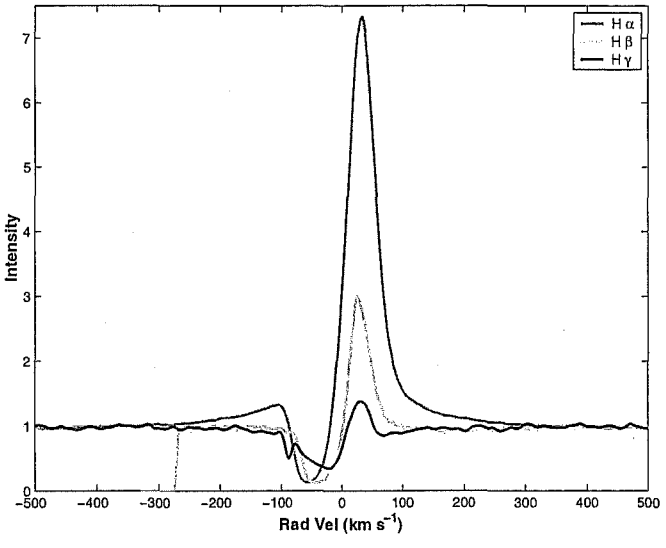

Figure 11.8: A comparison of theHα, Hβ and Hγ profiles of CPD-59 6723. The narrow absorption at ~ -90 km s^{-1} in the Hγ profile is an artefact.

11.4.3 Sodium D Lines

The mean échelle Na D line profile for CPD-59 6723 is displayed at the top of Figure 11.7b. It consists of a number of absorption features, which are sometimes combined with a variable night sky emission line. This unfortunately clouds the interpretation, but an estimate of the individual components are listed in Table 11.9 and illustrated in Figure 11.9 with a HERCULES spectrum (HJD 2452090). It would appear from the time series that most of the changes observed in the Na D line profile are due to variations in position and intensity of the night sky line.

The RMS errors on the Gaussian fits are approximately 0.008 Å. The heliocentric correction is -8.9 km s^{-1} and the stellar radial velocity is $+16\pm$

#	λ (Å)	W (Å)	Rad Vel (km s^{-1})	
			$\odot$ frame	$\star$ frame
1	5889.231	0.116	−37.4	53.6
2	5889.403	0.026	−28.7	45.0
3	5889.671	0.172	−15.0	31.2
4	5889.974	0.286	0.4	15.8
5	5890.395	0.114	21.8	−5.6
1	5895.202	0.073	−37.1	53.5
2	5895.391	0.024	−27.5	43.7
3	5895.730	0.178	−10.3	26.5
4	5895.969	0.178	1.9	14.3
5	5896.375	0.094	22.5	−6.3

Table 11.9: The components of the Na D lines of CPD-59 6723 determined from HERCULES spectra taken on the night of HJD 2452090. See Figure 11.9 for identifications.

2 km s^{-1} from two Si II ($\chi = 10.07$ eV) absorption lines.

As with many of the Na D line profiles encountered in this project there are several ways to interpret the structures, particularly close to the stellar velocity. In this instance it is even more complicated by the stellar radial velocity being small enough to encounter night sky emission features. The fibre-fed nature of HERCULES means that these are indistinguishable from potential non-terrestrial components as there is no unique spectrum from the sky for comparison. For example, component 3 could be an individual absorption feature or it could be due to night sky emission impinging upon a larger absorption feature. The simplest interpretation is that the features are all due to a combination of absorptions. This, however, means that there is no feature near the stellar velocity. Further fits interpreting component 4 as a larger absorption and 5 as an emission line were not as successful producing a much higher RMS of 0.05 Å.

To help untangle the components it was necessary to rely on other spectra. Using the spectrum of HJD 2451384 the radial velocity of the Ca II H and K lines were found to be −5.7 and −10.6 km s^{-1} respectively. Compared with the value from Kilkenny & Hill (1975)[104], this indicates a variable velocity. The stellar velocity taken from 5 other lines in the same spectrum was $+13 \pm 3$ km s^{-1}. Converting to the stellar rest frame, the H and K lines have an average outward velocity of +21 km s^{-1}. The FWHM of the two

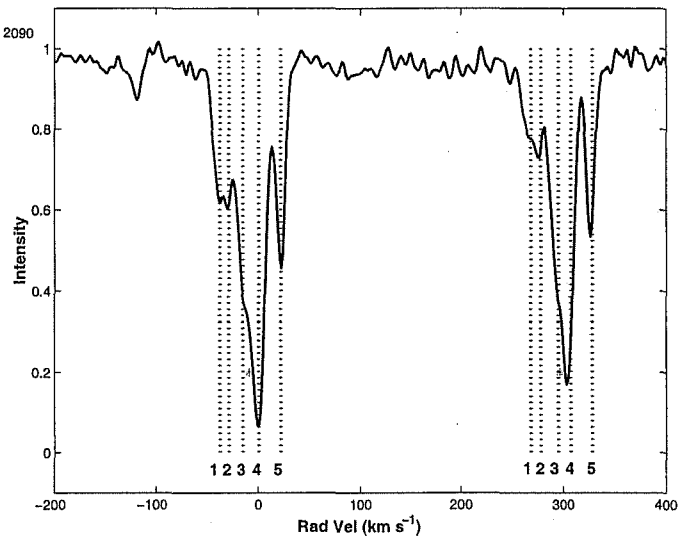

Figure 11.9: Na D line profile for CPD-59 6723. These normalized HERCULES spectra were taken on the night of HJD 2452090. The components are labelled according to Table 11.9.The asterisk marks the position of possible night sky lines.

lines was found to be 0.88 and 0.90 Å, or an average of 68 km s^{-1}. This is quite similar to the widths of other strong stellar lines. Coupled with their radial velocity variation, this would suggest that the H and K lines arise from matter in the vicinity of the star, not from interstellar space.

The line of sight to CPD-59 6723 intersects the Sagittarius ($d = 1500, z = -200$ pc) and Scutum-Crux ($d = 3600, z = -470$ pc) spiral arms with radial velocities of -31 and -68 km s^{-1} respectively. The radial velocity reaches -77 km s^{-1} at 4.1 kpc and peaks at about -108 km s^{-1} at a distance of 7 kpc. This indicates that the star, which has a mean radial velocity on the order of $+15$ km s^{-1}, is not moving with the Galactic disk.

The stellar frame velocities of the Na D line components indicate that components 1 and 2 are from matter which is moving very rapidly away from the star, exceeding the typical ejection velocities seen in PN (15 km s^{-1}, van der Veen et al. 1993[192]) by about 20 km s^{-1}. Component 2 is a fair match to the heliocentric velocity of the Sagittarius arm and since it is constant, it is most likely a foreground object.

11.4.4 Iron II line profiles

Like HD 168607, CPD-59 6723 displays a wide variety of Fe II line profile shapes. The strongest lines are from RMT 42 at $\lambda\lambda 4923, 5018$ and 5169. These show distinctive P Cygni profiles which also seems to be composed of multiple absorptions. Similar structures are seen in lines of RMT 48 and 49. Other Fe II observed are from multiplets 37 and 38.

In Figure 11.10 the mean line profiles for the three most prominent Fe II multiplets are displayed. They clearly exhibit P Cygni profiles, but show more structure than the Balmer lines. This is not surprising, as these lines have a lower opacity than the hydrogen lines and we are thus able to see more clearly through various shells. Hutsemékers & Van Drom (1991)[90] assigned double absorptions to different shells surrounding the star. The velocities of these components are indicated by the dotted lines b and d in Figure 11.10 at heliocentric radial velocities of -39 and -16 km s^{-1} respectively. It is possible that these shells are also responsible for Na D line components 1 and 3 in Table 11.9. The terminal velocity of the wind, indicated by line 'a' at the blue lip of the absorption profile, is approximately -80 km s^{-1}, or $+96$ km s^{-1} in the stellar rest frame. From §11.4.2 the corresponding figure for the Hα profile is -110 km s^{-1}.

There are also Fe II emission peaks observed at other wavelengths. These are due to the Lyα fluorescence. From the low energy a^4D states the ion is excited by Lα into the $5p$ and $4s$ states at much higher energies (Johansson &

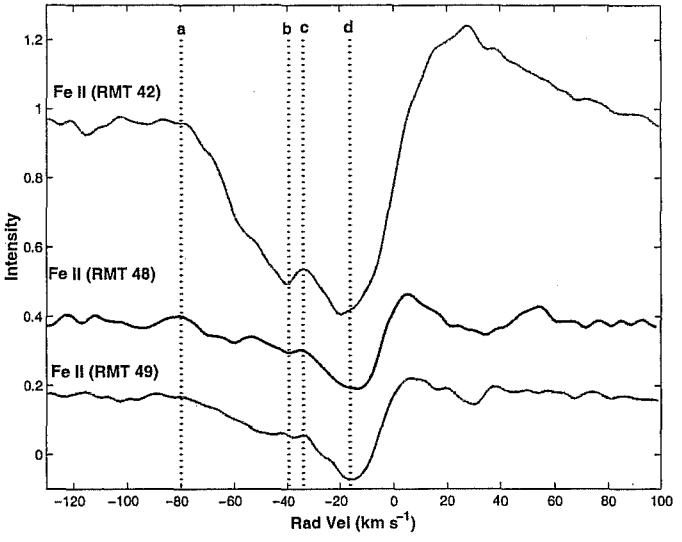

Figure 11.10: Line profiles for Fe II multiplets RMT 42, 48 and 49 for CPD-59 6723. The dotted lines indicate the velocities of the features mentioned in the text.

Jordan 1984)[97]. For these the upper level is the (5D)5p^{6}F° level decaying into the e^6D levels. This is similar to the pumping of the high O I levels by Lyβ which gives rise to strong O I lines in low gravity G, K and M stars.

11.5 Discussion

In Figure 11.11 the Hα profile of CPD-59 6723 is compared with those of two luminous blue variable stars (LBV): HR Carinae and HD 168607. All three stars show prominent P Cygni profiles indicating significant mass loss, but that of CPD-59 6723 is smaller than the LBVs. The emission wings extend only about 400 km s^{-1} from the centre of the profile, the peak emission is considerably lower, and the blue absorption limit is at -110 km s^{-1} with no discernible structure within it. The LBVs have much wider emission wings ($\sim$ 1000 km s^{-1}), higher peaks, and the absorption limit is about -180 km s^{-1}, and also shows signs, especially in HR Carinae, of structure within the absorption profile.

CPD-59 6723 shows many of the spectral characteristics of LBVs, without the major changes on monthly or annual timescales. There are hints that it does change over the course of many years, as evidenced by the change

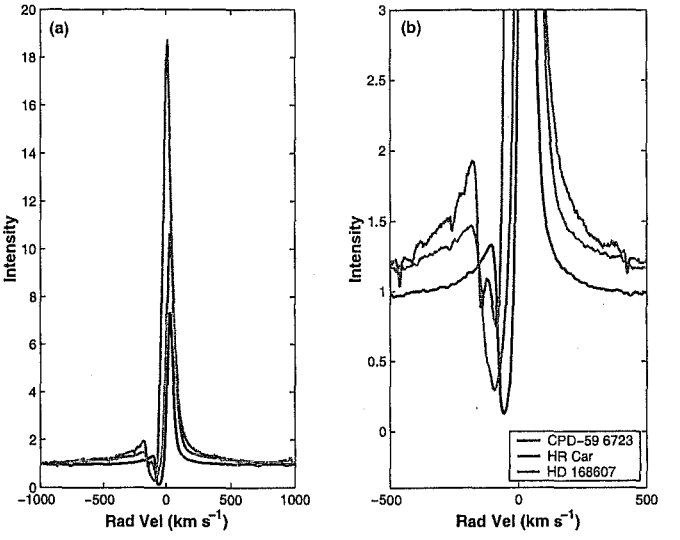

Figure 11.11: Hα profile of CPD-59 6723 compared to those of the luminous blue variables HR Carinae and HD 168607. (a) shows the extent of the emission and (b) is a close up of the central regions.

in Hβ since the late 1960s. The key difference between HR Carinae and CPD-59 6723 is in mass. Matter is being lost from both but at prodigiously higher rates in the LBVs.

11.6 Conclusions

Comparing MJUO $BVRI$ photometric data with those acquired about 30 years ago, presented in Table 11.2, shows that CPD-59 6723 has not undergone any significant changes in brightness or colour. What the programme did show is that the star has a variable brightness with a range of 0.283 magnitudes in V. We were unable to find a significant period to the variations, but the most significant peaks could be aliases of a 4.021 ± 0.003 d period.

The spectral energy distribution was best modelled with a B8 (11000 K) star with a 135 K dust shell. The derived total colour excess, $E(B - V) = 0.34$, and stellar temperature is quite consistent with the estimates of Oudmaijer (1996)[144]. The distance to the star was 4.1 kpc assuming that the star has $M_V = -4.2$.

From this distance and the 60 μm flux the total circumstellar mass (gas and dust) 0.01 $M_\odot$ at a radius of 3.1×10^3 $R_\star$ from the star. Compared with Oudmaijer's estimate for the *dust* mass of 8.2×10^{-5} $M_\odot$, derived assuming a distance to the star of 1 kpc, this is quite consistent. No clear indications of circumstellar absorption was found.

Spectroscopically radial velocity variations were found which, like the photometry, have a sizeable amplitude (14 km s^{-1} peak-to-peak) but no discernible period. Only the Hα absorption produced a characteristic period at 260 d but this was subsequently found to be due to a change in the line profile shape not its position.

Hα for CPD-59 6723 shows a prominent P Cygni profile in all of the MJUO spectra. The period mentioned above was found to be due to a smaller P Cygni profile which grew and shrank over about 110 d. This could be due to a discrete mass loss event which increased the amount of material in the wind responsible for the P Cygni feature near the systemic velocity, but then dispersed over the next 100 days. The terminal velocity of the wind, as measured in the position of the blue limit of the absorption component, is also quite stable.

The Na D line profiles are also quite stable and the variations in the profile are mainly due to night sky emission. Fitting only absorption components again failed to uncover a feature at the systemic velocity. Five components were fit to the profile, with components 1 and 2 having very high velocities in the stellar frame. Component 2 was a good match to the radial velocity predicted for a gas cloud that was part of the Sagittarius spiral arm.

P Cygni profiles are also visible in a number of Fe II multiplets, and indicate two shells of material around the star, at -39 and -16 km s^{-1}. These shells could also be responsible for Na D line components 1 and 3.

Compared with two LBV stars, CPD-59 6723 showed similar features but on a smaller scale and with less indication of structure. For example the Hα features of HR Carinae and HD 168607 have wider wings and a higher terminal velocity than CPD-59 6723. HR Carinae also shows variable and complex structure in the Hα absorption feature. This is probably because the mass loss which powers these lines in HR Carinae and HD 168607 are considerably stronger due to the stars being very massive and a lot more luminous.

Chapter 12

Summary and future work

A programme of photometric and spectroscopic observations has been undertaken in order to investigate some of the physical properties of post-AGB stars and some related objects. These observations have been used to gain an insight into the nature of these stars.

12.1 Variability

12.1.1 Photometry

All of the stars observed in this programme are photometrically variable. The principle periods detected conform loosely to a decrease in the period as the temperature of the star increases. This is what is expected from the classical pulsation law:

$$P = Q\rho^{-\frac{1}{2}} \tag{12.1}$$

which relates the pulsational period P and the mean stellar density ρ. In post-AGB evolution the stars evolve to higher temperatures at constant luminosity without losing large amounts of matter. This means that over the course of this phase of evolution, the mean stellar density will increase, and thus the pulsation period will go down.

HD 179821, the second coolest star in the sample, has the longest period (193 d), while CPD-59 6723, the hottest post-AGB star, showed evidence of oscillations on timescales of just 4 days. The ranges and inconsistent amplitudes of the V-band magnitudes are consistent with what other authors have reported for post-AGB stars. This behaviour also includes HD

95767 and HD 172481 at the times when the F-star dominates the V-band photometry.

Exceptions to this trend are AI CMi and HD 70379. AI CMi has its photometry driven by the formation of TiO in its atmosphere, a consequence of cooler temperatures rather than changes in radius. HD 70379 on the other hand does show clear radius changes in synchronization with the brightness variations. However, the range of brightness in V, is approximately double that of post-AGB stars with similar periods.

The behaviour is also consistent with the earlier work of Zalewski (1993) [217] and others which showed that for post-AGB stars a number of modes of oscillation are stable. Their interaction will lead to inconsistent amplitudes and periods observed in the light curve. Inspection of the model light curves in Fokin et al. (2001)[60] for a $0.8M_{\odot}$ star over a range of luminosities and temperatures reveals more complicated behaviour as the luminosity increases. Lower mass models have significantly larger amplitudes and longer primary periods.

12.1.2 Radial velocities

As with the photometry, all of the stars in this project showed radial velocity variations. These can be almost entirely attributed to radial motion of the stellar envelope, with the longer periods also belonging to the cooler stars.

The hottest stars also showed that they possessed expanding atmospheres, as the radial velocities of low excitation potential lines (which form higher in the stars' atmospheres) were significantly blue-shifted with respect to the higher potential lines which form lower down. These stars are able to exhibit more obvious signs of mass loss, in particular P Cygni profiles in Hα.

12.2 Mean radial velocities

Most of the stars in our programme have mean velocities which could be produced by stars moving with the mean Galactic rotation (see Table 12.1). This places these stars at very large distances from the Sun and the Galactic plane, out of the thin disk but still able to be classified as thick disk objects.

HD 95767 and CPD-59 6723 have mean radial velocities of about -25 and $+15$ km s^{-1} respectively. Although these are not particularly high, they cannot be explained by Galactic rotation. In the former case the velocity exceeds the maximum predicted by only 8 km s^{-1} which can probably be accounted for by motion of the star with respect to its part of the Galaxy.

However CPD-59 6723 is more intractable, showing a recessional velocity while the line of sight predicts a blue-shift.

HD 172481 is the clearest case of a star not following the Galactic rotation curve. It has a very high approach velocity, which allows the Na D lines to separate into two groups: one associated with the star and the other with material in the Galaxy. Allowing for its reduced metallicity indicates that the star is probably a halo object. Hence the high radial velocity.

12.3 Distance estimates

In Table 12.1 are presented the distance estimates for the programme stars from four methods. A_V assumes that the interstellar matter is responsible for all of the extinction; Na D uses the sodium D lines to identify Galactic spiral arms; Gal rot uses the radial velocity of the star and the Galactic rotation curve: and O I employs the equivalent width of the λ7774 O I multiplet.

Star	Distance (kpc)			
	A_V	Na D	Gal Rot	O I
AI CMi	2.9	4.0	4.0	-
HD 179821	4.0	3.0	6.0	13
SAO 209008	2.0	1.7	1.7	-
HD 70379	3.4	6.0	6.0	7.5
HD 95767	1.7	1.9	u	13
HD 172481	3.1	5.1	u	7.8
HD 168625	3.6	1.9	2.5	-
HD 168607	3.8	1.9	2.8	-
CPD-59 6723	4.1	1.5	u	-

Table 12.1: The distances derived to the stars from various methods. A dash indicates an unmeasured quantity and u denotes that the method does not limit the distance.

The first two methods provide limits, A_V is an upper limit and Na D a lower limit. For HD 179821, SAO 209008, HD 168625, HD 168607, CPD-59 6723, and probably HD 95767, the distances are consistent. For the other stars the lower limit imposed by the Na D lines is larger than the upper limit place upon the distance from the extinction.

Using the Galactic rotation curve to predict the distances of stars prob-

ably works the best for the objects close to the Galactic plane. Indeed those stars with the lowest Galactic latitudes, are also the ones least likely to be post-AGB stars. They have near solar metal abundances and low radial velocities.

It was originally hoped that the λ7774 O I feature would provide an additional, independent estimate of the luminosities of the stars. However, using the calibration of Arellano Ferro et al. (1991)[3] produced values which indicated stars which were much more luminous than other wise indicated. Faraggiana et al. (1988)[55] found that their model λ7774 O I line strength showed a more complicated behaviour than a simple dependence on luminosity (surface gravity). They point out that the line centre is formed higher in the atmosphere and is thus enhanced. A new calibration of this parameter is required to account for stars with such low surface gravities as these.

12.3.1 Binarity

Only one star, HD 95767, shows any clear evidence of binarity based upon the behaviour of its radial velocity curve. However the period was too long to be fully covered by this programme and were unable to determine a period for the orbit.

HD 172481 also shows evidence of a companion through the appearance of TiO bands at certain photometric phases. Neither of these stars shows the depleted abundance patterns associated with other post-AGB binary stars, which suggests that other factors, probably related to the stars evolution on the AGB, are responsible for such abundances.

12.4 Circumstellar matter & reddening

The stars in this programme contain circumstellar matter which has been fit by blackbodies with quite similar temperatures despite the very large range of effective stellar temperatures.

In Figure 12.1 we show the relationship between the dust temperature ($T_{\rm dust}$) and the stellar effective temperature ($T_{\rm eff}$) assuming a range of ejection velocities. These represent the final velocity of the the superwind achieved in the late AGB phase. To simplify things some assumptions have been made, e.g., a constant annual increase in effective stellar temperature ($T_{\rm eff}$), constant expansion velocity ($v_{\rm exp}$), constant stellar luminosity (L) and that the dust is in thermal equilibrium with the radiation from the star. The radius of the star is given by:

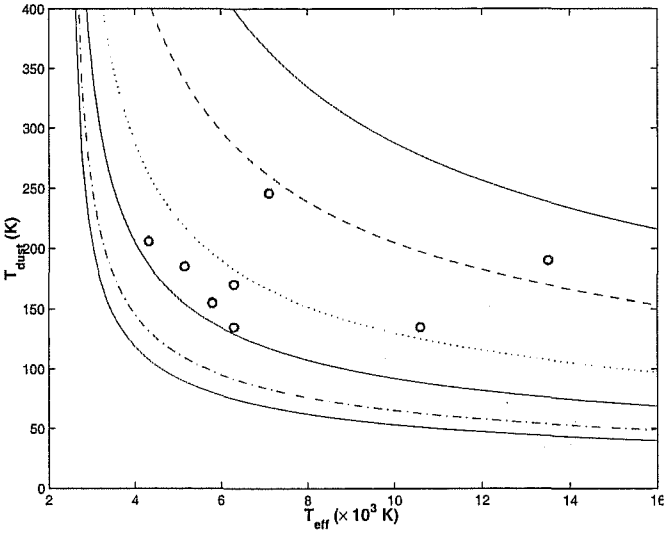

Figure 12.1: Dust and stellar temperatures for the stars in this programme compared with predicted temperature behaviour. The different lines represent different expansion velocities (bottom to top): 15, 10, 5, 2.5, 1, and 0.5 km s^{-1}.

$$R_\star = \sqrt{\frac{L}{4\pi\sigma T_{\rm eff}^4}}. \tag{12.2}$$

Combining this with equation 2.10, and using $R_{\rm dust} = v_{\rm exp}t$, means that:

$$\begin{aligned} T_{\rm dust} &= T_{\rm eff} / \sqrt{\frac{2v_{\rm exp}t}{\sqrt{\frac{L}{4\pi\sigma T_{\rm eff}^4}}}}, \\ &= \sqrt{\frac{L^{1/2}}{2v_{\rm exp}t\sqrt{4\pi\sigma}}}, \\ &\propto \frac{1}{\sqrt{t}}, \end{aligned} \tag{12.3}$$

i.e., that the temperature of the dust is inversely proportional to the square root of the time since ejection of the shell. This is why the model predicts such a rapid decline in dust temperature (the stellar temperature increases incrementally with time and can thus be used as a de facto time co-ordinate). The faster the rate of ejection, the faster the temperature drops.

Most of the stars in the sample can be fit with an expansion velocity of just between about 2 and 5 km s^{-1}. The two stars which don't follow this are HD 172481 and HD 168625. The former is a binary star and the latter is most likely a massive star undergoing bursts of mass-loss.

No hot dust shells have been found around the stars in this project. HD 172481 was found to have a triple peaked SED due to a cool stellar companion rather than hot dust. Despite having the lowest mass of circumstellar material HD 172481 was the only star for which interstellar extinction which could not account for the total extinction. An additional 0.5 mag is required account for the observed colours. AI CMi, SAO 209008, HD 70379 and CPD-59 6723 had extinctions at the high end of the error bars on the predicted interstellar extinction. Note that these values are predicated on the idea that there is no circumstellar excess. In general one would expect the circumstellar material to account for at most, a few tenths of a magnitude to the extinction as the shells are optically thin and will extend only for a couple of tenths of a parsec.

The circumstellar masses derived from the IRAS 60 μm fluxes are listed in Table 12.2 along with the radii from the central star. The biggest factor in these masses is the distance. Not only are these fairly uncertain in themselves, but the masses are calculated by using the square of the distance.

Star	M_{CS} ($\times 10^{-3}$ $M_{\odot}$)	R_{CS} ($R_{\star}$)
AI CMi	3.9	170
HD 179821	400	700
SAO 209008	1.4	390
HD 70379	5.5	775
HD 95767	0.37	343
HD 172481	0.07	246
HD 168625	42	2500
CPD-59 6723	11	3100

Table 12.2: Circumstellar masses (M_{CS}) and radii (R_{CS}) estimated for programme stars from the 60 μm flux.

12.5 Hα profiles

One of the strongest threads connecting these stars is the structure and variability of their Hα profiles (see Figure 12.2), particularly with the G- and F-stars in the programme.

The origin of the emission features for the later type stars has to lie close to the star as changes are observed over weekly timescales. Taking the distance between the two peaks of the residual Hα profiles ($\sim$ 50 km s^{-1}) to be indicative of the velocities of the material involved in the emission profile, means that the size of the Hα emission regions are about 30 million kilometres, which is on the order of a stellar radius.

The shapes of the various residual spectra for these stars, with their self-absorbed, twin peaked shape, are somewhat reminiscent of the Hα profiles of Be stars. These stars generate their emission from a disk of material which lies close to the star. However in post-AGB stars these seem rather unlikely. Apart from HD 172481 none of the stars show significant levels of extra mid-infrared emission expected from hot dust. In this case the additional infrared flux comes from a cool companion star rather than a circumstellar disk close to the star.

A better fit to the appearance and behaviour of the post-AGB Hα profiles are those of metal-deficient red giant stars, which show the same variable peaks flanking a deep absorption core. These also vary on timescales of weeks to months. The model for this outlined in Smith & Dupree (1988)[175] has three parts to the Hα profile:

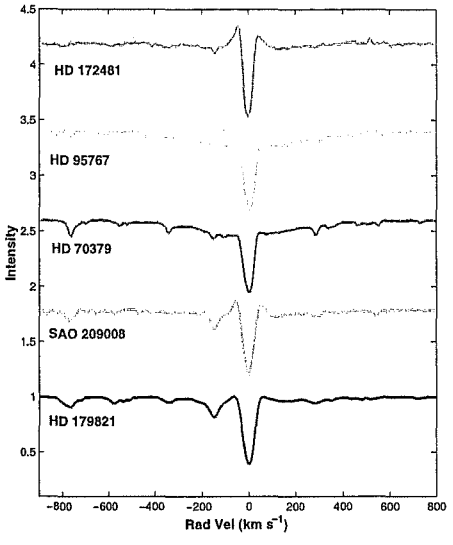

Figure 12.2: Comparison of the mean Hα profiles for the F- and G-type stars presented in this thesis.

1. normal stellar absorption profile;
2. emission arising in the stellar chromosphere;
3. absorption from a stellar wind.

Components 2 and 3 are shown fitted to a residual Hα profile of HD 70379 from which has been removed the wide stellar absorption wings. Variability is attributed to a pseudo-steady outflow of material generated by atmospheric pulsations which produce density and velocity changes. The overall mass-loss is reflected in the fact that the mean spectra have the blue wavelength peak at lower intensities than the red one. The emission is formed in a region centred upon the star and the absorption in the material leaving the star. Using the simple recombination model of Cohen (1976)[35] and the residual spectra, .i.e., the non-stellar part of the Hα profiles, the estimated mass loss rate from equation 8.1 is of the order of 10^{-7} $M_{\odot}$ yr^{-1}, which agrees well with the mass loss rates for post-AGB stars in Schönberner & Steffen (2001)[171].

Further evidence of the exo-photospheric origin of the Hα absorption core comes from the periodogram analyses of the radial velocities. These clearly show that the variation in this feature has different periods to those of the

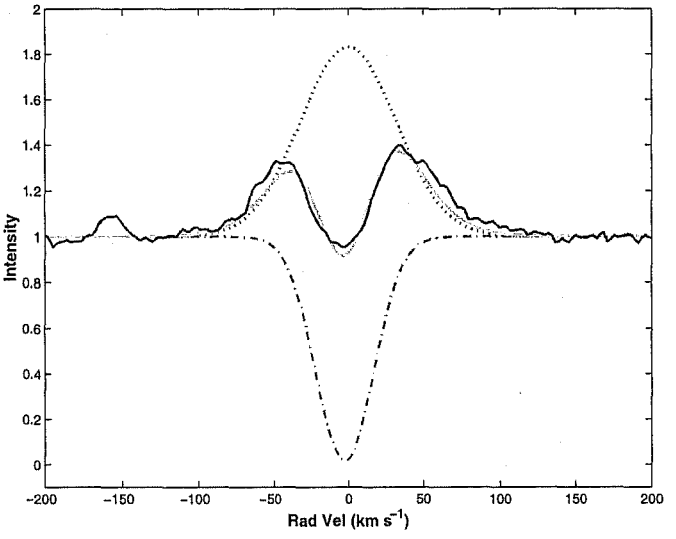

Figure 12.3: Gaussian fits to cool post-AGB star central Hα emission. The individual components are the broken lines, with solid lines representing the combined profile and a stellar line (darker). The components are explained in the text.

neutral metal lines and therefore does not form in the same layers. Although this is somewhat complicated by the emission which tends to "damp" the amplitude of the changes in Hα.

12.6 Sodium D line profiles

The Na D lines for these stars, shown in Figure 12.4, are complex, as one would expect for stars that show evidence of mass loss and whose sight lines cover several kiloparsecs of the Galaxy. However, these profiles generally lack a photospheric component, if we assume that they are composed of multiple absorptions. The absorptions closest to the systemic velocity, in general, are bisected by a local maximum very close to that velocity. An alternative model was explored in a number of cases to account for this which requires the peak to be due to an emission line which is superimposed upon a wide deep line, which incorporates the two smaller absorptions required in the former model. Both of these features had velocities similar to the systemic velocity, with the emission often being red-shifted, implying in-falling material. In some cases this produced a fit which did not conform to the shape of the profiles and required additional small features to adjust the shape of one side of the large absorption. Additionally some of the absorption features are too large to be due to photospheric sodium.

One possible resolution, inspired by AI CMi, is that the emission is blue-shifted, with respect to an unseen photospheric component. In deep minima, AI CMi shows many inverse P Cygni-like line profiles. They consist of a photospheric absorption and a narrow blue-shifted emission line. A strong emission is seen in the Na D lines too, which fades as the star brightens, in the same way as the other lines. This, plus a similar radial velocity means that these features are formed in the same parts of the stellar atmosphere. Thus for the Na D emission to be in-falling while the other similar lines are outflowing is not physically consistent.

If instead the sodium responsible for the emission is also outflowing from the star, then the large absorption can be broken into two sections, with one part photospheric and the other due to either circumstellar or interstellar clouds. This has been done in Figure 12.5, where the échelle spectrum from HJD 2451132 has been treated in this way. The fit has not been optimized as this new prescription requires three components to be fit to a section of profile which can also be fit with just two. Such two components may be able to fit the data but they do not reflect the underlying physical basis for the line shape, which is better expressed by three line.

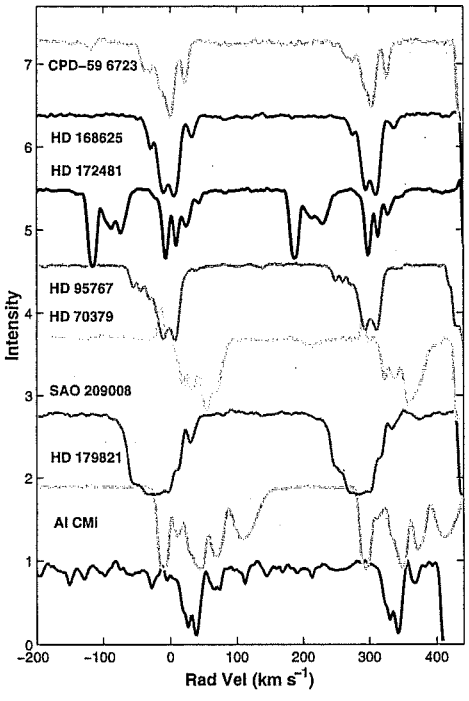

Figure 12.4: The Na D line profiles for the stars in this thesis.

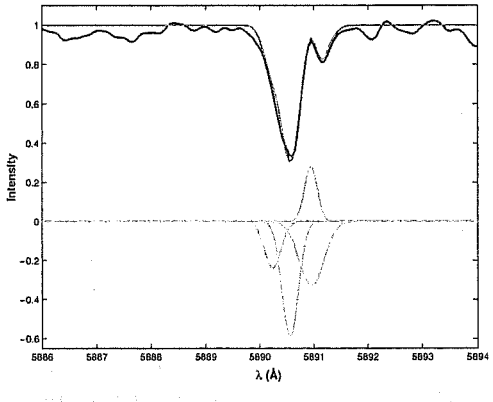

Figure 12.5: Compromise fit to the Na D_2 line of AI CMi. The fitted profile is shown with the observed and the components uses are displaced downwards.

For stars other than AI CMi it should be pointed out that, the F-stars in particular, show a number of emission features in other low excitation potential lines so that there is very likely to be a sodium emission component.

A number of interstellar features were identified from this effort though and it was possible to use some of them to assign lower limits for the distances to the stars (see Table 12.1).

Even with a resolving power of 42000 some of the profiles were unsuccessfully fit and it will need considerably higher resolution spectra to probe for a stellar line in between these two.

12.7 Evolutionary considerations

One of the clearest indicators of evolution on the AGB is the presence of lithium in a stellar atmosphere. Part of the the spectral region we monitored contained the Li I resonance line at 6708 Å. This is more of a problem for the cooler stars as this line is naturally stronger in their spectra due to its low excitation potential. Only HD 172481 has this line. At face value this would indicate that the star has been massive enough to recently have had the bottom of the convective envelope included in the nucleosynthesis reactions, under so-called hot bottom burning. However, the additional presence of a low-mass Mira companion, anomalous radial velocity, slightly low metallicity, require a lower mass object and the alternative cool bottom processing scenario to produce the lithium and transport it to the surface before it is destroyed in the central regions.

HD 168625 and HD 168607 are not post-AGB stars. They have luminosities which are very high and low radial velocities. There are similarities with post-AGB stars. HD 168607 had key spectral features, Hα and Fe II line profiles in particular, in common with CPD-59 6723.

HD 95767 has been regarded as a post-AGB star largely because it is an optically bright supergiant star with an infrared excess. This project has shown that the star is part of a binary system. Moreover it is this companion which causes the episodic mass loss that we see as a detached dust shell, taking what is probably a normal F-supergiant and making it look like a post-AGB star.

SAO 209008 is another star which has features in common with a likely post-AGB star, HD 179821. Both have the same contemporary mass loss regime as seen by their Hα profiles, similar temperatures and wide spectral lines. However, SAO 209008 does not appear to be as evolved as HD 179821. In Figure 12.6 we can see that the neutral carbon multiplet RMT 26 is

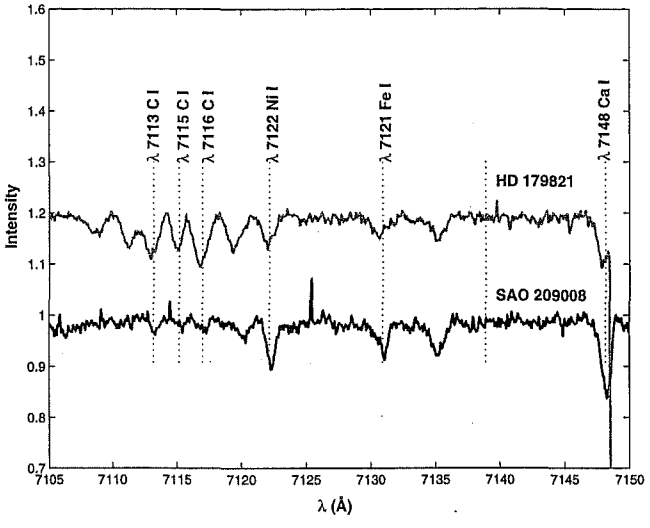

Figure 12.6: Comparison of C I (RMT 26) lines for SAO 209008 and HD 179821. The spectra have been shifted into the respective stellar rest frames.

clearly defined in HD 179821 but is almost absent from the spectrum of SAO 209008. Short of a full abundance analysis it would appear that SAO 209008 has not yet had the opportunity to dredge up some of the processed nuclear material from its central regions.

AI CMi exhibits unusual chemical abundances, high radial velocity and shares many photometric and spectroscopic variability patterns with RV Tauri stars, particularly R Scuti. The main difference is that the light curve does not show the pattern expected for RV Tauri stars of alternating deep and shallow minima. This is reflected in the periodograms which do not show a peak at twice the frequency of the principal.

12.8 Future work

Further investigation into the nature of such a heterogeneous group of stars is needed. This needs to proceed with both observational data and model predictions.

An extension of the work carried out in this project would suffice for some of the stars. For example determining the orbital period of HD 95767 and the time evolution of Hα in HD 168625.

Some of the work with the Na D lines can be resolved by observing the stars with the HERCULES spectrograph at different times of the year so that any night emission features lie outside of the profile. Further work observing nearby stars will also allow for a more accurate placement of interstellar features. This applies for the diffuse interstellar bands as well as the Na D lines. The stars which this technique will be most useful for are HD 168625, HD 168607 and SAO 209008, as they lie near open clusters which provide a benchmark in terms of a number of stars at a known distance.

This programme has collected time resolved spectroscopy and photometry which would be well supplemented by high quality, one-off spectra to further investigate aspects of the stars which are unresolved.

A number of the programme stars have yet to be observed for maser emission: HD 70379, CPD-59 6723 and HD 172481. Such observations would provide us with information about the circumstellar chemistry and the expansion velocities of the gas and dust shells. Infrared imaging would allow the mass loss history of HD 95767 (which may undergo periodic mass loss events) to be investigated. Although not a post-AGB star, its low surface gravity and infrared characteristics offer a chance to explore the mechanisms by which post-AGB stars can eject material. HD 172481, with its Mira companion, is a prime target for investigation with infrared imaging. As a binary star, is likely to show a complex structure in its circumstellar envelope.

Models also need to be developed that can explain the photometric and radial velocity variations in these stars. Of particular interest is HD 70379 which exhibits two periods of oscillation simultaneously. The outburst of HD 95767 is another individual event that remains to be fully explored. Modelling is also needed to derive reddenings and distances to these stars which incorporates the circumstellar environment.

Perhaps a wavelet and seasonal period analysis could be applied to the stars for which long base line photometry has been published. It has recently been drawn to my attention that as well as HD 179821, HD 168625 and HD 168607 have large photometric datasets available to be analysed in this way. For the other stars in this programme the sampling rate is too erratic for such analysis to be of use. Wavelet analysis has been used to show the evolution of different pulsational periods over time. This provides useful information for models of stellar structure.

Chapter 13

Acknowledgments

First and foremost, maximum respect to the trinity that put up with the inconsistencies of my work (in no particular order): Peter Cottrell, Karen Pollard and Michael Albrow. They somehow managed to hang in there and put up with my idiosyncrasies, as well as explaining how to acquire and manipulate spectra, and numerous discussions on what the stars were up to.

John Hearnshaw deserves a mention too for writing letters that got me money and general all around encouragement.

Alan Gilmore and Pam Kilmartin, for providing me with the photometry that comprised a big part of this project. And also for help with the foibles of the 1-m telescope. And the occasional roast. Also at the Mountain I'd like to thank Steve Barlow and Nigel Frost for keeping the bits working. Nige gets a special mention for the football he taped.

This project made use of the effort saving devices: Astrophysical Data Service; the SIMBAD database; Skyview; National Institute of Standards and Technology and Vienna Atomic Line Database. Thanks also to the writers and maintainers of the Starlink software used to manipulate spectra. And also to the folks at Matlab which was used to generate the graphs for the thesis.

I would like to thank the IAU and the Royal Society of New Zealand for paying the costs of my travel and accommodation for IAU Symposium 191 in Montpellier.

Thanks also to the graduate types for providing help and a few laughs. In particular to John Pritchard for putting up with my frequent requests for computer help. Orlon Peterson for help coping with vaguaries of the ECHOMOP. Stuart, Glen, Lyndon, Liz, and the rest of the crew for the odd bit of help but also the opportunity to spout gubbins and have a laugh.

Thanks to the Pooley family and MacKnight clans on both sides of the world for encouragement and cheap digs.

Most thanks to Janine, for sticking with me despite it taking so long.

Bibliography

[1] T. Aikawa. *Astrophys. J.*, 374:700, 1991.

[2] A. Arellano Ferro. *Rev. Mexicana Astronom. Astrofís.*, 11:113, 1985.

[3] A. Arellano Ferro, S. Giridhar, and A. Goswami. *Monthly Notices Roy. Astronom. Soc.*, 250:1, 1991.

[4] F. Arenou, M. Grenon, and A. Gómez. *Astronom. and Astrophys.*, 258:104, 1992.

[5] V. P. Arkhipova, N. P. Ikonnikova, R. I. Noskova, G.V. Sokol, and S.Y. Shugarov. *Astron. Letters*, 27:156, 2001.

[6] M. Asplund. In Le. Bertre et al. [113], page 481.

[7] P. W. Baker. *Publ. Astronom. Soc. Pacific*, 86:33, 1974.

[8] L. A. Balona. *Monthly Notices Roy. Astronom. Soc.*, 201:105, 1982.

[9] S. I. Barnes, M. Clark, P. L. Cottrell, J. B. Hearnshaw, O. K. L. Peterson, K. R. Pollard, J. D. Pritchard, A. Richards, and W. Tobin. *Southern Stars*, 39:1, 2000.

[10] D. Barthès, A. Lèbre, D. Gillet, and N. Mauron. *Astronom. and Astrophys.*, 359:168, 2000.

[11] S. A. Becker and I. Iben Jr. *Astrophys. J.*, 232:831, 1979.

[12] S. A. Becker and I. Iben Jr. *Astrophys. J.*, 237:111, 1980.

[13] T. R. Bedding, A. A. Zijlstra, A. Jones, and G. Foster. *Monthly Notices Roy. Astronom. Soc.*, 301:1073, 1998.

[14] A. P. Bernat and D. L. Lambert. *Publ. Astronom. Soc. Pacific*, 90:520, 1978.

[15] D. Bersier. *Astronom. and Astrophys.*, 308:514, 1996.

[16] M. S. Bessell. *Publ. Astronom. Soc. Pacific*, 91:589, 1979.

[17] T. Blöcker. PhD thesis, University of Kiel, 1993.

[18] T. Blöcker. *Acta Astron.*, 299:755, 1993.

[19] T. Blöcker. *Astronom. and Astrophys.*, 299:755, 1995.

[20] T. Blöcker. In Le. Bertre et al. [113], page 21.

[21] E. Bogaert. PhD thesis, Leuven University, Belgium, 1994.

[22] A. I. Boothroyd and I.-J. Sackmann. *Astrophys. J.*, 328:653, 1988.

[23] A. I. Boothroyd and I.-J. Sackmann. *Astrophys. J.*, 392:L71, 1992.

[24] A. I. Boothroyd and I.-J. Sackmann. *Astrophys. J.*, 510:232, 1999.

[25] A. I. Boothroyd, I.-J. Sackmann, and S. C. Ahern. *Astrophys. J.*, 416:762, 1993.

[26] V. Bujarrabal, J. Alcolea, and P. Planesas. *Astronom. and Astrophys.*, 257:701, 1992.

[27] E. M. Burbidge, G. R. Burbidge, W. A. Fowler, and F. Hoyle. *Rev. Mod. Phys.*, 29:547, 1957.

[28] A. G. W. Cameron. *Astrophys. J.*, 121:144, 1955.

[29] A. G. W. Cameron. *Astronom. J.*, 65:485, 1960.

[30] A. G. W. Cameron and W. A. Fowler. *Astrophys. J.*, 164:111, 1971.

[31] J. A. Cardelli, G. C. Clayton, and J. S. Mathis. *Astrophys. J.*, 345:245, 1989.

[32] B. S. Carter. *Monthly Notices Roy. Astronom. Soc.*, 242:1, 1990.

[33] J. N. Chengalur, B. M. Lewis, J. Eder, and Y. Terzian. *Astrophys. J. Suppl.*, 89:189, 1993.

[34] E. L. Chentsov and L. Luud. *Astrofizika*, 31:5, 1989.

[35] J. G. Cohen. *Astrophys. J.*, 203:L127, 1976.

[36] P. L. Cottrell and D. L. Lambert. *Astrophys. J.*, 261:595, 1982.

[37] Charles R. Cowley. *An introduction to cosmochemistry.* Cambridge University Press, 1995.

[38] A. N. Cox, editor. *Allen's astrophysical quantities.* Springer-Verlag, New York, 4th edition, 2000.

[39] P. David, A. M. Le Squeren, and P. Sivagnanam. *Astronom. and Astrophys.*, 277:453, 1993.

[40] C. de Jager. *Astronom. and Astrophys. Rev.*, 8:145, 1998.

[41] C. de Jager and H. Nieuwenhuijzen. *Astronom. and Astrophys.*, 177:217, 1987.

[42] J. F. Dean. *IAU Inform. Bull. Var. Stars*, 1892:1, 1980.

[43] W. Dehnen and J. J. Binney. *Monthly Notices Roy. Astronom. Soc.*, 298:387, 1998.

[44] B. T. Draine and H. M. Lee. *Astrophys. J.*, 285:89, 1984.

[45] J. R. Ducati, M. Bevilacqua, S. B. Rembold, and D. Ribeiro. *Astrophys. J.*, 558:309, 2001.

[46] A. K. Dupree, L. Hartmann, and E. H. Avrett. *Astrophys. J.*, 281:L37, 1984.

[47] O. J. Eggen. *Astrophys. J.*, 195:661, 1975.

[48] O. J. Eggen. *Astronom. J.*, 88:386, 1983.

[49] O. J. Eggen. *Astronom. J.*, 102:1826, 1991.

[50] O. J. Eggen. *Astronom. J.*, 103:1318, 1992.

[51] P. Ehrenfreund, J. Cami, E. Dartois, and B. H. Foing. *Astronom. and Astrophys.*, 317:L28, 1997.

[52] J. Einasto. Galactic mass modeling. In W. B. Burton, editor, *The large-scale characteristics of the galaxy*, IAU symposium 84, page 451, Dordrecht, 1979. IAU, D. Reidel Publishing Co.

[53] D. Engels and B. M. Lewis. *Astronom. Astrophys. Suppl. Ser.*, 116:117, 1996.

[54] A. Evans, C. M. Callus, J. S. Albinson, P. A. Whitelock, I. S. Glass, B. Carter, and G. Roberts. *Monthly Notices Roy. Astronom. Soc.*, 234:755, 1988.

[55] R. Faraggiana, M. Gerbaldi, C. van 't Veer, and M. Floquet. *Astronom. and Astrophys.*, 201:259, 1988.

[56] J. D. Fernie. *Astrophys. J.*, 243:576, 1981.

[57] J. D. Fernie. Luminous high-latitude stars. volume 45, page 253, San Francisco, 1993. Astron. Soc. Pac.

[58] J. D. Fernie and D. D. Sasselov. *Publ. Astronom. Soc. Pacific*, 101:513, 1989.

[59] M. P. Fitzgerald. *Astronom. J.*, 73:983, 1968.

[60] A. B. Fokin, A. Lèbre, H. Le Coroller, and D. GIllet. *Astronom. and Astrophys.*, 378:546, 2001.

[61] T. Fujii, Y. Nakada, and M. Parthasarathy. *Astronom. and Astrophys.*, 385:894, 2002.

[62] P. García-Lario, A. Manchado, S. R. Pottasch, J. Suso, and R. Olling. *Astronom. Astrophys. Suppl. Ser.*, 82:497, 1990.

[63] P. García-Lario, T. Sivarani, M. Parthasarathy, and A. Manchado. Post-agb objects as a phase of stellar evolution. In Szczerba and Górny [180], page 309.

[64] A. Gautschy. *Monthly Notices Roy. Astronom. Soc.*, 265:340, 1993.

[65] A. Gautschy and H. Saio. *Ann. Rev. Astron. & Astrophys.*, 34:551, 1996.

[66] D. Gillet, A. Duquennoy, P. Bouchet, and C. Gouiffes. *Astronom. and Astrophys.*, 215:316, 1989.

[67] D. Gillet, E. Maurice, P. Bouchet, and R. Ferlet. *Astronom. and Astrophys.*, 148:155, 1985.

[68] S. Giridhar, A. Arellano Ferro, and P. Mathias. *Bull. Astron. Soc. India*, 29:289, 2001.

[69] S. Giridhar, A. Arellano Ferro, and L. Parrao. *Publ. Astronom. Soc. Pacific*, 109:1077, 1997.

[70] T. M. Gledhill, A. Chrysostomou, J. H. Hough, and J. A. Yates. *Monthly Notices Roy. Astronom. Soc.*, 322:321, 2001.

[71] T. M. Gledhill and M. Takami. *Astronom. and Astrophys.*, 328:266, 2001.

[72] R. O. Gray. *Astronom. and Astrophys.*, 265:704, 1992.

[73] R. O. Gray and E. H. Olsen. *Astronom. Astrophys. Suppl. Ser.*, 87:541, 1991.

[74] H. J. Habing. *Astronom. and Astrophys. Rev.*, 7:97, 1996.

[75] J. Hakkila, J. M. Myers, B. J. Stidham, and D. H. Hartman. *Astronom. J.*, 114:204, 1997.

[76] A. Harpaz. *Stellar evolution.* A K Peters, Wellesley, Massachusetts, 1994.

[77] J. B. Hearnshaw. *Proc. Astronom. Soc. Australia*, 3:102, 1977.

[78] J. B. Hearnshaw, S. I. Barnes, G. M. Kershaw, N. Frost, G. Graham, R. Ritchie, and G. R. Nankivell. *Experimental Astronomy*, 13:59, 2002.

[79] G. H. Herbig. *Astrophys. J.*, 196:129, 1975.

[80] G. H. Herbig. *Ann. Rev. Astron. & Astrophys.*, 33:19, 1995.

[81] R. H. Hildebrand. *Q. J. Roy. Astron. Soc.*, 24:267, 1983.

[82] P. W. Hill, D. Kilkenny, and I. G. van Breda. *Monthly Notices Roy. Astronom. Soc.*, 168:451, 1974.

[83] R. W. Hiltner. *Astrophys. J. Suppl.*, 2:389, 1956.

[84] R. W. Hobbs. *Astronom. J.*, 66:517, 1961.

[85] J. H. Horne and S. L. Baliunas. *Astrophys. J.*, 302:757, 1986.

[86] S. B. Howell, B. W. Bopp, and P. V. Noah. *Astronom. J.*, 95:762, 1983.

[87] B. J. Hrivnak, S. Kwok, and K .M. Volk. *Astrophys. J.*, 346:265, 1989.

[88] B. Hrivnak et al. Post-agb objects as a phase of stellar evolution. In Szczerba and Górny [180], page 101.

[89] R. M. Humphreys. *Astronom. Astrophys. Suppl. Ser.*, 19:243, 1975.

[90] D. Hutsemékers and E. Van Drom. *Astronom. and Astrophys.*, 248:141, 1991.

[91] D. Hutsemékers, E. Van Drom, G. Gosset, and J. Melnick. *Astronom. and Astrophys.*, 290:906, 1994.

[92] I. Iben Jr and A. Renzini. *Astrophys. J.*, 259:L79, 1982.

[93] C. Jaschek and M. Jaschek. *The behaviour of chemical elements in stars.* Cambridge University Press, 1995.

[94] L. Jeannin, A. B. Fokin, D. Gillet, and I. Baraffe. *Astronom. and Astrophys.*, 314:L1, 1996.

[95] P. Jenniskens and F.-X. Désert. *Astronom. Astrophys. Suppl. Ser.*, 106:39, 1994.

[96] S. Johansson. *Phys. Scr.*, 18:217, 1978.

[97] S. Johansson and C. Jordan. *Monthly Notices Roy. Astronom. Soc.*, 210:239, 1984.

[98] A. Jorissen. In Le. Bertre et al. [113], page 437.

[99] E. Josselin and A. Lèbre. *Astronom. and Astrophys.*, 367:826, 2001.

[100] M. Jura, T. Velusamy, and M. W. Werner. *Astrophys. J.*, 556:408, 2001.

[101] M. Jura and M. W. Werner. *Astrophys. J.*, 525:L113, 1999.

[102] P. C. Keenan and J. A. Hynek. *Astrophys. J.*, 111:1, 1950.

[103] P. N. Kholopov, editor. *General catalogue of variable stars.* Nauka Publishing House, Moscow, 1985.

[104] D. Kilkenny and P. H. Hill. *Monthly Notices Roy. Astronom. Soc.*, 172:649, 1975.

[105] D. Kilkenny, P. H. Hill, and Th. Schmidt-Kaler. *Monthly Notices Roy. Astronom. Soc.*, 171:353, 1975.

[106] V. G. Klochkova and V. E. Panchuk. *Bull. Special Astrophys. Obs.*, 14:5, 1996.

[107] V. G. Klochkova, V. E. Panchuk, and E. L. Chentsov. *Astronom. and Astrophys.*, 323:789, 1997.

[108] J. R. Kozok. *Astronom. Astrophys. Suppl. Ser.*, 62:7, 1985.

[109] S. Kwok, K. Y. L. Su, and J. A. Stoesz. Post-agb objects as a phase of stellar evolution. In Szczerba and Górny [180], page 115.

[110] D. L. Lambert, K. H. Hinkle, and R. E. Luck. *Astrophys. J.*, 333:917, 1988.

[111] J. C. Lattanzio. In R. Weinberger and A. Acker, editors, *Planetary Nebulae*, volume 155, page 235. I.A.U., 1993.

[112] J. C. Lattanzio. In *2nd Oak Ridge Symp. on atomic and nuclear astrophysics.* IOP Publishing Ltd, 1997.

[113] T. Le. Bertre, A. Lèbre, and C. Waelkens, editors. IAU Symposium 191, San Fransisco, 1999. Astronomical society of the Pacific.

[114] H. Le Coroller, A. Lébre, D. Gillet, and E. Chapellier. *Astronom. and Astrophys.*, 400:613, 2003.

[115] A. Lèbre, N. Mauron, D. Gillet, and D. Barthès. *Astronom. and Astrophys.*, 310:923, 1996.

[116] H.-W. Lee. *Astrophys. J.*, 541:L25, 2000.

[117] R. S. Lewis, S. Amari, and E. Anders. *Nature*, 348:293, 1990.

[118] L. Likkel. *Astrophys. J.*, 344:350, 1989.

[119] C. Livingstone. Analysing the light curve and spectra of nova sagittarius 1999. Master's thesis, University of Canterbury, 2000.

[120] M. Livio and N. Soker. *Astrophys. J.*, 329:764, 1988.

[121] N. R. Lomb. *Astrophys. and Space Sci.*, 39:447, 1976.

[122] S. H. Lublow and P. Artymowicz. In A. Duquennoy and M. Mayor, editors, *Binaries as tracers of stellar formation*, page 145, Cambridge, 1992. Cambridge University Press.

[123] R. E. Luck and H. E. Bond. *Astrophys. J.*, 342:476, 1989.

[124] M. Lugaro, F. Herwig, J. C. Lattanzio, R. Gallino, and O. Straniero. *Astrophys. J.*, 586:1305, 2003.

[125] D. J. MacConnell and W. P. Bidelmann. *Astronom. J.*, 81:225, 1976.

[126] E. A. Mallia and B. E. J. Pagel. *Monthly Notices Roy. Astronom. Soc.*, 184:55, 1978.

[127] A. Manchado, S. R. Pottasch, P. García-Lario, C. Esteban, and A. Mampaso. *Astronom. and Astrophys.*, 214:139, 1989.

[128] N. Markova. *Astronom. Astrophys. Suppl. Ser.*, 144:391, 2000.

[129] P. Massey, K. Degoiia-Eastwood, and E. Waterhouse. *Astronom. J.*, 121:1050, 2001.

[130] D. Mihalas and J. Binney. *Galactic astronomy: Structure and kinematics.* W. H. Freeman & Co., San Francisco, USA, 2nd edition, 1981.

[131] D. Minniti, J. Liebert, E. W. Olszewski, and White S. D. M. *Astronom. J.*, 112:590, 1996.

[132] A. S. Miroschnichenko, J. Fabregat, K. S. Bjorkman, D. C. Knauth, N. D. Morrison, A. E. Tarasov, P. Reig, I. Negueruela, and P. Blay. *Astronom. and Astrophys.*, 377:485, 2001.

[133] A. F. J. Moffat, M. P. Fitzgerald, and P. D. Jackson. *Astrophys. J.*, 215:106, 1977.

[134] C. E. Moore. *A multiplet table of astrophysical interest.* National Bureau of Standards, Washington D. C., 1972.

[135] W. W. Morgan, Code A. D., and A. E. Whitford. *Astrophys. J. Suppl.*, 2:41, 1955.

[136] G. Nave., S. Johansson, R. C. M. Learner, A. P. Thorne, and Brault. J. W. *Astrophys. J. Suppl.*, 94:221, 1994.

[137] Th. Neckel, G. Klare, and M. Sarcander. *Astronom. Astrophys. Suppl. Ser.*, 42:251, 1980.

[138] A. Nota, A. Pasquali, M. Clampin, D. Pollacco, S. Scuderi, and M. Livio. *Astrophys. J.*, 473:946, 1996.

[139] L.-A. Nyman, R. S. Booth, U. Carlstrom, H. J. Habing, A. Heske, R. Sahai, R. Stark, W. E. C. J. van der Veen, and A. Winnberg. *Astronom. Astrophys. Suppl. Ser.*, 93:121, 1992.

[140] S. F. Odenwald. *Astrophys. J.*, 307:711, 1986.

[141] A. Omont, C. Loup, T. Forveille, P. te Lintel Hekkert, H. Habing, and P. Sivagnanam. *Astronom. and Astrophys.*, 267:515, 1993.

[142] P. S. Osmer. *Astrophys. J. Suppl.*, 24:247, 1972.

[143] D. E. Osterbrock, J. P Fulbright, A. R. Martel, M. J. Keane, S. C. Trager, and G. Basri. *Publ. Astronom. Soc. Pacific*, 108:277, 1996.

[144] R. D. Oudmaijer. *Astronom. and Astrophys.*, 306:823, 1996.

[145] R. D. Oudmaijer, W. E. C. J. van der Veen, L. B. F. M. Waters, N. R. Trams, C. Waelkens, and E. Engelsman. *Astronom. Astrophys. Suppl. Ser.*, 96:625, 1992.

[146] B. Paczyński. *Astrophys. J.*, 202:558, 1975.

[147] M. Parthasarathy, J. Vijapurkar, and J. S. Drilling. *Astronom. Astrophys. Suppl. Ser.*, 145:269, 2000.

[148] A. Pasquali, A. Nota, L. J. Smith, S. Akiyama, M. Messineo, and M. Clampin. *Astronom. J.*, 124:1625, 2002.

[149] R. W. B. Pearse and A. G. Gaydon. *The identification of molecular spectra*, volume 4th ed. Chapman and Hall, 1976.

[150] M. A. C. Perryman, L. Lindegren, J. Kovalevsky, E. Høg, U. Bastian, P. L. Bernacca, M. Crézé, F. Donati, M. Grenon, F. van Leeuwen, H. van der Marel, F. Mignard, C. A. Murray, R. S. Le Poole, H. Schrijver, C. Turon, F. Arenou, M. Froeschlé, and C. S. Petersen. *Astronom. and Astrophys.*, 323:49L, 1997.

[151] A. K. Pierce and J. B. Breckenridge. *Kitt Peak National Observatory*, 1974.

[152] N. E. Piskunov, F. Kupka, T. A. Ryabchikova, W. W. Weiss, and C. S. Jeffery. *Astronom. Astrophys. Suppl. Ser.*, 112:525, 1995.

[153] D. J. Pooley, P. L. Cottrell, K. R. Pollard, and M. D. Albrow. In Le. Bertre et al. [113], page 618.

[154] D. J. Pooley, P. L. Cottrell, K. R. Pollard, and M. D. Albrow. Astronomical society of Australia, 2000.

[155] D. M. Popper and C. K. Seyfert. *Publ. Astronom. Soc. Pacific*, 52:401, 1940.

[156] S. R. Pottasch and M. Parathasarathy. *Astronom. and Astrophys.*, 192:182, 1988.

[157] D. Prialnik. *Introduction to the theory of stellar structure and evolution.* Cambridge University Press, Cambridge, 2000.

[158] B. E. Reddy and B. J. Hrivnak. *Astronom. J.*, 117:1834, 1999.

[159] B. E. Reddy and M. Parthasarathy. *Astronom. J.*, 112:2053, 1996.

[160] D. Reimers. In B. Baschek, W. H. Kegel, and G. Traving, editors, *Problems in stellar atmospheres and envelopes*, page 229, Berlin, 1975. Springer.

[161] A. Renzini. Physical processes in red giants. page 431. Dordrecht:Reidel, 1981.

[162] M. Reyniers and H. Van Winckel. *Astronom. and Astrophys.*, 365:465, 2001.

[163] M. Robberto and T. M. Herbst. *Astrophys. J.*, 498:400, 1998.

[164] F. J. Rogers and C. A. Iglesias. *Science*, 263:50, 1994.

[165] I.-J. Sackmann and A. I. Boothroyd. *Astrophys. J.*, 392:L71, 1992.

[166] J. D. Scargle. *Astrophys. J.*, 263:835, 1982.

[167] H. Scheffler and H. Elsässer. *Physics of the Galaxy and interstellar matter.* Springer-Verlag, Berlin, 1988.

[168] R. E. Schild, R. F. Garrison, and W. A. Hiltner. *Astrophys. J. Suppl.*, 51:321, 1983.

[169] D. Schönberner. *Astronom. and Astrophys.*, 79:108, 1979.

[170] D. Schönberner. *Astrophys. J.*, 272:708, 1983.

[171] D. Schönberner and M. Steffen. Post-agb objects as a phase of stellar evolution. In Szczerba and Górny [180], page 85.

[172] M. Schwarzschild. In P. T. Oosterhoff, editor, *Transactions of the IAU Vol VIII*, page 811. Cambridge University Press, 1952.

[173] M. Schwarzschild and Härm R. *Astrophys. J.*, 142:855, 1965.

[174] D. Sinachopoulos. *Astronom. Astrophys. Suppl. Ser.*, 76:189, 1988.

[175] G. H. Smith and A. K. Dupree. *Astronom. J.*, 95:1547, 1988.

[176] B. T. Soifer, W. L. Rice, J. R. Mould, F. C. Gillet, M. Rowan Robinson, and H. J. Habing. *Astrophys. J.*, 304:651, 1986.

[177] M. Steffen and D. Schönberner. Post-agb objects as a phase of stellar evolution. In Szczerba and Górny [180], page 131.

[178] C. Sterken. *Astronom. and Astrophys.*, 57:361, 1977.

[179] C. Sterken, T. Arentoft, H. W. Duerbeck, and E. Brogt. *Astronom. and Astrophys.*, 349:532, 1999.

[180] R. Szczerba and S. K. Górny, editors. *Post-AGB objects as a phase of stellar evolution*, volume 265 of *ASSL*. Kluwer Academic Publishers, 2001.

[181] J. H. Taylor and J. M. Cordes. *Astrophys. J.*, 411:674, 1993.

[182] P. te Lintel Hekkert, J. L. Casswell, H. J. Habing, R. F. Haynes, and R. P. Norris. *Astronom. Astrophys. Suppl. Ser.*, 327:90, 1991.

[183] F. Thévenin, G. Jasniewicz, and M. Parthasarathy. *Astronom. and Astrophys.*, 359:138, 2000.

[184] W. Tobin, J. B. Hearnshaw, and R. Ritchey. *Southern Stars*, 37:197, 1998.

[185] N. R. Trams. *Astronom. and Astrophys.*, 218:L1, 1989.

[186] N. R. Trams, L. B. F. M. Waters, and C. Waelkens. *Astronom. Astrophys. Suppl. Ser.*, 87:361, 1991.

[187] Y. Tuchman, A. Lèbre, M. O. Mennessier, and A. Yarri. *Astronom. and Astrophys.*, 271:501, 1993.

[188] J. A. Valenti, N. Piskunov, and C. M. Johns-Krull. *Astrophys. J.*, 498:851, 1998.

[189] S. van den Bergh. *J. Roy. Astron. Soc. Can.*, 82:13, 1988.

[190] W. E. C. J. van der Veen and H. J. Habing. *Astronom. and Astrophys.*, 194:125, 1988.

[191] W. E. C. J. van der Veen, H. J. Habing, and T. R. Geballe. *Astronom. and Astrophys.*, 226:108, 1989.

[192] W. E. C. J. van der Veen, N. R. Trams, and L. B. F. M. Waters. *Astronom. and Astrophys.*, 269:231, 1993.

[193] A. M. van Genderen. *Astronom. and Astrophys.*, 88:77, 1980.

[194] A. M. van Genderen and P. S. Thé. *Astronom. and Astrophys.*, 64:L1, 1978.

[195] A. M. van Genderen, F. C. van den Bosch, F. Dessing, G. C. Fehmers, J. van Grunsven, R. van der Heiden, A. M. Janssens, R. Kalter, R. L. J. van der Meer, R. van Ojik, J. M. Smit, and M. J. Zijdeveld. *Astronom. and Astrophys.*, 264:88, 1992.

[196] P. A. M. van Hoof, R. D. Oudmaijer, and Waters. L. B. F. M. *Monthly Notices Roy. Astronom. Soc.*, 289:371, 1997.

[197] F. van Leeuwen, A. M. van Genderen, and I. Zegelaar. *Astronom. Astrophys. Suppl. Ser.*, 128:117, 1998.

[198] H. van Winckel. *Astronom. and Astrophys.*, 319:561, 1997.

[199] H. Van Winckel. In Le. Bertre et al. [113], page 465.

[200] H. Van Winckel, C. Waelkens, and Waters. L. B. F. M. *Astronom. and Astrophys.*, 293:L25, 1995.

[201] H. Van Winckel, C. Waelkens, and L. B. F. M. Waters. *Astronom. and Astrophys.*, 306:L37, 1996.

[202] E. Vassiliadis and P. R. Wood. *Astrophys. J.*, 413:641, 1993.

[203] K. A. Venn. *Astrophys. J.*, 449:839, 1995.

[204] K. A. Venn and D. L. Lambert. *Astrophys. J.*, 363:234, 1990.

[205] K. A. Venn, S. J. Smartt, D. J. Lennon, and P. L. Dufton. *Astronom. and Astrophys.*, 334:987, 1998.

[206] K. M. Volk and S. Kwok. *Astrophys. J.*, 315:654, 1987.

[207] K. M. Volk and S. Kwok. *Astrophys. J.*, 342:345, 1989.

[208] G. Von Helden, A. G. G. M. Tielens, D. Van Heijensbergen, M. A. Duncan, S. Hony, L. B. F. M. Waters, and G. Meijer. *Science*, 288:313, 2000.

[209] G. Wallerstein, T. S. Jacobsen, P. L. Cottrell, M. Clark, and M. D. Albrow. *Monthly Notices Roy. Astronom. Soc.*, 259:474, 1992.

[210] G. J. Wasserburg, A. I. Boothroyd, and I.-J. Sackmann. *Astrophys. J.*, 447:L37, 1995.

[211] L. B. F. M. Waters, F. J. Molster, T. de Jong, D. A. Beintema, and et al. *Astronom. and Astrophys.*, 315:L361, 1996.

[212] L. B. F. M. Waters, C. Waelkens, M. Mayor, and N. R. Trams. *Astronom. and Astrophys.*, 269:242, 1993.

[213] P. Whitelock and F. Marang. *Monthly Notices Roy. Astronom. Soc.*, 323:L13, 2001.

[214] D. Whittet and I. G. van Breda. *Monthly Notices Roy. Astronom. Soc.*, 192:467, 1980.

[215] W. J. Wilson, P. R Schwartz, G. Neugebauer, P. M. Harvey, and E. E. Becklin. *Astrophys. J.*, 177:523, 1972.

[216] B. Wolf and O. Stahl. Inverse p cygni-type profiles in the spectrum of the luminous blue variable s doradus. *Astronom. and Astrophys.*, 235:340, 1990.

[217] J. Zalewski. Pulsational properties of post-agb stars. *Acta Astron*, 43:431, 1993.

[218] L. Začs, V. E. Klochkova, V. E. Panchuk, and R. Spēlmanis. *Monthly Notices Roy. Astronom. Soc.*, 282:1171, 1996.

[219] L. Začs, M. R. Schmidt, and R. Szczerba. *Astronom. and Astrophys.*, 306:903, 1999.

[220] M. Zeilik and E. v. P. Smith. *Introductory astronomy and astrophysics.* Saunders College, Philadelphia, 1987.

[221] E. Zinner and S. Amari. In Le. Bertre et al. [113], page 59.

[222] B. Zuckerman and H. M. Dyck. *Astrophys. J.*, 311:345, 1986.

[223] B. Zuckerman and K. Y. Lo. *Astronom. and Astrophys.*, 173:263, 1987.

Appendix A

Photometric data for post-AGB stars

This appendix contains the tabulated V-band and colour photometry for the programme post-AGB stars. They are presented in the same order as the respective chapters. The column HJD refers to the heliocentric Julian Date of the observation (−2450000). A dash indicates that that datum was too inconsistent and was culled.

Table A.1: AI CMi photometry from MJUO.

HJD	V	$(B-V)$	$(V-R)$	$(V-I)$
0876.0369	8.441	1.592	0.805	1.700
0907.9470	8.085	1.604	0.839	1.659
0919.9527	8.003	1.616	0.852	1.559
0921.9564	7.997	1.616	0.852	-
0938.8440	8.094	1.655	0.870	-
0944.8769	8.178	1.688	0.890	1.602
1145.0590	9.343	1.282	0.678	1.851
1158.1121	9.163	1.336	0.669	1.900
1203.1007	8.741	1.396	0.709	1.773
1205.0668	8.730	1.409	0.719	1.771
1211.0428	8.658	1.425	0.731	1.772
1211.9148	8.651	1.428	0.729	1.780
1221.0629	8.564	1.467	0.752	1.756
1227.0585	8.564	1.500	0.764	1.756

continued over

Table A.1: *continued*

HJD	V	$(B-V)$	$(V-R)$	$(V-I)$
1230.9630	8.578	1.514	0.767	1.742
1236.9737	8.627	1.568	0.725	1.718
1238.9772	8.698	1.553	0.762	1.808
1248.9832	8.874	1.526	0.747	1.873
1254.9502	8.896	1.542	0.754	1.889
1263.9173	8.956	1.613	0.791	1.913
1268.9379	8.820	1.553	0.768	1.867
1272.9309	8.754	1.591	0.761	1.815
1276.8831	8.717	1.582	0.764	1.837
1279.9103	8.718	1.582	0.777	1.839
1294.8422	8.577	1.652	0.815	1.790
1301.8814	8.496	1.689	0.822	1.760
1306.8388	8.405	1.696	0.846	1.738
1308.8702	8.380	1.686	0.840	1.701
1315.8220	8.446	1.711	0.840	1.749
1426.2439	8.259	1.608	0.780	1.658
1450.1845	8.067	1.614	0.817	1.676
1476.1529	8.287	1.606	0.805	1.723
1505.0539	8.469	1.589	0.802	1.760
1529.0501	8.396	1.650	0.816	1.752
1552.1439	8.460	1.624	0.806	1.728
1570.0924	8.271	1.597	0.800	1.599
1575.0600	8.169	1.576	0.794	1.562
1593.0145	7.984	1.609	0.815	1.531
1596.9280	8.005	1.617	0.820	1.546
1600.9773	8.029	1.621	0.791	-
1605.9679	8.048	1.645	0.819	1.565
1611.9326	8.120	1.632	0.821	1.588
1617.8971	8.231	1.626	0.817	1.650
1622.9172	8.346	1.616	0.807	1.660
1628.9572	8.441	1.592	0.805	1.718
1661.8803	8.632	1.534	0.789	1.794
1672.8489	8.640	1.543	0.792	1.795
1674.8686	8.647	1.520	0.781	1.797
1685.8305	8.775	1.530	0.782	1.818
1690.8233	8.928	1.476	0.790	1.895

continued over

Table A.1: *continued*

HJD	V	$(B-V)$	$(V-R)$	$(V-I)$
1852.1304	9.530	1.401	0.732	1.898
1854.0702	9.493	1.406	0.721	1.875
1878.0085	8.914	1.400	0.709	1.882
1897.0465	8.336	1.526	0.798	1.740
1916.0364	8.131	1.622	0.829	1.648
1920.9579	8.133	1.648	0.826	1.626
1928.0522	8.234	1.657	0.842	1.660
1930.9597	8.276	1.660	0.831	1.659
1939.0326	8.396	1.629	0.840	1.693
1957.9567	8.661	1.604	0.819	1.761
1960.9617	8.706	1.647	0.829	1.818
1975.8991	8.755	1.562	0.864	1.967
1977.9587	8.793	1.577	0.792	1.859
1978.8837	8.810	1.573	0.797	1.858
1982.9286	8.919	1.536	0.807	1.903
1983.8507	8.937	1.560	0.791	1.911
1984.9703	8.957	1.564	0.771	1.910
1987.9886	9.036	1.526	0.787	1.951
1988.9315	9.043	1.540	0.787	1.947
1990.9702	9.064	1.512	0.776	1.958
1991.9104	9.072	1.506	0.774	1.952
1998.9582	9.091	1.414	0.748	1.929
2003.8824	9.252	1.351	0.719	1.965
2006.9077	9.336	1.308	0.703	1.968
2012.9100	9.412	1.247	0.688	1.907
2020.9260	9.502	1.235	0.678	1.925
2043.8148	9.507	1.261	0.670	1.904
2052.8365	9.503	1.330	0.680	1.978
2058.8106	9.513	1.343	0.700	1.995
2177.2038	8.476	1.491	0.769	1.790
2219.0665	8.387	1.572	0.813	1.651
2229.0943	-	1.567	0.795	1.643
2256.0309	8.244	1.636	0.818	1.600
2298.0799	8.724	1.503	0.750	1.833
2306.9553	8.966	1.463	0.699	1.865
2319.9609	9.309	1.362	0.688	1.857

continued over

Table A.1: *continued*

HJD	V	$(B-V)$	$(V-R)$	$(V-I)$
2320.9331	9.325	1.354	0.698	1.855
2321.9437	9.336	1.345	0.668	1.823
2333.9238	9.258	1.286	0.641	1.733
2338.9766	9.225	1.267	0.653	1.728

Table A.2: HD 179821 photometry from MJUO.

HJD	V	$(B-V)$	$(V-R)$	$(V-I)$
0737.9313	8.089	1.598	0.811	1.622
0742.8877	8.064	1.595	0.814	1.676
0922.1193	8.044	1.537	0.794	1.602
0943.2083	7.999	1.518	0.776	1.598
0948.1046	7.993	1.519	0.786	1.585
0950.1374	7.993	1.519	0.792	1.588
0981.1337	7.970	1.502	0.785	1.607
0985.1380	7.963	1.509	0.776	1.571
0992.1520	7.972	1.512	0.783	1.569
0998.0936	7.975	1.519	0.773	1.571
1013.0436	8.002	1.521	0.806	1.602
1029.0239	7.988	1.535	0.817	1.632
1043.9351	8.008	1.532	0.814	1.638
1084.9155	7.969	1.521	0.784	1.567
1303.2065	7.950	1.544	0.811	1.640
1309.2259	7.943	1.526	0.791	1.615
1336.1779	7.988	1.528	0.812	1.638
1369.1011	7.957	1.532	0.815	1.640
1374.0676	7.945	1.525	0.817	1.641
1380.1154	7.932	1.534	0.813	1.634
1384.1508	7.927	1.514	0.813	1.630
1398.0866	7.917	1.512	0.802	1.610
1408.0406	7.905	1.493	0.811	1.605
1414.0639	7.910	1.498	0.799	1.617
1448.9375	7.996	1.536	0.839	1.650
1630.2169	7.991	1.544	0.827	1.646

continued over

Table A.2: *continued*

HJD	V	$(B-V)$	$(V-R)$	$(V-I)$
1688.1729	8.043	1.549	0.834	1.659
1715.2075	8.028	1.540	0.809	1.632
1727.1109	8.033	1.545	0.824	1.659
1731.1972	8.029	1.531	0.820	1.663
1749.0565	7.989	1.540	0.819	1.637
1770.0970	7.943	1.526	0.813	1.630
1799.0187	7.893	1.499	0.792	1.599
2014.2270	7.947	1.528	0.800	1.612
2055.1277	8.027	1.495	0.795	1.597
2066.1824	8.038	1.490	0.801	1.608
2115.0819	7.920	1.446	0.774	1.566
2137.9985	7.958	1.477	0.789	1.596

Table A.3: HD 70379 photometry from MJUO.

HJD	V	$(B-V)$	$(V-R)$	$(V-I)$
0907.9882	8.996	0.707	0.423	0.768
0910.0193	8.977	0.689	0.413	0.783
0920.0018	8.851	0.601	0.376	0.713
0922.0391	8.815	0.625	0.377	0.670
0922.9707	8.832	0.603	0.356	0.716
0937.9125	8.854	0.588	0.343	0.673
0941.9566	8.897	0.622	0.364	0.718
0944.9147	8.934	0.629	0.384	0.728
0947.9166	8.981	0.652	0.382	0.739
0949.9642	8.998	0.724	0.371	0.723
0960.8829	9.200	0.765	0.465	0.875
0961.8792	9.210	0.791	0.435	0.813
0967.9088	9.267	0.850	0.449	0.844
0968.8722	9.280	0.831	0.466	0.868
1145.0131	9.067	0.726	0.428	0.801
1203.1277	9.030	0.682	0.417	0.774
1204.1226	9.032	0.693	0.412	0.778
1205.0939	9.027	0.687	0.406	0.773

continued over

Table A.3: *continued*

HJD	V	$(B-V)$	$(V-R)$	$(V-I)$
1211.1049	9.028	0.687	0.402	0.777
1213.0542	9.038	0.707	0.404	0.765
1218.0790	9.030	0.686	0.403	0.774
1221.1474	9.039	0.674	0.395	0.761
1231.0184	9.046	0.706	0.410	0.791
1239.0349	9.079	0.706	0.428	0.801
1249.0557	9.073	0.709	0.425	0.811
1261.9941	8.997	0.680	0.415	-
1268.9566	8.912	0.646	0.367	0.725
1271.9037	8.933	0.635	0.380	0.724
1276.9470	8.960	0.641	0.383	0.738
1294.8874	9.066	0.701	0.414	0.794
1301.9003	9.100	0.734	0.440	0.794
1306.9331	9.120	0.739	0.440	-
1496.1012	9.067	0.724	0.426	0.802
1505.0833	9.029	0.716	0.415	0.794
1557.0561	9.104	0.733	0.434	0.798
1575.0829	9.178	0.765	0.450	0.830
1593.0382	9.013	0.689	0.420	0.788
1606.0608	8.839	0.581	0.357	0.701
1619.9583	8.856	0.579	0.358	0.681
1628.9892	8.946	0.622	0.376	0.710
1663.8566	9.196	0.784	0.448	0.834
1672.9123	9.124	0.747	0.449	0.841
1685.8665	8.986	0.687	0.416	0.780
1720.8345	8.918	0.656	0.367	0.698
1725.8207	8.954	0.675	0.378	0.758
1730.8170	9.034	0.678	0.422	0.783
1853.0728	9.015	0.688	0.413	0.785
1896.1308	8.987	0.691	0.401	0.766
1916.1422	8.992	0.669	0.404	0.769
1921.0496	8.972	0.687	0.395	0.757
1928.0813	8.978	0.688	0.406	0.763
1930.9774	8.990	0.687	0.417	0.783
1939.0885	8.986	0.688	0.421	0.783
1959.0255	9.041	0.708	0.426	0.792

continued over

Table A.3: *continued*

HJD	V	$(B-V)$	$(V-R)$	$(V-I)$
1977.9964	9.027	0.711	0.411	0.784
1978.9638	9.035	0.700	0.419	0.800
1982.9928	9.046	0.712	0.417	0.798
1988.0484	9.056	0.712	0.418	0.810
1991.9464	9.035	0.699	0.413	0.798
1999.0547	9.024	0.679	0.419	0.797
2006.0030	8.982	0.679	0.405	0.786
2012.9612	8.938	0.690	0.391	0.772
2021.0039	8.905	0.669	0.392	-
2043.8958	8.962	0.663	0.395	0.761
2052.8756	8.997	0.693	0.419	0.778
2058.9333	9.025	0.686	0.444	0.813
2065.8676	9.077	0.706	0.448	0.813
2071.8380	9.110	0.721	0.415	0.788
2219.0922	8.957	0.666	0.393	0.743
2256.1156	8.997	0.663	0.404	0.751
2298.1264	9.122	0.762	0.428	0.815
2320.0598	8.974	0.676	0.392	0.757
2321.0274	8.968	0.670	0.403	0.768
2339.0496	8.928	0.658	0.393	0.751

Table A.4: HD 95767 photometry from MJUO.

HJD	V	$(B-V)$	$(V-R)$	$(V-I)$
1227.1786	8.785	0.701	0.458	0.909
1231.0652	8.781	0.700	0.455	0.904
1237.0168	8.810	0.696	0.455	0.913
1239.0686	8.808	0.700	0.456	0.920
1249.1192	8.848	0.709	0.458	0.925
1252.0481	8.852	0.717	0.452	0.923
1269.0021	8.859	0.721	0.458	0.928
1271.9484	8.857	0.725	0.459	0.927
1277.0159	8.843	0.724	0.455	0.930
1294.9242	8.766	0.689	0.441	0.888

continued over

Table A.4: *continued*

HJD	V	$(B-V)$	$(V-R)$	$(V-I)$
1296.9691	8.756	0.687	0.438	0.912
1301.9697	8.745	0.663	0.445	0.881
1302.9399	8.738	0.663	0.427	0.877
1306.0115	8.722	0.664	0.429	0.869
1308.9490	8.736	0.663	0.432	0.873
1317.4169	8.748	0.700	0.429	0.876
1327.0184	8.819	0.703	0.466	0.930
1333.9392	8.830	0.696	0.456	0.934
1339.8813	8.833	0.712	0.456	0.923
1347.9356	8.837	0.717	0.453	0.919
1357.8359	8.842	0.722	0.463	0.928
1363.9058	8.818	0.705	0.463	0.927
1368.9051	8.789	0.725	0.452	0.920
1373.9500	8.775	0.713	0.451	0.919
1379.9958	8.766	0.702	0.464	0.920
1383.8677	8.766	0.696	0.443	0.902
1389.8755	8.767	0.683	0.442	0.872
1397.8765	8.782	0.685	0.440	0.891
1407.9115	8.805	0.697	0.431	0.901
1411.8647	8.805	0.705	0.446	0.900
1416.8332	8.826	0.711	0.450	0.903
1557.1157	8.871	0.732	0.468	0.928
1575.1448	8.894	0.742	0.469	0.944
1593.1279	8.871	0.719	0.469	0.941
1606.1243	8.758	0.707	0.456	0.907
1611.1099	8.773	0.680	0.443	0.894
1620.0816	8.789	0.697	0.440	0.905
1629.0724	8.828	0.724	0.458	0.928
1661.9971	8.834	0.722	0.464	0.934
1669.9851	8.810	0.703	0.454	0.919
1673.9048	8.809	0.706	0.442	0.922
1685.9265	8.847	0.706	0.453	0.914
1714.9199	8.915	0.724	0.472	0.937
1721.8645	8.891	0.737	0.453	0.928
1726.9235	8.901	0.722	0.472	0.937
1729.9180	8.881	0.734	0.463	0.925

continued over

Table A.4: *continued*

HJD	V	$(B-V)$	$(V-R)$	$(V-I)$
1741.9153	8.885	0.735	0.470	0.932
1754.9079	8.932	0.745	0.470	0.950
1769.8934	8.957	0.742	0.472	0.954
1780.9215	8.901	0.725	0.468	0.937
1853.1386	8.886	0.723	0.452	0.911
1897.1110	8.920	0.716	0.465	0.922
1921.1119	8.935	0.698	0.443	0.890
1928.1119	8.905	0.694	0.440	0.882
1930.9942	8.892	0.696	0.444	0.876
1939.1525	8.894	0.685	0.432	0.879
1978.0230	8.858	0.681	0.431	0.867
1979.0338	8.860	0.665	0.436	0.877
1983.0357	8.849	0.672	0.426	0.874
1984.0832	8.834	0.685	0.421	0.867
1985.0064	8.838	0.679	0.432	0.864
1989.0597	8.848	0.659	0.428	0.867
1991.0141	8.837	0.669	0.411	0.855
1992.0000	8.836	0.667	0.419	0.866
1999.1199	8.836	0.664	0.416	0.866
2006.0571	8.827	0.663	0.431	0.866
2012.9993	8.814	0.680	0.415	0.862
2018.0498	8.828	0.674	0.430	0.868
2023.0094	8.841	0.682	0.438	0.872
2042.0193	8.835	0.668	0.447	0.931
2052.9224	8.829	0.709	0.444	0.888
2056.0431	8.839	0.696	0.450	0.909
2059.9302	8.816	0.697	0.443	0.893
2062.9777	8.817	0.694	0.444	0.896
2065.8992	8.818	0.692	0.445	0.885
2078.8514	8.771	0.670	0.434	0.891
2114.8909	8.811	0.674	0.444	0.897
2121.8607	8.817	0.695	0.437	0.901
2133.8832	8.829	0.701	0.435	0.888
2137.9346	8.810	0.696	0.454	0.906
2143.8676	8.811	0.695	0.457	0.892
2219.1546	8.782	0.693	0.433	0.900

continued over

Table A.4: *continued*

HJD	V	$(B-V)$	$(V-R)$	$(V-I)$
2258.0651	8.774	0.681	0.420	0.886
2312.9973	8.795	0.697	0.452	0.900
2320.0724	8.763	0.684	0.441	0.897
2321.0406	8.764	0.684	0.452	0.900
2322.0685	8.772	0.686	0.437	0.881
2339.0752	8.758	0.676	0.430	0.875

Table A.5: HD 172481 photometry from MJUO.

HJD	V	$(B-V)$	$(V-R)$	$(V-I)$
0742.9790	9.185	0.644	0.339	1.013
0910.2098	9.253	0.581	0.343	0.905
0920.1005	9.210	0.591	0.348	0.934
0922.1000	9.200	0.594	0.348	0.915
0942.0630	9.054	0.651	0.411	1.167
0948.0468	9.043	0.675	0.421	1.202
0950.0864	9.036	0.678	0.421	1.198
0961.1747	9.012	0.722	0.438	1.156
0981.0756	9.096	0.702	0.440	1.292
0984.1433	9.124	0.708	0.448	1.249
0985.0773	9.131	0.732	0.459	1.314
0998.0482	9.188	0.663	0.441	1.213
1012.1116	9.223	0.642	0.411	1.226
1013.2660	9.219	0.638	0.417	1.228
1028.9996	9.286	0.641	0.392	1.163
1044.0507	9.251	0.569	0.390	1.117
1109.9617	9.093	0.494	0.310	0.711
1124.9218	9.096	0.550	0.291	0.731
1272.1996	9.073	0.621	0.400	1.194
1280.2448	9.073	0.623	0.401	1.208
1303.1896	9.140	0.629	0.395	1.209
1306.1885	9.130	0.625	0.404	1.210
1316.2602	9.104	0.627	0.397	1.189
1336.1463	9.107	0.610	0.385	1.129

continued over

Table A.5: *continued*

HJD	V	$(B-V)$	$(V-R)$	$(V-I)$
1368.1135	9.071	0.578	0.350	0.929
1374.1201	9.079	0.589	0.358	0.911
1380.1776	9.112	0.588	0.374	0.902
1384.1369	9.110	0.619	0.346	0.880
1398.1472	9.096	0.596	0.349	0.825
1408.0730	9.080	0.568	0.324	0.780
1413.9417	9.084	0.580	0.330	0.807
1416.0667	9.103	0.579	0.331	0.795
1444.9901	9.140	0.623	0.339	0.791
1449.0260	9.131	0.635	0.327	0.777
1459.9684	9.169	0.633	0.344	0.814
1475.9382	9.105	0.598	0.352	0.801
1630.1657	8.988	0.615	0.403	1.184
1674.9894	9.098	0.623	0.364	0.977
1688.1463	9.122	0.619	0.364	0.939
1715.1750	9.064	0.595	0.341	0.846
1730.1193	9.097	0.578	0.339	0.795
1749.0004	9.078	0.593	0.345	0.795
1754.1050	9.069	0.584	0.341	0.781
1769.0467	9.010	0.582	0.334	0.763
1779.9859	9.086	0.596	0.328	0.771
1798.9846	9.157	0.622	0.352	0.820
1838.9223	9.116	0.600	0.375	0.937
1851.9040	9.067	0.637	0.370	1.056
1857.9031	9.032	0.645	0.388	1.080
1992.1695	9.141	0.607	0.334	0.885
2000.1686	9.144	0.609	0.354	0.870
2014.1957	9.162	0.599	0.351	0.839
2055.0802	9.095	0.586	0.342	0.779
2063.2443	9.081	0.578	0.326	0.755
2066.1488	9.090	0.584	0.335	0.754
2133.2105	9.139	0.591	0.340	0.823
2153.0900	9.056	0.606	0.351	0.966
2162.9664	9.028	0.611	0.380	1.098
2176.9612	9.011	0.652	0.397	1.203

Table A.6: HD 168625 photometry from MJUO.

HJD	V	$(B-V)$	$(V-R)$	$(V-I)$
0910.1944	8.352	1.497	0.879	1.851
0920.0682	8.404	1.502	0.886	1.833
0922.0815	8.370	1.511	0.884	1.841
0942.0435	8.376	1.496	0.895	1.855
0948.0319	8.371	1.484	0.880	1.835
0949.0325	8.400	1.514	0.892	1.846
0961.1919	8.372	1.502	0.885	1.862
0969.0284	8.357	1.486	0.886	1.851
0981.0586	8.368	1.503	0.879	1.818
0984.1185	8.370	1.491	0.875	1.836
0985.0546	8.379	1.491	0.889	1.830
1028.9808	8.396	1.503	0.882	1.850
1272.1821	8.380	1.487	0.891	1.860
1302.1800	8.356	1.524	0.900	1.905
1336.1316	8.378	1.506	0.871	1.833
1374.1053	8.338	1.495	0.890	1.849
1380.1640	8.306	1.500	0.868	1.808
1384.1195	8.384	1.491	0.897	1.865
1398.1289	8.374	1.494	0.890	1.849
1400.0657	8.409	1.480	0.886	1.840
1413.9216	8.424	1.494	0.878	1.836
1416.0444	8.424	1.500	0.891	1.848
1444.9756	8.321	1.505	0.893	1.846
1475.9233	8.345	1.518	0.859	1.823
1674.9690	8.355	1.504	0.879	1.829
1688.1305	8.398	1.490	0.882	1.850
1715.1581	8.383	1.502	0.879	1.829
1730.1031	8.373	1.500	0.883	1.841
1770.0361	8.419	1.497	0.893	1.845
1798.9666	8.323	1.499	0.877	1.841
1853.8983	8.392	1.514	0.912	1.843
2014.1774	8.401	1.485	0.887	1.849
2063.2115	8.377	1.504	0.882	1.854
2066.1328	8.366	1.504	0.873	1.841
2138.0911	8.377	1.496	0.921	1.836

continued over

Table A.6: *continued*

HJD	V	$(B-V)$	$(V-R)$	$(V-I)$
2162.9504	8.399	1.495	0.882	1.847
2180.9814	8.375	1.506	0.881	1.816
2478.1637	8.344	1.499	0.868	1.800
2484.1041	8.356	1.492	0.876	1.834

Table A.7: HD 168607 photometry from MJUO.

HJD	V	$(B-V)$	$(V-R)$	$(V-I)$
0910.1922	8.138	1.665	1.021	2.088
0922.0813	8.110	1.660	1.012	2.064
0942.0435	8.185	1.656	1.020	2.070
0948.0311	8.196	1.663	1.006	2.055
0961.1874	8.215	1.656	1.017	2.073
0969.0245	8.232	1.659	1.006	2.084
0981.0565	8.214	1.652	1.005	2.034
0984.1172	8.181	1.646	1.002	2.045
0985.0539	8.176	1.648	1.002	2.033
1028.9808	8.087	1.651	1.002	2.061
1272.1820	8.177	1.627	0.996	2.051
1302.1799	8.162	1.639	1.010	2.091
1336.1307	8.270	1.641	0.996	2.040
1374.1041	8.246	1.628	0.987	2.013
1380.1655	8.385	-	1.042	2.063
1384.1196	8.259	1.620	1.008	2.050
1398.1304	8.164	1.645	1.010	2.051
1416.0443	8.140	1.646	0.996	2.059
1444.9748	8.156	1.667	0.993	2.035
1475.9234	8.156	1.661	0.971	2.034
1674.9691	8.223	1.641	1.000	2.038
1688.1274	8.213	1.656	1.007	2.061
1715.1582	8.131	1.654	1.012	2.070
1730.1028	8.224	1.641	1.001	2.037
1770.0376	8.305	1.635	1.018	2.054
1798.9680	8.236	1.657	1.012	2.075

continued over

Table A.7: *continued*

HJD	V	$(B-V)$	$(V-R)$	$(V-I)$
2014.1789	8.220	1.643	1.015	2.061
2063.2129	8.103	1.654	1.014	2.084
2066.1323	8.099	1.646	1.001	2.066
2138.0926	8.038	1.666	1.068	2.073
2162.9505	8.139	1.648	1.015	2.080
2180.9828	8.080	1.678	1.024	2.074
2478.1636	8.208	1.659	1.003	2.002
2484.1041	8.263	1.654	1.023	2.077

Table A.8: CPD-59 6723 photometry from MJUO.

HJD	V	$(B-V)$	$(V-R)$	$(V-I)$
1055.9375	9.897	0.298	0.253	0.498
1084.9324	9.851	0.310	0.249	0.424
1203.1381	9.998	0.293	0.223	0.481
1205.1587	9.980	0.316	0.242	0.497
1213.1137	9.998	0.320	0.256	0.496
1252.1641	9.872	0.307	0.258	0.526
1262.1962	9.984	0.317	0.252	0.566
1272.1452	9.876	0.299	0.225	0.455
1277.1753	9.840	0.321	0.229	0.459
1294.9777	9.993	0.285	0.244	0.409
1302.1430	10.005	0.315	0.257	0.456
1303.1184	9.985	0.304	0.247	0.502
1306.1315	9.906	0.273	0.241	0.463
1317.1579	9.849	0.312	0.258	0.482
1334.1430	9.785	0.294	0.237	0.472
1356.0733	9.945	0.289	0.228	0.485
1369.0517	9.868	0.327	0.253	0.514
1374.1477	9.855	0.294	0.246	0.480
1380.1463	9.871	0.294	0.235	0.487
1384.1013	9.862	0.284	0.217	0.436
1397.1293	9.850	0.304	0.227	0.456
1408.0527	9.963	0.292	0.239	0.467

continued over

Table A.8: *continued*

HJD	V	$(B-V)$	$(V-R)$	$(V-I)$
1414.0226	9.901	0.287	0.239	0.460
1416.0263	9.872	0.255	0.273	0.520
1444.9224	9.857	0.295	0.260	0.496
1449.9513	9.888	0.296	0.241	0.480
1620.9773	9.940	0.324	0.260	0.500
1630.0347	9.833	0.276	0.213	0.455
1664.0355	10.016	0.308	0.242	0.484
1665.0401	10.023	0.280	0.217	0.460
1673.2173	9.878	0.304	0.230	0.467
1688.0077	10.007	0.295	0.245	0.495
1722.1247	9.990	0.272	0.244	0.465
1730.0644	9.980	0.294	0.229	0.489
1754.1500	9.801	0.289	0.246	0.476
1768.9783	9.915	0.312	0.247	0.490
1798.9351	9.912	0.320	0.229	0.480
1801.9414	9.908	0.301	0.258	0.476
1983.2095	9.870	0.286	0.212	0.442
1991.2020	9.908	0.293	0.250	0.476
2001.1573	9.949	0.288	0.226	0.467
2014.1128	9.948	0.314	0.243	0.482
2054.9982	9.910	0.287	0.232	0.452
2060.0612	9.855	0.303	0.232	0.504
2066.0476	9.943	0.285	0.222	0.449
2079.9821	9.995	0.319	0.259	0.522
2115.1664	10.003	0.259	0.238	0.458
2121.9936	9.862	0.316	0.262	0.527
2138.0599	9.860	0.308	0.234	0.465
2152.9822	9.831	0.319	0.254	0.524
2164.0127	9.981	0.308	0.240	0.519
2182.9205	9.946	0.281	0.248	0.494
2220.8901	9.857	0.294	0.233	0.494

Appendix B

Echelle Observing Log

Observing logs for the high resolution spectra acquired for stars in this thesis. Unless otherwise specified the spectra are taken with the échelle spectrograph in the red region (see §3.1.1).

Column	Comments
Object	Star name.
Date	dd/mm/yy format.
File	Fits file name.
Observer	**DJP**= Daniel Pooley. **KRP**= Karen Pollard. **MDA**= Michael Albrow. **PLC**= Peter Cottrell.
Exp	Exposure time in seconds.
Notes	**RED-**: Échelle spectrum from the red minus region. **BLUE**: Blue grating échelle spectrum. **BLUE-**: Alternate blue grating échelle spectrum. Not used in this project. **VIS**: Échelle spectrum made with the visual grating. Not used in this project. **HERC**(n): HERCULES spectrum, where n is the fibre number. **Unred**: Unreduced spectrum. Could be due to very low S/N, arc spectrum shifts.

Table B.1: Key to the observing log.

Object	Date	File	Obs	Exp	Notes
AI CMi	07/01/98	f0820026	DJP	2400	
	08/01/98	f0821019	DJP	2400	
	14/11/98	f1132029	DJP	2400	
	15/11/98	f1133034	DJP	2400	
	16/11/98	f1134030	DJP	3000	Blue
	22/12/98	f1170025	KRP	2400	
	24/12/98	f1172024	DJP	2400	
	26/12/98	f1174022	DJP	2400	
	30/12/98	f1178026	DJP	2400	Red-
	11/01/99	f1190017	MDA	2700	
	12/01/99	f1191020	MDA	2700	
	17/01/99	f1196025	MDA	3600	
	11/02/99	f1221022	DJP	3600	
	12/02/99	f1222018	DJP	3600	Red-
	13/02/99	f1223015	DJP	3600	Blue
	15/02/99	f1225013	KRP	2400	
	17/02/99	f1227013	KRP	2400	
	21/02/99	f1231017	KRP	1800	
	09/03/99	f1247016	DJP	2400	
	11/03/99	f1249018	DJP	2400	
	14/03/99	f1252008	DJP	2400	
	06/05/99	f1305008	DJP	2400	
	07/05/99	f1306010	DJP	2700	Red-
	08/05/99	f1307005	DJP	2400	Red-
	18/08/99	f1409045	DJP	1800	
	08/01/00	f1552007	PLC	2700	
	12/01/00	f1556019	PLC	2700	
	22/03/00	f1626004	DJP	2400	
	23/03/00	f1627013	DJP	2400	
	24/03/00	f1628008	DJP	3000	Vis
	25/03/00	f1629007	DJP	2700	
	26/03/00	f1630016	DJP	2400	
	27/03/00	f1631011	DJP	2400	
	30/03/00	f1634008	DJP	2400	
	10/04/00	f1645006	DJP	2700	
	11/04/00	f1646020	DJP	3000	
	12/04/00	f1647016	DJP	2400	
	13/04/00	f1648010	DJP	2400	

Object	Date	File	Obs	Exp	Notes
AI CMi	21/04/00	f1656005	DJP	2700	
	03/05/00	f1668006	DJP	2400	
	15/05/00	f1680006	DJP	2400	
	16/05/00	f1681005	DJP	3000	
	20/06/00	f1716002	DJP	3600	
	15/09/00	f1803037	DJP	2280	
	16/09/00	f1804042	DJP	3000	
	18/10/00	f1836025	DJP	3600	
	19/10/00	f1837021	DJP	7200	
	03/11/00	f1852014	DJP	5400	
	16/12/00	f1895017	DJP	7200	
	06/01/01	f1916010	DJP	5400	
	24/04/01	f2024007	DJP	5400	
	26/04/01	f2026006	DJP	5400	
	08/02/02	f2314042	DJP	3694	Herc(3)
HD 70379	07/01/98	f0820029	DJP	2400	
	09/01/98	f0822023	DJP	2400	
	24/02/98	f0868014	DJP	2400	
	13/11/98	f1131036	DJP	2400	
	16/11/98	f1134032	DJP	2400	Blue
	22/12/98	f1170034	KRP	2400	
	25/12/98	f1173027	DJP	2400	
	26/12/98	f1174028	DJP	2400	
	30/12/98	f1178023	DJP	2400	Red-
	11/01/99	f1190023	MDA	2700	
	12/01/99	f1191026	MDA	2700	
	17/01/99	f1196028	MDA	2700	
	11/02/99	f1221025	DJP	2700	
	12/02/99	f1222021	DJP	2700	Red-
	13/02/99	f1223017	DJP	3600	Blue
	17/02/99	f1227022	KRP	2400	
	21/02/99	f1231023	KRP	2400	
	09/03/99	f1247024	DJP	2400	
	11/03/99	f1249022	DJP	2400	
	14/03/99	f1252012	DJP	2400	
	06/05/99	f1305017	DJP	2400	
	07/05/99	f1306010	DJP	2700	Red-

Object	Date	File	Obs	Exp	Notes
HD 70379	08/05/99	f1307008	DJP	2400	Red-
	10/05/99	f1309010	DJP	2400	
	28/05/99	f1327004	DJP	3000	
	08/01/00	f1552013	PLC	3600	
	11/01/00	f1555022	PLC	3600	
	22/03/00	f1626007	DJP	2400	Unred
	23/03/00	f1627019	DJP	2400	
	25/03/00	f1629010	DJP	2700	
	26/03/00	f1630019	DJP	2400	
	27/03/00	f1631020	DJP	2400	
	30/03/00	f1634014	DJP	2400	
	10/04/00	f1645011	DJP	2400	
	11/04/00	f1646028	DJP	2400	
	12/04/00	f1647019	DJP	2400	
	13/04/00	f1648013	DJP	2400	
	21/04/00	f1656010	DJP	2700	
	03/05/00	f1668015	DJP	2400	
	15/05/00	f1680014	DJP	2700	
	16/05/00	f1681013	DJP	2700	
	19/06/00	f1715005	DJP	3000	
	20/06/00	f1716006	DJP	3600	
	18/10/00	f1836029	DJP	3600	
	22/10/00	f1840026	DJP	7200	
	03/11/00	f1852018	DJP	5400	
	08/11/00	f1857014	DJP	10800	Unred
	17/12/00	f1896009	DJP	7200	Unred
	06/01/01	f1916014	DJP	5400	
	24/04/01	f2024011	DJP	5400	
	01/07/01	f2092004	DJP	3840	Herc(1)
HD 95767	24/02/98	f0868020	DJP	2400	
	12/07/98	f1007016	DJP	2400	
	14/07/98	f1009012	DJP	2400	
	11/02/99	f1221033	DJP	2700	
	12/02/99	f1222027	DJP	2700	Red-
	20/02/99	f1230043	KRP	1800	
	21/02/99	f1231038	KRP	1800	
	09/03/99	f1247030	DJP	2400	

Object	Date	File	Obs	Exp	Notes
HD 95767	11/03/99	f1249038	DJP	2400	
	14/03/99	f1252024	DJP	2400	
	04/05/99	f1303013	DJP	2400	
	07/05/99	f1306025	DJP	2700	Red-
	08/05/99	f1307014	DJP	2400	Red-
	09/05/99	f1308013	DJP	3000	Blue
	28/05/99	f1327012	DJP	3000	
	05/06/99	f1335018	MDA	2400	
	09/06/99	f1339016	MDA	2400	
	23/07/99	f1383010	DJP	2400	
	24/07/99	f1384010	DJP	3000	Blue
	09/08/99	f1400012	DJP	2400	
	18/08/99	f1409007	DJP	2400	
	23/03/00	f1627022	DJP	2400	
	24/03/00	f1628017	DJP	2400	Vis
	25/03/00	f1629019	DJP	2400	
	26/03/00	f1630025	DJP	2400	
	27/03/00	f1631023	DJP	2400	
	28/03/00	f1632008	DJP	2400	
	30/03/00	f1634023	DJP	2400	
	10/04/00	f1645022	DJP	2400	
	12/04/00	f1647025	DJP	2400	
	13/04/00	f1648025	DJP	2400	
	21/04/00	f1656016	DJP	2400	
	05/05/00	f1670006	DJP	2400	
	14/05/00	f1679009	DJP	2400	
	19/05/00	f1684009	DJP	2400	
	21/05/00	f1686010	DJP	2400	
	20/06/00	f1716010	DJP	3000	
	17/12/00	f1896017	DJP	2400	
	18/12/00	f1897013	DJP	7200	
	06/01/01	f1916018	DJP	5400	
	24/04/01	f2024015	DJP	5400	
	26/04/01	f2026014	DJP	5400	
	23/05/01	f2053013	DJW	2700	
	25/05/01	f2055009	DJW	2700	
	27/05/01	f2057005	DJW	2700	
	29/06/01	f2090004	DJP	2600	Herc(1)

Object	Date	File	Obs	Exp	Notes
HD 95767	01/07/01	f2092007	DJP	3300	Herc(1)
	02/07/01	f2093004	DJP	3240	Herc(3)
	09/02/02	f2315015	DJP	5220	Herc(1)
CPD-59 6723	15/06/98	f0980031	MDA	1800	
	12/07/98	f1007039	DJP	2400	
	13/07/98	f1008025	DJP	2400	
	06/08/98	f1032016	DJP	2400	
	04/05/99	f1303028	DJP	2400	
	18/05/99	f1318007	KRP	2400	
	24/05/99	f1323035	KRP	3000	
	28/05/99	f1327034	DJP	3000	
	22/07/99	f1382024	DJP	2400	
	24/07/99	f1384022	DJP	3000	Blue
	27/07/99	f1387004	DJP	2700	Red-
	09/08/99	f1400030	DJP	2700	
	18/08/99	f1409019	DJP	3600	
	21/08/99	f1412013	DJP	2400	Blue-
	27/03/00	f1631035	DJP	2700	
	13/04/00	f1648037	DJP	2700	
	21/04/00	f1656033	DJP	2700	
	03/05/00	f1668039	DJP	2700	
	16/05/00	f1681030	DJP	3000	
	21/05/00	f1686031	DJP	3000	
	19/06/00	f1715029	DJP	3000	
	21/06/00	f1717017	DJP	3000	
	10/07/00	f1736005	DJP	3000	
	23/07/00	f1749013	DJP	3000	
	09/08/00	f1766017	DJP	3600	
	20/08/00	f1777017	DJP	3600	
	16/09/00	f1804014	DJP	3600	
	24/04/01	f2024035	DJP	5400	
	29/06/01	f2090019	DJP	3615	Herc(1)
	01/07/01	f2092013	DJP	3802	Herc(3)
SAO 209008	15/06/98	f0980054	MDA	1800	
	20/06/98	f0985033	KRP	1800	
	14/07/98	f1009025	DJP	2400	

Object	Date	File	Obs	Exp	Notes
SAO 209008	06/08/98	f1032013	DJP	2400	
	06/05/99	f1305023	DJP	2400	
	27/05/99	f1326022	DJP	3000	
	20/07/99	f1380009	DJP	2400	
	09/08/99	f1400036	DJP	2400	
	12/08/99	f1403019	DJP	2400	
	23/08/99	f1414019	DJP	2400	
	25/03/00	f1629028	DJP	2100	
	27/03/00	f1631041	DJP	2400	
	12/04/00	f1647042	DJP	2400	
	21/04/00	f1656039	DJP	2400	
	03/05/00	f1668047	DJP	2400	
	14/05/00	f1679033	DJP	759	
	19/05/00	f1684022	DJP	2400	
	19/06/00	f1715037	DJP	3000	
	21/06/00	f1717025	DJP	3000	
	10/07/00	f1736009	DJP	2400	
	23/07/00	f1749017	DJP	2400	
	09/08/00	f1766021	DJP	2700	
	20/08/00	f1777021	DJP	2700	
	15/09/00	f1803005	DJP	3000	
	17/09/00	f1805005	DJP	3000	
	21/09/00	f1809005	DJP	3000	
	19/10/00	f1837005	DJP	3000	
	20/10/00	f1838005	DJP	2280	
	21/10/00	f1839002	DJP	9000	
	22/10/00	f1840006	DJP	9000	
	26/04/01	f2026026	DJP	5400	
	26/06/01	f2087025	DJP	3327	Herc(1)
	30/06/01	f2091025	DJP	3000	Herc(1)
HD 168625	13/07/98	f1008032	DJP	2400	
	06/08/98	f1032021	DJP	2400	
	08/08/98	f1034021	DJP	2400	
	06/05/99	f1305032	DJP	2400	
	23/05/99	f1322068	KRP	2400	
	28/05/99	f1327037	DJP	3000	
	10/06/99	f1340040	MDA	2400	

Object	Date	File	Obs	Exp	Notes
HD 168625	20/07/99	f1380012	DJP	2400	
	22/07/99	f1382032	DJP	2400	
	24/07/99	f1384025	DJP	3000	Blue
	25/07/99	f1385004	DJP	2400	Red-
	10/08/99	f1401032	DJP	2400	
	20/08/99	f1411018	DJP	2400	
	22/08/99	f1413004	DJP	2400	Blue-
	23/08/99	f1414022	DJP	2400	
	26/03/00	f1630043	DJP	2400	
	28/03/00	f1632031	DJP	2400	
	11/04/00	f1646055	DJP	2400	
	21/04/00	f1656044	DJP	2400	
	03/05/00	f1668051	DJP	2400	
	14/05/00	f1679037	DJP	2400	
	21/05/00	f1686039	DJP	2400	
	20/06/00	f1716034	DJP	2700	
	10/07/00	f1736013	DJP	2700	
	23/07/00	f1749021	DJP	2700	
	08/08/00	f1765008	DJP	3000	
	16/09/00	f1804018	DJP	3000	
	26/04/01	f2026036	DJP	2400	
	29/06/01	f2090022	DJP	1802	Herc(1)
HD 168607	14/07/98	f1009028	DJP	2400	
	06/05/99	f1305034	DJP	2400	
	22/07/99	f1382035	DJP	1800	
	21/06/00	f1717029	DJP	1800	
	29/06/01	f2090024	DJP	2701	Herc(1)
HD 172481	20/06/98	f0985045	KRP	2400	
	13/07/98	f1008035	DJP	2400	
	07/08/98	f1033037	DJP	2400	
	08/08/98	f1034026	DJP	2400	unred
	13/11/98	f1131010	DJP	1800	
	14/03/99	f1252050	DJP	1200	
	14/03/99	f1252053	DJP	1200	
	04/05/99	f1303034	DJP	2400	
	06/05/99	f1305029	DJP	3600	

Object	Date	File	Obs	Exp	Notes
HD 172481	07/05/99	f1306045	DJP	2700	Red-
	09/05/99	f1308026	DJP	3000	Blue
	10/05/99	f1309022	DJP	2400	
	18/05/99	f1318022	KRP	2400	
	24/05/99	f1323044	KRP	3000	
	25/05/99	f1324021	DJP	2700	
	28/05/99	f1327043	DJP	3000	
	04/06/99	f1334095	MDA	1800	
	20/07/99	f1380017	DJP	2700	
	22/07/99	f1382038	DJP	2400	
	24/07/99	f1384028	DJP	3000	Blue
	25/07/99	f1385007	DJP	3000	Red-
	09/08/99	f1400039	DJP	2400	
	12/08/99	f1403022	DJP	2400	
	18/08/99	f1409025	DJP	3600	
	20/08/99	f1411024	DJP	2400	
	21/08/99	f1412016	DJP	3600	Blue-
	22/08/99	f1413007	DJP	3600	Blue-
	23/08/99	f1414025	DJP	2400	
	24/03/00	f1628035	DJP	2700	Vis
	25/03/00	f1629041	DJP	2700	
	27/03/00	f1631044	DJP	2400	
	11/04/00	f1646058	DJP	2400	
	12/04/00	f1647047	DJP	2700	
	13/04/00	f1648040	DJP	2400	
	21/04/00	f1656047	DJP	2700	
	03/05/00	f1668055	DJP	2700	
	16/05/00	f1681038	DJP	3600	
	19/05/00	f1684026	DJP	2400	
	21/05/00	f1686043	DJP	3600	
	19/06/00	f1715045	DJP	3000	
	20/06/00	f1716039	DJP	2700	
	21/06/00	f1717037	DJP	3000	
	10/07/00	f1736021	DJP	2700	
	11/07/00	f1737029	DJP	3600	
	13/07/00	f1739013	DJP	3000	
	23/07/00	f1749029	DJP	2700	
	24/07/00	f1750009	DJP	3600	

Object	Date	File	Obs	Exp	Notes
HD 172481	25/07/00	f1751009	DJP	3600	
	09/08/00	f1766029	DJP	3600	
	20/08/00	f1777029	DJP	3600	
	15/09/00	f1803013	DJP	3600	
	16/09/00	f1804022	DJP	3600	
	21/09/00	f1809013	DJP	3600	
	18/10/00	f1836005	DJP	7200	
	04/11/00	f1853002	DJP	7200	
	08/11/00	f1857006	DJP	7200	
	25/04/01	f2025029	DJP	4020	
	26/04/01	f2026040	DJP	5400	
	26/06/01	f2087027	DJP	-	Herc(1),unred
	29/06/01	f2090032	DJP	3627	Herc(1)
	30/06/01	f2091031	DJP	2700	Herc(1)
	01/07/01	f2092034	DJP	6442	Herc(2)
HD 179821	06/08/98	f1032025	DJP	2400	
	08/08/98	f1034029	DJP	2400	Bad
	14/11/98	f1132006	DJP	1800	
	04/05/99	f1303037	DJP	2400	
	07/05/99	f1306048	DJP	2400	Red-
	09/05/99	f1308029	DJP	3000	Blue
	18/05/99	f1318076	KRP	2400	
	24/05/99	f1323047	KRP	2400	
	28/05/99	f1327046	DJP	2400	
	05/06/99	f1335073	MDA	2400	
	08/06/99	f1338015	MDA	2400	
	20/07/99	f1380020	DJP	2400	
	24/07/99	f1384031	DJP	3000	Blue
	25/07/99	f1385010	DJP	2400	Red-
	10/08/99	f1401035	DJP	2400	
	12/08/99	f1403025	DJP	2400	
	20/08/99	f1411021	DJP	2400	
	22/08/99	f1413010	DJP	2400	Blue-
	12/04/00	f1647050	DJP	1800	
	13/04/00	f1648045	DJP	2400	
	21/04/00	f1656050	DJP	2400	
	03/05/00	f1670039	DJP	2400	

Object	Date	File	Obs	Exp	Notes
HD 179821	16/05/00	f1681042	DJP	3000	
	19/05/00	f1684030	DJP	2400	
	19/06/00	f1715041	DJP	3000	
	21/06/00	f1717033	DJP	3000	
	10/07/00	f1736017	DJP	2700	
	13/07/00	f1739009	DJP	3000	
	23/07/00	f1749025	DJP	2700	
	25/07/00	f1751005	DJP	3600	
	09/08/00	f1766025	DJP	3000	
	20/08/00	f1777025	DJP	2700	
	15/09/00	f1803009	DJP	3000	
	21/09/00	f1809009	DJP	3000	
	18/10/00	f1836009	DJP	2645	
	03/11/00	f1852002	DJP	5400	
	24/04/01	f2024031	DJP	5400	
	30/06/01	f2091028	DJP	2856	Herc(1)
	01/07/01	f2092019	DJP	3099	Herc(3)
	02/07/01	f2093016	DJP	7740	Herc(3)

Appendix C

Radial velocity data for post-AGB stars

This appendix contains the tabulated radial velocities for the programme post-AGB stars. They are presented in the same order that the respective chapters appear. The column HJD refers to the heliocentric Julian Date of the observation (−2450000). A blank indicates a void datum.

HJD (−2450000)	λ5432 Fe I		λ5615 Fe I		λ5853 Ba II		λ6757 S I		λ7896 Mg II	
	RV (km s^{-1})	Err (km s^{-1})	RV (km s^{-1})	Err (km s^{-1})	RV (km s^{-1})	Err (km s^{-1})	RV (km s^{-1})	Err (km s^{-1})	RV (km s^{-1})	Err (km s^{-1})
666.097	87.37	0.71	81.46	1.24	83.44	1.30			93.25	0.20
1131.862	81.91	3.43					77.91	1.36	89.86	1.57
1303.252	84.92	0.65	77.18	0.72	81.96	0.43	76.59	0.94	89.27	0.55
1318.132	83.62	0.46	78.95	0.17	80.48	0.33	79.33	0.56	87.76	0.60
1323.146	86.01	0.40	80.67	0.90	83.35	0.32	77.84	0.93	90.56	0.29
1327.216	85.00	0.65	81.12	0.36	82.24	0.11			89.87	0.80
1335.159	84.22	0.28	79.56	0.24	81.51	0.87	81.63	0.50	91.32	0.62
1338.125	84.80	0.22	81.09	0.36	83.03	0.23	81.78	0.24	91.97	0.38
1380.092	92.13	0.50	85.45	0.44	88.89	0.17	82.05	1.14	95.96	0.61
1401.056	90.96	0.83	83.67	0.53	86.27	0.17			94.90	1.23
1403.027	90.07	1.01	84.32	0.15	88.13	0.92	82.57	0.14	95.03	0.75
1410.922	89.91	1.07	81.17	0.53			79.76	0.93	91.21	0.16
1647.249	90.23	0.38	83.54	0.67	89.95	2.34			93.40	0.47
1648.250	90.26	0.96	84.19	0.12	89.90	0.41	81.84	1.25	92.51	0.58
1656.243	90.43	0.22	86.26	0.38	89.65	0.48	82.93	1.06	94.37	0.10
1681.171	92.76	0.40	88.41	0.10	92.63	0.19	84.73	0.66	94.18	0.08
1684.219	95.00	0.21	88.79	1.44	94.47	0.45	86.31	1.07	96.91	0.70
1715.129	94.63	0.41	85.51	1.09	95.41	0.41	86.43	0.59	95.96	0.66
1717.108	91.78	0.42	82.90	3.17	95.42	0.71			96.30	0.91
1736.050	91.08	0.50	86.00	0.19			86.56	1.71	99.77	1.06
1739.035	90.96	0.41	87.06	0.96					99.05	0.41
1749.062	93.39	0.82	87.81	1.34			89.51	0.75	98.12	0.57
1751.077	93.18	0.15	87.43	0.58	93.05	0.13	87.95	0.56	98.89	0.40
1765.987	93.92	0.11	88.39	0.58	93.73	1.41	87.14	1.11	96.24	0.44
1777.017	94.42	0.78	88.69	1.27	92.98	0.28	83.87	2.28	95.69	1.11
1802.890	93.80	1.94	83.40	0.62	87.77	0.98				
1835.936			77.42	2.13			79.83	0.36	89.55	0.49
1851.833			76.42	0.78			75.95	0.91	87.18	0.11
2024.176	97.15	1.00	89.22	0.09	96.53	0.60			93.79	0.56
Mean	90.14	0.70	83.79	0.76	88.67	0.60	82.50	0.91	93.67	0.59
σ	4.05	0.67	3.83	0.68	5.20	0.54	3.88	0.50	3.46	0.35
n	27		28		22		21		28	

Table C.1: Radial velocities for three low and two high excitation potential lines of HD 179821.

HJD (−2450000)	λ6347 Si II RV (km s^{-1})	λ6347 Si II Err (km s^{-1})	λ6371 Si II RV (km s^{-1})	λ6371 Si II Err (km s^{-1})	λ6562 Hα RV (km s^{-1})	λ6562 Hα Err (km s^{-1})	λ8446 O I RV (km s^{-1})	λ8446 O I Err (km s^{-1})	λ8498 Ca II RV (km s^{-1})	λ8498 Ca II Err (km s^{-1})
666.097	85.42	1.09	84.47	0.45	91.02	1.03	90.85	0.34	94.19	2.98
1131.862	78.27	0.46	77.19	0.45	88.86	1.12	83.62	1.68	91.40	2.17
1303.252	82.13	0.43	80.87	0.26	96.76	0.18	88.16	0.20	92.59	1.35
1318.132	81.50	0.15	81.59	0.04	95.97	0.07	84.82	0.13	91.45	1.33
1323.146	83.29	0.09	82.39	0.17	96.04	0.52	87.42	0.45	93.22	1.59
1327.216	82.46	0.21	82.34	0.10	94.54	0.12	89.44	0.50	93.01	1.40
1335.159	82.62	0.30	82.83	0.23	93.91	0.84	90.32	0.25	93.00	1.50
1338.125	83.10	0.53	83.04	0.52	92.27	0.13	87.68	0.48	92.21	1.45
1380.092	87.05	1.08			92.09	1.40	92.22	0.71	94.44	1.80
1401.056	87.54	0.46	86.76	1.31	92.40	1.31	92.39	0.62	92.42	1.62
1403.027	88.09	1.31	87.27	1.07	93.53	0.73	93.87	1.01	92.75	1.54
1410.922	86.40	1.30	85.13	1.12	93.43	1.11	90.76	1.02	92.88	1.81
1647.249	85.91	0.16	86.35	0.87	92.66	0.03	90.42	0.71	92.65	1.17
1648.250	86.27	0.63			93.21	0.12	91.37	0.43	92.86	1.46
1656.243	87.02	0.68			93.55	0.39	91.97	0.44	94.24	1.11
1681.171	89.98	0.70	90.68	0.34	95.51	0.41	95.24	0.92	94.46	0.65
1684.219	92.06	0.75	90.98	0.98	96.15	0.17	95.40	0.40	95.29	0.80
1715.129	88.33	1.06			97.56	0.30			96.16	0.38
1717.108	87.65	1.19			96.82	0.51			96.01	0.61
1736.050	87.42	1.12			96.77	0.79	92.76	0.26	94.68	0.14
1739.035	88.19	0.66			96.35	0.61	91.04	0.16	94.76	0.62
1749.062	87.58	1.33			96.47	0.77	91.40	1.04	95.13	0.48
1751.077	88.15	0.85			96.41	0.64	92.42	1.07	94.43	0.78
1765.987	88.83	0.78			95.34	0.57	93.39	0.76	93.83	0.63
1777.017	89.17	1.24	88.59	0.75	95.36	0.18	93.47	1.03	93.63	0.44
1802.890	89.36	0.39			96.47	0.20	95.55	0.71	93.38	0.21
1835.936	81.07	1.14	81.42	0.07	94.66	0.41	86.67	0.60	92.91	0.69
1851.833	80.09	1.09	79.91	1.19	93.97	0.40	85.16	0.85	93.50	0.63
2024.176	91.10	0.68			96.51	0.86	95.51	0.40	94.05	0.23
Mean	86.07	0.75	84.22	0.58	94.64	0.55	90.86	0.64	93.64	1.09
σ	3.45	0.39	3.81	0.43	2.08	0.39	3.33	0.36	1.21	0.66
n	29		17		29		27		29	

Table C.2: Radial velocities for high excitation potential lines and λ8498 Ca II of HD 179821.

HJD (−2450000)	λ5429 Fe I RV (km s^{-1})	λ5429 Fe I Err (km s^{-1})	λ5434 Fe I RV (km s^{-1})	λ5434 Fe I Err (km s^{-1})	λ5572 Fe I RV (km s^{-1})	λ5572 Fe I Err (km s^{-1})	λ5615 Fe I RV (km s^{-1})	λ5615 Fe I Err (km s^{-1})	λ5853 Ba II RV (km s^{-1})	λ5853 Ba II Err (km s^{-1})
980.065									−17.62	0.43
985.038	−14.81	0.10	−18.51	1.70	−19.10	0.40	−17.36	1.45	−15.68	0.43
1009.059	−14.85	0.33	−13.73	0.94	−17.10	0.37	−15.41	0.92	−16.55	0.12
1031.949	−11.39	0.37	−11.86	0.27	−12.52	0.24	−13.81	0.49	−12.58	0.15
1305.009	−17.88	0.58	−21.61	0.50	−21.79	0.99	−21.95	0.18	−24.23	0.88
1326.030	−1.40	0.67	−10.29	4.07	−3.39	1.97	−6.56	0.40	−8.75	0.45
1379.971	−16.32	0.21	−16.90	0.78			−19.78	0.42		
1400.077	−22.67	0.77	−25.94	0.68	−27.01	1.07	−25.77	0.21	−23.97	0.22
1402.961	−21.63	0.20	−24.41	0.95	−21.41	0.36	−24.48	0.32	−24.64	0.70
1413.955	−22.17	0.24	−21.13	0.28	−18.86	0.57	−20.66	0.28	−18.45	0.50
1629.201			−15.99	0.91	−15.73	0.85	−17.15	0.64	−14.42	0.29
1647.183	−14.81	0.31	−18.19	1.35	−17.42	0.74	−16.94	0.17	−18.16	0.16
1656.149	−16.31	0.61	−17.30	0.24	−17.43	0.18	−17.52	0.28	−18.23	0.79
1668.110	−16.72	0.55	−16.47	0.10	−13.04	0.18	−14.22	0.22	−16.95	0.31
1684.145	−11.40	0.98	−14.24	1.35	−17.01	0.22	−17.03	0.46	−13.86	0.30
1715.076	−20.09	1.00	−19.83	0.07	−18.66	1.00	−18.39	0.74	−18.78	0.16
1717.038	−19.22	0.22	−19.76	0.14	−17.23	0.22	−17.99	0.51	−18.37	0.49
1735.975			−21.49	1.36	−19.28	0.33	−18.51	0.68	−19.39	0.25
1748.989	−26.94	0.67	−28.15	0.56	−28.34	0.12	−25.03	0.47	−27.18	0.36
1765.937	−29.67	0.09	−28.01	0.97	−27.83	0.64	−28.74	0.29	−30.56	0.41
1776.983	−28.03	0.27	−28.19	0.17	−27.24	0.35	−27.35	0.52	−28.54	0.32
1802.858	−17.82	0.44	−17.63	0.65	−16.73	0.52	−17.34	0.70	−18.00	0.23
1804.849	−17.98	1.90							−16.81	0.35
1836.848	−8.63	0.19	−11.71	0.24	−9.40	0.34	−9.94	0.21	−10.22	0.38
1837.870	−7.91	1.86	−9.75	1.23	−10.64	0.11	−10.92	1.25	−8.45	1.44
1838.882	−7.91	0.80	−8.86	0.77	−8.96	0.34	−8.23	0.40	−10.31	0.30
1839.883	−8.47	0.28	−8.90	0.49	−10.30	0.41	−8.78	0.23	−9.44	0.37
2026.105	−23.84	0.81	−33.64	0.23						
Mean	−16.75	0.58	−18.56	0.81	−17.35	0.52	−17.59	0.50	−17.70	0.42
σ	6.93	0.47	6.64	0.81	6.38	0.42	5.94	0.32	6.04	0.28
n	25		26		24		25		26	

Table C.3: Radial velocities for low excitation potential lines of SAO 209008.

HJD (−2450000)	λ6347 Si II RV (km s^{-1})	λ6347 Si II Err (km s^{-1})	λ6371 Si II RV (km s^{-1})	λ6371 Si II Err (km s^{-1})	λ6562 Hα RV (km s^{-1})	λ6562 Hα Err (km s^{-1})	λ7442 N I RV (km s^{-1})	λ7442 N I Err (km s^{-1})	λ8446 O I RV (km s^{-1})	λ8446 O I Err (km s^{-1})
980.065	−19.47	1.77	−17.51	1.30	−25.79	1.33	−15.90	0.68		
985.038	−18.80	2.14	−17.41	1.49	−26.76	1.17	−16.17	0.24	−13.02	0.97
1009.059	−15.92	1.20	−15.66	1.82	−28.51	0.15	−15.32	0.65	−8.71	0.28
1031.949	−14.44	1.48	−14.48	1.71	−27.53	0.04	−14.01	1.00	−7.70	1.03
1305.009	−18.39	1.02	−18.82	0.27	−12.89	1.90	−20.46	0.73	−14.58	0.14
1326.030	−12.88	0.78	−12.26	1.22	−9.35	2.65	−15.53	1.69		
1379.971	−16.73	0.08	−17.89	0.34	−12.02	1.34	−18.36	0.21	−13.12	0.24
1400.077	−22.95	0.33	−22.61	0.24	−15.47	0.80	−20.08	0.06	−18.49	0.32
1402.961	−21.88	0.13	−22.38	0.43	−14.11	0.88	−21.11	0.21	−19.33	0.28
1413.955	−22.76	0.34	−21.31	0.73	−15.76	1.11	−21.42	0.11	−18.86	0.03
1629.201	−14.25	0.11	−13.19	0.24	−20.86	0.49	−15.26	0.14		
1647.183	−15.02	0.35	−14.40	0.23	−18.34	0.13	−16.08	0.59	−11.26	0.32
1656.149	−16.85	0.14	−15.56	0.18	−17.83	0.29	−17.60	0.27	−13.82	0.19
1668.110	−15.60	0.40	−13.53	0.65	−17.48	0.43	−14.88	0.66	−12.22	0.29
1684.145	−13.03	1.04	−13.43	0.74	−15.27	0.27	−14.02	0.24	−9.95	0.23
1715.076	−18.33	0.63	−17.43	0.28	−16.44	0.54	−18.54	0.50	−12.77	0.38
1717.038	−17.92	0.58	−17.35	0.68	−16.65	0.57	−18.35	0.37	−14.36	0.12
1735.975	−21.44	1.15	−19.36	1.05	−16.46	0.36	−19.70	0.40	−16.96	0.56
1748.989	−26.73	0.26	−24.88	0.23	−17.52	0.22	−23.70	1.03	−22.14	0.23
1765.937	−27.88	0.42	−26.25	0.56	−18.76	0.40	−26.61	0.17	−23.40	0.41
1776.983	−27.91	0.89	−25.32	0.43	−19.79	0.85	−25.26	0.24	−22.26	0.20
1802.858	−18.40	0.82	−16.43	0.86	−20.14	0.80	−15.84	0.41	−13.51	0.19
1804.849	−18.66	0.80	−15.21	3.27	−19.35	1.14	−15.80	1.81		
1836.848	−10.27	0.68	−8.52	0.78	−15.62	0.85	−9.64	0.31	−4.91	0.06
1837.870	−10.76	0.80	−8.63	0.92	−16.20	1.00	−9.09	0.75	−6.31	0.30
1838.882	−9.48	0.66	−8.12	0.92	−15.18	1.02	−9.35	0.32	−5.09	0.03
1839.883	−9.81	0.62	−8.27	0.53	−16.19	1.48	−9.19	0.12	−5.71	0.56
2026.105	−19.38	0.50	−19.49	0.56	−9.53	0.05	−23.33	1.37	−15.01	0.27
2091.040	−15.19	0.84			−16.07	0.38				
Mean	−17.63	0.72	−16.63	0.81	−17.65	0.78	−17.16	0.55	−13.48	0.32
σ	5.02	0.49	5.05	0.66	4.73	0.59	4.67	0.46	5.46	0.25
n	29		28		29		28		24	

Table C.4: Radial velocities for high excitation potential lines of SAO 209008.

HJD (−2450000)	λ5429 Fe I RV (km s^{-1})	λ5429 Fe I Err (km s^{-1})	λ5434 Fe I RV (km s^{-1})	λ5434 Fe I Err (km s^{-1})	λ5615 Fe I RV (km s^{-1})	λ5615 Fe I Err (km s^{-1})	λ5853Ba II RV (km s^{-1})	λ5853Ba II Err (km s^{-1})	λ6162 Ca I RV (km s^{-1})	λ6162 Ca I Err (km s^{-1})
821.134	67.78	0.03	66.06	0.05	65.23	0.07	68.44	0.40	66.71	0.44
823.149	66.23	0.12	67.34	0.04			68.95	0.20	64.66	1.25
868.515	55.11	1.22	57.22	0.75	54.40	1.35	55.93	0.84	55.61	0.20
1131.150	55.83	0.20	56.09	0.11	56.31	0.48	55.60	0.06	55.36	0.07
1170.101	65.53	1.29	64.51	0.20			66.77	0.23		
1173.076	65.12	1.41	66.19	0.11			67.72	0.17		
1174.094	64.53	1.29	66.75	0.94	61.38	0.29	67.40	0.37	64.70	0.73
1196.105	58.19	0.60	58.84	0.22			57.17	1.10		
1221.063	59.67	0.09	60.72	0.17	58.70	0.24	61.64	0.14	60.47	0.11
1227.047	58.96	0.73	57.63	0.07			58.94	0.04		
1230.975	59.50	0.93	59.82	0.05			61.55	0.36		
1246.962	61.89	0.73	60.61	0.62			63.15	0.25		
1248.979	64.14	0.58	63.17	0.30			64.19	0.50		
1251.890	63.18	0.79	63.28	0.06			64.37	0.20		
1304.930	57.75	0.59	57.54	0.60			58.71	0.29		
1326.763	64.12	0.09	63.85	0.10			64.29	0.17		
1552.112	58.23	0.11	58.81	0.30			60.74	0.20		
1555.065	58.92	0.46	57.92	0.70			59.42	0.23		
1626.985	55.66	0.43	55.29	0.84	55.56	0.51	54.90	0.40	54.73	0.41
1644.873	54.36	0.15	55.04	0.15	53.27	1.03	55.43	0.15	55.06	0.40
1645.973							55.22	0.01	55.07	0.03
1646.950	55.30	0.27	56.85	0.22	55.58	0.95	56.49	0.18	55.18	0.08
1647.859							57.34	0.26	56.96	0.22
1655.849	60.23	0.13	60.51	0.35	57.48	1.18	60.79	0.01	61.09	0.03
1667.873	65.11	0.14	67.24	0.26	65.42	0.77	67.85	0.03	66.07	0.10
1679.860	66.35	0.58	66.97	0.50	62.74	0.46	67.89	0.10		
1680.861	66.30	0.69	67.00	0.10	63.02	0.62	67.23	0.12		
1714.785	62.23	0.50	62.51	0.46	59.23	0.37	63.97	0.46	60.16	0.19
1715.812	61.13	0.95	62.92	0.12	59.61	0.43	64.32	0.53	59.79	0.08
1836.170	59.17	0.76	60.00	0.06	58.42	0.61	61.43	0.14	57.20	0.86
1840.154	58.76	0.29	60.25	0.95	56.34	0.72	59.20	0.34	56.88	0.05
1852.116	55.82	0.04	57.19	0.12	56.23	0.66	56.68	0.06	56.68	0.01
1857.060	54.34	0.83	57.52	0.12	56.33	1.47	57.03	0.07	58.58	0.01
1916.036	63.42	0.78	68.22	0.78			66.17	0.22	63.68	0.15
2023.913	63.51	0.08	63.00	0.17	61.51	1.03	64.18	0.04	63.01	0.29
Mean	60.80	0.54	61.42	0.32	58.78	0.70	61.75	0.25	60.38	0.27
σ	4.03	0.41	4.03	0.29	3.58	0.38	4.54	0.23	5.99	0.31
n	33		33		19		35		22	

Table C.5: Radial velocities for low excitation potential lines of HD 70379.

HJD (−2450000)	λ6347 Si II RV (km s^{-1})	λ6347 Si II Err (km s^{-1})	λ6371 Si II RV (km s^{-1})	λ6371 Si II Err (km s^{-1})	λ6562 Hα RV (km s^{-1})	λ6562 Hα Err (km s^{-1})	λ8446 OI RV (km s^{-1})	λ8446 OI Err (km s^{-1})	λ8498 Ca II RV (km s^{-1})	λ8498 Ca II Err (km s^{-1})
821.134	67.74	0.11	66.81	0.26	67.20	0.32				
823.149	66.61	0.26	67.13	0.05	67.39	0.15	72.59	0.14	67.70	0.23
868.515	56.80	0.74	58.02	1.30	62.80	0.99	60.55	1.04	62.68	2.27
1131.150	56.82	0.92	57.54	0.08	63.83	0.14	63.68	0.53	63.24	3.04
1170.101	60.92	1.37	60.46	0.30	63.00	0.19	66.86	0.48	61.56	0.25
1173.076	60.97	0.61	60.41	0.35	64.29	0.29	65.22	0.69	65.18	0.34
1174.094	60.73	0.30	62.20	0.74	65.76	1.11	66.04	1.51	63.58	0.45
1196.105	58.95	0.74	60.42	0.24	61.52	1.48	64.93	0.28	62.56	0.61
1221.063	60.83	0.64	62.66	0.40	64.17	0.05	66.28	1.05	64.50	0.64
1227.047	56.88	0.75	57.04	0.41	56.99	0.36	62.63	0.58	59.56	0.44
1230.975	60.24	0.71	59.74	0.70	62.50	0.24	63.10	1.49	64.18	0.51
1246.962	58.15	0.98	59.97	0.95	60.79	0.61	65.88	0.54	60.79	0.34
1248.979	60.61	1.01	59.12	0.16	61.75	0.24				
1251.890	62.14	0.73	62.25	0.77	62.48	0.43				
1304.930	60.33	0.49	60.31	0.51	60.52	0.99	66.72	0.34	60.96	1.37
1326.763	61.96	0.54	61.72	0.34	65.66	0.15	68.15	0.61	64.93	0.32
1552.112	57.10	0.62	56.74	0.21	64.29	1.57	62.96	0.75	62.82	2.71
1555.065	57.72	0.55	58.23	0.17	63.01	1.37	62.11	0.55	64.02	1.87
1626.985	57.52	0.53	58.54	0.36	72.89	1.72	60.45	2.28	69.92	0.52
1644.873	56.32	0.93	57.33	1.06	64.30	1.65	60.20	0.29	62.21	3.65
1645.973	56.34	1.05	56.91	0.91	59.66	0.43	60.22	0.30	63.05	2.67
1646.950	56.88	1.02	58.21	0.78	62.38	1.09	61.45	0.26	62.99	3.14
1647.859	57.28	0.37	58.44	0.39	60.34	0.49	61.66	0.23	62.52	2.39
1655.849	62.57	0.83	62.29	0.48	63.69	0.57	66.97	0.36	64.40	1.77
1667.873	67.62	0.46	69.05	0.87	68.08	0.52	70.14	0.67	67.47	0.08
1679.860	64.74	0.83	64.45	0.86	65.37	1.09	71.15	0.65	65.66	0.39
1680.861	64.36	0.39	63.39	0.33	65.43	1.23	68.14	0.26	67.07	0.22
1714.785	60.38	0.70	61.26	0.13	70.22	0.27	68.84	1.46	67.07	0.57
1715.812	61.17	0.27	61.97	0.39	70.01	0.31	67.19	1.65	68.73	0.30
1836.170	58.20	0.47	59.25	0.22	67.25	0.22	63.72	0.63	67.02	0.73
1840.154	57.76	0.09	58.35	0.13	66.55	0.65	62.27	0.16	66.18	0.58
1852.116	58.83	0.21	60.80	0.71	63.24	1.32	63.00	0.24	62.09	2.37
1857.060	59.36	0.21	59.41	0.46	60.52	1.13	62.32	0.27	60.56	2.59
1916.036	62.37	0.96	62.94	0.49	65.55	0.90	65.59	0.17	66.74	0.44
2023.913	62.57	0.48	62.07	0.27	62.69	0.08	68.09	0.60	62.97	0.62
Mean	60.28	0.62	60.73	0.48	64.17	0.70	64.97	0.66	64.22	1.20
σ	3.17	0.30	2.96	0.31	3.26	0.51	3.31	0.52	2.56	1.09
n	35		35		35		32		32	

Table C.6: Radial velocities for high excitation potential lines and λ8498 Ca II of HD 70379.

HJD (−2450000)	λ5432 Fe I RV (km s^{-1})	λ5432 Fe I Err (km s^{-1})	λ5572 Fe I RV (km s^{-1})	λ5572 Fe I Err (km s^{-1})	λ5615 Fe I RV (km s^{-1})	λ5615 Fe I Err (km s^{-1})	λ5853 Ba II RV (km s^{-1})	λ5853 Ba II Err (km s^{-1})	λ5857 Ca I RV (km s^{-1})	λ5857 Ca I Err (km s^{-1})
668.827							−9.86	0.47	−19.30	0.78
868.618	−18.73	0.29	−19.40	1.07	−21.13	0.99	−17.50	0.43	−20.16	0.66
1006.860	−21.39	0.69					−22.20	1.11	−22.14	0.31
1221.162	−25.96	0.24	−27.68	0.67	−28.44	0.35	−25.87	0.45	−27.86	0.10
1230.067	−27.94	1.81	−29.38	1.40	−31.08	0.47	−29.00	1.35	−27.64	0.21
1231.119	−29.35	0.13	−30.01	0.12	−31.62	0.24	−26.37	0.30	−27.99	0.81
1247.031	−28.79	0.21					−31.21	0.11	−28.98	0.21
1302.942	−24.02	0.69	−27.84	0.67	−28.97	0.20	−24.81	0.63	−31.23	1.12
1326.852	−34.65	0.60	−37.39	0.64	−41.64	1.61	−36.76	0.80	−36.34	0.04
1334.872	−34.18	0.50	−33.61	0.68	−34.68	0.60	−35.78	1.09	−32.52	0.23
1338.853	−30.97	0.06	−30.96	0.05	−33.15	0.74	−34.76	0.54	−29.83	0.25
1382.833	−30.21	0.07	−31.78	0.15	−31.45	0.54	−26.92	0.11	−31.36	0.25
1399.801	−29.48	0.18	−30.43	0.05	−29.94	0.17			−31.38	0.24
1408.814	−32.59	0.82	−36.24	0.26	−39.58	0.97	−36.75	0.04	−35.62	1.23
1627.050	−38.01	0.59	−38.68	0.04	−38.86	0.18	−37.80	0.64	−36.23	0.34
1629.007	−37.03	0.09	−37.58	0.26	−38.60	0.18	−36.73	1.02	−33.56	0.14
1630.041	−37.67	0.28	−35.65	0.24	−40.31	1.23	−34.60	1.73	−34.56	0.09
1632.002	−35.57	0.21	−37.43	0.36	−38.51	1.05	−38.19	0.78	−37.23	0.32
1644.988	−32.98	0.31	−31.81	0.12	−34.63	0.88	−33.86	0.20	−30.75	0.18
1647.033	−31.31	0.22	−32.07	0.38	−34.29	0.91	−33.24	0.07	−31.86	0.18
1647.973	−30.20	0.28	−30.02	0.25	−32.59	0.35	−32.81	0.03	−30.30	0.20
1655.931	−27.71	0.05	−28.14	0.12	−28.89	0.29	−29.47	0.40	−29.64	0.59
1669.931	−29.09	0.35	−29.29	0.92	−30.30	0.52	−27.41	0.42	−30.08	0.17
1678.837	−32.97	0.32	−30.58	1.66	−29.36	1.79	−29.34	0.45	−27.32	1.78
1683.833					−32.15	2.03	−28.86	0.37	−32.48	1.04
1715.873	−31.39	0.23	−30.48	0.86	−32.05	0.79	−28.71	0.04	−30.51	0.35
1896.153			−26.91	0.88			−28.30	0.04	−24.11	0.48
1897.030			−27.30	1.08	−27.13	0.40	−27.89	0.15	−24.47	0.72
1916.100	−22.85	0.30					−23.71	0.05		
2023.988			−12.10	0.46	−11.52	0.07			−18.23	1.10
2025.949	−6.33	0.29	−9.77	0.71	−7.42	0.07	−3.10	0.50		
2052.881	−7.68	0.54	−8.17	0.21	−10.39	0.24	−2.43	0.13	−11.25	0.20
2054.816	−7.90	1.10	−10.12	0.35	−10.76	0.62	−1.19	0.70	−12.17	1.55
2056.861	−9.66	0.38	−10.04	0.40	−10.31	2.14	−1.49	0.26	−8.05	0.81
2089.799			−12.96	0.13						
2091.850			−11.36	0.20						
2092.907			−12.04	0.36						
2092.907										
Mean	−25.38	0.43	−24.37	0.46	−28.96	0.71	−24.06	0.47	−26.62	0.55
σ	10.24	0.37	10.56	0.40	9.83	0.58	12.62	0.41	8.33	0.46
n	32		36		29		35		34	

Table C.7: Radial velocities for low excitation potential lines of HD 95767.

HJD	λ6347 Si II		λ6371 Si II		λ6562 Hα		λ8446 O I		λ8498 Ca II	
(−2450000)	RV (km s^{-1})	Err (km s^{-1})	RV (km s^{-1})	Err (km s^{-1})	RV (km s^{-1})	Err (km s^{-1})	RV (km s^{-1})	Err (km s^{-1})	RV (km s^{-1})	Err (km s^{-1})
668.827	−16.98	1.26	−17.50	2.00	−17.44	1.63				
868.618	−17.94	1.31	−17.96	1.07	−18.47	0.61	−12.31	1.09	−13.73	0.34
1006.860	−20.26	0.81	−21.54	0.62	−22.94	0.82	−14.42	0.09	−17.12	0.33
1221.162	−27.73	0.56	−26.62	0.13	−26.63	0.10	−22.05	0.22	−21.57	0.76
1230.067	−27.90	0.30	−29.92	0.39	−28.65	0.81	−21.11	1.08	−24.89	0.34
1231.119	−30.53	1.86	−29.64	0.53	−30.16	0.81	−24.63	0.73	−24.62	0.48
1247.031	−29.93	1.01	−29.99	0.72	−33.57	1.12	−21.50	0.68	−27.05	0.02
1302.942	−25.68	1.06	−26.79	0.73	−30.93	0.15	−21.47	1.40	−29.82	1.05
1326.852	−36.75	0.14	−37.06	0.66	−33.70	1.99	−28.20	0.65	−30.53	0.12
1334.872	−32.12	0.19	−31.13	0.06	−32.02	1.11	−28.03	0.31	−31.00	0.43
1338.853	−30.67	0.33	−31.70	0.50	−32.21	0.99	−27.90	0.28	−31.15	0.29
1382.833	−30.04	0.03	−30.16	0.45	−27.72	0.84	−27.44	0.20	−25.98	1.32
1399.801	−30.95	0.45	−30.45	0.23	−27.29	0.62	−26.67	0.54	−25.08	1.68
1408.814	−35.55	0.58	−33.85	1.06	−30.48	0.24	−29.06	0.98	−27.91	2.35
1627.050	−37.50	0.70	−37.61	0.87	−26.18	0.67	−33.41	0.35	−22.41	0.15
1629.007	−37.38	1.21	−34.61	0.85	−26.30	0.40	−29.21	0.53	−25.84	0.07
1630.041	−37.22	1.49	−36.12	0.94	−27.05	0.83	−30.96	0.84	−28.03	0.10
1632.002	−36.87	0.24	−35.90	0.34	−27.10	1.25	−30.38	0.18	−25.36	0.29
1644.988	−33.35	1.30	−31.08	0.68	−27.93	0.99	−28.11	0.46	−24.46	0.41
1647.033	−32.49	1.26	−30.82	0.99	−28.08	0.42			−24.35	0.02
1647.973	−31.28	1.00	−29.25	0.34	−28.19	0.41	−28.71	0.57	−23.91	0.13
1655.931	−30.12	0.50	−27.84	0.18	−26.87	0.21	−23.17	0.22	−24.28	0.49
1669.931	−30.72	0.77	−29.47	0.17	−26.16	0.19	−27.28	1.37	−22.02	0.30
1678.837	−29.89	1.93	−28.69	1.83	−24.97	0.20	−23.69	1.23	−23.59	0.72
1683.833	−31.99	1.84	−34.32	1.19	−26.99	0.24	−28.51	2.26	−23.38	0.12
1715.873	−31.88	0.93			−24.74	0.14	−26.58	0.51	−21.31	0.58
1896.153					−30.89	0.19	−20.80	0.34	−29.52	0.15
1897.030	−29.43	2.16	−32.19	1.79	−29.57	0.05	−21.65	1.10	−31.13	0.16
1916.100					−26.94	0.18			−28.60	0.10
2023.988	−10.17	0.72	−10.13	1.57	−17.00	0.34	−4.13	0.57	−19.13	0.36
2025.949	−10.77	1.46	−10.60	0.33	−14.34	0.23	−3.77	0.67		
2052.881	−13.00	0.85	−13.40	0.39						
2054.816	−11.93	0.18	−10.90	0.39						
2056.861	−13.35	1.05	−11.37	0.39						
Mean	−26.31	0.90	−26.07	0.72	−26.82	0.61	−23.76	0.69	−25.10	0.47
σ	9.11	0.56	9.07	0.50	4.68	0.48	7.32	0.48	4.20	0.53
n	35		33		31		28		29	

Table C.8: Radial velocities for high excitation potential lines and λ8498 Ca II of HD 95767.

HJD (−2450000)	λ5432 Fe I RV (km s^{-1})	λ5432 Fe I Err (km s^{-1})	λ5572 Fe I RV (km s^{-1})	λ5572 Fe I Err (km s^{-1})	λ5588 Ca I RV (km s^{-1})	λ5588 Ca I Err (km s^{-1})	λ5615 Fe I RV (km s^{-1})	λ5615 Fe I Err (km s^{-1})	λ5857 Ca I RV (km s^{-1})	λ5857 Ca I Err (km s^{-1})
669.066			−80.12	1.19	−84.18	0.80	−83.95	0.83		
748.947	−88.97	0.28	−88.71	0.44	−88.56	0.36	−93.42	0.10	−89.30	0.48
985.113	−95.29	0.24	−90.37	0.74	−84.81	0.41	−87.80	0.19	−86.90	0.61
1008.170	−95.25	3.27								
1028.958			−89.51	0.72	−88.64	0.99			−87.66	0.93
1033.052	−94.22	0.20			−86.34	0.21	−88.19	1.41		
1130.863	−90.99	0.04	−89.27	0.15	−88.04	0.14				
1252.230	−82.21	0.13	−92.17	0.15	−86.60	0.14	−88.63	0.14		
1303.218	−86.46	1.74	−84.67	1.01	−86.71	0.27	−87.45	0.62	−90.22	0.56
1305.088					−87.58	0.35				
1317.710			−85.80	0.05	−83.32	0.06	−83.78	0.45	−83.22	0.05
1323.110			−83.52	0.23	−83.28	0.01	−84.28	0.26		
1327.177			−84.87	0.23	−84.88	0.07	−85.00	0.00	−85.80	0.06
1334.224			−83.04	0.15	−80.78	0.39	−81.42	0.49	−83.03	0.07
1380.056	−83.70	0.81	−85.68	0.45	−84.62	0.14	−83.07	0.12	−85.30	0.45
1400.117	−81.56	0.49	−82.18	0.02	−82.06	0.03	−81.70	0.29	−83.68	0.21
1402.994	−82.58	0.08	−84.36	0.26	−82.04	0.07	−81.78	0.04	−82.84	0.59
1409.029	−82.35	0.04	−84.01	0.26	−86.86	0.53	−84.35	0.21	−84.61	0.26
1410.967	−81.74	0.10	−83.09	0.16	−85.97	0.55	−86.20	0.31	−86.55	0.14
1414.023			−85.77	0.04	−82.11	0.63	−84.01	0.99	−83.12	0.61
1629.231	−80.33	0.20	−84.96	0.16	−84.16	0.85	−82.69	0.28	−81.22	1.39
1647.218			−86.28	0.96	−84.11	0.20	−85.30	0.21	−82.79	0.18
1648.215	−86.54	0.75	−90.16	2.91	−84.67	0.48	−85.77	1.12	−87.85	0.28
1656.212	−84.03	0.11	−87.01	0.43	−86.45	0.19	−86.19	0.74	−85.79	1.02
1668.189			−83.69	0.72	−82.25	0.05	−83.01	0.37	−85.41	0.12
1681.127	−80.16	0.67	−83.54	0.03	−81.63	0.02	−82.39	0.30	−84.25	0.16
1684.184	−82.34	0.16	−85.84	0.16	−85.82	0.14	−85.29	0.33	−83.46	0.18
1715.170	−83.07	0.18	−84.96	0.21	−84.42	0.11	−83.85	0.39	−84.30	0.60
1716.164	−84.06	0.90	−85.89	0.14	−83.01	0.27	−83.86	0.35		
1717.148	−85.11	0.47	−84.61	0.89	−83.98	0.51	−85.01	0.50	−87.42	2.29
1736.086	−82.54	0.77	−84.96	0.22	−81.86	0.12	−83.51	0.93	−82.90	0.14
1737.048	−81.66	0.46	−83.77	0.23	−83.04	0.12	−84.20	1.29	−80.41	1.22
1739.076	−82.19	0.37	−83.29	0.70	−82.70	0.06	−86.76	0.59	−85.32	0.12
1749.098	−84.41	1.36	−83.62	0.88	−81.70	1.57				
1750.051	−81.60	0.62			−80.69	0.20	−83.18	1.33	−83.48	0.63
1751.124	−84.75	0.11	−84.65	1.27	−83.34	0.24			−85.81	0.16
1766.029	−86.74	0.56	−82.74	0.27	−80.26	0.33	−82.46	0.44	−86.91	0.21
1777.060	−86.60	2.20	−88.70	0.09	−84.16	0.36	−86.04	0.41	−83.07	2.34
1802.936	−84.18	2.08	−87.42	0.97	−85.95	0.28	−85.50	0.54		
1804.029	−84.50	0.20	−87.59	1.30	−85.89	0.06	−86.09	0.30	−86.10	0.36
1835.871			−80.27	0.51	−79.80	0.17	−81.14	0.75	−83.07	0.84
1852.846	−79.51	0.17	−81.57	0.17	−81.98	0.41	−79.72	0.33	−82.32	0.35
1856.850	−81.71	0.53	−83.72	0.45	−83.57	0.44	−80.64	0.94	−83.76	0.40
2025.246	−80.83	0.69	−83.10	2.20	−80.11	0.13	−79.98	0.43		
2026.248	−79.34	0.32	−79.66	0.33	−79.45	0.04	−79.39	0.11	−80.47	0.83
Mean	−84.49	0.66	−85.10	0.55	−84.02	0.33	−84.28	0.50	−84.66	0.55
σ	4.13	0.75	2.83	0.59	2.48	0.35	2.76	0.37	2.34	0.56
n	35		41		45		39		34	

Table C.9: Radial velocities for low excitation potential lines of HD 172481.

HJD	λ6347 Si II		λ6371 Si II		λ6562 Hα		λ8446 O I		λ8498 Ca II	
	RV	Err	RV	Err	RV	Err	RV	Err	RV	Err
(−2450000)	(km s^{-1})	(km s^{-1})	(km s^{-1})	(km s^{-1})	(km s^{-1})	(km s^{-1})	(km s^{-1})	(km s^{-1})	(km s^{-1})	(km s^{-1})
669.066	−87.51	1.01	−83.35	0.67	−77.99	0.24	−77.21	1.62	−76.20	0.82
748.947	−89.96	0.24	−90.67	0.58	−80.50	0.74	−84.18	0.12	−78.01	0.19
985.113	−88.57	2.20	−89.88	0.82	−79.85	0.02	−80.82	0.24	−79.75	0.33
1008.170	−95.87	0.54	−95.17	2.07	−82.59	0.19			−81.22	0.26
1028.958					−82.65	0.14			−80.60	0.18
1033.052	−91.53	2.08	−91.03	0.55	−82.79	0.25			−81.04	0.22
1130.863	−87.76	0.57	−87.06	1.08	−81.13	0.11			−82.00	1.39
1252.230	−88.02	1.05	−88.62	1.39	−79.87	0.60	−81.66	0.53	−79.39	1.15
1303.218			−89.29	2.49	−83.99	0.22	−82.25	0.74	−81.72	0.33
1305.088	−89.03	2.03	−86.18	2.14	−85.64	0.63			−83.16	0.05
1317.710	−88.31	1.30	−84.96	1.48	−81.98	0.16	−83.31	0.54	−79.87	0.07
1323.110	−87.17	1.77	−85.24	0.99	−82.76	0.06			−81.23	0.03
1327.177	−86.04	0.88	−86.66	0.97	−85.36	0.34			−82.04	0.12
1334.224	−82.68	1.31	−81.12	0.71	−81.94	0.21	−78.57	1.51	−79.33	0.24
1380.056	−88.04	1.46	−84.05	0.60	−79.12	0.03	−78.96	0.40	−79.37	0.05
1382.093	−88.27	0.12	−88.75	0.52	−81.97	0.46				
1400.117	−83.48	1.03	−84.20	0.14	−79.16	0.22	−79.97	0.57	−80.08	0.24
1402.994	−84.06	0.37	−83.52	0.23	−78.70	0.30	−77.64	0.12	−76.95	0.18
1409.029	−84.46	0.98	−85.42	0.53	−80.09	0.56	−78.90	0.91	−80.86	0.59
1410.967	−84.41	0.41	−85.42	0.38	−80.07	0.61	−75.52	0.41	−82.01	0.37
1414.023	−84.98	1.08	−81.23	0.36	−78.61	0.21			−78.78	0.09
1629.231			−83.44	0.95	−78.02	0.30	−82.98	0.42	−80.20	0.81
1646.227	−85.57	3.35	−85.35	2.22	−79.08	0.45	−77.40	3.27	−78.90	0.10
1647.218	−85.01	0.54	−86.55	1.03	−78.67	0.15	−78.58	0.18	−79.52	0.94
1648.215	−85.04	0.29	−86.72	0.58	−79.02	0.34	−82.33	1.34	−79.07	0.77
1656.212	−85.43	0.47	−86.07	1.02	−78.05	0.09	−79.09	0.72	−76.52	0.27
1668.189	−85.92	0.17	−83.88	0.78	−78.25	0.11	−78.96	0.50	−77.52	0.60
1681.127	−83.22	0.34	−84.49	0.49	−79.64	0.33	−79.49	1.16	−79.08	0.45
1684.184	−84.94	0.28	−82.96	0.08	−82.40	0.24	−78.95	0.38	−80.54	0.21
1715.170	−84.94	0.33	−84.06	0.24	−78.44	0.09	−79.92	0.25	−79.67	1.29
1716.164	−83.76	0.24	−82.86	0.46	−80.09	0.64	−77.69	0.39	−79.89	0.65
1717.148	−85.69	0.47	−84.17	1.24	−79.46	0.90	−79.82	0.82	−79.33	0.49
1736.086	−86.85	0.47	−81.72	0.24	−80.80	0.41	−80.87	0.88	−80.68	0.55
1737.048	−84.07	0.51	−82.22	0.55	−81.84	0.44	−79.10	0.31	−80.74	0.90
1739.076	−83.70	0.78	−83.03	0.68	−80.56	0.26	−74.58	0.14	−80.77	0.74
1749.098	−84.19	1.74	−84.00	1.80	−81.55	0.57	−79.98	0.57	−80.62	0.79
1750.051	−83.68	0.80			−80.85	0.56	−79.09	0.57	−80.41	0.26
1751.124	−83.91	1.16	−81.75	0.25	−80.80	0.30	−80.48	0.67	−80.10	0.61
1766.029	−88.00	0.54	−84.97	0.36	−80.65	0.21	−81.79	0.37	−81.12	0.27
1777.060	−85.28	0.23	−85.64	1.47	−82.04	0.66	−81.40	0.52	−82.91	0.19
1802.936	−84.67	1.03			−82.78	0.34	−80.11	0.43	−83.06	0.10
1804.029	−85.05	0.78	−85.21	0.49	−82.86	0.13	−79.83	0.28	−86.39	0.22
1835.871	−83.54	1.27	−82.01	1.14	−82.23	0.67	−76.52	0.26	−84.27	0.18
1852.846	−81.49	0.25	−80.84	0.15	−80.10	0.36	−74.57	0.13	−82.73	0.45
1856.850	−82.68	0.37	−81.79	0.11	−80.38	0.43	−75.97	0.25	−81.50	0.71
2025.246	−81.98	0.36	−79.67	0.19	−83.81	0.18	−79.09	0.21	−83.88	0.66
2026.248	−81.35	0.23	−80.40	0.45	−83.58	0.11	−76.83	0.36	−85.56	0.76
Mean	−85.68	0.85	−84.90	0.81	−80.91	0.33	−79.33	0.61	−80.62	0.45
σ	2.77	0.68	3.15	0.61	1.94	0.21	2.30	0.58	2.12	0.34
n	44		44		47		38		46	

Table C.10: Radial velocities for high excitation potential lines and λ8498 Ca II of HD 172481.

HJD (−2450000)	λ6347 Si II RV (km s^{-1})	λ6347 Si II Err (km s^{-1})	λ6371 Si II RV (km s^{-1})	λ6371 Si II Err (km s^{-1})	λ5453 S II RV (km s^{-1})	λ5453 S II Err (km s^{-1})	λ6578 C II RV (km s^{-1})	λ6578 C II Err (km s^{-1})	λ5875 He I RV (km s^{-1})	λ5875 He I Err (km s^{-1})
1008.135	10.50	0.95	9.97	1.26	12.76	1.74	17.03	1.12	18.51	2.24
1032.028							11.30	1.28	15.08	1.15
1034.028	0.98	0.75	−4.12	2.80			2.04	2.48		
1305.130	6.42	0.37	7.02	0.46	13.01	2.71	15.44	0.76	17.09	1.39
1322.136	0.58	0.90	−0.53	0.75			8.65	1.07	14.24	0.37
1327.097	−3.44	0.87	−3.35	0.60	3.89	0.98	6.63	0.78	11.71	0.48
1340.092	9.29	3.07	9.35	1.05			14.10	0.35	19.37	0.92
1380.007	0.62	0.27	1.50	1.34	5.09	0.29	8.69	0.84	9.37	0.76
1382.032	−3.16	1.07	−1.50	1.71			5.97	0.50	8.44	1.68
1401.023	5.99	1.46	7.41	1.98	6.26	4.24			15.38	2.08
1410.888							7.99	1.88	16.26	1.03
1413.988	3.95	1.20	6.42	2.31	13.09	1.02	14.26	1.84	17.32	1.76
1630.238	4.72	0.94	3.93	0.30	8.14	2.36	9.51	2.39	16.18	0.88
1632.193							11.11	2.22	15.32	1.28
1646.198			0.14	0.74			11.37	1.51	11.84	0.39
1656.177			3.35	0.99					16.96	0.74
1668.145	11.34	2.81	11.81	1.76			15.54	1.87	19.06	0.34
1679.158			3.04	2.37	7.06	2.96			13.05	0.82
1716.083	1.49	0.68	4.09	0.98	11.66	1.68	13.80	0.41	19.00	0.96
1736.020	3.32	1.53					14.26	1.93	16.50	0.24
1749.031	7.38	0.88	7.66	2.25	8.86	2.51	13.59	1.44	12.24	1.11
1764.832	8.29	0.86	8.76	0.64	11.25	3.32	13.92	1.49	22.14	1.08
1803.990					7.27	2.19	10.51	1.87	11.60	0.22
2026.169	−4.05	0.89	−1.21	1.18	9.15	3.06	6.01	0.76	9.52	1.17
Mean	3.78	1.15	3.88	1.34	9.04	2.24	11.03	1.37	15.05	1.00
σ	4.83	0.75	4.76	0.73	3.10	1.08	3.89	0.66	3.59	0.56
n	17		19		13		21		23	

Table C.11: Radial velocities of HD 168625.

HJD (−2450000)	λ6347 Si II RV (km s^{-1})	λ6347 Si II Err (km s^{-1})	λ6562 Hα RV (km s^{-1})	λ6562 Hα Err (km s^{-1})	λ6383 Fe II RV (km s^{-1})	λ6383 Fe II Err (km s^{-1})	λ5453 S II RV (km s^{-1})	λ5453 S II Err (km s^{-1})	λ5875 He I RV (km s^{-1})	λ5875 He I Err (km s^{-1})
979.980	0.70	0.19	−53.91	0.28					17.72	0.14
1007.123	2.99	0.92	−55.95	0.56			6.61	2.22	12.11	1.81
1007.969	4.74	0.19	−56.40	0.76						
1031.985	1.80	0.49	−52.78	1.48	−0.22	0.06			16.83	0.26
1303.142	11.86	0.59	−57.54	0.72	4.86	0.15	17.24	0.52		
1317.571	−5.11	0.12	−55.79	0.46						
1323.028	−2.32	0.98	−55.47	0.73	12.73	0.04	7.45	0.10	8.48	1.47
1327.054	1.29	0.19	−57.69	0.84	−1.16	0.47	5.60	1.14	13.11	1.09
1381.959	9.03	0.19	−54.59	0.77					19.22	1.91
1400.001	−5.86	1.06	−56.70	0.86						
1408.946	−2.62	0.18	−56.63	0.54	7.91	0.50			17.91	0.42
1626.212	9.07	0.43	−54.93	0.53	7.53	0.10	18.59	0.89	22.81	1.91
1648.184	3.88	0.39	−53.55	1.61			5.71	0.14		
1656.100	16.82	1.02	−52.86	1.40	6.47	3.19				
1668.067	−0.81	0.84	−51.79	1.32	1.93	0.48			14.10	2.61
1681.063	−0.91	0.52	−49.06	0.46	2.50	0.20	1.26	1.31	6.99	0.69
1715.034	−3.02	0.27	−49.16	0.15					17.91	2.53
1716.990	0.56	2.51	−49.37	0.46	6.27	0.19				
1735.943	5.35	0.53	−50.98	0.05			13.53	2.41	21.33	2.17
1748.958	0.70	1.49	−53.13	0.39	1.65	0.11	13.02	1.38	10.69	0.91
1765.897	−2.26	0.23	−52.84	0.38						
1776.934	4.06	1.00	−52.64	0.43			13.20	3.67	17.77	1.75
1803.942	8.54	1.59	−54.87	0.48	3.94	0.07				
2024.249	0.45	0.28	−52.13	0.74	3.82	0.09	8.52	1.23	13.27	0.98
Mean	2.46	0.67	−53.78	0.68	4.48	0.43	10.07	1.36	15.35	1.38
σ	5.52	0.58	2.55	0.41	3.76	0.84	5.41	1.06	4.58	0.80
n	24		24		13		11		15	

Table C.12: CPD-59 6723 radial velocities from MJUO for λ6562 Hα, λ6347 Si II, λ6383 Fe II, λ5453 S II and λ5875 He I.

Index